Lehrstuhl für Elektrische Antriebssysteme und Leistungselektronik
der Technischen Universität München

A High Performance Power Supply based on a Four-Leg Three-Level NPC Converter for Non-linear and Unbalanced Systems

Felix Eduardo Rojas Lobos

Vollständiger Abdruck der von der Fakultät für Elektrotechnik und Informationstechnik der Technischen Universität München zur Erlangung des akademischen Grades eines

Doktor-Ingenieurs

genehmigten Dissertation.

Vorsitzender: Univ.-Prof. Dr.-Ing. Rolf Witzmann
Prüfer der Dissertation:
1. Univ.-Prof. Dr.-Ing. Ralph Kennel
2. Prof. Jon Clare,
   The University of Nottingham / UK

Die Dissertation wurde am 30.12.2015 bei der Technischen Universität München eingereicht und durch die Fakultät für Elektrotechnik und Informationstechnik am 08.06.2016 angenommen.

To my beloved son Julian Rojas

Acknowledgment

In first place I would like to thanks my parents, Ximena and Felix, for their unconditional love and support during all my life, which allows me to be the man who I am now. Likewise, I want to thank to the love of my life, Daniela, for her unlimited love and invaluable support, encouragement and patient throughout these years, which helped me to successfully finish this work.

I also want to thank to Prof. Dr. Ralph Kennel for his support and advice during these four years at his chair. Specially thanks for encourage me always to give my best, give me the freedom to think and try by myself and for your willingness to always help me when I required it.

A special paragraph deserves Prof. Roberto Cardenas, who has been a very important person in my professional development since my bachelor studies. Thank you for all the time you have dedicated to guide me and advice me during this dissertation.

My special thanks to the Power Electronics Machines and Control (PEMC) group of the Nottingham University, England, for their warm welcome during my stay at their group and their technical support throughout this work. Special thanks to Prof. Dr. Jon Clare, Prof. Dr. Pat Wheeler, Dr. Alan Watson and Prof. Dr. Pericles Zanchetta for their willingness and constructive comments, which help me to improve this work.

Finally, I would like to thank to the Chilean research commission "Comisión Nacional de Investigación Científica y Tecnológica" (CONICYT) and the German Academic Exchange Service "Deutscher Akademischer Austauschdienst" (DAAD) for their financial support during this years.

Munich, 10 December 2015
Felix Rojas

Abstract

Throughout this work, the reader will find a comprehensive review and discussion about the state of the art and future perspectives of power electronics converters implemented in four-wire applications. The three-dimensional Space Vector Modulation (SVM) problem for this kind of converters is extensively discussed in this dissertation and a simple modulation algorithm for a three-level four-leg NPC converter is proposed and successfully validated in an experimental rig. Furthermore, additional issues barely reported in the literature for the four-leg NPC converter, such as: design of different switching patterns without requirement of Look-up Tables (LUT), the capability for balancing the voltages on the dc-link capacitors under unbalanced and non-linear loads, the overmodulation problem in a three-dimensional space and study of the switching frequency of the devices of the converter under modulation of non-sinusoidal and non-balanced voltages, are widely discussed.

Afterwards, the proposed modulation technique is implemented in an aerospace application as a Ground Power Unit (GPU), also known as Ground Power Supply. This power supply provides fixed sinusoidal phase-to-neutral voltages of $400Hz$ and $110V$ to an unbalanced and non-linear load, exploiting the capabilities of the four-leg NPC converter to handle with zero-sequence components. For successfully achieve this purpose, resonant controllers are implemented for compensation of until eleventh order harmonics, which are suitable solution for this application, providing excellent steady-state and transient performance.

Kurzfassung

In dieser Arbeit wird dem Leser ein umfassender Überblick über den Stand der Technik sowie Zukunftsperspektiven für Umrichter mit 4 Zweigen in vierphasigen Systemen präsentiert. Die dreidimensionale Raumzeigermodulation für diese Art von Umrichtern wird in dieser Arbeit ausführlich diskutiert und ein neuer einfacher Modulationsalgorithmus für einen drei-Level NPC Umrichter mit 4 Zweigen vorgestellt. Anschließend wird dieses Verfahren experimentell am Prüfstand untersucht. Darüber hinaus werden weitere Probleme für drei-level NPC Umrichter mit 4 Zweigen in dieser Dissertation analysiert und diskutiert, wie zum Beispiel: Entwurf unterschiedlicher Pulsmuster ohne Umsetzungstabellen zu benötigen, die Fähigkeit zum Ausgleich der Spannungen an den Zwischenkreiskondensatoren für unsymmetrische und nichtlineare Lasten, die Übermodulation in einem dreidimensionalen Raum und eine Untersuchung der Schaltfrequenz des Umrichters für Modulation von nichtsinusförmigen und unsymmetrischen Spannungen. Danach wird das vorgeschlagene Modulationsverfahren in einer Luft-und Raumfahrt Anwendung als Ground Power Unit (GPU), die auch als Bodenstromversorgung bekannt ist, implementiert. Diese Stromversorgung speist eine unsymmetrische und nichtlineare Last mit einer festen sinusförmigen Phasenspannung von 400 Hz und 110 V, wobei die Fähigkeit des drei-Level Umrichters mit 4 Zweigen, die Nullkomponenten des Stromes einzustellen, ausgenutzt wird. Zu diesem Zweck werden Resonanzregler zur Kompensation von Harmonischen bis zur elften Ordnung implementiert. Es wird nachgewiesen, dass Resonanzwandler eine funktionierende Lösung für diese Anwendung darstellen und eine ausgezeichnete stationäre und transiente Funktion erzielt werden kann.

Contents

CHAPTER 1

Introduction

The general structure of an electrical interconnected system is presented in Fig. 1.1, which can be divided into three main sectors: generation, transmission and distribution systems. The interconnection of several generation units to provide energy to the end consumers sets up a complex network, which first approaches were established around the early 20^{th} century. For many decades this system was controlled by semi-automatic mechanical methods, based on a demand-driven operation. By that, the inertia of the huge electrical generators incorporated in the generation sector are fundamental to ensure the stability of the system, as their stored energy (inertia) allows to overcome unfavorable transients conditions, such as temporal failures or connection/disconnection of large loads [1]. Furthermore, the inductive nature of the long transmissions lines facilitates the control of frequency and voltage magnitude along the system [1]. Thereby, the active power delivered by generators can be directly associated to the control of the system frequency, while its reactive power, along with the use of reactive passive elements, is associated to the control of the voltage magnitude at the different bars of the interconnected system. Under this scenario, the three actors of the system were clearly identifiable and coordinated by a Transmission (TSO) and Distribution System Operator (DSO) to maintain an stable operation of the system.

After the first mercury arc valve was invented and used as the first rectifier by Peter Cooper Hewitt in 1902 [3], a tremendous growth in research and development of power electronics devices and applications started in this field and it is still being carried out until today. Thereby, in 1920 the first mercury arc valve based rectifier came into the market and was implemented in several low and high power industrial application, such as: rectification for public lighting, railway applications, High Voltage Direct Current Systems (HVDC) or battery chargers [4]. It was not until the 60's, with the introduction of solid state semiconductors, that low-power mercury arc valves were replaced by solid stated semiconductors. Consequently, with the fast development of solid state semiconductors, in 1975 they became also available in the market for of high-power ranges, leaving obsolete the mercury arc valves.

Since 1975, the solid state semiconductors boosted the development of more sophisticated

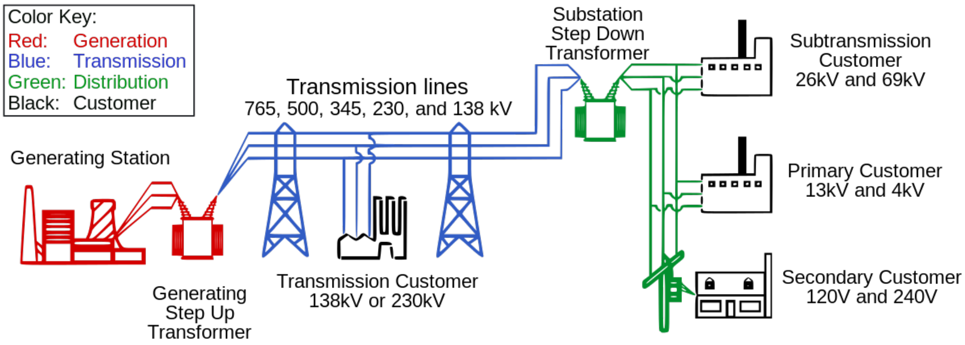

Figure 1.1: Simple representation of a typical electrical system composed of Generation, Transmission and Distribution sectors. Diagram obtained from [2].

power electronic devices, such as IGBTs, IGCTs, GTOs, MOSFETS and Diodes [5]. By that, several high performance applications have been introduced into the market in the last four decades, such as: electrical drives for electrical machines, Uninterruptible Power Supply, Dynamic Voltage Restorers, Active Filters, Static VAR Compensators, *dc* power supplies and Active Front End rectifiers among others [5]. This fast development, along with the fast improvement of efficiency and reduction of prices on renewable energy systems, such as: Fuel Cell, photovoltaic cells and wind mills, have been changing the structure of the generation sector during the last decade. Thus, instead of incorporation of the typical huge generation power plants, several groups of small generation units, known also as Distributed Power Generation (DPG), are being incorporated to the electrical system every year [6, 7]. Fig. 1.2 shows the summary of the incorporation of installed power capacity for the last 15 years in the European Union, presented by *The European Wind Energy Association* (EWEA) [8]. As it can be seen, in 2014 the Renewable Energy System (RES) represents almost the 80% of the installed capacity.

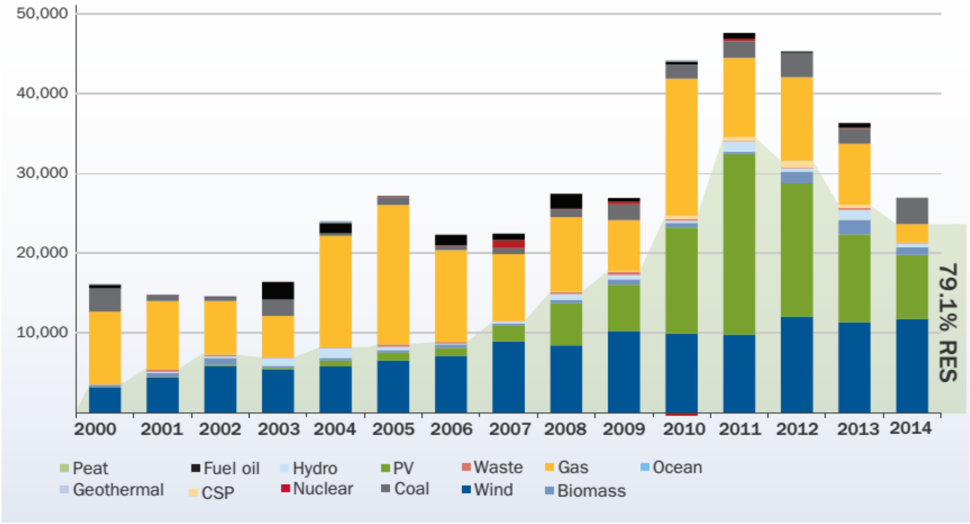

Figure 1.2: Growth of the installed power generating capacity per year in MW and Renewable Energy System (RES) share (%) . Diagram obtained from [8].

In this context, the use of power electronic converters is essential for the incorporation of RES into the electric system. These interfaces can be used not only for delivering the energy from the renewable source to the grid, but also for creating a more flexible and efficient electrical system [6, 7]. Thereby, the incorporation of local generation units into the distribution grids, together with the fast incorporation of electromobility and government policies to promote the installation of RES by the end customers is leading to a new paradigm in the electrical sector, known as μGrids, which modifies the typical Generation-Transmission-Distribution structure to a decentralized system, where the generation sector is spread all over the network. Fig. 1.3, shows a typical scheme of a μGrid, which can be considered as a four-wire network, where several different customers are connected to the phase-to-neutral voltages of the grid. This network provides several advantages compared to a standard electrical system, such as:

- Distributed Power Generation. Theoretically allows island operation mode.
- Bi-directional Power Flow.
- Active demand Management.
- Full controllability under faults and transients periods.

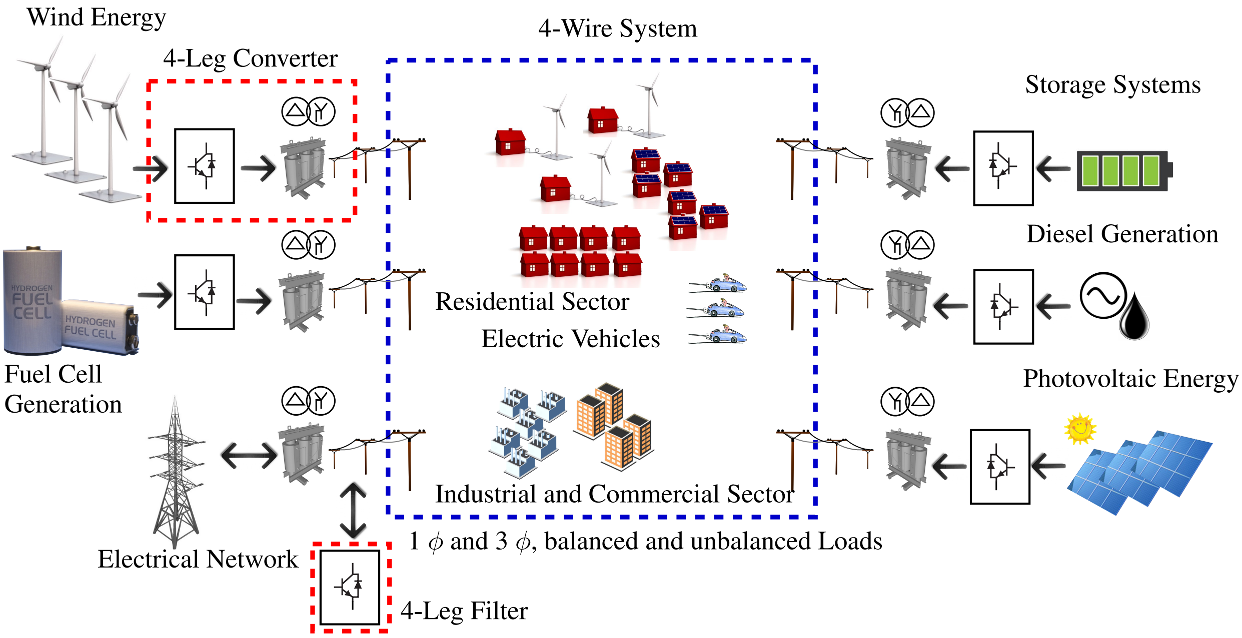

Figure 1.3: Representation of a μGrid connected to the electrical main grid. Delta-Wye transformer can be replaced by four-leg converters.

As presented in Fig. 1.3, a μGrid does not represent necessarily an isolated system, but it is integrated into the electrical main grid. This enables island operation mode in case of grid outage, providing a more reliable uninterrupted energy service to the final customers. However nowadays, due to the lack of hierarchical controllability by DSOs and TSOs and the poor capability of the power converters to work as interconnected units, the operation of a μGrid is restricted only to grid connection, limiting the isolated operation mode to prevent prospective damage to electrical system [6, 7]. This considerably limits the real potential of the system, depriving of energy to customers when it is not strictly necessary. Naturally, this represents a new challenge to the TSOs and DSOs and has been already acknowledge by the European authorities through the *European Distribution System Operators* (EDSO) for Smart Grids and the *Agency for Cooperation of Energy Regulators* (ACER), who highlighted the importance of TSO-DSO cooperation for a efficient development of electrical grids [9].

The regulation of isolated operation and the control of the interconnected power electronic converters to maintain an stable grid represent one of the important challenges for the coming years, which can be considered the first transition step in the constitution of a new structure of an electrical system. Thereby, the development of new topologies and control strategies for controlling power flows, regulating voltage and frequency and compensating harmonic distortion among interconnected power electronic converters plays a fundamental role to achieve this efficient, flexible and reliable future network.

In this context four-leg converters play an important role, as they are the most efficient manner to directly connect the generation unit to a four-wire network through a back-to-back converter, avoiding expensive and bulky transformers, which have to be oversize and to handle the unbalanced and distorted currents typically produced in distribution systems. Furthermore, four-leg converters can be operated to support the network for compensating voltage unbalance, regulating voltage frequency, injecting reactive power or compensating harmonic distortion at the grid voltages.

A particular interesting application for four-leg converters is found in the aerospace industry. Due to the high power rate of the electric network inside modern commercial aircrafts, a plane itself can be conceptually considered as an isolated μGrid. In order to provide the aircraft with electrical energy when it is landed, the use of an external $90kVA$ to $2MW$ power supply is required, known as Ground Power Unit (GPU). This GPU must supply $400Hz$, $115Vrms$ phase-to-neutral voltages [10] to the aircraft. The different unbalanced and nonlinear equipment connected to its electrical grid, along with the $400Hz$ frequency required for the supplied voltages makes this application a very challenging technical task.

Regardless of the application, either $50Hz/60Hz$ in domiciliary μGrid or $400Hz$ aircraft electrical grid, the development of an efficient modulation algorithm, definition of switching patterns and a suitable external control strategy that effectively compensates the system unbalances and nonlinearities is a matter of high interest for future applications.

1.1 Technical Framework

Since the first experimental validation of a four-leg converter at the end of the 1990' [11–14], several works have reported in the literature for achieving an effective modulation algorithm for this kind of converters. Most of these works can be grouped in applications for two-level four-leg converters [15–20] or four-leg Matrix converters [21–23]. However when Medium Voltage (MV) connection is required and/or high efficiency is desirable, the reduction of switching frequency and Total Harmonic Distortion (*THD*) become key issues and conventional matrix converters or two-level voltage source inverters (VSI) are less attractive or unfeasible solutions. Consequently, four-leg multilevel converters, such as the four-leg Neutral-Point-Clamped (NPC) converter, arise an interesting alternative.

A three-level NPC converter has considerable advantages compared to a conventional two-level converter. For instance, NPC converters can be connected to medium voltage systems without a power transformer being required [7] and they can operate with a relatively high effective switching frequency, reducing the total harmonic distortion at the grid/load side [24]. Moreover, for a similar application, an NPC converter requires smaller power filter when compared with a conventional two-level VSI [25]. In addition, lower *dv/dt* values, higher efficiency and less stress in the devices are also considered important advantages of the NPC converter, which can be exploit in four-wire applications.

The use of Pulse Width Modulation (PWM) applied independently to each leg of a four-leg NPC converter has been addressed in [15, 26–28]. However those strategies do not allow selection of variable vector switching sequences and they do not use all the vector redundancies to control voltage balance on the dc-link capacitors, which is important when a low switching frequency is required. Implementation of non-linear controllers such as Finite-Set Model Predictive Control (FS-MPC), to track output voltage and current references have been also reported in [19, 29, 30]. However, the variability of the switching frequency and the variable control performance at different operating points are important drawbacks of this approach. Some approaches of Three-Dimensional Space Vector Modulation in *abc* [18, 31] and $\alpha\beta\gamma$ coordinates frame [17, 32–37] have been also reported for multilevel four-leg converters. However, they are either simulations or algorithms implemented in abc coordinates, where the direct control of the zero-sequence of the converter is not possible. Thereby, the development of a simple and efficient modulation algorithm in $\alpha\beta\gamma$ coordinates for multilevel four-leg converters, which allows easy implementation of different switching patterns, implementation of overmodulation techniques or balance of the dc-link voltage capacitors, remains still a matter of discussion in the literature.

Throughout this work, the reader will find a comprehensive review and discussion about the state of the art and future perspectives of power electronics converters implemented in four-wire applications. The three-dimensional Space Vector Modulation (SVM) problem for this kind of converters is extensively discussed in this dissertation and a simple modulation algorithm for a three-level four-leg NPC converter is proposed and successfully validated in an experimental rig. Consequently, the proposed modulation technique is implemented as a GPU, exploiting the capabilities of the four-leg NPC converter to handle zero-sequence components. In order to achieve this purpose, resonant controllers are implemented for compensation of until eleventh order harmonics, demonstrating that it is a suitable solution for this application, providing excellent steady-state and transient performance.

1.2 Contributions

The contributions of this work can be summarized as follows:

- A three-dimensional Space Vector Modulation (SVM) algorithm in $\alpha\beta\gamma$ coordinates is proposed and experimentally validated in a four-leg NPC converter. This algorithm uses the symmetry of the $\alpha\beta\gamma$ modulation space to reduce the complexity the modulation problem to a simple two-dimensional solution. Moreover, its generality makes it easily implementable in any kind of four-leg topology.

- A simple algorithm to design different switching patterns without need of extensive Look-up Tables (LUT) is proposed and validated in a four-leg NPC converter. This algorithm allows to fix the switching frequency and shape the harmonic spectrum of the modulated waveform according the the requirements of the application.
- A method to actively balance the voltages on the dc-link capacitors of the four-leg NPC converter using its redundant vectors has been implemented. The limitations for the dc-link voltage balancing under different non-linear and unbalanced loads is theoretically discussed and experimentally validated.
- An three-dimensional overmodulation algorithm in $\alpha\beta\gamma$ coordinate frame is proposed and experimentally validated. This algorithm limits the reference vector the the allowable modulation space avoiding the incorporation of additional low order or non-characteristics harmonics into the modulated waveforms.
- Finally, the aforementioned techniques are successfully validated in the four-leg NPC converter implemented as a GPU. The balance of the voltages in the dc-link capacitors, fixed switching frequency and compensation of high order harmonics is obtained, performing an excellent steady-state and transient response.

1.3 Outline

The rest of this work is divided in six Chapter . First, a summary of the modulation techniques used in three-leg converters, which can be extended to four-leg converters, is presented in Chapter 2. Thereafter, an extensive review of the state of the art of control strategies for three-leg four-wire and four-leg power electronic converters connected to four-wire systems is presented in Chapter 3. In order to implement a GPU, Chapter 4 presents the design of resonant controllers for compensation of harmonic distortion. The discretization of this controller for real implementation is also discussed in this chapter. Once the reported literature of four-leg converters has been reviewed and the control structure for a GPU has been discussed, the proposed SVM algorithm for a three-level four-leg NPC converter and its experimental validation is presented in Chapter 5. This modulation algorithm is used in Chapter 6, where a GPU is experimentally tested using resonant controllers for compensation of nonlinearity and unbalance components. Finally, Chapter 7 presents the final conclusions of this work and an outlook to continue future research in this field.

CHAPTER 2

Background Theory

Abstract: *This chapter provides the theoretical background of modulation strategies implemented in two-level and three-level NPC converter. The chapter focuses on Space Vector Modulation and provides a complete review of its most important features such as arrangement of switching patterns, overmodulation strategies and methods for balancing the dc-link voltages in a NPC converter.*

The two-level voltage source inverter (VSI) and three-level Neutral Point Clamped (NPC) VSI have been subject of intensive research during the past decades [5]. The first has become the standard topology for most of the low voltage applications such as: electric drives, power conditioners, uninterruptible power supplies and grid connected converters, while the three-level NPC converter was introduced as a solution for medium voltage range [24] and has been extensively used in electric drive and grid connected applications [38]. Furthermore, it has been also preferred in applications where high efficiency is required, as photovoltaic applications [39], [40].

Two important groups of control techniques have been proposed in the literature for synthesize an output voltage in a VSI. In the first group, the output voltage of a VSI is modulated based on a linear approximation, using the available switching states of the converter. These methods are usually known as Pulse Width Modulation (PWM) Techniques, or open-loop PWM techniques, and are mainly divided as Carrier-Based PWM and Space Vector PWM (SVPWM) (or simply Space Vector Modulation (SVM)) [41], [42]. On the other hand, a second group of techniques indirectly modulate the output voltage by using non-linear control techniques such as: predictive control [43] [44], hysteresis comparators [42] or look-up tables based methods such as: Optimal Pulse Patterns (OPP) [45] or Space Vector based Current Controllers [46]. Most of these methods are also known as close-loop PWM techniques [47].

The open-loop PWM techniques provide fixed and controllable switching frequency, which yields to fixed switching power losses and also a predefined harmonic spectrum. They have been preferred in several industrial applications and became the most standard and mature technique implemented in three-leg converters [42, 47]. This Chapter presents an overview of the current state of open-loop Pulse Width Modulation (PWM) techniques applied to two- and three-level NPC VSIs.

2.1 The Two-level Voltage Source Inverter

Fig. 2.1 shows the circuit diagram of a two-level VSI. This converter possesses six switches denoted as S_a, S_b, S_c and $\bar{S}_a$, $\bar{S}_b$, $\bar{S}_c$. In order to avoid short circuits, switches $\bar{S}_i$ represents always the complementary state of the switches S_i, for $i \in \{a, c, b\}$. The dc-link voltage has been virtually split into two *dc* voltage sources, creating a middle point denoted as z, which is used as reference point for obtaining the output voltages v_{iz} for $i \in \{a, b, c\}$.

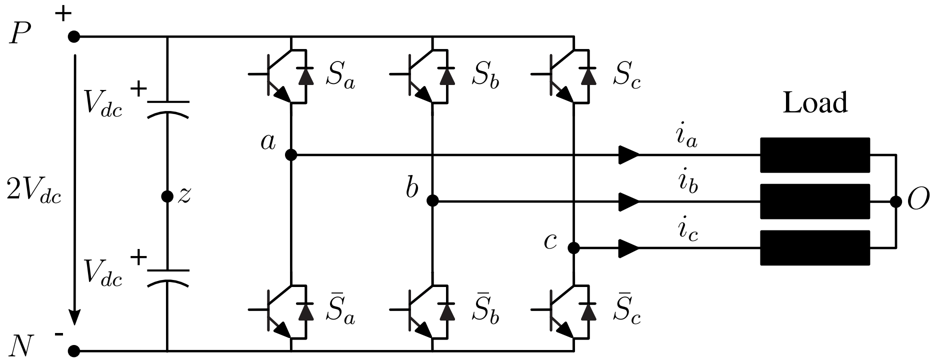

Figure 2.1: Two-level Voltage Source Inverter Topology connected to a three-phase balanced load.

2.1.1 Carrier-Based Pulse Width Modulation

A three-phase VSI aims to convert the *dc* voltage, $2V_{dc}$, into a balanced and symmetrical three-phase sinusoidal system. For this purpose, the sinusoidal carrier-based Pulse Width Modulation (SPWM) was early introduced in 1964 [48], which successfully accomplished control of the output voltages in a power electronic converter. Usually in this method, each leg of the converter is controlled independently based on the comparison of a triangular waveform, or also known as carrier waveform, with a sinusoidal reference, or modulating, waveform. This method, also named *suboscillation* method [42], is illustrated in Fig. 2.2.

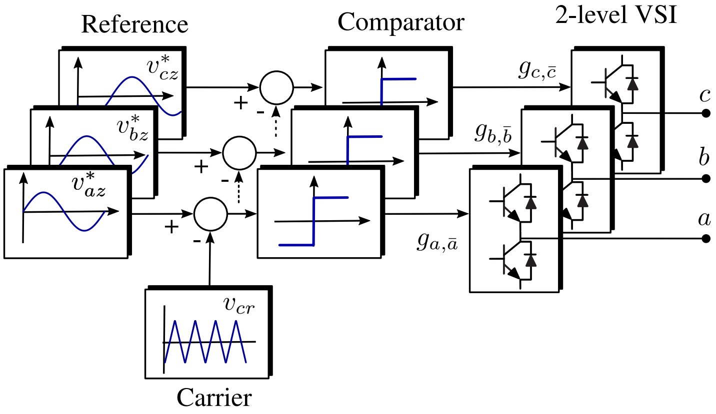

Figure 2.2: Diagram for individual pulse width modulators for each phase of a two-level VSI.

From Fig. 2.2, v_{az}^*, v_{bz}^* and v_{cz}^* represent the normalized input references of (2.1) to (2.3) and v_{cr} is the normalized triangular carrier wave, whose peak value is equal to $\hat{v}_{cr}$=1. Thereafter, $g_{i,\bar{i}}$, for $i \in \{a, b, c\}$, represents the trigger signals for each device of the converter presented in Fig. 2.1, which are obtained as a result of the comparison between the references and the carrier waveform.

$$v_{az}^* = \hat{v}^* \sin(\omega t) \tag{2.1}$$

$$v_{bz}^* = \hat{v}^* \sin\left(\omega t - \frac{2\pi}{3}\right) \tag{2.2}$$

$$v_{cz}^* = \hat{v}^* \sin\left(\omega t + \frac{2\pi}{3}\right) \tag{2.3}$$

$$\hat{v}^* = \frac{v_{max}}{V_{dc}} \tag{2.4}$$

$$\omega = 2\pi f_1 \tag{2.5}$$

Fig. 2.3 shows the comparison of a $50Hz$ sinusoidal reference with a $450Hz$ carrier waveform. The output voltages v_{az} and v_{bz} are depicted in the figure as result of the comparison between modulating and the carrier waveforms. Thereby, when the carrier wave is greater than the modulating wave v_{iz}^*, the switch S_i is switched-off. Likewise, the switch S_i is switched-on for $v_{cr} \leq v_{iz}^*$, while $\bar{S}_i$ is always the complement of S_i, for $i \in \{a, b, c\}$. Finally, Fig. 2.3 shows the output line-to-line voltage v_{ab}, which represent the effective output voltage of the VSI. Although not showed, voltages v_{bc} and v_{ca} are identical to v_{ab} but shifted in 120° and 240° respectively.

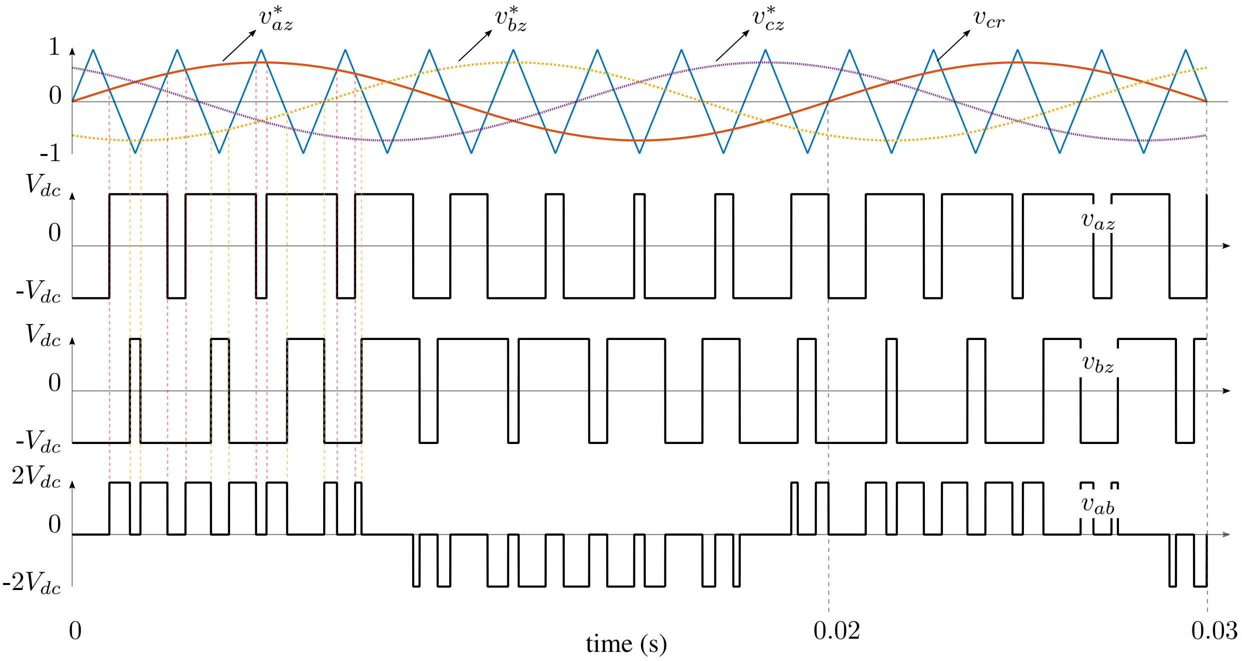

Figure 2.3: Sinusoidal PWM method for three reference values v^*_{az}, v^*_{bz}, v^*_{cz} and a carrier wave v_{cr}. For the sinusoidal waveforms, the frequency f_1 is equal to $50Hz$ and for the carrier f_{cr}=$450Hz$. The amplitude modulation index m_a has been set to 0.75.

In order to regulate the frequency and amplitude of the output voltages, the following two indices are defined as:

$$m_a = \frac{\hat{v}^*}{\hat{v}_{cr}} \tag{2.6}$$

$$m_f = \frac{f_{cr}}{f_1}, \tag{2.7}$$

where m_a is called amplitude modulation index and is defined as the ratio between the normalized amplitudes of the reference signals $\hat{v}^*$, and the triangular wave, $\hat{v}_{cr}$. Similarly, m_f is called the frequency modulation index, defined as the ratio between the the frequency of the carrier f_{cr} and the fundamental frequency of the reference waveform f_1. Commonly, the peak amplitude of the reference signals $\hat{v}^*$, changes according to the loads requirements, while the amplitude of the triangular wave, $\hat{v}_{cr}$, remains constant. Thus, m_a defines the magnitude of the modulated output voltage. In order to modulate the output voltages in a linear range, the amplitude of the references $\hat{v}^*$ can not be greater than $\hat{v}_{cr}$, i.e. $m_a \leq 1$. When m_a is equal to one, the modulated waves v_{iz}, for $i \in \{a, b, c\}$ posses a fundamental component with a magnitude equal to V_{dc}, which generates a line-to-line voltage with a peak magnitude equal to $\sqrt{3}V_{dc}$.

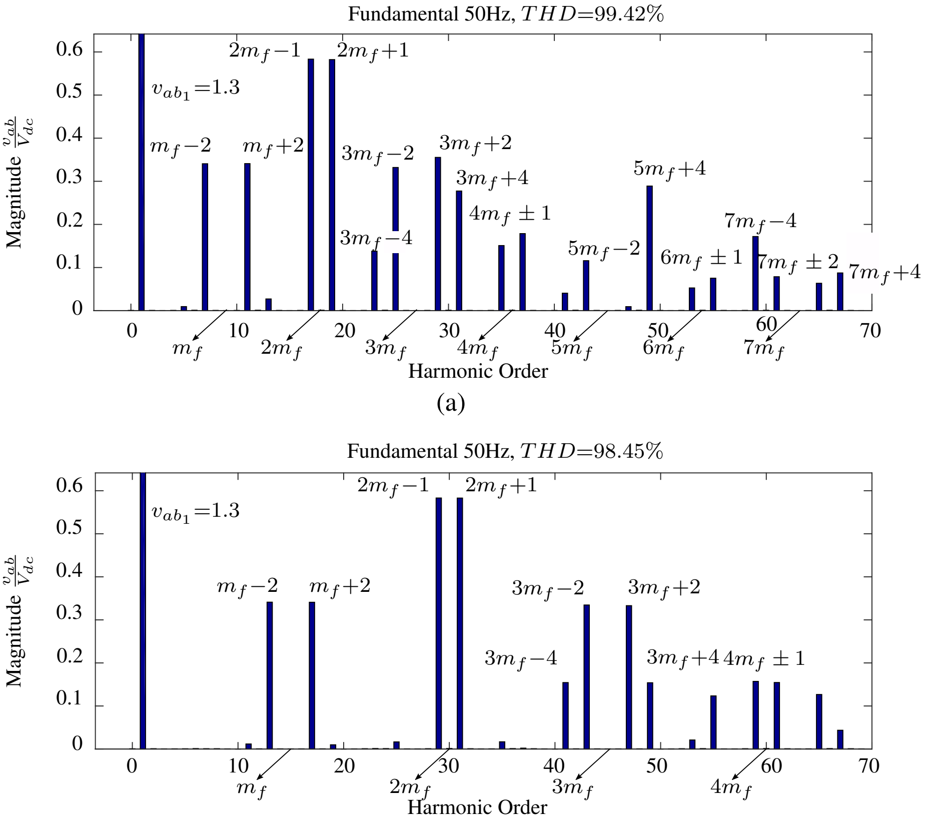

(a)

(b)

Figure 2.4: Fast Fourier Transformation (FFT) for the line-to-line voltage v_{ab} using SPWM with (a) m_f=9 and m_a=0.75 and (b) m_f=15 and m_a=0.75. The amplitude are given as peak magnitudes normalized respect to V_{dc}.

Fig. 2.4a shows the harmonic spectrum of the voltage v_{ab} of Fig. 2.3. As it can be appreciated, the magnitude for the fundamental component is equal to $1.3V_{dc}$, which is equivalent to: $m_a\,\sqrt{3}\,V_{dc}$, for m_a=0.75. This shows that the regulation of the output voltage is accomplished linearly for $m_a \leq 1$. Additionally, two issues can be noticed from the harmonic spectrum: a) the harmonic components for orders less than $m_f - 2$ are negligible and b) the harmonic components are always around the harmonic-orders $n \cdot m_f$, for $n \in \mathbb{N}$, where for each n the harmonic components are present at $n \cdot m_f \pm k$, for $k \in \mathbb{Z}$ [41]. This is valid always for $m_f \geq 9$ and multiple of 3.

The magnitude and number of the harmonic components $n \cdot m_f \pm k$, change with m_a and m_f. Thereby, for instance, Fig. 2.4b shows the results for increasing the carrier frequency to $650Hz$ (m_f=15). Similarly to Fig. 2.4a, as m_a has not changed its value, the magnitude of the fundamental component remains equal to $1.3 \cdot V_{dc}$. Additionally, the harmonic components are also found at $n \cdot m_f \pm k$. However, the increase of m_f provides a more symmetrical harmonic spectrum and shift the harmonic components to higher order frequencies.

2.1.1.1 Operation Modes

When the frequency of the controlled waveform f_1 changes during operation, as in electric drive applications, two possible operation modes can be implemented [42]. In the first method, called

Asynchronous PWM, the frequency of the carrier signal f_{cr} is not modified when the frequency f_1 changes. Therefore, the frequency modulation index m_f takes non-integer values and the harmonic components of the modulated waveforms are continuously spread across the harmonic spectrum. On the other hand, by *Synchronous PWM*, the frequency of the carrier signal f_{cr} is instantaneously modified according to f_1 in order to maintain a constant frequency modulation index m_f. Hence, the modulated waveforms perform a harmonic spectrum as presented in Fig. 2.4. *Asynchronous PWM* method has been recognized because of its simplicity, usually implemented with analogue circuits. However, the fast incorporation of digital processor and real time computers in last decades have enabled an easy implementation of *Synchronous PWM* as well.

Besides the harmonic spectrum, the main difference between *Synchronous PWM* and *Asynchronous PWM* technique, relies on the switching frequency performed by each device of the converter presented in Fig. 2.1. From Fig. 2.3, it can be seen that v_{az} possesses nine positive and negative pulses in one fundamental period T_1. Thus, S_a and $\bar{S}_a$ are switched-on and -off nine times in a fundamental period T_1, performing a switching frequency per device f_{sw} equal to $9f_1$ or equivalently:

$$f_{sw}{=}m_f f_1{=}f_{cr} \tag{2.8}$$

From this formulation it is straightforward that the *Asynchronous PWM* method generates a constant switching frequency for each device of the converter presented in Fig. 2.1, while *Synchronous PWM* changes the switching frequency of the devices according to f_{cr}.

2.1.1.2 Zero-Sequence Injection

The injection of a zero-sequence component to the sinusoidal reference voltages v_{iz}^*, for $i \in \{a, b, c\}$, have been extensively studied in the literature as a method to increase the linear range of the SPWM method [49]. This injection does not produce any additional distortion to the line-to-line voltages v_{ab}, v_{bc} or v_{ca}, because the zero-sequence component is completely eliminated after subtracting the phase-voltages v_{iz} to obtain the line-to-line voltages. The incorporation of a zero sequence component to the reference values v_{iz}^* flats the top of the sinusoidal reference wave, allowing compensation of a higher fundamental waveform (see Fig. 2.5). Although several zero-sequence signal injection methods have been proposed in the literature, only a few of them have gained acceptance and popularity in the scientific community, mainly because of their effectiveness and simple implementation [42]. By that, the injection of third-harmonic component to the reference sinusoidal wave v_{iz}, for $i \in \{a, b, c\}$, is considered as the standard zero-sequence signal injection method in the literature. This method is known as third-harmonic injection PWM (THIPWM), where the reference signals for each phase are described as:

$$v_{az}^{**} = v_{az}^* + v_{3th}^* = \hat{v}^* \sin(\omega t) + \frac{\hat{v}^*}{6} \sin(3\omega t) \tag{2.9}$$

$$v_{bz}^{**} = v_{bz}^* + v_{3th}^* = \hat{v}^* \sin\left(\omega t - \frac{2\pi}{3}\right) + \frac{\hat{v}^*}{6} \sin(3\omega t) \tag{2.10}$$

$$v_{cz}^{**} = v_{cz}^* + v_{3th}^* = \hat{v}^* \sin\left(\omega t + \frac{2\pi}{3}\right) + \frac{\hat{v}^*}{6} \sin(3\omega t), \tag{2.11}$$

In order to maximize $\hat{v}^*$, the amplitude of the third harmonic has to be equal to one sixth of the amplitude of the fundamental reference [41]. Thus, $\hat{v}^*$ can reach a peak value of $\frac{2}{\sqrt{3}}$ before v_{iz}^{**} exceeds the amplitude of the carrier wave, i.e. $\hat{v}_{cr}$=1. This is shown in Fig. 2.5. Therefore, the use of THIPWM increases the linear range of modulation to $m_a \leq \frac{2}{\sqrt{3}}$, boosting the modulated phase voltages v_{iz} in 15%. This results in output phase-voltages with a fundamental magnitude of $\frac{2}{\sqrt{3}}V_{dc}$. Equivalently, the maximum peak value for the fundamental line-to-line voltage under THIPWM is equal to $2V_{dc}$.

Additionally, some methods use injection of discontinuous zero-sequence waveforms to boost the output voltages [49–51]. This so called *Discontinous PWM* methods are not as simple as THIPWM, but they provide lower harmonic distortion of the output voltages and higher controllability of the switching power losses for overmodulation range, i.e. for $m_a \geq \frac{2}{\sqrt{3}}$. Particularly, Depenbrock's PWM [52] and Ogasawar's PWM [53] have been recognized because of their easy implementation and high performance.

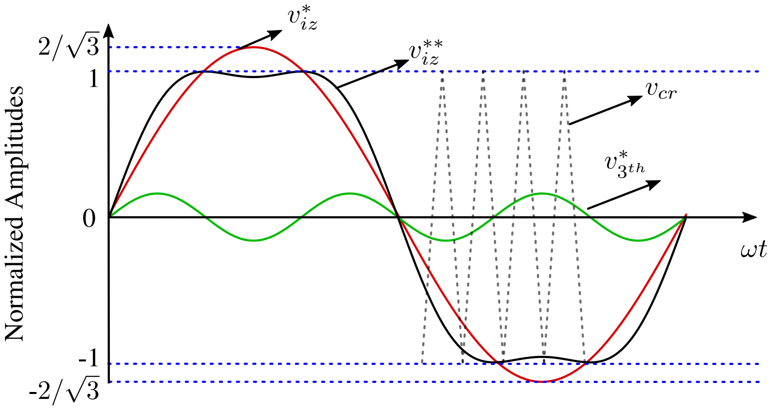

Figure 2.5: Third Harmonic Injection PWM (THIPWM) Method for the maximum achievable magnitudes. The subindex i represents each phase of the converter. $i \in \{a, b, c\}$.

It is important to mention that the maximum feasible fundamental component for the phase voltages v_{iz} is obtained under *six-step* operation mode. In this operation mode, no switching takes place within half cycle of each reference waveform and either a positive or negative voltage level is only applied depending on the polarity of the reference signal. The fundamental component under this operation has a magnitude of:

$$\hat{v}_{6step}=\frac{4}{\pi}V_{dc} \tag{2.12}$$

Some references define the amplitude modulation index based on this maximum achievable value. Therefore, the maximum amplitude modulation index is defined as 1, only achievable under *six-step* operation. In order to avoid confusions, the following table summarizes the maximum output voltage and amplitude modulation indices for both nomenclatures.

Table 2.1: Summary of Carrier based PWM Methods

PWM Method	Definition m_a	Maximum m_a	Max. fundamental component of v_{az}, v_{bz}, v_{cz}	Max. fundamental component of v_{ab}, v_{bc}, v_{ca}
SPWM	$\frac{\hat{v}^*}{\hat{v}_{cr}}$	1	V_{dc}	$\sqrt{3}V_{dc}$
THIPWM	$\frac{\hat{v}^*}{\hat{v}_{cr}}$	$\frac{2}{\sqrt{3}} \approx 1.15$	$\frac{2}{\sqrt{3}}V_{dc}$	$2V_{dc}$
SPWM	$\frac{\hat{v}^*}{\hat{v}_{6step}}$	$\frac{\pi}{4} \approx 0.785$	V_{dc}	$\sqrt{3}V_{dc}$
THIPWM	$\frac{\hat{v}^*}{\hat{v}_{6step}}$	$\frac{\pi}{2\sqrt{3}} \approx 0.907$	$\frac{2}{\sqrt{3}}V_{dc}$	$2V_{dc}$

2.1.2 Space Vector Modulation

Although Carrier-Based PWM techniques were for several years the predominant technique used for the control of power electronics converters, with the incorporation of digital real-time control platforms, Space Vector Modulation (SVM) technique became, and is still today, the most widely used and preferred technique for controlling power converters [54], [41]. SVM techniques posses several advantages compared to Carrier-Based PWM methods, such as: inherent injection of zero-sequence component, possibility of implementing different switching patterns for shaping harmonic spectrum or distributing the power losses, less ripple on the output currents/voltages, more flexibility for implementing overmodulation algorithms and also provides a more intuitive implementation for digital controllers [42]. This section introduces the principles of operation and presents a review through the literature for the most relevant issues of SVM technique.

2.1.2.1 Space of Vectors

From Fig. 2.1 it is possible to define the vector $\boldsymbol{v}_{abc}^{i}$ as the normalized states of the output voltages for the i^{th} switching combination, given by:

$$\boldsymbol{v}_{abc}^{i} = \frac{1}{V_{dc}} \left[v_{az}, v_{bz}, v_{cz} \right] \tag{2.13}$$

The operation of the converter of Fig. 2.1 allows eight possible switching combination, which generate the output voltages. The output voltages and the states of the switches are summarized in Table 2.2.

The vector defined in (2.13) can be expressed in an equivalent orthogonal system, denoted as $\alpha\beta\gamma$ coordinate system, where the zero-sequence is independently expressed over the γ axis. For this purpose, the following linear transformation, introduced by Clarke [55] in 1951, can be used:

$$\boldsymbol{T}_{abc}^{\alpha\beta\gamma} = \frac{2}{3} \begin{bmatrix} 1 & -1/2 & -1/2 \\ 0 & \sqrt{3}/2 & -\sqrt{3}/2 \\ 1/2 & 1/2 & 1/2 \end{bmatrix} \tag{2.14}$$

Table 2.2: Summary of the output Switching Combinations for a two level-VSI.

Output phase-voltages $\boldsymbol{v}^{i}_{abc}{=}V_{dc}^{-1}\,[v_{az}, v_{bz}, v_{cz}]$	Output phase-to-phase voltages $\boldsymbol{v}^{i}_{ph\text{-}ph}{=}V_{dc}^{-1}\,[v_{ab}, v_{bc}, v_{ca}]$	On-State Switch
$\boldsymbol{v}^{0}_{abc}=[\ 1,\ 1,\ 1]$	$\boldsymbol{v}^{0}_{ph\text{-}ph}=[0, 0, 0]$	S_a, S_b, S_c
$\boldsymbol{v}^{7}_{abc}=[\text{-}1, \text{-}1, \text{-}1]$	$\boldsymbol{v}^{7}_{ph\text{-}ph}=[0, 0, 0]$	$\bar{S}_a$, $\bar{S}_b$, $\bar{S}_c$
$\boldsymbol{v}^{1}_{abc}=[\ 1, \text{-}1, \text{-}1]$	$\boldsymbol{v}^{1}_{ph\text{-}ph}=[2, 0, \text{-}2]$	S_a, $\bar{S}_b$, $\bar{S}_c$
$\boldsymbol{v}^{2}_{abc}=[\ 1,\ 1, \text{-}1]$	$\boldsymbol{v}^{2}_{ph\text{-}ph}=[0, 2, \text{-}2]$	S_a, S_b, $\bar{S}_c$
$\boldsymbol{v}^{3}_{abc}=[\text{-}1,\ 1, \text{-}1]$	$\boldsymbol{v}^{3}_{ph\text{-}ph}=[\text{-}2, 2, 0]$	$\bar{S}_a$, S_b, $\bar{S}_c$
$\boldsymbol{v}^{4}_{abc}=[\text{-}1,\ 1,\ 1]$	$\boldsymbol{v}^{4}_{ph\text{-}ph}=[\text{-}2, 0, 2]$	$\bar{S}_a$, S_b, S_c
$\boldsymbol{v}^{5}_{abc}=[\text{-}1, \text{-}1,\ 1]$	$\boldsymbol{v}^{5}_{ph\text{-}ph}=[0, \text{-}2, 2]$	$\bar{S}_a$, $\bar{S}_b$, S_c
$\boldsymbol{v}^{6}_{abc}=[\ 1, \text{-}1,\ 1]$	$\boldsymbol{v}^{6}_{ph\text{-}ph}=[2, \text{-}2, 0]$	S_a, $\bar{S}_b$, S_c

where the coefficient $\frac{2}{3}$ have been chosen for maintaining the same amplitudes for the signals in both representations, i.e. *abc* and $\alpha\beta\gamma$. However, transforming an electrical system from *abc* to $\alpha\beta\gamma$ using (2.14) yields to two systems which posses different active and reactive power magnitudes. Thereby, when a power invariant transformation is required, this coefficient is substituted by $\sqrt{\frac{2}{3}}$. Applying (2.14) to the eight phase-voltages $\boldsymbol{v}^{i}_{abc}$, represented in the first column of the Table 2.2, the vectors in $\alpha\beta\gamma$ coordinates are obtained, and presented in Table 2.3, which represent the possible voltages generated by the converter in the $\alpha\beta\gamma$ space.

As it was presented previously in Section 2.1.1, the injection of any zero-sequence component, i.e. three identical signals injected in each phase of the converter, to the phase voltages of the converter can boost the output line-to-line voltages without introducing any additional distortion. As the γ axis directly represents the zero-sequence of a system, when the $\alpha\beta\gamma$ coordinate system is used for representation of the possible switching combination, the magnitudes present at the γ component can take any value, giving an extra degree of freedom to the system. Thereby, the γ component can be neglected and the eight different vectors generated by the converter, $\boldsymbol{v}^{k}_{\alpha\beta\gamma}$ $k \in \{0, 1, ..., 7\}$, can be represented in the $\alpha\beta$ plane. Fig. 2.6a shows the space vector diagram for a two-level VSI, where the vectors $\boldsymbol{v}^{0}_{\alpha\beta}$ and $\boldsymbol{v}^{7}_{\alpha\beta}$ are placed at the origin of the system, known as *zero vectors*. The vectors $\boldsymbol{v}^{1}_{\alpha\beta}$ to $\boldsymbol{v}^{6}_{\alpha\beta}$, also known as *active vectors*, are symmetrically placed each 60°, generating voltage in the four different quadrants of the $\alpha\beta$ plane and dividing the region into six different *sectors*. As the *zero* and *active vectors* are placed always in the same position, they are also known as *stationary vectors*.

Once all the possible states of the converter have been represented in the $\alpha\beta$ plane, a reference vector has to be also characterized in this plane for achiving its modulation. Hence, applying (2.14) to the three-phase reference system already presented in (2.1) to (2.3), but shifted in 90° for convenience on the equations, the following vector is obtained:

Table 2.3: Output Switching Combinations in $\alpha\beta\gamma$ and *abc* coordinates.

Output phase-voltages in $\alpha\beta\gamma$ $\boldsymbol{v}^{k}_{\alpha\beta\gamma}= \left[v_\alpha, v_\beta, v_\gamma\right]$	Output phase-voltages $\boldsymbol{v}^{i}_{abc}=V_{dc}^{-1}\left[v_{az}, v_{bz}, v_{cz}\right]$
$\boldsymbol{v}^{7}_{\alpha\beta\gamma}=[\ 0,\ 0,\ 1]$	$\boldsymbol{v}^{7}_{abc}=[\ 1,\ 1,\ 1]$
$\boldsymbol{v}^{0}_{\alpha\beta\gamma}=[\ 0,\ 0, \text{-}1]$	$\boldsymbol{v}^{0}_{abc}=[\text{-}1, \text{-}1, \text{-}1]$
$\boldsymbol{v}^{1}_{\alpha\beta\gamma}=\left[\ \frac{4}{3},\ 0, \text{-}\frac{1}{3}\right]$	$\boldsymbol{v}^{1}_{abc}=[\ 1, \text{-}1, \text{-}1]$
$\boldsymbol{v}^{2}_{\alpha\beta\gamma}=\left[\ \frac{2}{3},\ \frac{2\sqrt{3}}{3},\ \frac{1}{3}\right]$	$\boldsymbol{v}^{2}_{abc}=[\ 1,\ 1, \text{-}1]$
$\boldsymbol{v}^{3}_{\alpha\beta\gamma}=\left[\text{-}\frac{2}{3},\ \frac{2\sqrt{3}}{3}, \text{-}\frac{1}{3}\right]$	$\boldsymbol{v}^{3}_{abc}=[\text{-}1,\ 1, \text{-}1]$
$\boldsymbol{v}^{4}_{\alpha\beta\gamma}=\left[\text{-}\frac{4}{3},\ 0,\ \frac{1}{3}\right]$	$\boldsymbol{v}^{4}_{abc}=[\text{-}1,\ 1,\ 1]$
$\boldsymbol{v}^{5}_{\alpha\beta\gamma}=\left[\text{-}\frac{2}{3}, \text{-}\frac{2\sqrt{3}}{2}, \text{-}\frac{1}{3}\right]$	$\boldsymbol{v}^{5}_{abc}=[\text{-}1, \text{-}1,\ 1]$
$\boldsymbol{v}^{6}_{\alpha\beta\gamma}=\left[\ \frac{2}{3}, \text{-}\frac{2\sqrt{3}}{2},\ \frac{1}{3}\right]$	$\boldsymbol{v}^{6}_{abc}=[\ 1, \text{-}1,\ 1]$

$$\boldsymbol{v}^{*}_{\alpha\beta\gamma} = \hat{v}^{*}\cos\left(\omega t\right)\hat{e}_{\alpha} + \hat{v}^{*}\sin\left(\omega t\right)\hat{e}_{\beta} + 0\hat{e}_{\gamma} \tag{2.15}$$

$$|\boldsymbol{v}^{*}_{\alpha\beta\gamma}| = \hat{v}^{*} \tag{2.16}$$

$$\angle\boldsymbol{v}^{*}_{\alpha\beta\gamma} = \theta = \omega t \tag{2.17}$$

this reference vector, also depicted in Fig. 2.6a and denoted as $\boldsymbol{v}^{*}_{\alpha\beta}$, possesses a constant amplitude equal to $\hat{v}^{*}$ and describes a circumference over the $\alpha\beta$ plane. Additionally, its phase shift is denoted as θ and its rotational speed is given by:

$$\omega = 2\pi f_1, \tag{2.18}$$

where f_1 is the fundamental frequency of the reference signals. From Fig. 2.6a, the maximum permissible magnitude for the reference vector, $\boldsymbol{v}^{*}_{\alpha\beta}$, before it exceeds the borders of the hexagon, is equal to $\frac{2}{\sqrt{3}}$. Therefore, equivalently to the THIPWM method, the maximum amplitude for the fundamental component of the reference signals is equal to $\hat{v}^{*} = \frac{2}{\sqrt{3}}$. Nevertheless, for the SVM method, the incorporation of the zero-sequence is not explicitly presented in the reference vector, it is actually inherently incorporated in the method as each of the stationary vectors posses a zero-sequence component (see Table 2.3). Equivalently to the PWM methods, an amplitude modulation index can be defined as (2.19), where its limits for linear operation are given in (2.20).

$$m_a = \frac{v_{max}}{V_{dc}} = \hat{v}^* \tag{2.19}$$

$$0 \leq m_a \leq \frac{2}{\sqrt{3}} \tag{2.20}$$

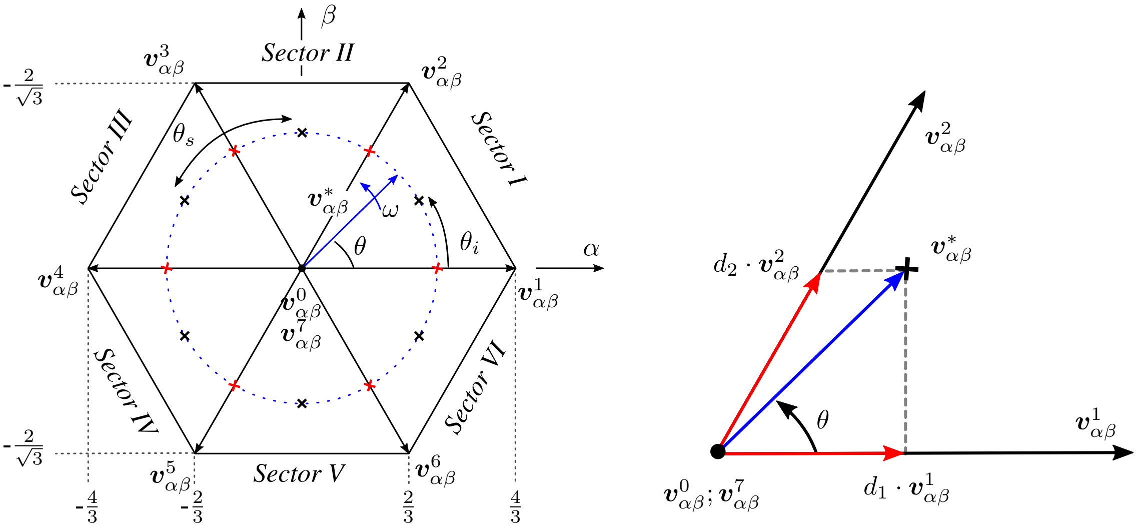

(a) (b)

Figure 2.6: (a) Space Modulation Region for a two-level VSI and (b) close look of *sector I* with the vectors that approximate $\boldsymbol{v}^*_{\alpha\beta}$ in one sampling time.

2.1.2.2 Dwell Time Calculation and Reference Vector Sampling

The principle of operation of the SVM method is based on the *volt-second balancing*. Hence, the reference vector is periodically sampled over a cycle, where each of the sampled value can be approximated applying two *active vectors* and the *zero vectors* during one sampling interval defined as T_s. The time that each *stationary vector* needs to be applied within T_s for approximating the reference value is known as *dwell time*. The number of sampled values over a cycle is defined as:

$$\Lambda = \frac{T_1}{T_s} \tag{2.21}$$

From Fig. 2.6a, and denoted with red and black crosses, two possible sets of sampled values over a cycle for $\Lambda = 6$ are shown. Although the angle between two samples is fixed by T_s, and equivalently defined as:

$$\theta_s{=}2\pi\frac{T_s}{T_1}, \tag{2.22}$$

the position of the sampled values in the $\alpha\beta$ plane depends on the initial sampling angle θ_i. Thereby, for obtaining a symmetrically sampled reference vector on the $\alpha\beta$ plane, the sampling angles for each of the Λ sampled values are defined as:

$$\theta_{sp}^{k} = \theta_i + k\theta_s; \qquad k \in \{0, 1, .., \Lambda - 1\} \tag{2.23}$$

$$\theta_i = \pi\frac{T_s}{T_1} = \frac{\pi}{\Lambda} \tag{2.24}$$

where θ_{sp}^{k} represent the angle for the k^{th} sampled value.

Although the *symmetrical sampling* of the reference vector is not mandatory for implementing SVM, its implementation results in a better harmonic spectrum of the modulated waveform, which is specially important in low switching frequency applications. Furthermore, it allows even harmonics elimination, which is relevant for grid connected applications [54].

When the approximation of a sampled reference vector is achieved using its two closest *stationary vectors* at each sampling time T_s, the switching losses are minimized, voltage harmonic spectrum is improved and the currents ripple is minimized [50]. Thus, Fig. 2.6b shows a sampled reference vector being modulated with its two closest *stationary vector* in *Sector I*. Additionally the proportional lengths of the *stationary vectors* required for modulating this reference value are also depicted, which represent the length of the *stationary vectors* multiplied by its *dwell time*. In order to calculate the *dwell times* for each of the selected *stationary vectors* of Fig. 2.6b, the following equation must be solved:

$$\boldsymbol{v}_{\alpha\beta}^{*} \cdot T_s = \boldsymbol{v}_{\alpha\beta}^{1} \cdot d_1 + \boldsymbol{v}_{\alpha\beta}^{2} \cdot d_2 + \boldsymbol{v}_{\alpha\beta}^{0} \cdot d_0 \tag{2.25}$$

$$T_s = d_0 + d_1 + d_2 \tag{2.26}$$

Substituting (2.15) and the components of $\boldsymbol{v}_{\alpha\beta}^{1}$ and $\boldsymbol{v}_{\alpha\beta}^{2}$, obtained from Table 2.3, in (2.25) and (2.26) the *dwell times* for the each vector of the *sector I* can be obtained as:

$$d_1 = \frac{T_s\sqrt{3}\hat{v}^{*}}{2}\sin\left(\frac{\pi}{3} - \theta\right) \tag{2.27}$$

$$d_2 = \frac{T_s\sqrt{3}\hat{v}^{*}}{2}\sin\left(\theta\right) \tag{2.28}$$

$$d_0 = T_s - d_1 - d_2, \qquad \theta \in \left[0, \frac{\pi}{3}\right[\tag{2.29}$$

Although (2.27) to (2.29) were obtained for the *Sector I*, they can be used for any *sector* by replacing θ for $\hat{\theta}$, where $\hat{\theta}$ is defined as:

$$\hat{\theta} = \theta - (k - 1)\frac{\pi}{3}, \qquad \textit{for}\ k \in \{1, 2, 3, 4, 5, 6\}, \tag{2.30}$$

and k represents the sector of the sampled reference value.

2.1.2.3 Switching Sequence and Harmonic Spectrum

Once obtained the *stationary vectors* and their respective *dwell times*, a certain sequence to arrange these vectors through the sampling time T_s has to be defined. For each sampling time, always two *active vectors* and the *zero vector*, which possesses two redundancies ($\boldsymbol{v}_{\alpha\beta\gamma}^{0}$ and

$\boldsymbol{v}^{7}_{\alpha\beta\gamma}$), are selected. The order in which these switching states are applied defines the switching losses and harmonic spectrum of the output modulated waveform. This is the main criteria for selecting a certain switching sequence, which is always a trade-off between the switching losses and the harmonic spectrum of the modulated waveforms.

The basic principle for achieving a proper switching sequence requires that during the sampling time T_s, only one device turns off and a second device, from the same leg, turns on during the transition from one vector to another. This principle has been named as *minimum switching transition* throughout this work.

Considering the *minimum switching transition* constrain, the possible sequences that can be arranged with the three selected *stationary vectors* is considerably reduced and mainly divided in two groups. These are named as named *Single-Redundancy Sequence* and *Non-Redundancy Sequence* throughout this work. The first group uses both redundancies of the *zero vectors*, i.e. $\boldsymbol{v}^{0}_{\alpha\beta\gamma}$ and $\boldsymbol{v}^{7}_{\alpha\beta\gamma}$, while a second group uses only one redundancy, either $\boldsymbol{v}^{0}_{\alpha\beta\gamma}$ or $\boldsymbol{v}^{7}_{\alpha\beta\gamma}$, for achieving modulation of the reference sampled value at each sampling time T_s. Thereby, *Single-Redundancy Sequence* improves the harmonics spectrum at expenses of higher switching losses , while *Non-Redundancy Sequence* is usually implemented when reduction of the switching losses is required, as in soft-switching techniques for high power applications [56], [54]. Additionally, each of these groups can be subdivided into *Symmetrical* or *Asymmetrical Sequence*.

a) *Single-Redundancy Sequences* for two-level VSI:

Fig. 2.7a and Fig. 2.7b show the *Single-Redundancy Symmetrical* and *Single-Redundancy Asymmetrical* sequences for the selected vectors of *sector I* respectively. Although both patterns perform the same switching frequency over a fundamental cycle, the *Single-Redundancy Symmetrical* sequence offers a better voltage harmonic distortion. On the other hand, the *Single-Redundancy Asymmetrical* sequence aligns three switching commutation at the transition between two sampling times, which is used in soft-switching commutation techniques for reducing the switching losses [38]. Furthermore, it can be noticed that for both sequences the *minimum switching transition* rule is accomplished.

Comparing Fig. 2.7a and Fig. 2.7b with Fig. 2.7c and Fig. 2.7d, an alternative sequence can be generated when starting with $\boldsymbol{v}^{7}_{\alpha\beta\gamma}$ instead of $\boldsymbol{v}^{0}_{\alpha\beta\gamma}$. As the vector $\boldsymbol{v}^{0}_{\alpha\beta\gamma}$ generates negative phase voltages at each output phase of the converter (v_{az}, v_{bz} and v_{cz}), the sequences starting with $\boldsymbol{v}^{0}_{\alpha\beta\gamma}$ are named as *n-type*, while the sequences staring with $\boldsymbol{v}^{7}_{\alpha\beta\gamma}$ are defined as *p-type*. Although both sequences can look different, they are identical but shifted in half sampling time. Alternating *n-* and *p-type* sequences over a fundamental cycle allows shape of the harmonic spectrum and control over the distribution of the power losses among the switches of a VSI, as shown latter in this section.

The average switching frequency performed by each device over one fundamental period T_1 is defined as $\bar{f}_{dev_i}$. This value can be expressed as the addition of two terms and obtained as:

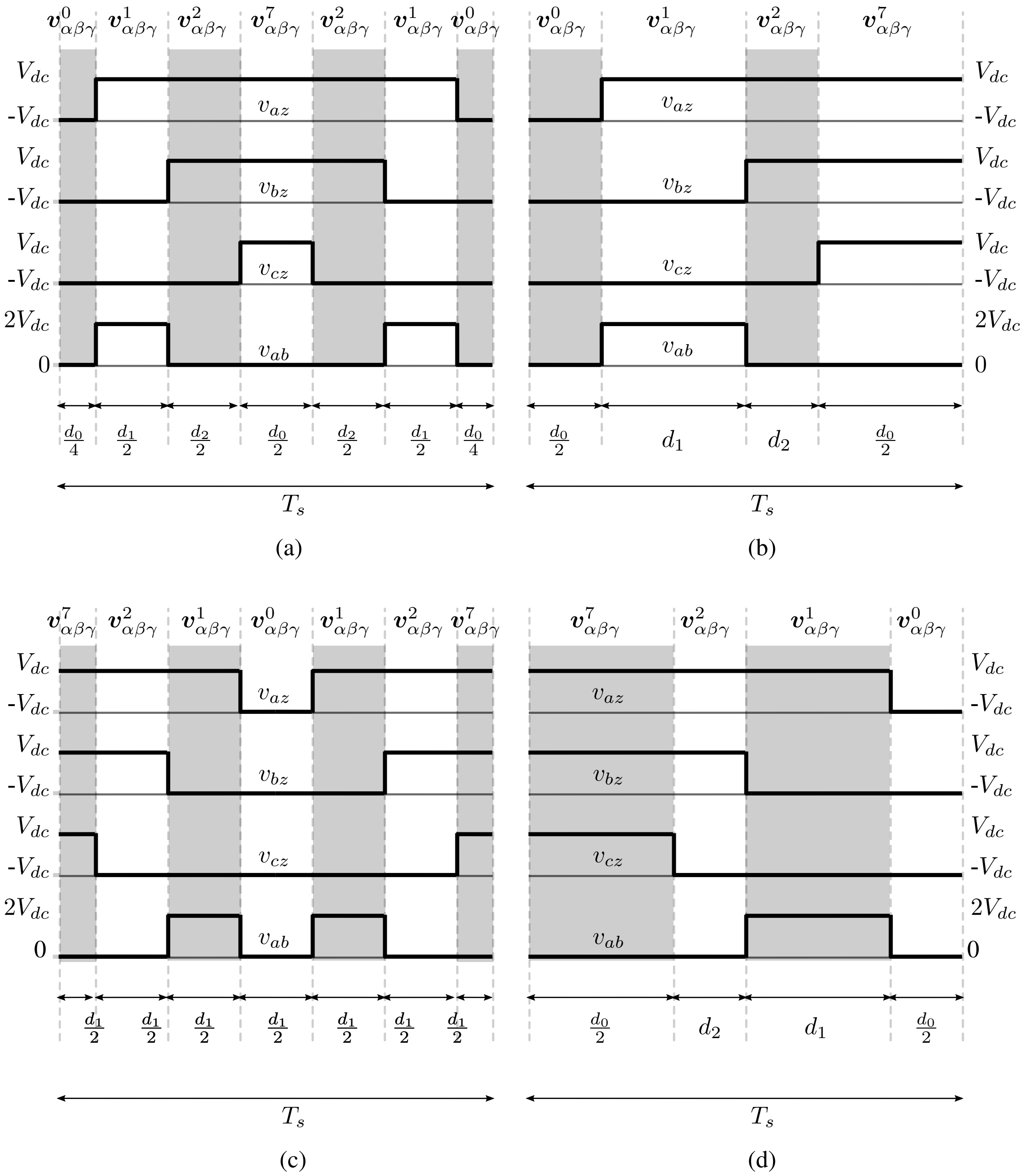

(a) (b) (c) (d)

Figure 2.7: Different *Redundant* switching sequences. (a) *Single-Redundancy Symmetric n-type* sequence, (b) *Single-Redundancy Asymmetric n-type* sequence, (c) *Single-Redundancy Symmetric p-type* sequence and (d) *Single-Redundancy Asymmetric p-type* sequence.

$$\bar{f}_{dev_i} = \bar{f}^s_{dev_i} + f^f_{dev_i} \tag{2.31}$$

$$\bar{f}^s_{dev_i} = \sum_{n=1}^{\Lambda} \frac{f^{s_n}_{dev_i}}{\Lambda} \tag{2.32}$$

$$f^f_{dev_i} = \frac{k_i}{2} f_1, \tag{2.33}$$

where the index dev_i represents the i^{th} device among the 8 that compose the two-level converter. The term $f^{s_n}_{dev_i}$ in (2.32) represents the switching frequency perform by the i^{th} device at each sampling time T_s, where the index s_n represents the n^{th} sampling interval over T_1 (the total of intervals in one period is equal to (2.21)). Therefore, using (2.21), the general expression of (2.32) is obtained for calculating the average switching frequency for the i^{th} device over one fundamental period T_1.

Equation (2.32) computes the average of the switching commutations inside each sampling interval T_s. However, it does not deal with the extra switching commutations involved during the transition from one sampling time to another. These extra transitions occur when the final vector of a sequence is not equal to the first vector of the sequence applied in the next sampling time and is represented as $f^f_{dev_i}$. This extra switching commutations are mainly generated when alternating between *n-* and *p-type* patterns or when using *Asymmetric* sequences. Thereby, an increment of the switching frequency over one fundamental period is generated, which can be calculated as (2.33), where f_1 is the fundamental frequency and k_i represents the total number of on and off commutations, generated by the i^{th} device, during all the transition between two sampling times along one fundamental period.

Table A.1 and Table A.2 from Appendix A show the sequences over one fundamental cycle for the *Single-Redundancy Symmetric n-type* and the *Single-Redundancy Symmetric p-type* sequence. For both cases, as no alternation of *n-p type* pattern is used, the last vector of a sequence is always the same vector that starts the following sequence, even when changing between two sectors. Additionally, all the devices of the converter are switched-on and-off one time at every sampling time T_s. Thus, the average switching frequency for every device over one fundamental cycle is calculated as:

$$\bar{f}^s_{dev_i} = f_s \tag{2.34}$$

$$f^f_{dev_i} = 0 \tag{2.35}$$

$$\bar{f}_{dev_i} = f_s + 0 = f_s \tag{2.36}$$

On the other hand, Table A.3 and Table A.4 of Appendix A, present the switching pattern over one cycle for the *Single-Redundancy Asymmetric p-type* and the *Single-Redundancy Asymmetric n-type* sequence respectively. Evidently, the three phases perform an extra commutation not only changing from one sector to another, but also during the transition between every sampling time. Thereby, the switching frequency is calculated as:

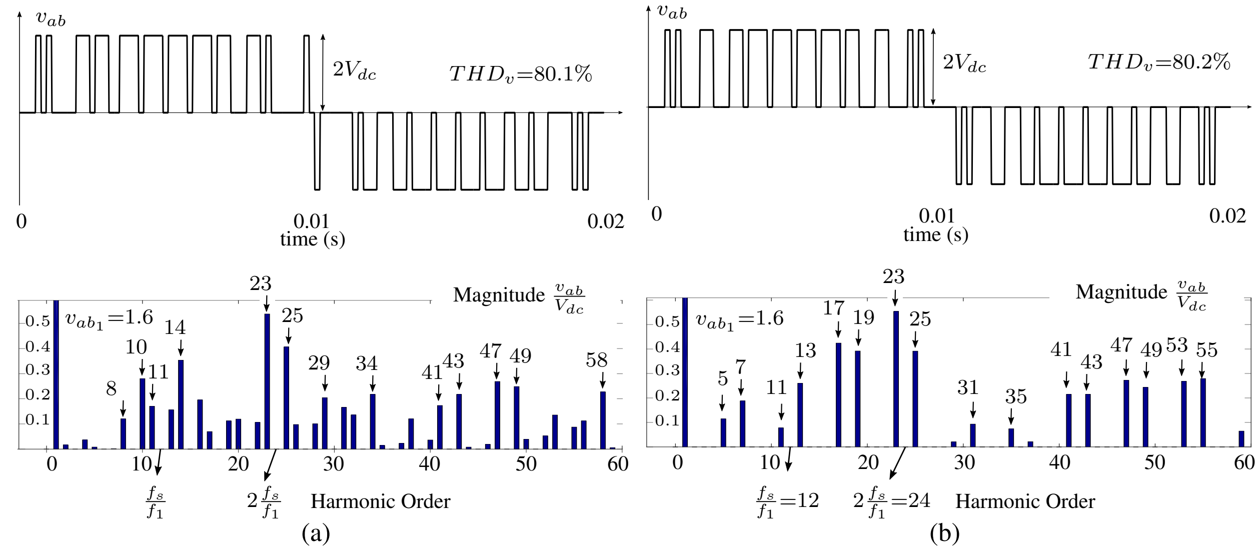

(a) (b)

Figure 2.8: Output modulated waveform v_{ab} for a reference vector with fundamental frequency f_1=$50Hz$, $m_a = 0.8\frac{2}{\sqrt{3}}$, f_s=$600Hz$ and its harmonic spectrum for a *Single-Redundancy Symmetric* sequence (a) without even-order harmonic elimination ($\bar{f}^s_{dev_i}$=$600Hz$) and (b) with even-order harmonics elimination ($\bar{f}^s_{dev_i}$=$750Hz$).

$$\bar{f}^s_{dev_i} = \frac{f_s}{2} \tag{2.37}$$

$$f^f_{dev_i} = \frac{\Lambda}{2} f_1 = \frac{f_s}{2} \tag{2.38}$$

$$\bar{f}_{dev_i} = \frac{1}{2}\left(f_s + \Lambda f_1\right) = f_s \tag{2.39}$$

where Λ was defined in (2.21). Hence, both sequences, *Single-Redundancy Symmetric* and *Single-Redundancy Asymmetric*, perform same switching frequency, but, as mentioned above, they generate different harmonic spectrum and power losses. Additionally, alternating between *Single-Redundancy Asymmetric p-type* and *Single-Redundancy Asymmetric n-type* every sampling time results in a switching frequency equal to $\bar{f}_{dev_i}$=$\frac{f_s}{2}$ per device, with $f^f_{dev_i} = 0$.

Fig. 2.8a shows the output modulated waveform for a *Single-Redundancy Symmetric p-type* sequence. As it can be seen, the modulated wave is not half-wave symmetrical, producing even-order harmonics. This could be not acceptable in grid-connected application, where even-order harmonics are stringently restricted by the standard IEEE 519-1992 [57]. This issue can be solved by alternating the sequences between *Redundant Symmetric p-type* and *Single-Redundancy Symmetric n-type* each 60° as shown in Fig. 2.9. Fig. 2.8b shows the output waveform and harmonic spectrum obtained applying this alternated sequence. Comparing both harmonic spectrum it can be noticed that the even-order harmonics have been eliminated, but the odd harmonics have increased in order to compensate this elimination. Table A.5 in Appendix A summarizes the sequence for each sub-sector of Fig. 2.9. From this table, it can be noticed that an extra switching is generated in every leg of the converter at each time that the sequence

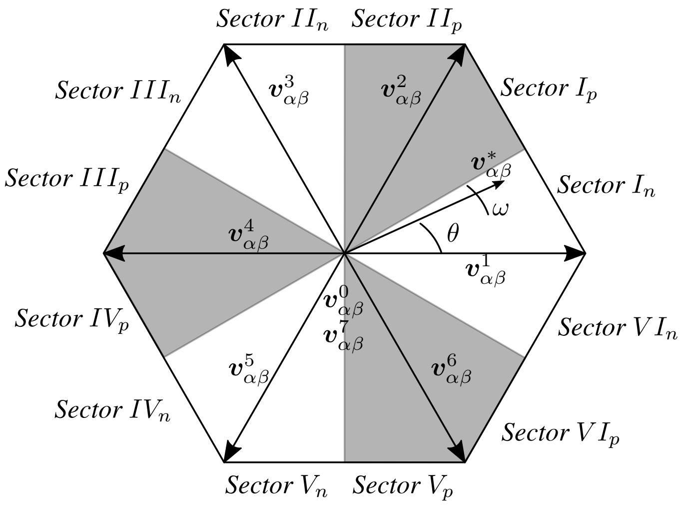

Figure 2.9: Division of the Modulation Region of a two-level VSI for implementation of Even-Order harmonics elimination. The six sectors have been subdivided, were the index *p* denotes use of the *type-p* sequence and the index *n* the use of *type-n* sequence.

changes from *p*- to *n-type* pattern. Thereby, the switching frequency per device for the even-harmonic elimination sequence is calculated as:

$$\bar{f}^{s}_{dev_i} = f_s \tag{2.40}$$

$$f^{f}_{dev_i} = \frac{6}{2} f_1 = 3 f_1 \tag{2.41}$$

$$\bar{f}_{dev_i} = f_s + 3 f_1 \tag{2.42}$$

Thus, for eliminating the even-order harmonics an increment of $3f_1$ per device is required. As f_1 is usually much smaller than f_s, the increment in the switching frequency is commonly negligible. Therefore, the switching frequency and the harmonic distortion are practically the same for both sequences. It is important to notice that for achieving even-harmonic elimination a *symmetrical sampling* is required.

b) ***Non-Redundancy Sequences*** for two-level VSI:

Equivalently to Fig. 2.7, in Fig. 2.10 the different patterns for a *Non-Redundancy* sequence are shown. As it can be seen, either for *Symmetric* or *Asymmetric* patterns, this sequence maintains one of the legs clamped to the same voltage. For that reason, it is also known as *Flat-top Modulation* or *Discontinuous Modulation*. Table A.6 and Table A.7 from Appendix A show the sequence for a complete fundamental cycle for the *Non-Redundancy Symmetric n-type* sequence and the *Non-Redundancy Symmetric p-type* sequence respectively. From these tables, it can be noticed that each phase of the converter is clamped to one phase during one third of the cycle ($\frac{2\pi}{3}$), reducing the switching frequency for every device in one third and calculated as:

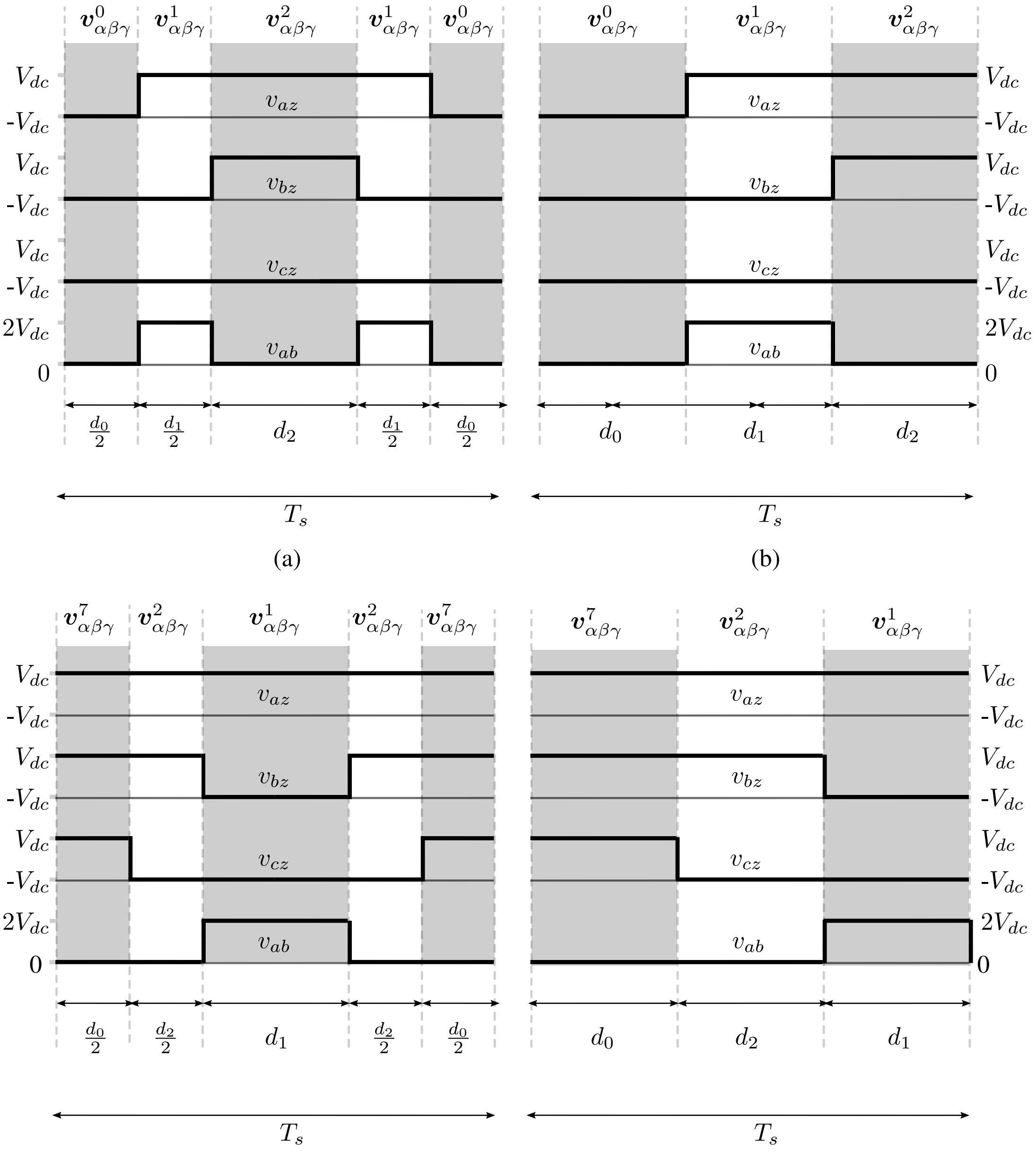

(a) (b)

(c) (d)

Figure 2.10: Different *Non-Redundancy* switching sequences. (a) *Non-Redundancy Symmetric n-type* sequence, (b) *Non-Redundancy Asymmetric n-type* sequence, (c) *Non-Redundancy Symmetric p-type* sequence and (d) *Non-Redundancy Asymmetric p-type* sequence.

$$\bar{f}^{s}_{dev_i} = \frac{2}{3} f_s \tag{2.43}$$

$$f^{f}_{dev_i} = 0 \tag{2.44}$$

$$\bar{f}_{dev_i} = \frac{2}{3} f_s \tag{2.45}$$

Although the switching frequency is equal for all devices, each leg of the converter is clamped to either the positive or the negative pole for one third of the fundamental period, which results in an unequally distribution of the conduction power losses among the switches. Applying the *Non-Redundancy Symmetric n-type* sequence with the same parameters as showed in Fig. 2.8, the harmonic distortion of the modulated wave increases to approximately 92%. Nevertheless, the switching frequency per device is reduced to $\bar{f}_{dev_i} = 400Hz$.

Alternating, for every sector, between *Non-Redundancy Symmetric n-* and *p-type* sequences [54], each leg of the converter can be clamped to negative and to the positive pole for one sixth of the fundamental period. This allows equal distribution of the conduction power losses among the switches over a fundamental cycle as shown in Table A.8. Similarly to even-order harmonic elimination pattern, the switching frequency per device is increased and can be calculated as:

$$\bar{f}^{s}_{dev_i} = \frac{2}{3} f_s \tag{2.46}$$

$$f^{f}_{dev_i} = \frac{6}{2} f_1 = 3 f_1 \tag{2.47}$$

$$\bar{f}^{s}_{dev_i} = \frac{2}{3} f_s + 3 f_1 \tag{2.48}$$

Using this sequence, the power losses can be reduced up to a 50% for a load with unitary power factor [58], [50], [20].

2.1.3 Overmodulation Strategy

As it was presented in the previous section, in order to achieve a modulation within the linear range, the path for the reference vector has to be enclosed by the hexagon of Fig. 2.6. Thereby, the amplitude of the reference vector is limited to $m_a \leq \frac{2}{\sqrt{3}}$. However, the reference vector can be synthesized further of this region when a proper overmodulation algorithm is applied. This method is based on the *volt-second balancing* and can be divided into two operation modes [59]. Fig. 2.11a shows the overmodulation in operation *Mode I*. In this case, when the reference vector is placed beyond the hexagon, its path is limited to the corresponding borders of the hexagon. Then, a new reference path is generated around the corners, which has to compensated the *volt-seconds* lost during the portion where the reference vector was out of the modulation region. The overmodulated path is marked as a red line in Fig. 2.11a. Thereby, over a cycle, the same *volt-seconds* are modulated by the original circular path (blue dotted line of Fig. 2.11a) and the overmodulated limited path (red line of Fig. 2.11a).

It is evident that there is a point where the available region around the corners of the hexagon will not be enough for compensating the *volt-seconds* lost across the trajectory of the path.

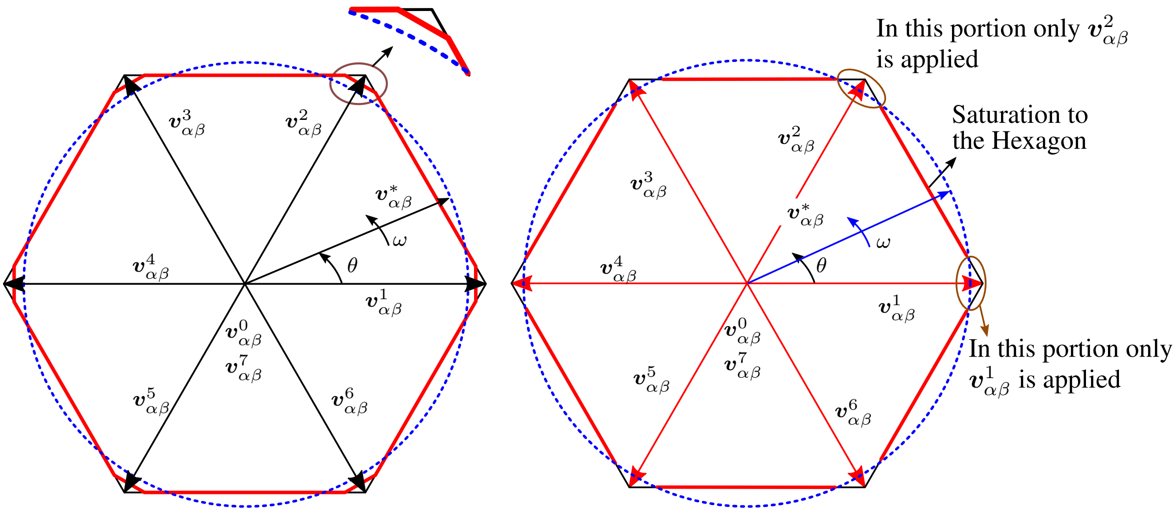

(a) (b)

Figure 2.11: Overmodulation method in (a) *Mode I* and (b) *Mode II* operation.

This limit is achieved for $m_a \approx 1.212$. Once this limit is achieved, the *Mode II* is implemented. Under this operation mode, there is no trajectory for compensating the non-modulated *volt-seconds*, but one of the active vectors is applied until the trajectory of the reference path intersects the hexagon. Fig. 2.11b shows this procedure. Thereby, from this figure and looking at *sector I*, the vector $v^1_{\alpha\beta\gamma}$ is applied during the time that the reference path is inside the hexagon, after that, the path is limited to the border of the hexagon and is modulated by $\boldsymbol{v}^1_{\alpha\beta\gamma}$ and $\boldsymbol{v}^2_{\alpha\beta\gamma}$ (the *zero vector* is not used). Evidently, for a circular reference path that completely encloses the hexagon ($m_a \geq \frac{4}{3}$), no borders of the hexagon are used and only the *active vectors* are used every $60°$. This results in the *six-step* operation mode, producing the maximum allowable output phase-voltage ($\hat{v}_{6step}{=}\frac{4}{\pi}V_{dc}$ in (2.12)).

It is important to mention that the use of overmodulation introduces low-order harmonics, which are no characteristics of the SVM operated under the linear region. Additionally, although the fundamental component is boosted, it differs from the reference value not only in magnitude but also on its phase shift. This can be harmful for controlling power conditioners, where the phase shift of the fundamental and harmonics modulated voltages are crucial for a proper compensation [60].

2.2 The Three-level Neutral Point Clamped VSI

Introduced in 1981 [24], the three-level Neutral Point Clamped (NPC) VSI has become today a standard topology for medium-voltage (MV) drives in the industry [38]. Additionally, it has also been preferred in low voltage range when high efficiency is required, as for photovoltaic applications [40] [39]. Compared to a two-level VSI, a three-level VSI offers several advantages, such as: reduction of the *dv/dt* and the corresponding Electromagnetic Interference (EMI), improvement of the output harmonic spectrum because of its three-level nature, reduction of the switching frequency per device and, maybe its main feature, distribution of the device blocking voltage, where each device of the converter withstand only half of the dc-link voltage. Usually a three-level NPC converter operates in applications up to a range of $4.16kV$, composed of either IGBT or IGCT semiconductor devices, where the latter are usually preferred for high power applications. Currently, IGBTs posses a maximum collector-emitter blocking voltage of $6.5kV$ at $600A$, while for a IGCT the maximum blocking voltage is $6.5kV$ at $4.2kA$ [61], [45]. Fig. 2.12 shows the topology of a thee-leg three-level NPC converter. It is composed of twelve switches with their respective antiparallel diodes, named as S_{1i}, S_{2i}, $\bar{S}_{1i}$ and $\bar{S}_{2i}$ and six clamped diodes denoted as D_i and $\bar{D}_i$ for $i \in \{a, b, c\}$. Furthermore, for achieving its three-level nature, the dc-link is split by two capacitors, namely C_1 and C_2, which voltages must remain balanced to V_{dc} for proper operation.

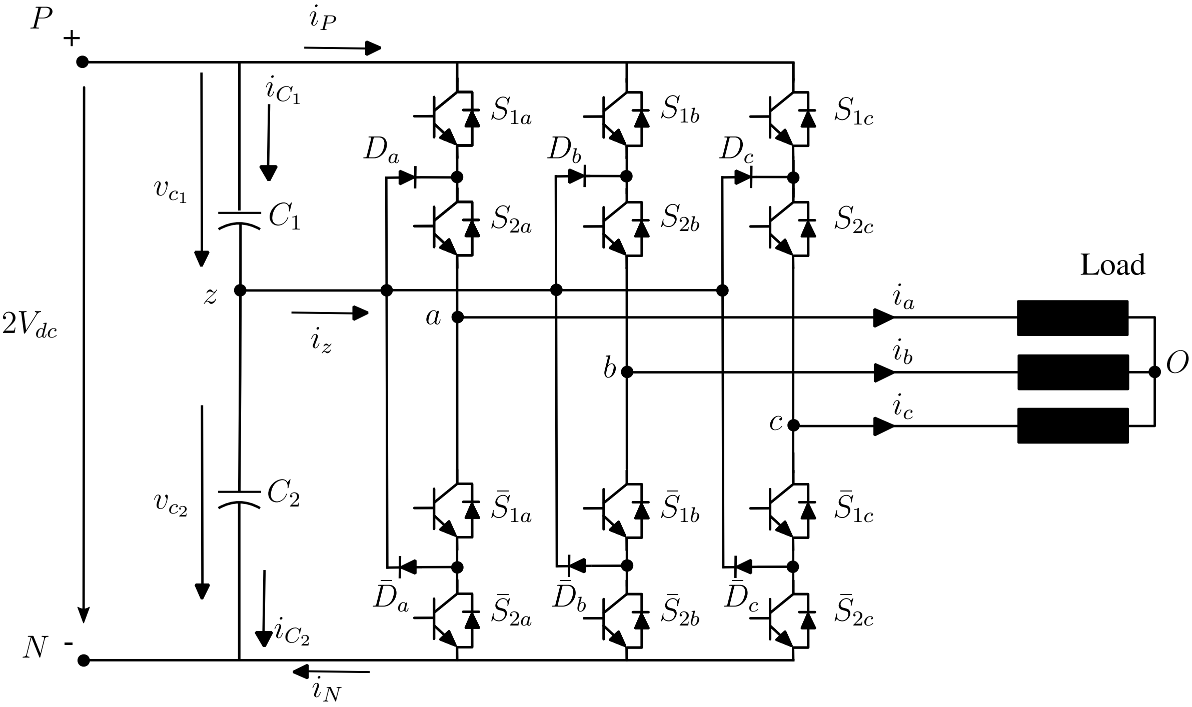

Figure 2.12: Three-level Neutral Point Clamped Topology.

2.2.1 Principle of Operation

Each leg of the converter presented in Fig. 2.12 can generate three different phase voltages v_{iz} for $i \in \{a, b, c\}$. Fig. 2.13 shows the three permitted states for the phase a of the converter, considering that the voltages v_{c_1} and v_{c_2} are balanced to V_{dc}. As it can be seen in Fig. 2.13a, when the upper switches are closed, the output phase voltage (v_{iz}) produced by the VSI is V_{dc}. Similarly when the middle switches are closed , Fig. 2.13b, the output phase voltage is zero. Finally, from Fig. 2.13c, when the bottom switches are closed, the output voltage is equal to -V_{dc}. Thereby, the three-level NPC can produce three different levels at the output phase voltages, namely V_{dc}, 0 or -V_{dc}.

From Fig. 2.13 the conduction of the semiconductors under different operation modes can be appreciated. The conduction of the different devices in one leg depends on relation between the direction of the output current i_a and polarity of the output voltage v_{az}, i.e. the power factor of the load. Thus, considering Fig. 2.13a and a positive load current i_a, the current flows only

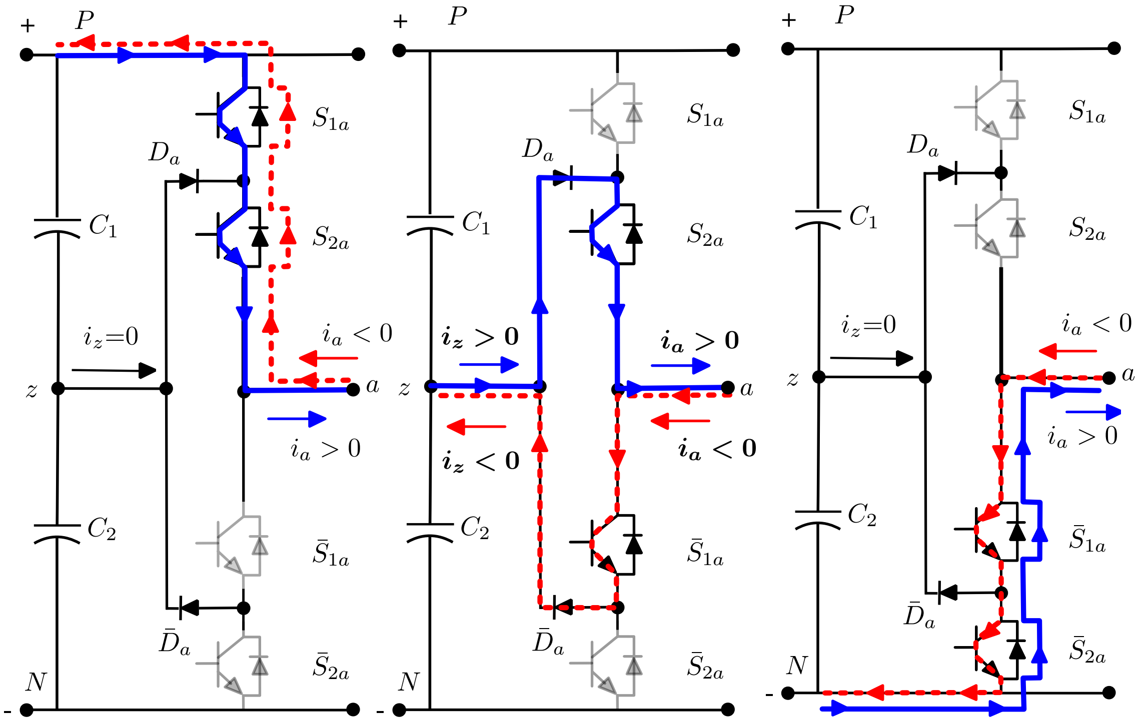

(a) (b) (c)

Figure 2.13: Switching states and semiconductor devices conduction for (a) positive, (b) zero and (c) negative output phase voltages.

through the switches S_{1a} and S_{2a}, avoiding conduction of all diodes. This is shown with a blue line in Fig. 2.13a. Contrary, for $i_a < 0$ and maintaining the same switching combination, the current flows through the antiparallel diodes of switches S_{1a} and S_{2a}, showed with a dotted red line in Fig. 2.13a. Based on the same procedure, Fig. 2.13b and Fig. 2.13c show the conduction of the semiconductors for the two remaining switching combinations.

From the previous discussion it can be also concluded that each device withstand only half of the dc-link voltage at each switching state. In real implementation a proper sequence is performed during the transition from one state to another to avoid transients overvoltages [54]. Additionally, when the middle switches are closed, a current flows through the neutral-point z, which imbalance the voltages in each of the two capacitors C_1 and C_2. This represents the main drawbacks of the NPC converter and special strategies to maintain these voltages balanced have been reported in the literature and summarized in Section 2.2.3 of this Chapter .

Considering that each leg of the converter can generate three possible phase voltages, the current through the neutral-point i_z can be calculated as:

$$i_z = \sum_{x=a,b,c} \bar{S}_{1x} S_{2x} i_x, \tag{2.49}$$

where $\bar{S}_{1x}$ and $S_{2x} \in \{1, 0\}$ and indicates whether the switch is close ("1") or open ("0") respectively.

2.2.2 Space Vector Modulation

Similarly to the two-level VSI, Carrier-Based PWM and Space Vector Modulation algorithms presented in Subsection 2.1.2 can be extended to be applied in Multilevel converters [38]. For the Carrier-Based PWM method, two triangular carrier references are generated and compared with the positive and negative semi-cycle of reference signals. This is also known as level-shifted PWM, which represents the natural extension of the bipolar PWM method [41]. As a result of this comparison, the control signals to trigger the four switches of each leg are obtained. This method presents equivalent characteristics as for a two-level inverter, presented in Subsection 2.1.1, which after injection of third harmonic reaches a maximum modulation index equal to $\frac{2}{\sqrt{3}}$ [41]. Although this method is effective and simple, it does not allow modification of the switching patterns, which is very important in medium voltage range, where low switching frequency ranges are required. Furthermore, as the switching sequences can not be arranged, it is not a suitable technique for implementing advanced methods for balancing the voltages of the dc-link capacitors, which is a key issue in a NPC converter. Thereby, an extension of the Space Vector Modulation algorithm presented in Subsection 2.1.2 is required for achieving a more flexible and sophisticated control algorithm for a to three-level NPC converter which is presented in this Section .

2.2.2.1 Space of Vectors

Considering that each leg of the converter produces three possible switching combination, the three-level NPC converter possesses 3^3=27 different switching states, namely $[v_{az}, v_{bz}, v_{cz}]$, which generate 19 different line-to-line voltages. Table A.9 from Appendix A summarizes all these possible switching combinations, which have been normalized as presented in (2.13). Additionally, applying the Clarke transformation presented in (2.14) to each of these switching combination, its $\alpha\beta\gamma$ representation is obtained and also presented in Table A.9. Furthermore, this table also present the current through the neutral-point, calculated as (2.49), generated by each switching combination.

Fig. 2.14 shows the representation of the 27 different *stationary vectors* in the $\alpha\beta$ plane for a three-level NPC converter. As it was previously discussed in Subsection 2.1.2, the γ component can be neglected, as it represents an independent variable which can unrestrictedly variate without negatively affecting the modulated signals. As it can be seen in Fig. 2.14, only 19 vectors are depicted in the $\alpha\beta$ plane and differentiated as *zero*, *small*, *medium* and *large* vectors. The eight remaining vectors, to complete the 27 combinations, are represented as two redundancies for the *zero* vector and one redundancy for each of the *small vectors* (see Table A.9). Although the switching combination of a *redundant* vector are not identical, they share the same $\alpha\beta$ components, i.e. generate the same line-to-line voltages, which place them in the same position in the $\alpha\beta$ plane and can be considered as equivalent vectors for modulating the output voltages. *Redundant vectors* are very important in a NPC converter, as they produces the same output line-to-line voltages, but generate opposite current through the neutral-point (i_z), which allows the balance of the voltages in the capacitors v_{c_1} and v_{c_2}.

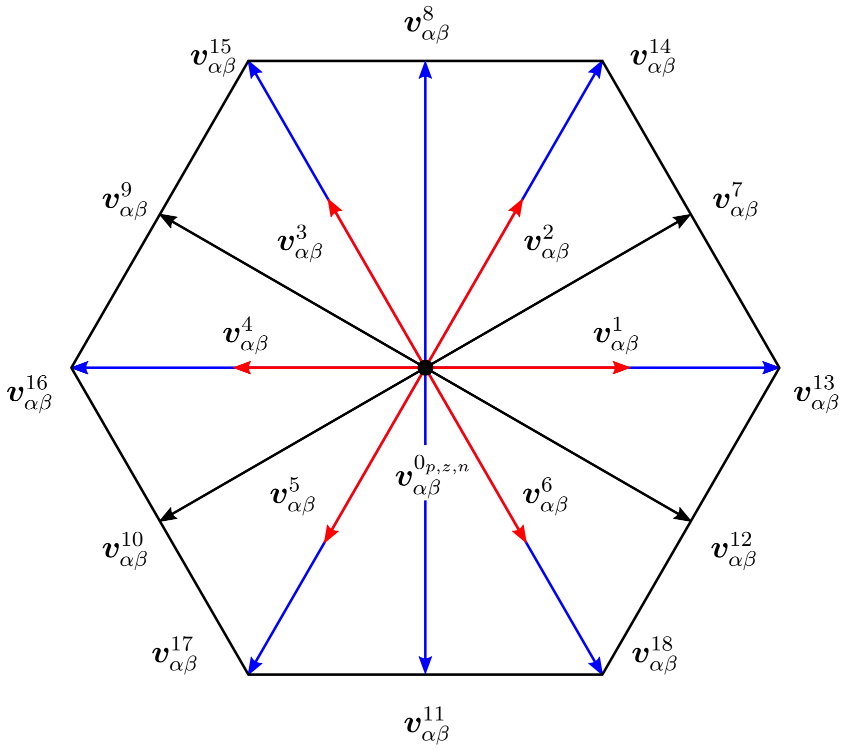

Figure 2.14: *Stationary vectors* generated by the three-level NPC Converter. $v_{\alpha\beta\gamma}^{0}$ is known as *zero vector*, $v_{\alpha\beta\gamma}^{1}$ to $v_{\alpha\beta\gamma}^{6}$ as *Small vectors*, $v_{\alpha\beta\gamma}^{7}$ to $v_{\alpha\beta\gamma}^{12}$ as *Medium vectors* and $v_{\alpha\beta\gamma}^{13}$ to $v_{\alpha\beta\gamma}^{18}$ as *Large vectors*. *Small* and *Zero vectors* are also known as *Redundant vectors*.

2.2.2.2 Dwell-time Calculation

Once obtained the space of vectors, the reference vector must be represented inside this region to be synthesized at each sampling time T_s. Similarly to a two-level VSI, the reference vector can be also represented as (2.15). Fig. 2.15 shows the modulation region and the reference vector placed in *Sector III*. Beside of being divided into the standard six *sectors*, the additional vectors of this topology subdivide each *sector* into four regions, denoted as $\rho \in \{1, 2, 3, 4\}$. Each of these regions define the smaller triangle that can contain the reference vector. Consequently, the three vectors that compose one triangle will be used for modulating the sampled reference value at each sampling time T_s.

In order to achieve the modulation of the reference vector, first its sector and region has to be identified by a simple algorithms using the vector angle θ and its magnitude $|\boldsymbol{v}_{\alpha\beta}^{*}|$ [62]. Let us consider the reference vector of Fig. 2.15, placed in *sector III*, *region 2 ($\rho = 2$)*. By that, the *stationary vectors* that modulate the reference at this sampling time are: $\boldsymbol{v}_{\alpha\beta\gamma}^{3}$, $\boldsymbol{v}_{\alpha\beta\gamma}^{4}$ and $\boldsymbol{v}_{\alpha\beta\gamma}^{9}$. In order to calculate their *dwell times*, the following expression has to be fulfilled during the sampling time T_s:

$$\boldsymbol{v}_{\alpha\beta}^{*} \cdot T_s = \boldsymbol{v}_{\alpha\beta}^{4} \cdot d_1 + \boldsymbol{v}_{\alpha\beta}^{3} \cdot d_2 + \boldsymbol{v}_{\alpha\beta}^{9} \cdot d_3 \tag{2.50}$$

$$T_s = d_1 + d_2 + d_3, \tag{2.51}$$

Thus, the *dwell times* are obtained as:

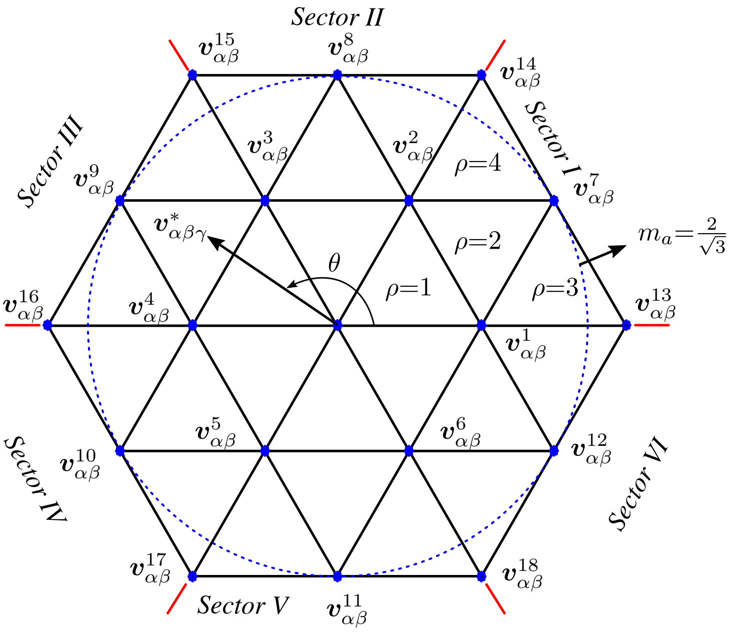

Figure 2.15: Modulation Region for a three-phase three-level NPC converter.

$$\begin{bmatrix} d_1 \\ d_2 \\ d_3 \end{bmatrix} = T_s \begin{bmatrix} v^4_\alpha & v^3_\alpha & v^9_\alpha \\ v^4_\beta & v^3_\beta & v^9_\beta \\ 1 & 1 & 1 \end{bmatrix}^{-1} \begin{bmatrix} v^*_\alpha \\ v^*_\beta \\ 1 \end{bmatrix}, \tag{2.52}$$

or alternatively, referencing the equation to only one of the *stationary vectors*:

$$\begin{bmatrix} d_1 \\ d_2 \end{bmatrix} = T_s \begin{bmatrix} v^4_\alpha - v^9_\alpha & v^3_\alpha - v^9_\alpha \\ v^4_\beta - v^9_\beta & v^3_\beta - v^9_\beta \end{bmatrix}^{-1} \begin{bmatrix} v^*_\alpha - v^9_\alpha \\ v^*_\beta - v^9_\beta \end{bmatrix} \tag{2.53}$$

$$d_3 = T_s - d_1 - d_2, \tag{2.54}$$

where the $\alpha\beta$ coordinates of each *stationary vector* are obtained from Table A.9. Although current Digital Signal Processors (DSP) can normally afford the inversion of the matrix presented in (2.52) or (2.53), the *dwell time* calculation can be also obtained from a preset look-up table [54] (see Table A.10 from Appendix A). Similarly to (2.27) to (2.29), the look-up table store the formulas for calculation of the *dwell times* for each sector and region according to the angle of the reference vector θ.

2.2.2.3 Switching Sequence and Harmonic Spectrum

Unlike the modulation region presented for the two-level VSI in Fig. 2.6a, each *sector* of the modulation region for a three-level NPC converter has been subdivided into four regions (see Fig. 2.15), forming regions that posses one (ρ=3 and ρ=4), two (ρ=2) or even three (ρ=1) *redundant vectors*.

From Fig. 2.15 it is seen that region ρ=1 is formed by the *zero* vector and two *small vectors*, ρ=2 is formed by two *small vectors* and one *medium* vector and regions ρ=3 and ρ=4 are formed by one *small*, one *medium* and one *large vector*. Therefore, considering the redundancies of each redundant vector, regions ρ=3 and ρ=4 posses four available switching combinations, region ρ=2 possesses five available switching combinations and region ρ=1 possesses seven available switching combination (*zero vector* possesses three redundancies), which could be used for modulating a reference vector at each sampling time. Thereby, using always all the available redundancies of the *small* and *zero vectors* would produce sequences with different number of switching transitions depending on the region where the reference vector is placed, generating different switching frequencies for each device of the converter. This is usually not desired and a sequence that produce the same switching frequency in every region is commonly implemented. This can be achieved by using the redundancies of only one *small vector* in each region.

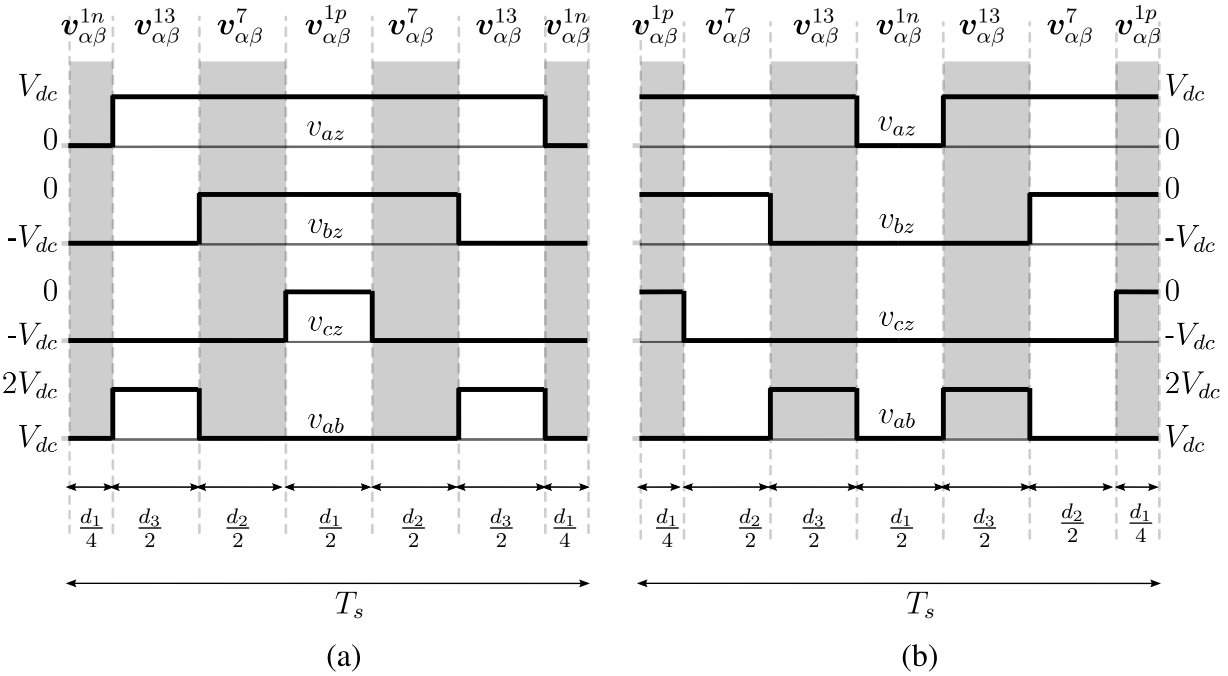

Figure 2.16: (a) *Single Redundancy Symmetric n-type* sequence and (b) *Single Redundancy Symmetric p-type* sequence for *sector I*, region ρ=3 of a three-level NPC converter.

Thereby, consequently with the definitions of Section 2.1.2.3, the *Single-Redundancy* sequence designates a sequence formed by using the redundancies of only one *small vector* at each sampling time. Satisfying the *minimum switching transition* principle introduced in Subsection 2.1.2, Fig. 2.16 shows the *Single-Redundancy Symmetric* patterns for a reference vector placed in *sector I*, *region 3* ($\rho = 3$). Fig. 2.16a shows a *Single Redundancy Symmetric n-type* sequence, while Fig. 2.16b shows the *Single Redundancy Symmetric p-type* sequence (*Symmetric* and *p-n type* definitions were presented in Subsection 2.1.2.3). Both sequences use the only redundant vector present at this region. Therefore, they represent the only two possible *Single Redundancy Symmetric* sequences for this region.

On the other hand, for a reference vector placed in regions ρ=1 or ρ=2, two possible *Single Redundancy Symmetric n-* and *p-type* sequences can be generated. Their difference depends on which *small vector* is used with redundancy. Fig. 2.17a and Fig. 2.17c show the two possible

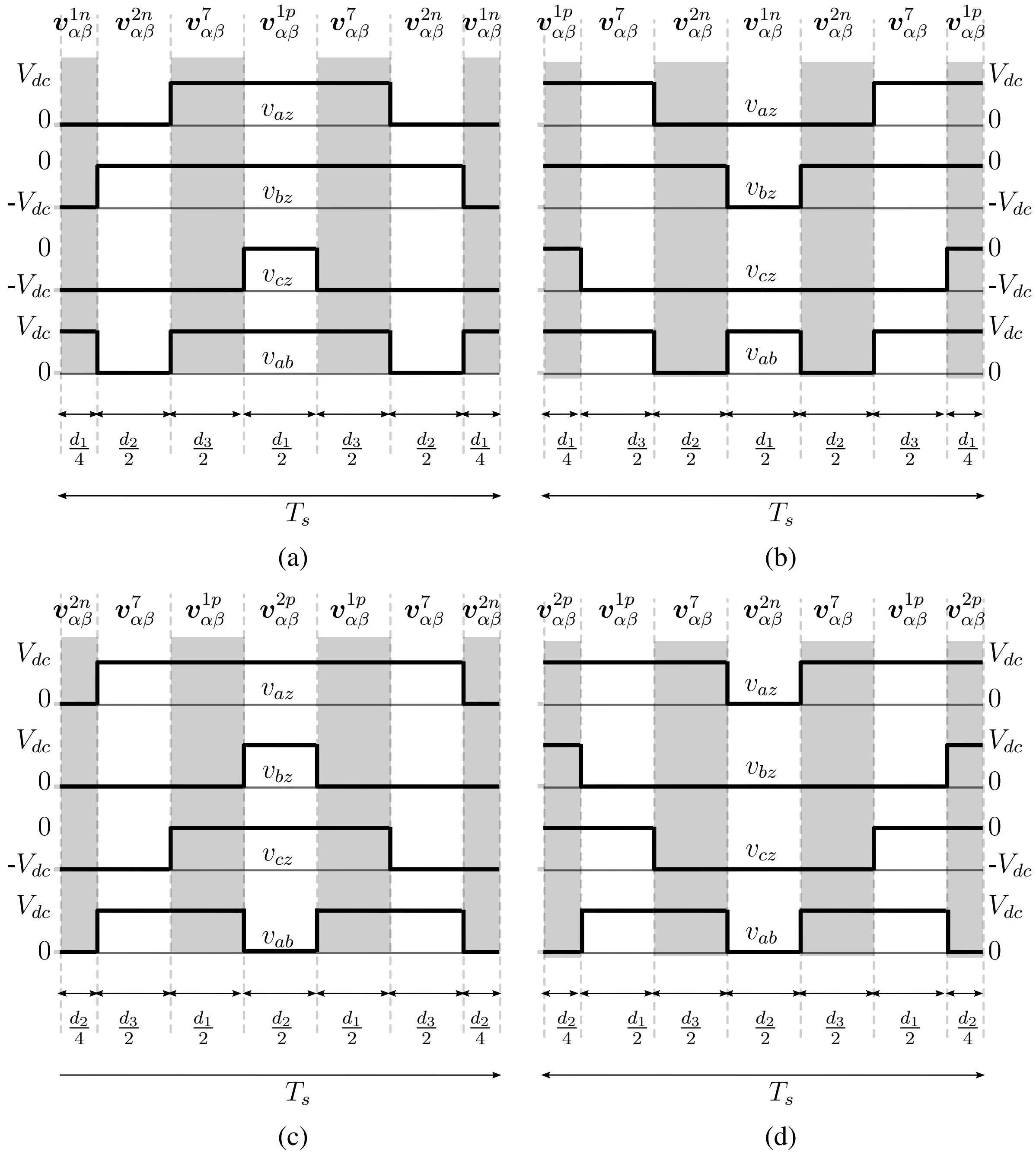

(a) (b) (c) (d)

Figure 2.17: (a) *Single Redundancy Symmetric n-A-type* sequence and (b) *Single Redundancy Symmetric p-A-type* sequence (c) *Single Redundancy Symmetric n-B-type* sequence and (d) *Single Redundancy Symmetric p-B-type* sequence for *sector I*, region ρ=2 of a three-level NPC converter.

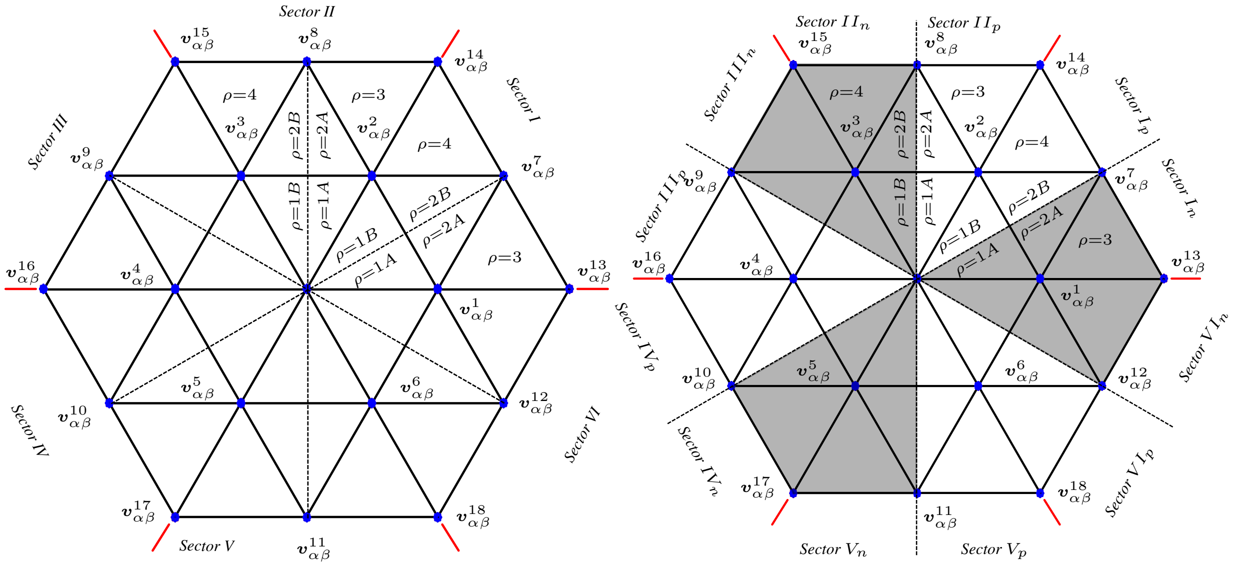

(a) (b)

Figure 2.18: Modulation region of the three-level NPC converter for (a) identification of sequences *type-A* and *type-B* and (b) identification of regions for *p-type* and *n-type* pattern used in even-order harmonics elimination. Sub index in each sector makes reference to the use of *p-type* or *n-type* sequences.

n-type sequences for a reference vector placed in *sector I*, *region 2 (*ρ=2*)*. The first uses the redundancies of $\boldsymbol{v}^1_{\alpha\beta}$ and is denoted with the character *A*, while the second uses the redundancies of $\boldsymbol{v}^2_{\alpha\beta}$ and is denoted with the character *B*. Similarly, Fig. 2.17b and Fig. 2.17d show the two equivalent *p-type* sequences. As it can be seen from Fig. 2.16 and Fig. 2.17, regardless of the region, the same number of switching transitions are performed for each leg of the converter. This produces a constant switching frequency for each device of the converter.

The selection of sequence *type-A* or *type-B* is based on the influence that each of the *small vectors* of one region has over the neutral-point balancing. In order to obtain proper balance of the neutral-point voltage, always the redundancy of the closest *small vector* to the reference vector has to be selected. This defines the use of *type-A* or *type-B* sequences.

Consequently, as shown Fig. 2.18a, regions ρ=1 and ρ=2 have been subdivided into ρ=$1A$, ρ=$1B$, ρ=$2A$ and ρ=$2B$, each sub-region defines the area where each *small vector* posses largest *dwell time*. Thus, always the redundancy of the *small vector* that posses the largest *dwell time* is used. Hence, for instance, for a vector placed in *sector I, region* ρ=$2A$ the redundancy of $\boldsymbol{v}^1_{\alpha\beta}$ is used, generating the sequences of Fig. 2.17a or Fig. 2.17b. Similarly, for a reference vector placed at *sector I, region* ρ=$2B$ the redundancy of $\boldsymbol{v}^2_{\alpha\beta}$ is used, generating the sequences of Fig. 2.17c or Fig. 2.17d.

The sequence arrangement of Fig. 2.18a presents the best trade-off among the switching frequency, harmonic spectrum and neutral-point voltage balance capability and is used in a wide range of applications [54]. Table A.11 from Appendix A provides the switching arrangement for each each sub-region of *sector I* of Fig. 2.18a. (same tables can be equivalently obtained for the other *sectors*).

From Fig. 2.13, it can be concluded that only two of the four switches in each leg are involved during the transition between two allowable states of the converter. Thereby, in order to switch-on and -off every switch in one leg, a transition of the type: P → O → N → O →P has to be accomplished. Considering that during the positive semi-cycle of each reference phase-voltage v^*_{iz}, for $i \in \{a, b, c\}$, the switches S_{2i} and $\bar{S}_{2i}$ do not commutate (same for S_{1i} and $\bar{S}_{1i}$ during the negative semi-cycle), the switching frequency for each device will be reduced by half during one fundamental cycle. Thereby, using Table A.11, the average switching frequency per device over one fundamental cycle can be calculated as (see (2.31)):

$$\bar{f}^s_{dev_i} = \frac{f_s}{2} \tag{2.55}$$

$$f^f_{dev_i} = \frac{f_1}{2} \tag{2.56}$$

$$\bar{f}^s_{dev_i} = \frac{f_s}{2} + \frac{f_1}{2} \tag{2.57}$$

where the switching frequency for each device is approximately half of the sampling frequency f_s. The additional term $\frac{f_1}{2}$ in the averaged switching frequency is originated because of the alternation on the redundancy of the two *small vectors* inside each region. This alternation can be avoided and the switching frequency would be reduced to $\frac{f_s}{2}$. However, this worsens the control over the neutral-point , reducing the switching frequency in a negligible value.

Additionally, alternating between *p-* and *n-type* patterns every 60° (as showed in Fig. 2.18b) elimination of the even-order harmonics can be achieved [63]. The sequences for each sub sector of *sector I* are presented in Table A.12 from Appendix A. The switching frequency per device is slightly increased implementing even harmonics elimination and can be calculated as:

$$\bar{f}^s_{dev_i} = \frac{f_s}{2} \tag{2.58}$$

$$f^f_{dev_i} = \frac{2}{2} f_1 = f_1 \tag{2.59}$$

$$\bar{f}^s_{dev_i} = \frac{f_s}{2} f_s + f_1 \tag{2.60}$$

Fig. 2.19 shows the output line-to-line voltages and harmonic spectrum with and without elimination of even-order harmonics for a three-level NPC VSI. As expected, the even harmonic are eliminated and both sequences present practically same harmonics distortion. This is achieved by an slight increase of the average switching frequency from $625Hz$ to $650Hz$. Additionally, the first dominant group of harmonic components is placed at twice the sampling frequency f_s. This is the main characteristic of the three-level NPC converter, where the modulated waveforms posses an equivalent harmonic frequency higher than the switching frequency of the devices.

Generating a *Non-Redundancy* sequence without using any redundancy of the *small vectors* can be also implemented, obtaining same conclusions as presented in Subsection 2.10. In this case, each phase of the converter is clamped to one phase for one third of the fundamental period. This reduces the switching frequency and power losses per device. Nevertheless, it worsens the harmonic spectrum and seriously affects the balance of the control over the voltage on the dc-link capacitors [64], [65]. This can be used when the power losses need to be minimized [54].

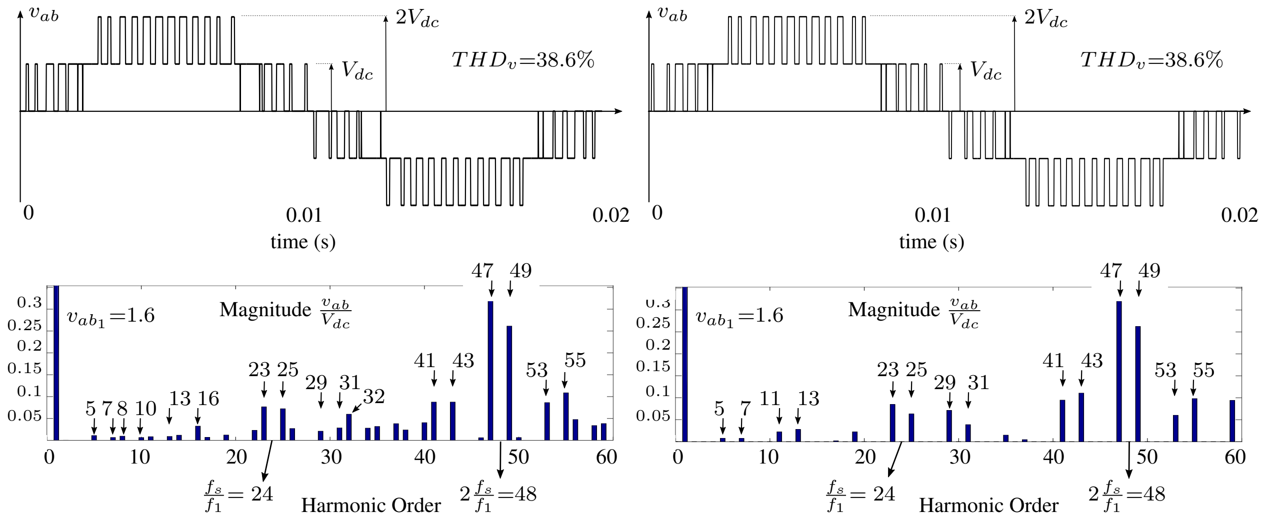

(a) (b)

Figure 2.19: Output modulated waveform v_{ab} for a reference vector with fundamental frequency f_1=50Hz, $m_a = 0.8\frac{2}{\sqrt{3}}$, f_s=1200Hz and its harmonic spectrum for a *Single-Redundancy Symmetric* sequence (a) without even-order harmonic elimination ($\bar{f}^s_{dev_i}$=625Hz) and (b) with even-order harmonics elimination ($\bar{f}^s_{dev_i}$=650Hz).

2.2.3 The Neutral Point Potential Problem

Maintain the balance of the voltages over the dc-link capacitors v_{c_1} and v_{c_2} is an important issue in a NPC VSI. From Table A.9 it can be observed that only *small* and *medium vectors* have an influence over the neutral-point voltage balancing, while *zero* and *large* vectors have no influence, i.e. $i_z = 0$. Furthermore, the two redundancies of one *small vector* generate two currents i_z with the same magnitude and opposite direction, while maintaining the same output line-to-line voltages. This feature is the basic principle used to compensate the current i_z over one sampling time T_s, which consequently allow the control over the voltages v_{c_1} and v_{c_2} of Fig. 2.12.

Let us assume that the previously defined *Single Redundancy* sequence is implemented. Thereby, only one redundant vector, i.e. *small vector*, is used at each sampling time T_s. Considering that the current i_z generated by each switching combination remains constant during the time that this vector is applying in T_s, the average current i_z over one sampling time can be expressed in a general form as:

$$\bar{i}_z = d_{1p} \cdot i_{z_1} + d_2 \cdot i_{z_2} + d_3 \cdot i_{z_3} - d_{1n} \cdot i_{z_1} \tag{2.61}$$

$$d_1 = d_{1p} + d_{1n} \tag{2.62}$$

where d_1, d_2 and d_3 represent the *dwell times* for each of the three vectors that compose a region, calculated in (2.50), and i_{z_1}, i_{z_2} and i_{z_3} represent the currents generated through the neutral-point by each of these three vectors, as presented in Table A.9. In this equation, the *dwell time* d_1 has been divided into d_{1p} and d_{1n} representing the only two redundancies of a *small vector* selected in each sampling time. Thereby, controlling the time distribution between d_{1p} and d_{1n}, and satisfying with (2.62), $\bar{i}_z$ and consequently the voltages v_{c_1} and v_{c_2} can be regulated during each sampling time.

Based on the previous discussion, several methods for controlling $\bar{i}_z$, i.e. controlling d_{1p} and d_{1n}, can be implemented. These methods can be mainly categorized as follow [66]:

a) Passive Control Scheme:

This open-loop method controls the neutral-point voltage by equally dividing the *dwell times* d_{1p} and d_{1n} over each sampling time. Thereby, considering that the measured line currents remain constant during T_s, the effect of i_{z_1} over $\bar{i}_z$ is completely eliminated (see (2.61)). Nevertheless, the average current $\bar{i}_z$ is not equal to zero, being affected by the two remaining currents, namely i_{z_2} and i_{z_3}.

Considering a system with symmetric and balanced currents, the effect of i_{z_2} and i_{z_3} over the current $\bar{i}_z$ is naturally compensated over one fundamental cycle. Thereby, the voltages on v_{c_1} and v_{c_2} oscillates around its middle point, i.e. V_{dc} (see Fig. 2.12) with a frequency equal to three times the fundamental frequency of the line currents [66]. The amplitude of this oscillation, i.e. its ripple, is a function of the power factor of the load, the magnitude of the line currents and the value of the capacitances C_1 and C_2. Generally, the ripple of the neutral-point voltage is minimum for power factor equal to one, while for pure inductive or capacitive loads it perform its maximum value. An empiric method for estimating the size of each capacitor regarding the nominal load current can be found in [66].

The natural the compensation of the current $\bar{i}_z$ over one fundamental period is possible only under the following conditions:

- Perfectly symmetric and balanced line currents.
- The size of the capacitor C_1 and C_2 must be identical.
- The sampling of the reference voltage vector must be accomplished as *Symmetric Sampling*.

When one of these criteria is not fulfilled, the voltages v_{c_1} and v_{c_2} diverge. Additionally, as no voltage or currents measurement are used, this methods can only maintain the initial condition of the voltages on C_1 and C_2, presenting problems after transient operation.

b) Hysteresis Control Scheme:

It is the simplest closed-loop control method for NP voltage balancing [67]. In this method, the direction of each phase current must be measured at each sampling time. Thus, the direction of the neutral-point current i_z is obtained and either d_{1p} or d_{1n} is used in order to compensate the deviation produced by i_z to the neutral-point voltage. This method provides good balance of the voltages v_{c1} and v_{c2} even for the conditions where the passive control scheme diverge. Additionally to the voltage oscillation of three times the fundamental frequency in v_{C_1} and v_{C_2}, this method introduces a ripple equal to the switching frequency, i.e. approximately half of the sampling frequency.

c) Active Control Scheme:

This is a more sophisticated closed-loop control technique, based on the measurement of v_{c_1} and v_{c_2} [68]. Using these measurements, an outer controller, usually a PI controller, provides a neutral-point current reference $\bar{i}_z^*$ at each sampling time. This control scheme is depicted in Fig. 2.20.

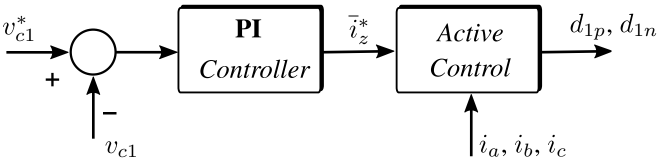

Figure 2.20: External closed-Loop controller for active control of the neutral-point current i_z.

Therefore, time distribution between d_{1p} and d_{1n} is controlled in order to equal $\bar{i}_z$ to $\bar{i}_z^*$ at each sampling time. Compared to the previous presented method, this method does not introduce high frequency ripple on the neutral-point and provides the best performance. Additionally, it provides balancing of the voltages v_{c_1} and v_{c_2} even after critical transients, unsymmetrical sampled reference, different size of dc-link capacitors or unbalanced currents. However, it can presents problem under unsymmetrical and non-sinusoidal currents, specially when they posses continuous *dc* components.

d) Other Control Schemes:

Another method that has gained attention lately is the so called, Virtual Space Vector PWM (VSVPWM) [69]. In this method, the vectors that modulate a reference vector are not obtained as the three nearest vectors that enclose the reference sampled value, but as a combination of vector that allows to obtain i_z=0 at each sampling time. This provides a better performance compared to the presented methods under unbalanced and non-linear loads or under the overmodulation region. However, it worsens the harmonic spectrum of the modulated output voltages and the power losses are increased.

A method for balancing the voltages on the dc-link capacitors under overmodulation operation has been proposed in [70]. This method analyses the reduced utilization of *small vectors* in the overmodulation range and proposes a suitable switching sequence to achieve balance of neutral-point voltage. It is important to mention that the outer boundaries of the modulation region for a two-level VSI or a three-level NPC are equivalent (same hexagon). Therefore, neglecting the problem of the neutral-point voltage balancing, the overmodulation method presented for a two-level in Subsection 2.1.3 can be also used in a three-level NPC converter [70].

CHAPTER 3

Control of Power Converters for four-wire Applications

Abstract: *This chapter provides an extensive review of the state of the art of power electronic converters for four-wire applications. A theoretical comparison between three-leg four-wire and four-leg converters is provided. Moreover, a detailed description of the reported SVM techniques for two-level and multilevel four-leg converters is provided and discussed in this chapter.*

Theoretical discussion about power converters for four-wire systems was early introduced in the late 1980's [71]. However, its implementation came just at the end of the 1990's, as a solution for mitigating the harmonics distortion present in four-wired unbalanced systems [11–14]. After this event, mainly two topologies were subject of intensive research for the following years, namely the two-level three-leg four-wire converter and the four-leg two-level converter. These topologies are depicted in Fig. 3.1 and represent the main focus of this chapter.

The three-leg four-wire converter of Fig. 3.1a splits the dc-link voltage to obtain the fourth wire, while a four-leg converter uses an extra leg for this propose. The extra wire provided by both converters allows circulation and control of the zero-sequence component, which is required in four wire applications, where the load is usually unbalanced and non-linear.

The additional leg in a four-leg converter provides additional number of switching combinations. Thereby, compared to the eight possible switching combinations of Fig. 3.1a (see Table 2.2 in Chapter 2.1.2), the two-level four-leg converter of Fig. 3.1b possesses sixteen switching combinations. These switching combinations are used for modulating the output phase-voltages of the converters presented in Fig. 3.1, i.e. v_{iz} in a three-leg four wire converter or v_{if} in a four-leg converter, for $i\{a, b, c\}$.

Consequently, from simple inspection of Fig. 3.1, three main advantages of the four-leg converters over the three-leg four-wire converters can be observed and are summarized as follows:

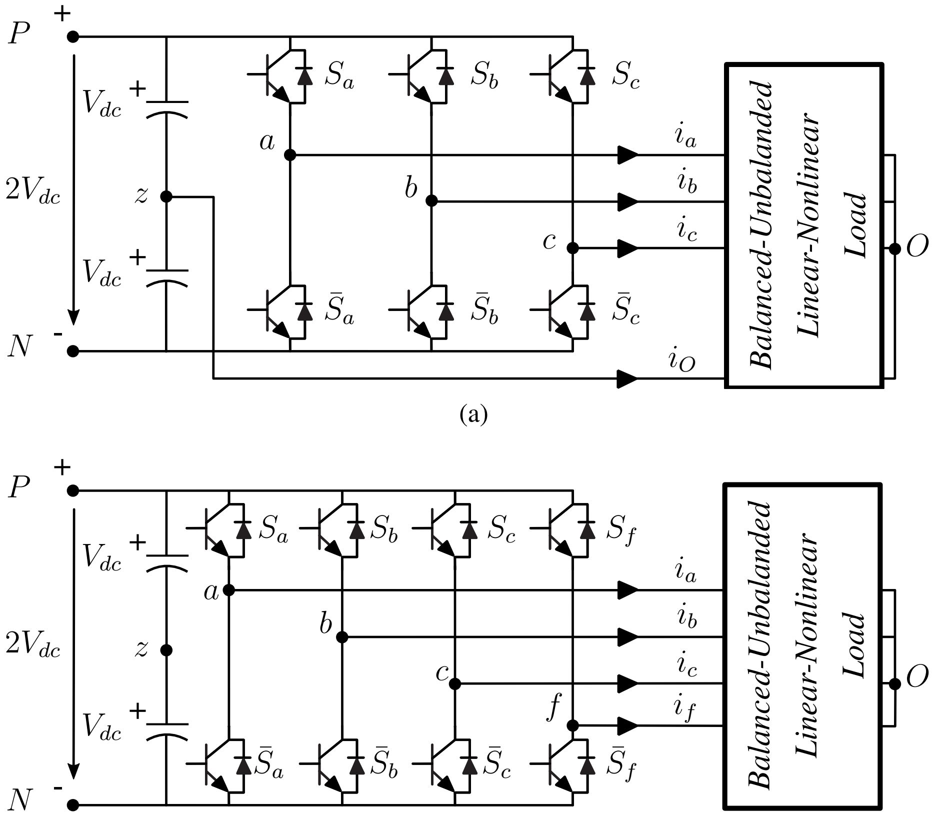

(a)

(b)

Figure 3.1: Topology for a (a) two-level three-leg four-wire converter and a (b) two-level four-leg converter.

- A four-leg converter uses full dc-link voltage ($2V_{dc}$) for modulating each half cycle of the output phase-voltages v_{if}, for $i \in \{a, b, c\}$. In contrast, a three-leg four-wire converter uses only the half of it. This increases the maximum achievable output phase-voltage for a four-leg converter in 15%, compared to a three-leg four-wire converter [35] (see Subsection 3.1.1).

- The incorporation of the fourth leg in a four-leg converter provides three different voltage levels in the phase-voltages v_{if}, for $i\{a, b, c\}$, namely $2V_{dc}$, 0 and $-2V_{dc}$. In contrast, for a three-leg four-wire converter only two levels are available, namely $V_{dc}/2$ and $-V_{dc}/2$. Therefore, a four-leg converter is able to modulate waveforms with improved harmonic spectrum.

- A four-leg converter handle the current through the neutral wire, i_f, with the additional fourth leg, while a three-leg four-wire converter need to split the dc-link capacitor. This introduces an extra complexity, as the capacitors must be balanced and an additional algorithm for achieving that balancing must be implemented. Furthermore, it worsens the harmonic distortion of the modulated waveform, as a trade-off between the optimal switching sequence arrangement and the balance of the voltage in the dc-link capacitors must be met. Additionally, the capacitors must be usually very large in order to provide the neutral current i_f without producing an unacceptable neutral-point voltage ripple [72].

Due to the advantages mentioned above, two-level four-leg converters have arisen as the preferred topology in the last decade and have been used several applications, such as: power quality enhancer [73–79] grid connected and island mode converters for DG [80–84], failure-tolerant converters [85,86], Uninterruptible Power Supply (UPS) [16,87], common-mode active filters [25, 88] and minimization of the common-mode leakage current in MV drives [89]. Besides the two-level three- and four-leg converters, additional topologies have been proposed as solutions for four-wire applications, such as: four-leg matrix converters for aerospace applications [21, 90, 91] and multilevel topologies, proposed as solution for medium voltage range applications, such as: three-level four-leg flying capacitor converter [92, 93] and four-leg NPC converter [28, 30, 85, 94]. The latter topology is extensively discussed in Chapter 5 and represents the focus of this thesis.

The modulation of the output voltages in four-wire converters become a more complex task compared with a three-phase VSI, as it requires control over the zero-sequence generated by the VSI. Several approaches for achieving modulation in four-wire converters have been proposed in the literature, the most relevant methods can be summarized as: closed-loop hysteresis current controllers in *abc* and $\alpha\beta\gamma$ coordinates [13,95–97], Carrier-Based PWM strategies for four-wire converters [15, 26–28], finite set model predictive control [19, 29, 30] and Three-Dimensional Space Vector Modulation in *abc* [18, 31] and $\alpha\beta\gamma$ coordinates frame [17, 32–37].

This chapter presents a review of the mentioned control strategies for four-wire converters. The chapter focuses in the Three-Dimensional Space Vector Modulation, as, to the opinion of the author and as it is discussed in this chapter, it arises as the most promising strategy for controlling converters for four-wire applications.

3.1 Three-Dimensional SVM for four-wire VSI

When the zero-sequence of a converter has to be controlled, the $\alpha\beta$ representation presented in Chapter 2 does not provide enough information for accomplishing the modulation. Therefore, a third coordinate, namely the zero-sequence component, has to be considered, resulting in a three-dimensional SVM. The three-dimensional SVM methods can be summarized in two groups: The Three-dimensional SVM in $\alpha\beta\gamma$ coordinates frame, introduce by Zhang et. al in 1997 [32, 34, 98] and its equivalent modulation in *abc* coordinates frame, introduced by Perales et. al in 2003 [18] and extended for multilevel converters in [31]. This section presents both methods and discuss its features.

3.1.1 Three-Dimensional SVM in $\alpha\beta\gamma$ reference frame

Three-dimensional SVM in $\alpha\beta\gamma$ coordinate frame is the natural extension of the two-dimensional SVM method discussed in Chapter 2. Using a third coordinate for representing the zero-sequence of the converter, a three dimensional space is generated. Thereby, and unlike the two-dimensional SVM method, the smallest region that contain a reference vector in the space is not a triangle, but a tetrahedron composed by four vectors. This section explains the procedure for obtaining these four vectors and how to calculate their corresponding *dwell times*. Additionally, the sequence arrangement and three-dimensional overmodulation method are also discussed.

3.1.1.1 Space of Vectors and Tetrahedron Identification

The four-leg converter of Fig. 3.1b possesses 16 different switching combination. These combinations are summarized in the first and second column of Table B.1 from Appendix B. From this table, $\boldsymbol{v}_{abcf}$ represents the phase-voltages of each leg respect to the reference point z and $\boldsymbol{v}_{abc_f}$ represents the *abc* voltages respect to the fourth leg f. Applying the Clarke transformation, presented in (2.14), to the 16 $\boldsymbol{v}_{abc_f}$ vectors of table Table B.1, the *stationary vectors* in $\alpha\beta\gamma$ coordinates are obtained. Each of these 16 vectors are denoted as $\boldsymbol{v}^{i}_{\alpha\beta\gamma}$ and presented in the third column of Table B.1.

Fig. 3.2a shows the space of vectors formed by the 16 different vectors of a two-level four-leg VSI in the $\alpha\beta\gamma$ space. This space represents the allowable volume where a reference vector can be placed and linearly modulated. Additionally, Fig. 3.2b shows the intersection between the region of Fig. 3.2a and the $\alpha\beta$ plane. This hexagon has been subdivided into six *sectors*, where each *sector* can be extended in the γ axis forming a pentahedron. The pentahedrons corresponding to each *sector* are shown in Fig. 3.3. Each of these pentahedrons are composed by seven vectors, where the vectors $\boldsymbol{v}^{0_p,0_n}_{\alpha\beta\gamma}$,$\boldsymbol{v}^{1}_{\alpha\beta\gamma}$ and $\boldsymbol{v}^{2}_{\alpha\beta\gamma}$ are common for every pentahedron. The seven vectors of each pentahedron generate four tetrahedrons, indicated with different colors in Fig. 3.3, which represents the smallest region that can contain a reference sampled value. Thereby, the first goal of the three-dimensional SVM is to generate an algorithm to find these four vectors at every sampling time.

Let us define a reference vector placed inside the region presented in Fig. 3.2a in a general form as:

$$\boldsymbol{v}^{*}_{\alpha\beta\gamma}= \left[v^{*}_{\alpha}, v^{*}_{\beta}, v^{*}_{\gamma}\right] \tag{3.1}$$

This vector is usually formed by unbalanced and non-sinusoidal components, describing any trajectory in the $\alpha\beta\gamma$ plane. Thereby, in order to identify the tetrahedron that enclose this vector at every sampling time, the following two steps are required:

- Similarly to Subsection 2.1.2, the *sector* of the reference vector $\boldsymbol{v}^{*}_{\alpha\beta\gamma}$ in the $\alpha\beta$ plane is identified. This is obtained based on the angle of the reference vector in the $\alpha\beta$ plane, calculated as:
$$\theta = atan\left(v^{*}_{\beta}/v^{*}_{\alpha}\right) \tag{3.2}$$
- Thereafter, the seven vectors that compose the pentahdron corresponding to the selected *sector* are loaded from a look-up table. In order to obtain the tetrahedron that contains the reference vector avoiding complex three-dimensional search, a simple comparison using the polarity of the reference vector in *abc* coordinates can be used. For instance, let us consider a reference vector placed in *sector III*, which polarities in *abc* are: $\boldsymbol{v}^{*}_{abc_f}= [-,+,-]$. From Fig. 3.3c, the only tetrahedron able to provide the suitable voltages for each phase of the converter is formed by the vectors $\boldsymbol{v}^{11}_{\alpha\beta\gamma}$, $\boldsymbol{v}^{0_p,0_n}_{\alpha\beta\gamma}$, $\boldsymbol{v}^{6}_{\alpha\beta\gamma}$ and $\boldsymbol{v}^{5}_{\alpha\beta\gamma}$. This combination is unique for each pentahedron, enabling simple identification of the tetrahedron.

Fig. 3.4a shows the modulation space formed by the eight switching combinations of the two-level three-leg four-wire VSI presented in Fig. 3.1a (vectors $v^{i}_{\alpha\beta\gamma}$ of this figure are referred

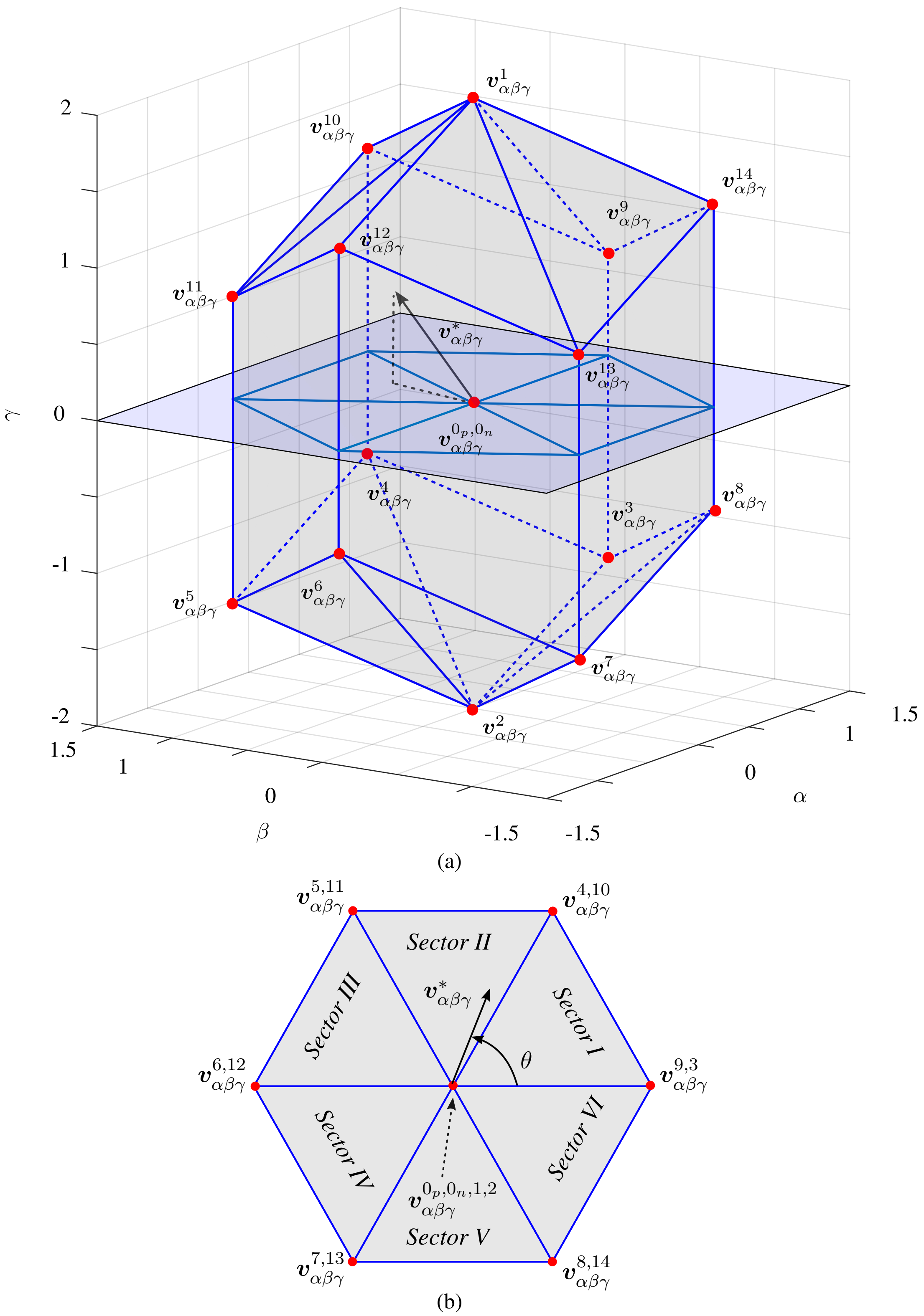

Figure 3.2: (a) Modulation region in the $\alpha\beta\gamma$ space for a two-level four-leg VSI and (b) its intersection with the $\alpha\beta$ plane.

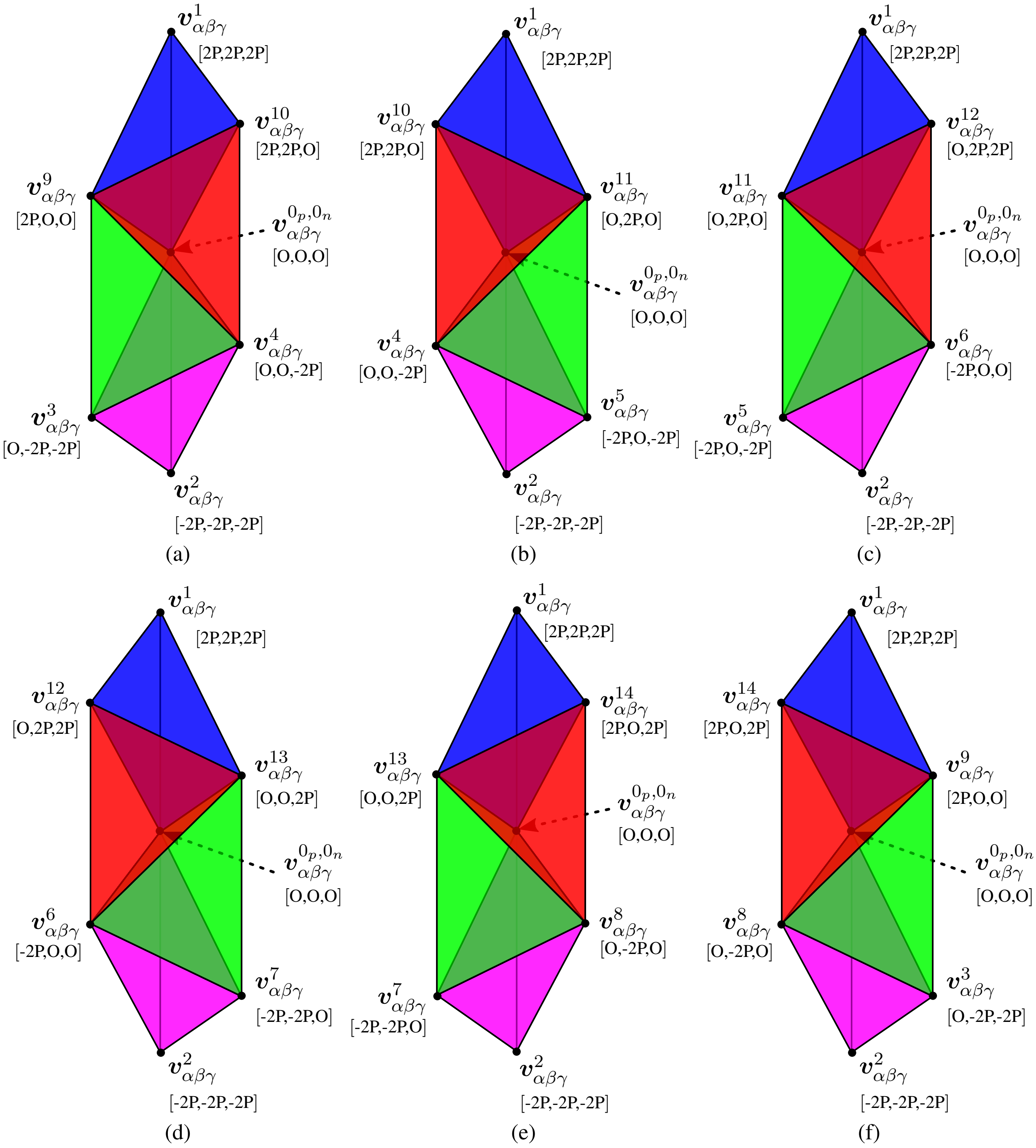

Figure 3.3: Pentahedrons formed by a two-level four-leg VSI. The pentahedrons are divided according to Fig. 3.2, for (a) *sector I*, (b) *sector II*, (c) *sector III*, (d) *sector IV*, (e) *sector V* and (f) *sector VI*.

to Table 2.3). Compared to Fig. 3.2a, this space limits the reference vector to a smaller region, reducing the compensation capability.

From Fig. 3.4a it can be seen that the projection of the *stationary vectors* of a three-leg four-wire converter into the $\alpha\beta$ plane are placed in the same position as for a four-leg converter (see Fig. 3.2b). However, the intersection of this region with the $\alpha\beta$ plane generates an smaller surface compared to Fig. 3.2b. Fig. 3.4b shows, with red dotted line, the intersection between the modulation region of Fig. 3.4a and the $\alpha\beta$ plane. Likewise, the outer hexagon represents the intersection surface obtained in Fig. 3.2b for a four-leg VSI. From this comparison it can be conclude that for a reference vector $\boldsymbol{v}^{*}_{\alpha\beta\gamma}$ which describe a circular trajectory in the $\alpha\beta$ plane, i.e. balanced and symmetric references, the three-leg converter provides a maximum modulation range of $m_a \leq 1$, while it limit is $m_a \leq \frac{2}{\sqrt{3}}$ in a four-leg converter. This results in output phase-voltages with a peak magnitude of V_{dc} for a three-leg four-wire and $\frac{2}{\sqrt{3}}V_{dc}$ for a four-leg converter. Thereby, the fourth leg increases the output phase-voltages in 15%. Although this definition does not compare the complete capability of the converter in the $\alpha\beta\gamma$ space, it is normally used as a comparison parameter. Furthermore, it is important to remark that the outer boundaries of the allowable modulation is independent of the number of levels of the converter. Therefore, this statement is also valid for multilevel converters.

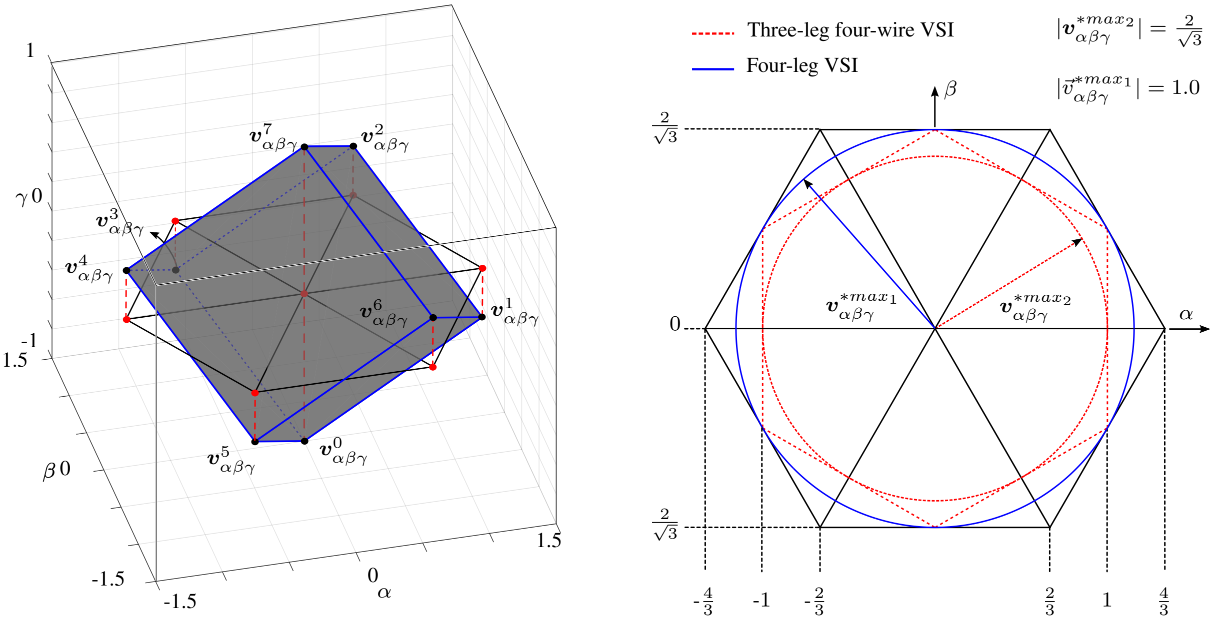

(a) (b)

Figure 3.4: (a) Modulation region in the $\alpha\beta\gamma$ space for a two-level three-leg four-wire VSI and (b) with red dotted line, its intersection with the $\alpha\beta$ plane. $\boldsymbol{v}^{*max_2}_{\alpha\beta\gamma}$ and $\boldsymbol{v}^{*max_1}_{\alpha\beta\gamma}$ denote the maximum amplitude of a reference vector rotating in the $\alpha\beta$ plane for a two-level three-leg four-wire and a four-leg VSI respectively.

3.1.1.2 Dwell-time calculation

Once obtained the four *stationary vectors* that form the tetrahedron that encloses the reference vector, their *dwell times* have to be calculated. Let us define the four selected *stationary vectors* in a general form as: $\boldsymbol{v}^{s_1}_{\alpha\beta\gamma}$, $\boldsymbol{v}^{s_2}_{\alpha\beta\gamma}$, $\boldsymbol{v}^{s_3}_{\alpha\beta\gamma}$ and $\boldsymbol{v}^{0}_{\alpha\beta\gamma}$. As the *zero vector* $\boldsymbol{v}^{0_p,0_n}_{\alpha\beta\gamma}$ is always present in every tetrahedron, it have been directly denoted as $\boldsymbol{v}^{0}_{\alpha\beta\gamma}$. Thereby, the *dwell time* for each of these vectors can be calculated as:

$$\begin{bmatrix} d_1 \\ d_2 \\ d_3 \end{bmatrix} = T_s \begin{bmatrix} v^{s1}_{\alpha} & v^{s2}_{\alpha} & v^{s3}_{\alpha} \\ v^{s1}_{\beta} & v^{s2}_{\beta} & v^{s3}_{\beta} \\ v^{s1}_{\gamma} & v^{s2}_{\gamma} & v^{s3}_{\gamma} \end{bmatrix}^{-1} \begin{bmatrix} v^{*}_{\alpha} \\ v^{*}_{\beta} \\ v^{*}_{\gamma} \end{bmatrix} \tag{3.3}$$

$$d_0 = T_s - d_1 - d_2 - d_3, \tag{3.4}$$

where T_s represents the sampling time and d_0 to d_3 the *dwell time* for the corresponding vectors $\boldsymbol{v}^{0}_{\alpha\beta\gamma}$ to $\boldsymbol{v}^{s3}_{\alpha\beta\gamma}$. The $\alpha\beta\gamma$ components of each of these vectors can be obtained form the third column of Table B.1 in Appendix B. In order to avoid the calculation of the inverse matrix presented in (3.3) at each sampling time, a preset look-up table with the values of the inverse matrix for each tetrahedron is usually employed [99].

3.1.1.3 Switching Sequences and Switching Frequency

In order to define the switching frequency of each device and the harmonic spectrum of the modulated waveforms, an appropriate switching pattern is required, which has to accomplish the *minimum switching transition* principle for minimizing output currents ripple and harmonic distortion. Fig. 3.5 shows the *Single-Redundancy Symmetric n-type* and *p-type* sequences, and the *Non-Redundancy Symmetric n-type* and *p-type* sequences for a two-level four-leg VSI. These sequences are defined based on the definitions presented in Subsection 2.1.2.3. The sequences of Fig. 3.5 are generated with the four *stationary vectors* that enclose the reference vector in a tetrahedron formed by the vectors: $\boldsymbol{v}^{10}_{\alpha\beta\gamma}$, $\boldsymbol{v}^{11}_{\alpha\beta\gamma}$, $\boldsymbol{v}^{0_n,0_p}_{\alpha\beta\gamma}$ and $\boldsymbol{v}^{4}_{\alpha\beta\gamma}$ in *sector II* (see Fig. 3.3b).

Fig. 3.5 presents the *Symmetric* sequences for modulating a reference vector at each sampling time, the equivalent *Asymmetric* sequences can be easily obtained using just half of the pattern during T_s (see Fig. 2.7 and Fig. 2.10). Thereby, similar conclusions to those presented in Subsection 2.1.2.3 can be obtained [20,41,54]:

- *Single-Redundancy Symmetric* sequences presented in Fig. 3.5a and Fig. 3.5b perform the lowest harmonic distortion and the highest switching frequency. Therefore, this pattern is commonly used in applications where a good harmonic distortion is required and the switching losses are not a critical issue.

- *Single-Redundancy Symmetric* and *Single-Redundancy Asymmetric* sequences perform the same switching frequency. However, *Asymmetric* sequences align four switching commutations simultaneously during the transition between two sampling times. This allows to synchronize the switching of the three phases minimizing the switching power losses, commonly used in soft-switching methods [20].

- *Non-Redundancy Symmetric or Asymmetric* sequences, presented in Fig. 3.5c and Fig. 3.5d, maintain one phase of the converter clamped at the same voltage level for each sampling time. As a results, each leg of the converters is at the same state for one third of the period. This reduces considerable the switching losses, but increase the harmonic distortion of the output voltages. Additionally, alternation between *n-type* and *p-type* sequences every

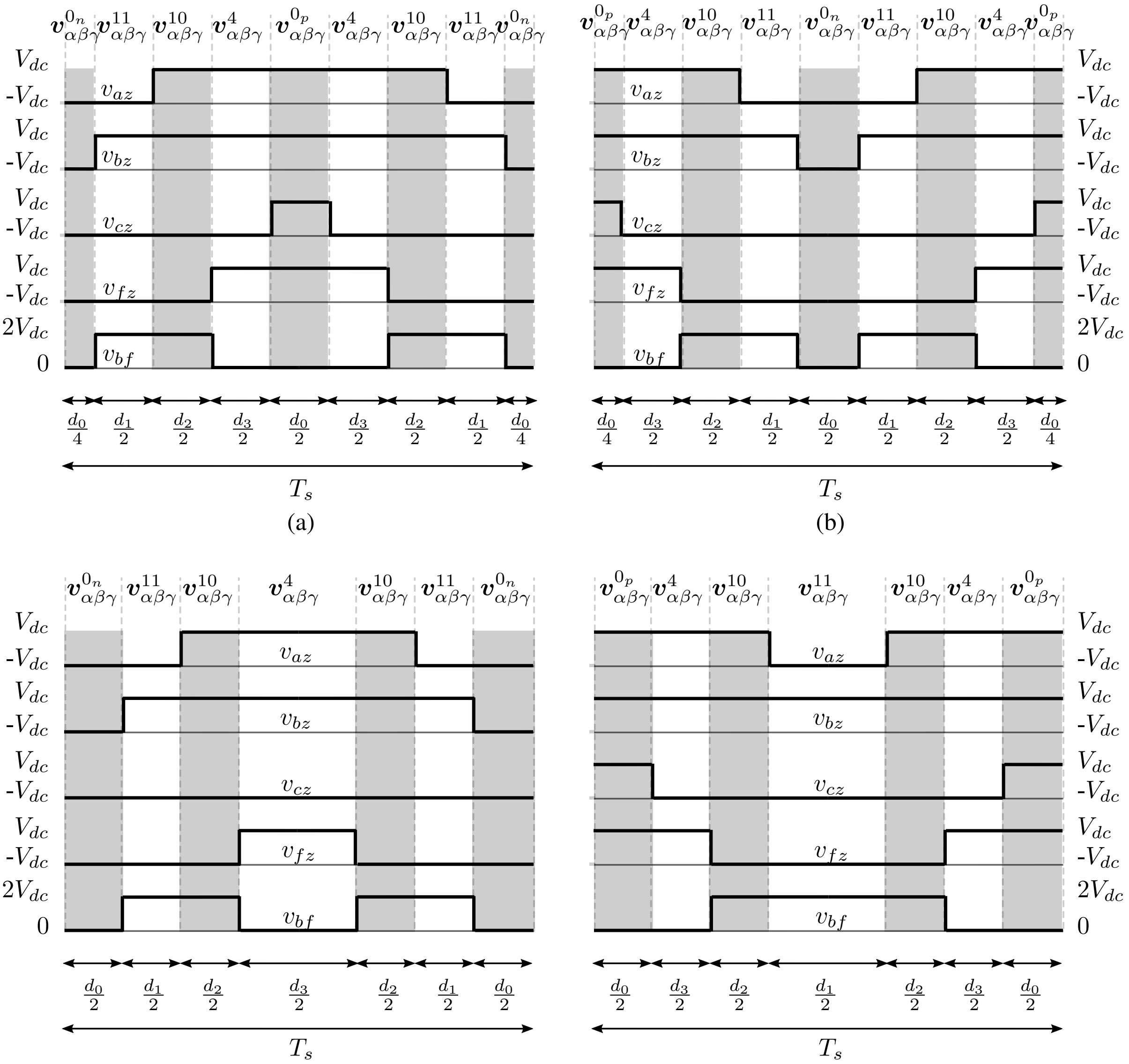

(a) (b) (c) (d)

Figure 3.5: Switching sequences for a two-level four-leg VSI. (a) *Single-Redundant Symmetric n-type* sequence, (b) *Single-Redundant Symmetric p-type* sequence, (c) *Non-Redundant Symmetric n-type* sequence and (d) *Non-Redundant Symmetric p-type* sequence.

60° avoids unequally distribution of the power losses among the semiconductors of the VSI (see Subsection 2.1.2.3).

The Table B.2 from Appendix B shows the *Single-Redundant Symmetric n-type* sequence for each tetrahedron of Fig. 3.3. From this table and considering (2.31) to (2.33), the switching frequency for each device of the four-leg VSI presented in Fig. 3.1b can be calculated as:

$$\bar{f}_{dev_i}^{s} = f_s \tag{3.5}$$
$$f_{dev_i}^{f} = 0 \tag{3.6}$$
$$\bar{f}_{dev_i} = f_s + 0 = f_s \tag{3.7}$$

Thereby, each leg of the converter posses the same switching frequency, this includes the fourth leg.

3.1.1.4 Three-Dimensional Overmodulation Method

An overmodulation method for three-dimensional SVM in $\alpha\beta\gamma$ coordinates was presented in [26,33]. This method instead of compensating the *volt-seconds* of the reference vector over one fundamental cycle, as presented in Subsection 2.1.3, it saturates the reference vector to either the borders the polygon presented in Fig. 3.2 or the borders of a cylinder cover at the top and at the bottom by a semi-sphere and paced inside the polygon of Fig. 3.2. The cylinder represents the extension into the γ axis of the maximum allowable circular path in the $\alpha\beta$ plane presented in Fig. 3.4b. This method can successfully limit the reference vector inside the modulation region. However, the saturation modifies the amplitude and phase shift of the fundamental and harmonics components of the modulated waveforms. This can affect the overall performance of VSI when is used for harmonics compensation. A method for solving this problem is presented in Section 5.6.

3.1.2 Three-Dimensional SVM in *abc* reference frame

Equivalently to the three-dimensional SVM algorithm in $\alpha\beta\gamma$ coordinate frame, an algorithm to modulate a reference vector in the *abc* coordinates frame have been recently presented in the literature [18, 31]. Compared to its analogue in $\alpha\beta\gamma$ coordinates, this method has gained attention mainly because its simplification in the identification of the four *stationary vectors* and in the *dwell time* calculation, avoiding the use of look-up tables.

In order to obtain the modulation region in the *abc* coordinate frame, the 16 switching combinations presented in the second column of Table B.2 have to be used. The modulation region formed by these 16 switching combinations is presented in Fig. 3.6. Note that in this figure the switching combinations of Table B.2 have been normalized in order to obtain points spaced by one integer value, which is required for implementing this algorithm.

Let us assume a reference vector placed inside the modulation region of Fig. 3.6 in *abc* coordinates as:

$$\boldsymbol{v}_{abc_f}^{*} = \left[v_{af}^{*}, v_{bf}^{*}, v_{cf}^{*}\right], \tag{3.8}$$

where the subindices of the voltages are referred to Fig. 3.1b. Calculating the smallest following integer of each coordinate of $\boldsymbol{v}_{abc_f}^{*}$ using the $\boldsymbol{floor}()$ function, a pivot vector can be calculated as:

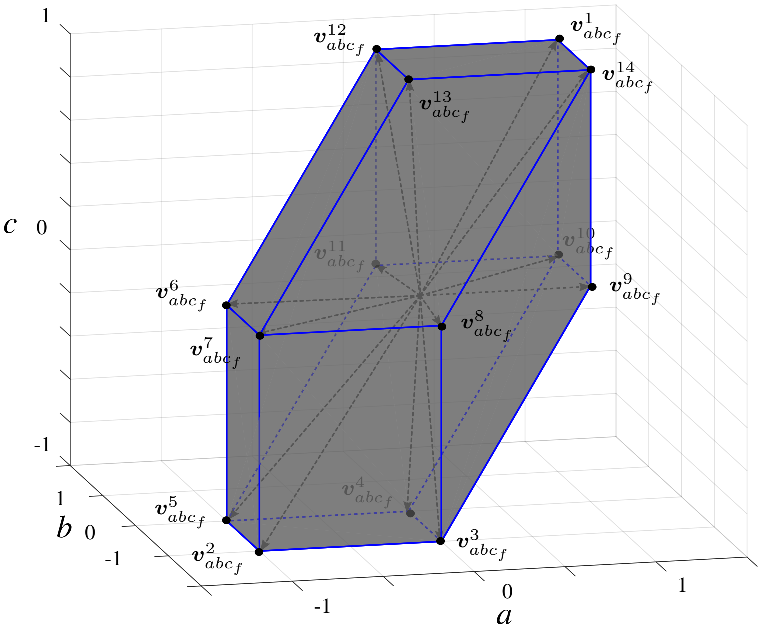

Figure 3.6: Modulation Region for a two-level four-leg converter in *abc* coordinate frame.

$$\hat{\boldsymbol{v}}^{*}_{abc_f} = \left[\hat{v}^{*}_{af}, \hat{v}^{*}_{bf}, \hat{v}^{*}_{cf}\right] \tag{3.9}$$

$$\hat{v}^{*}_{af} = \boldsymbol{floor}\left(v^{*}_{af}\right) \tag{3.10}$$

$$\hat{v}^{*}_{bf} = \boldsymbol{floor}\left(v^{*}_{bf}\right) \tag{3.11}$$

$$\hat{v}^{*}_{cf} = \boldsymbol{floor}\left(v^{*}_{cf}\right) \tag{3.12}$$

Thereby, the pivot vector $\hat{\boldsymbol{v}}^{*}_{abc_f}$ represents one of the 16 switching states of Table B.2. Based on this pivot vector, a cube that contains the reference vector can be generated. In order to obtain each vertex of this cube, the following eight possible switching combinations has to be generated:

- $\hat{\boldsymbol{v}}^{*}_{abc_f} = \left[\hat{v}^{*}_{af}, \hat{v}^{*}_{bf}, \hat{v}^{*}_{cf}\right]$
- $\hat{\boldsymbol{v}}^{*1}_{abc_f} = \left[\hat{v}^{*}_{af}+1, \hat{v}^{*}_{bf}, \hat{v}^{*}_{cf}\right]$
- $\hat{\boldsymbol{v}}^{*2}_{abc_f} = \left[\hat{v}^{*}_{af}+1, \hat{v}^{*}_{bf}+1, \hat{v}^{*}_{cf}\right]$
- $\hat{\boldsymbol{v}}^{*3}_{abc_f} = \left[\hat{v}^{*}_{af}, \hat{v}^{*}_{bf}+1, \hat{v}^{*}_{cf}\right]$
- $\hat{\boldsymbol{v}}^{*4}_{abc_f} = \left[\hat{v}^{*}_{af}, \hat{v}^{*}_{bf}, \hat{v}^{*}_{cf}+1\right]$
- $\hat{\boldsymbol{v}}^{*5}_{abc_f} = \left[\hat{v}^{*}_{af}+1, \hat{v}^{*}_{bf}, \hat{v}^{*}_{cf}+1\right]$
- $\hat{\boldsymbol{v}}^{*6}_{abc_f} = \left[\hat{v}^{*}_{af}+1, \hat{v}^{*}_{bf}+1, \hat{v}^{*}_{cf}+1\right]$
- $\hat{\boldsymbol{v}}^{*7}_{abc_f} = \left[\hat{v}^{*}_{af}, \hat{v}^{*}_{bf}+1, \hat{v}^{*}_{cf}+1\right]$

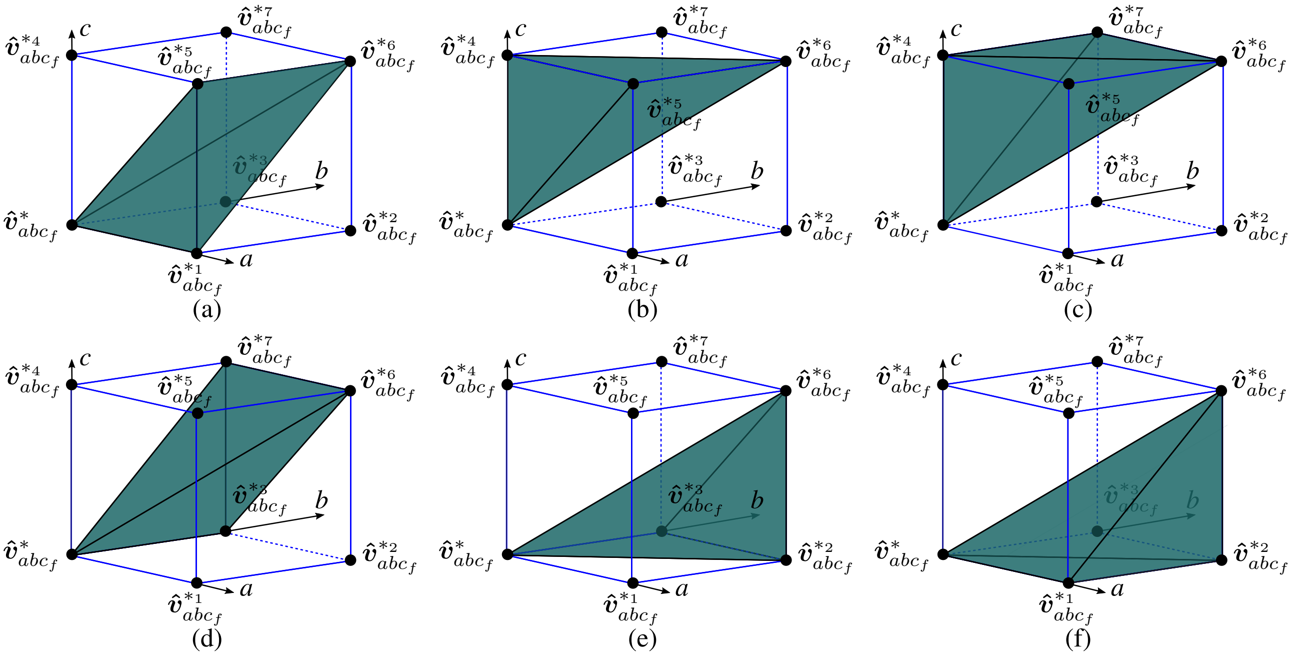

Figure 3.7: Six different tetrahedrons formed inside a predefined cube for identification of the reference vector $\boldsymbol{v}^*_{abc_f}$. Each tetrahedron is identified as (a) T_1, (b) T_2, (c) T_3, (d) T_4, (e) T_5 and (f) T_6.

Fig. 3.7 shows the cube formed by these eight vectors, plotted with a displaced center located at $\hat{\boldsymbol{v}}^*_{abc_f}$. Using the eight vertices of the cube, the six different tetrahedrons of Fig. 3.7 can be formed. Thereby, in order to identify the tetrahedron that contains the reference vector, a three dimensional search must be accomplished. This search compares the relative position of the reference vector respect of a minimum of three different $45°$ planes that cut the cube. This comparison is summarized in the diagram of Fig. 3.8.

After performing the algorithm presented in the diagram of Fig. 3.8, one of the six tetrahedrons of Fig. 3.7 is obtained, identifying the set of four *stationary vectors* that enclose the reference vector. Similarly to the three-dimensional SVM in $\alpha\beta\gamma$ coordinate frame, after obtaining the *stationary vectors*, the calculation of its *dwell-times* is required. This calculation is summarized in Table 3.1 for each tetrahedron of Fig. 3.7. As the pivot vector $\hat{\boldsymbol{v}}^*_{abc_f}$ changes accordingly with the reference vector $\boldsymbol{v}^*_{abc_f}$, this table provides the *stationary vectors* and *dwell-times* for the complete modulation region of Fig. 3.6.

The algorithm presented in the diagram of Fig. 3.8 achieves simple identification of the *stationary vectors* and calculation of their *dwell times* for modulating a reference vector in the *abc* reference frame. However, as it is a generic algorithm, it does not recognize whether the reference vector remains inside the region presented in Fig. 3.6 or not. This could results in selecting a set of *stationary vectors*, which do not belong to the allowable modulation space. In other words, these switching combinations could not be physically feasible by the converter. To assure proper operation of the converter under all conditions, avoiding erroneous selection of *stationary vectors* or *dwell times* calculation, identification of these non-feasible switching combinations is required, which would increase the computational burden. For the best knowledge of the author, a solution for this issue or an overmodulation method for limiting the reference

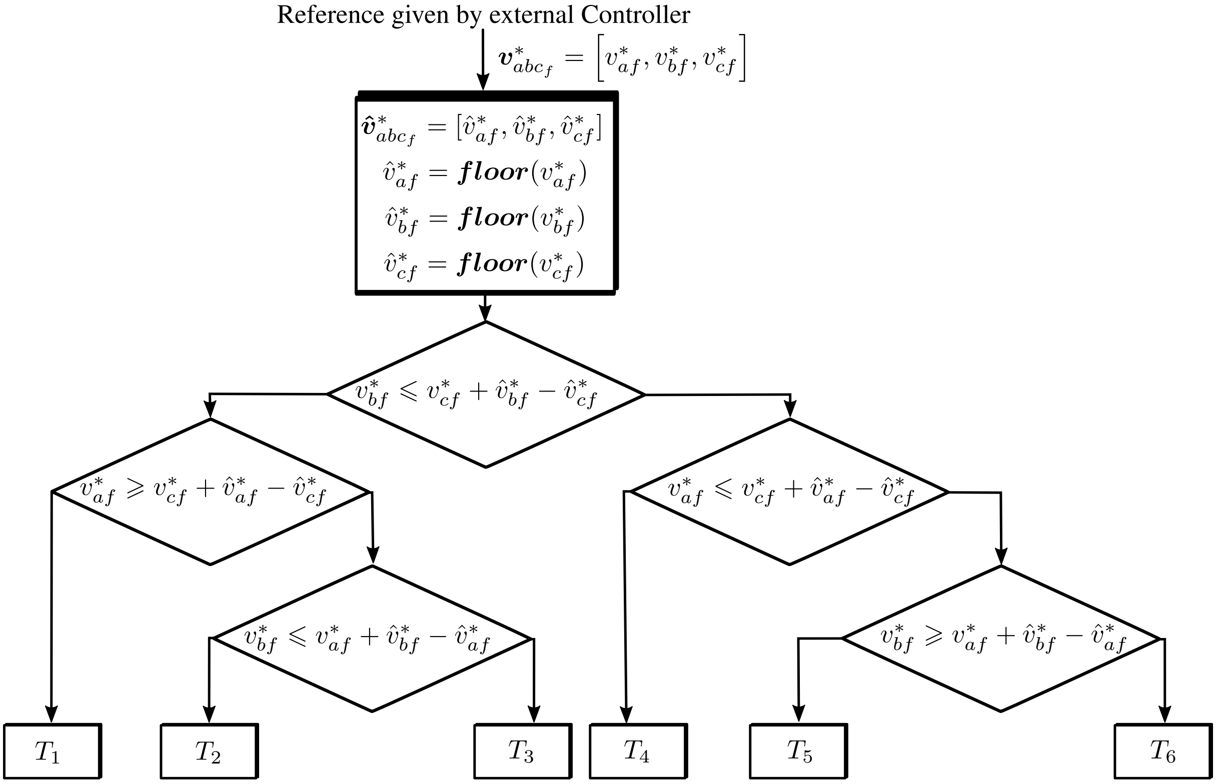

Figure 3.8: Diagram for tetrahedron identification. The selected tetrahedron definition, T_1 to T_6 are based on Fig. 3.7.

vector to the interior of the polygon presented in Fig. 3.2 have not been reported yet.

Table 3.1: *Dwell time* calculation and *Stationary vectors* in *abc* coordinates.

Tetrahedron	*Stationary vectors*	*Dwell time* calculation
T_1	$\hat{\boldsymbol{v}}^{*}_{abc_f}$ $\hat{\boldsymbol{v}}^{*1}_{abc_f}$ $\hat{\boldsymbol{v}}^{*5}_{abc_f}$ $\hat{\boldsymbol{v}}^{*6}_{abc_f}$	$d_1 = 1 + \hat{v}^*_{af} - v^*_{af}$ $d_2 = -\hat{v}^*_{af} + \hat{v}^*_{cf} + v^*_{af} - v^*_{cf}$ $d_3 = \hat{v}^*_{bf} - \hat{v}^*_{cf} - v^*_{bf} + v^*_{cf}$ $d_4 = -\hat{v}^*_{bf} + v^*_{bf}$
T_2	$\hat{\boldsymbol{v}}^{*}_{abc_f}$ $\hat{\boldsymbol{v}}^{*4}_{abc_f}$ $\hat{\boldsymbol{v}}^{*5}_{abc_f}$ $\hat{\boldsymbol{v}}^{*6}_{abc_f}$	$d_1 = 1 + \hat{v}^*_{cf} - v^*_{cf}$ $d_2 = \hat{v}^*_{af} - \hat{v}^*_{cf} - v^*_{af} + v^*_{cf}$ $d_3 = -\hat{v}^*_{af} + \hat{v}^*_{bf} + v^*_{af} - v^*_{bf}$ $d_4 = -\hat{v}^*_{bf} + v^*_{bf}$
T_3	$\hat{\boldsymbol{v}}^{*}_{abc_f}$ $\hat{\boldsymbol{v}}^{*4}_{abc_f}$ $\hat{\boldsymbol{v}}^{*6}_{abc_f}$ $\hat{\boldsymbol{v}}^{*7}_{abc_f}$	$d_1 = 1 + \hat{v}^*_{cf} - v^*_{cf}$ $d_2 = \hat{v}^*_{bf} - \hat{v}^*_{cf} - v^*_{bf} + v^*_{cf}$ $d_3 = \hat{v}^*_{af} - \hat{v}^*_{bf} - v^*_{af} + v^*_{bf}$ $d_4 = -\hat{v}^*_{af} + v^*_{af}$
T_4	$\hat{\boldsymbol{v}}^{*}_{abc_f}$ $\hat{\boldsymbol{v}}^{*3}_{abc_f}$ $\hat{\boldsymbol{v}}^{*6}_{abc_f}$ $\hat{\boldsymbol{v}}^{*7}_{abc_f}$	$d_1 = 1 + \hat{v}^*_{bf} - v^*_{bf}$ $d_2 = -\hat{v}^*_{bf} + \hat{v}^*_{cf} + v^*_{bf} - v^*_{cf}$ $d_3 = \hat{v}^*_{af} - \hat{v}^*_{cf} - v^*_{af} + v^*_{cf}$ $d_4 = -\hat{v}^*_{af} + v^*_{af}$
T_5	$\hat{\boldsymbol{v}}^{*}_{abc_f}$ $\hat{\boldsymbol{v}}^{*2}_{abc_f}$ $\hat{\boldsymbol{v}}^{*3}_{abc_f}$ $\hat{\boldsymbol{v}}^{*6}_{abc_f}$	$d_1 = 1 + \hat{v}^*_{bf} - v^*_{bf}$ $d_2 = \hat{v}^*_{af} - \hat{v}^*_{bf} - v^*_{af} + v^*_{bf}$ $d_3 = -\hat{v}^*_{af} + \hat{v}^*_{cf} + v^*_{af} - v^*_{cf}$ $d_4 = -\hat{v}^*_{cf} + v^*_{cf}$
T_6	$\hat{\boldsymbol{v}}^{*}_{abc_f}$ $\hat{\boldsymbol{v}}^{*1}_{abc_f}$ $\hat{\boldsymbol{v}}^{*2}_{abc_f}$ $\hat{\boldsymbol{v}}^{*6}_{abc_f}$	$d_1 = 1 + \hat{v}^*_{af} - v^*_{af}$ $d_2 = -\hat{v}^*_{af} + \hat{v}^*_{bf} + v^*_{af} - v^*_{bf}$ $d_3 = -\hat{v}^*_{bf} + \hat{v}^*_{cf} + v^*_{bf} - v^*_{cf}$ $d_4 = -\hat{v}^*_{cf} + v^*_{cf}$

3.1.3 Discussion on Three-Dimensional SVM Algorithms for four-wire Applications

This section has presented a review of the current state of the art for three-dimensional SVM algorithms proposed for controlling four-leg VSIs. Although SVM in $\alpha\beta\gamma$ or *abc* coordinates are equivalent from a mathematical point of view, there are important issues that has to be considered. The following points summarized the advantages offered by each method.

Advantages of three dimensional SVM in $\alpha\beta\gamma$ frame compared to its analogue in *abc* coordinates:

- The $\alpha\beta\gamma$ orthogonal frame provides the zero-sequence component of a system as an independent variable. This allows direct control and visualization of the zero-sequence component, which is the central feature of four-wire systems [95].
- The instantaneous power theory (*pq* theory) has been developed for compensating sys-

tems in presence of unbalances and harmonic distortion [100–102]. This theory has been developed in $\alpha\beta\gamma$ coordinate, not only because it allows identification of the zero-sequence, but also because it enables the separation of positive and negative sequences from the $\alpha\beta$ components, which is important for the realization of controllers in *dq* coordinate frame [6]. Thereby, close-loop controllers implemented in four-wire applications are usually design in the $\alpha\beta\gamma$ coordinates frame. The implementation of SVM in the $\alpha\beta\gamma$ space avoids extra transformation from $\alpha\beta\gamma$ to *abc* coordinate system, allowing simpler and unified implementation of the overall control scheme.

- As presented in Fig. 3.2, the modulation region of a four-leg converter in the $\alpha\beta\gamma$ space is basically an extension over the γ axis of the standard two-dimensional hexagon presented in Subsection 2.1.3. This enables simpler extension of the strategies used for generating switching sequences and selective harmonic elimination presented in Chapter 2, Subsection 2.1.3.
- The $\alpha\beta\gamma$ modulation region presented in Fig. 3.2 provides a geometry which enables an easy identification of a reference vector placed out of this space. This facilitates the implementation of overmodulation methods in a three dimensional space, as presented in [26, 33].

Advantages of three dimensional SVM in *abc* coordinate frame compared to its analogue in $\alpha\beta\gamma$ coordinate frame:

- The three-dimensional SVM in *abc* provides simpler identification of the set of *stationary vectors* that enclose a reference vector and simpler calculation of its *dwell-times* compared to its analogue in $\alpha\beta\gamma$ frame. This becomes an important issue for converters with several switching combinations, such as Multilevel converters.
- Due to generic structure of the three-dimensional SVM method in *abc* coordinates, it can be easily extended to Multilevel converters. Its implementation in a three-level four-leg NPC VSI was presented in [31]. Contrary, the huge number of tables required for implementing a three-dimensional SVM in $\alpha\beta\gamma$ frame makes this method impracticable for converters with high number of levels, at least in its current state.

The choice between these two methods is still not a resolved issue in the literature [103]. However, it can be said that for two-level VSIs the algorithm in $\alpha\beta\gamma$ has gained major attraction, while for multilevel converters the use of *abc* coordinates arises as a better alternative. Consequently, the aim of this thesis is to develop an algorithm that integrates the advantages of both methods, i.e. a method in $\alpha\beta\gamma$ coordinates frame, which perform fast identification of the *stationary vectors*, simple calculation of the *dwell times* and that can be easily extended to multilevel converters. This algorithm is presented in Chapter 5.

3.2 Other control Schemes for four-wire Applications

Besides the three-dimensional SVM algorithms presented in the previous sections, additional methods for accomplishing control of four-wire VSIs have been reported during the last two decades. This section briefly introduces the most relevant methods, which have gained interest in the research community.

3.2.1 Hysteresis PWM Current control

As a natural extension of the current controllers for the three-phase VSIs [46], the closed-loop Hysteresis PWM Current controllers were the first strategy used for accomplishing control of the output voltages in converters for four-wire applications, mainly three-leg four-wire VSIs.

The diagram of Fig. 3.9a shows the control scheme of the Hysteresis PWM Current control for the three-leg four-wire VSI presented in Fig. 3.1a. This scheme accomplishes the control of the output currents i_a, i_b and i_c by directly comparing the measured line currents with its arbitrary references, i_a^*, i_b^* and i_c^*, provided by an external controller. Note that these references can be non-sinusoidal as in a active filter (see Fig. 4.1). Thereby, the output of each hysteresis controller directly trigger the devices of each leg of the converter through the signals $g_{a,\bar{a}}$, $g_{b,\bar{b}}$ and $g_{c,\bar{c}}$. The width of the hysteresis band is denoted as ϵ and it is dynamically regulated by an additional controller, called *Voltage Balancing*. This controller regulates the width of the hyteresis band (ϵ) for actively balance the voltages v_{C_1} and v_{C_2} [11,13]. This controller performs the same features reported for three-phase converters, namely: high transient response, high frequency ripple in the controlled currents and a non-fixed switching frequency, i.e. spread voltage and current harmonic spectrum. A method that uses four hysteresis comparators applied to four-leg VSI is presented in [104].

Although this method affords good control of the line currents, the current through the neutral wire is not being directly controlled. This results in a neutral current i_z with a ripple up to three times higher compared to the line currents [95]. To solve this problem, Verdelho et. al. [14, 95, 105], proposed the hysteresis PWM current controller in $\alpha\beta\gamma$ coordinates presented in Fig. 3.9b. This controller uses the Clarke transformation presented in (2.14), to separates the zero-sequence of the reference currents from its $\alpha\beta$ active components. Thus, a direct control over the *abc* currents, represented by i_α and i_β, and over the current through the neutral wire i_z, represented by i_γ, is achieved. This results in four currents, namely i_a, i_b, i_c and i_f, that perform the same ripple.

From Fig. 3.9b, the outputs of the hysteresis controllers are denoted as d_α, d_β and d_γ and represents the entry of a preset look-up table to obtain a suitable switching combination of the converter. Thereby, the selected switching combination should generates a set of three voltages in the $\alpha\beta\gamma$ coordinates which compensates the direction (or sign) of d_α, d_β and d_γ. However, a two-level three-leg four-wire VSI posses only eight switching combinations, leaving entries of d_α, d_β and d_γ which can not be completely compensated. For solving this problem, a vector which partially accomplishes the requirements of d_α, d_β and d_γ is selected. The solution for selecting this vector is not unique and several option can be chosen. In [95] two different solutions are proposed. This problem can be overcome using a four-leg converter, which possesses a higher number of switching combinations. It is important to notice that in Fig. 3.9b, the balance of the voltages in the capacitors C_1 and C_2 is incorporated in the reference currents, which have been modified by an external controller. Thereby, when the reference currents i_α^*, i_β^* and i_γ^* are properly tracked, it will automatically balance the voltages on the dc-link capacitors [14].

A three-dimensional Hysteresis PWM Current controller was also introduced in [96,97,106]. This generates a cubical hysteresis region implemented directly in $\alpha\beta\gamma$ space. This method was implemented in cylindrical coordinate frames to facilitates the three-dimensional comparisons, required to identify when the reference vector is out of the hysteresis cube. As result, the method behaves similar to the already presented method that uses independent hysteresis controllers in

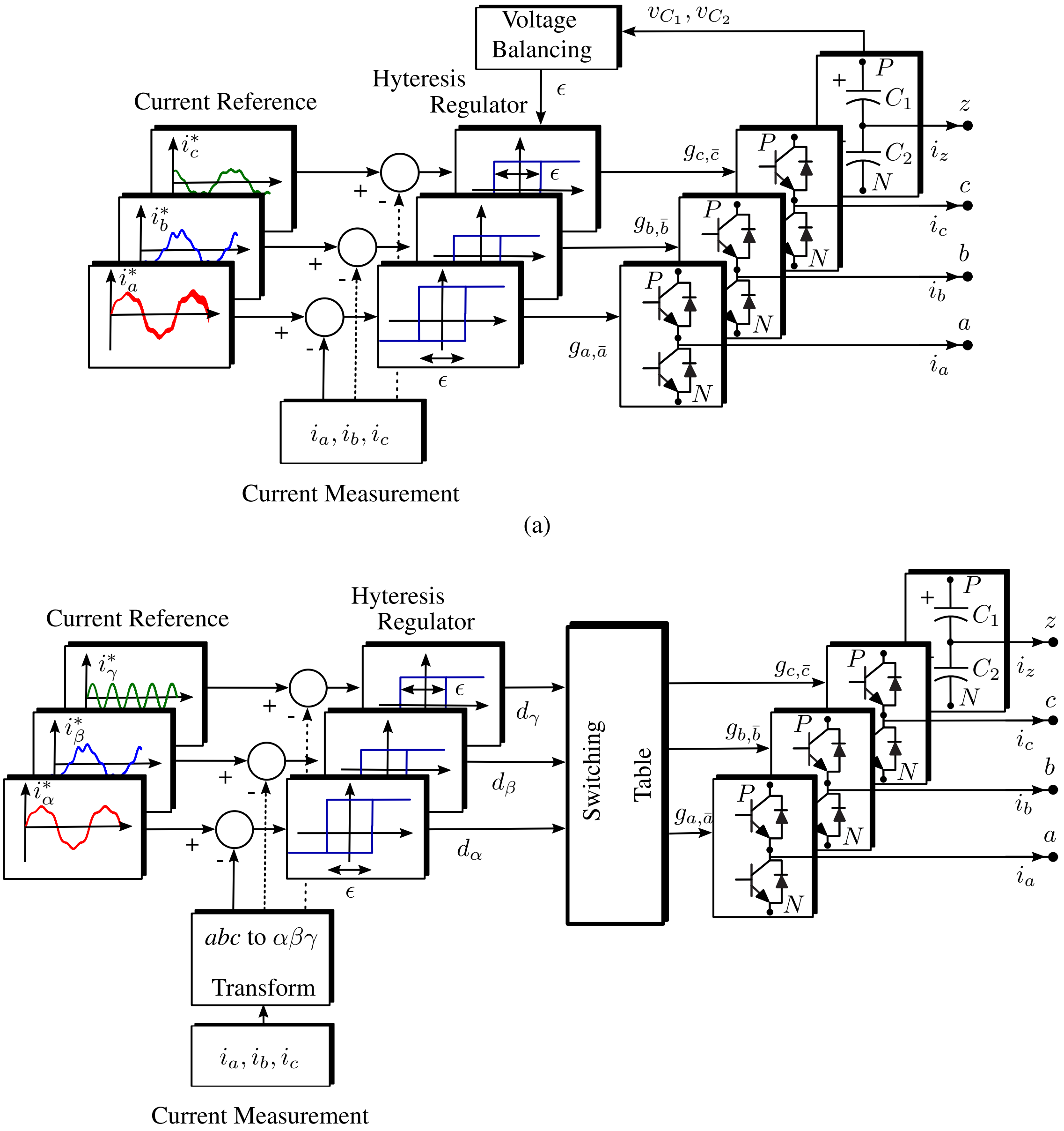

(a)

(b)

Figure 3.9: Closed-loop Hysteresis current PWM control scheme including balancing of the dc-link voltages for a three-leg four-wire VSIs in (a) and *abc* and (b) $\alpha\beta\gamma$ coordinates.

$\alpha\beta\gamma$ coordinates. Additionally it gives more flexibility for implementing switching sequences. The method successfully implemented in a two-level converter and also in a three-level three-leg four-wire NPC converter.

3.2.2 Carrier-Based PWM

This method has been already presented in Chapter 2 for standard three-leg VSIs. It uses the comparison of a triangular carrier with a modulating waveform to directly control the devices that modulate the output phase-voltages in a VSI. Accordingly, the SPWM method was introduced as the simplest method to achieve modulation of a three-leg VSI. This method only achieve a maximum linear modulation index of $m_a \leq 1$, but it maintains the phase-voltages v_{az}, v_{bz} and v_{cz} as sinusoidal waveforms, without incorporation of zero-sequence component. Considering that the voltages v_{az}, v_{bz} and v_{cz} are the phase-voltages to be modulated in a three-leg four-wire converter (see Fig. 3.1a), the SPWM method can be directly applied in this topology, performing similar characteristic as mentioned in Section 2.1.1 [107].

Unlike the three-leg four-wire converter, when a four-leg converter is implemented (see Fig. 3.1b), the voltages to be modulated are not longer referenced to the middle point of the dc-link, but to the fourth leg of the converter. Thereby, the output phase-voltages in a four-leg VSI are represented as:

$$v_{af} = v_{az} - v_{fz} \tag{3.13}$$

$$v_{bf} = v_{bz} - v_{fz} \tag{3.14}$$

$$v_{cf} = v_{cz} - v_{fz}, \tag{3.15}$$

where each voltage is limited by the dc-link magnitude as:

$$-v_{dc} \leq v_{az}, v_{bz}, v_{cz} \leq v_{dc} \tag{3.16}$$

$$-2v_{dc} \leq v_{af}, v_{bf}, v_{cf} \leq 2v_{dc}, \tag{3.17}$$

from these equations, four voltages respect to the middle point of the converter are obtained, namely v_{az}, v_{bz}, v_{cz} and v_{fz}. Therefore, if both components of any of the pairs $(v_{az}$, $v_{fz})$, $(v_{bz}$, $v_{fz})$ and $(v_{cz}$, $v_{fz})$ change in the same magnitude, it would not be noticed in the output voltages v_{af}, v_{bf} or v_{cf}, but it allows to modulate output phase-voltages with a higher fundamental component. This is the same principle used in the *zero-sequence injection* method presented in Section 2.1.1.

Let us consider a set of reference phase-voltages v^*_{af}, v^*_{bf} and v^*_{cf}, given by an external controller. In order to be able to implement a carrier based PWM algorithm, a suitable set of reference voltages v^*_{az}, v^*_{bz}, v^*_{cz} and v^*_{fz} have to be obtained to latter be compared with a triangular carrier waveform. This comparison should modulates the reference phase-voltages and maximize the utilization of the dc-link voltage. Hence, using (3.13) to (3.15), the reference values can be written as:

$$v^*_{az} = v^*_{fz} + v^*_{af} \tag{3.18}$$

$$v^*_{bz} = v^*_{fz} + v^*_{bf} \tag{3.19}$$

$$v^*_{cz} = v^*_{fz} + v^*_{cf} \tag{3.20}$$

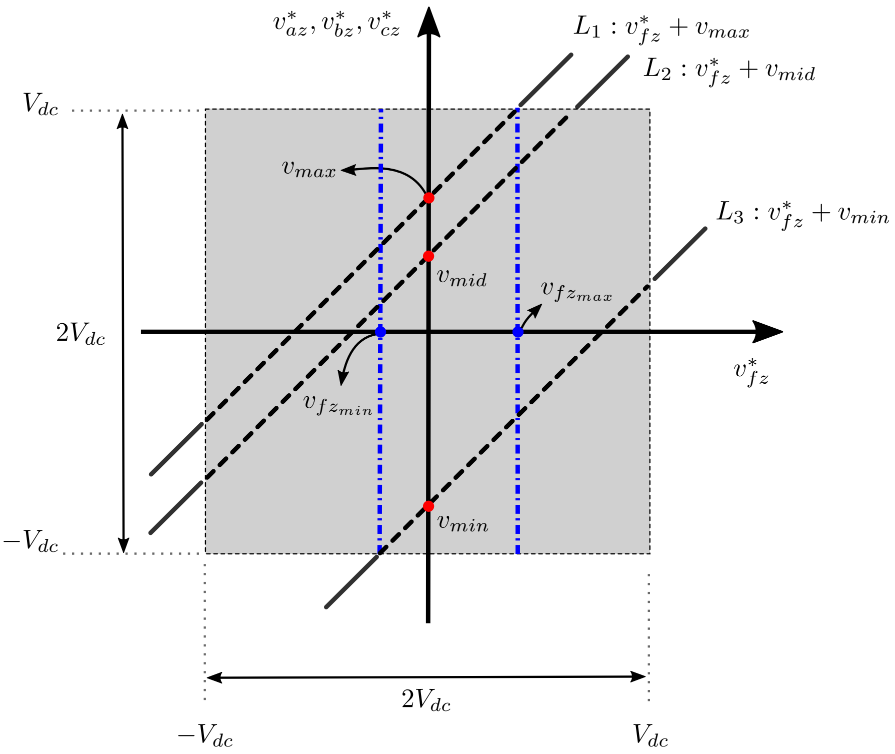

Figure 3.10: Limitation region for identification of the references voltages v_{az}^*, v_{bz}^*, v_{cz}^* and v_{fz}^*. $v_{max}{=}max\{v_{af}^*, v_{bf}^*, v_{cf}^*\}$, $v_{mid}{=}middle\{v_{af}^*, v_{bf}^*, v_{cf}^*\}$, $v_{min}{=}min\{v_{af}^*, v_{bf}^*, v_{cf}^*\}$.

Considering that v_{af}^*, v_{bf}^* and v_{cf}^* remain constant for a small sampling time and using v_{fz}^* as the abscissa and v_{az}^*, v_{bz}^*, v_{cz}^* as the ordinate of a Cartesian plane, each equation of (3.18) to (3.20) can be represented as a line with unitary slope over the planes: (v_{az}^*, v_{fz}^*), (v_{bz}^*, v_{fz}^*) and (v_{cz}^*, v_{fz}^*). This is shown in Fig. 3.10, where the three lines are represented as L_1, L_2 and L_3 in the terms of v_{min}, v_{mid} and v_{max}, which represent the maximum, middle and minimum value of the reference phase-voltages v_{af}^*, v_{bf}^* and v_{cf}^*. From this figure, it can be seen that the black dotted line represent the pairs (v_{az}^*, v_{fz}^*), (v_{bz}^*, v_{fz}^*) and (v_{cz}^*, v_{fz}^*) that generate constant phase-voltages v_{af}^*, v_{bf}^* and v_{cf}^* inside a feasible modulation region. Thereby, as v_{fz}^* is the common coordinate for the three coordinate pairs (v_{az}^*, v_{fz}^*), (v_{bz}^*, v_{fz}^*) and (v_{cz}^*, v_{fz}^*), the intersection of a vertical line with L_1, L_2 and L_3 gives a possible solution for modulating v_{af}^*, v_{bf}^* and v_{cf}^*. Fig. 3.10 shows, marked as three red points, this intersection for $v_{fz}^*{=}0$. This intersection points are obviously equal to the reference phase-voltages v_{af}^*, v_{bf}^* and v_{cf}^*, denoted as v_{min}, v_{mid} and v_{max} (see (3.18) to (3.20)). As the solution for v_{az}^*, v_{bz}^*, v_{cz}^* and v_{fz}^* must remain inside the feasible modulation region, the sector for placing this vertical line, i.e. the reference value of v_{fz}^*, is limited by:

$$v_{fz_{min}}^* \leq v_{fz}^* \leq v_{fz_{max}}^*, \tag{3.21}$$

denoted with blue dotted lines in Fig. 3.10 and calculated as:

$$v_{fz_{min}} = -V_{dc} - v_{min} \tag{3.22}$$
$$v_{fz_{max}} = V_{dc} - v_{max} \tag{3.23}$$

In order to obtain a switching pattern equivalent to the *Single-Redundancy Symmetric* sequence presented in Section 3.1.1 for a two-level four-leg VSI, the following criteria must be used for selecting v_{fz}^*:

$$\begin{aligned} v_{fz}^* &= -\frac{v_{max}}{2}; && \text{for} \quad v_{min} > 0 \\ v_{fz}^* &= -\frac{v_{min}}{2}; && \text{for} \quad v_{max} < 0 \\ v_{fz}^* &= -\frac{v_{max} + v_{min}}{2}; && \text{Otherwise} \end{aligned} \tag{3.24}$$

Once obtained v_{fz}^*, the references v_{az}^*, v_{bz}^* and v_{cz}^* are obtained from (3.18) to (3.20). Afterwards, this constant values are compared with one period of a triangular carrier during the next sampling time T_s, generating the trigger signals for the eight devices of the two-level four-leg VSI [15, 108]. This process is repeated at each sampling time.

The main advantage of this method rely on the simple calculation of the references leg voltages v_{az}^*, v_{bz}^*, v_{cz}^*, v_{fz}^* and the straight acquisition of the duty cycles of each device, obtained directly by comparison of the calculated references with a triangular carrier at each sampling time T_s. However, the calculation of v_{fz}^* to perform different switching patterns or to successfully accomplish overmodulation methods become complex and, to the best knowledge for the author, it has not been reported. Additionally, the utilization of the redundant switching combinations is very limited, as reported in its extension to multilevel converters [36, 109]. This become important in multilevel converters, where shape of the harmonic spectrum, balance of the voltages on the dc-link capacitors or distribution of the switches power losses are important issues. Thereby, the method can be a good alternative to the three-dimensional SVM methods for two-level four-leg converters, implemented with the *Single-Redundancy Symmetric* sequence. However, it does not provide enough flexibility for multilevel topologies.

3.2.3 Finite Set Model Predictive Control

Finite Set Model Predictive Control (FS-MPC) is a model-based control strategy that has gained attention in the power electronics research community during the last decades [38, 43, 44, 110]. Although predictive control is a very well established control theory implemented in industrial applications already in the 1970's [111, 112], it was not until the develop of very fast microprocessors that it was of interest in the power electronics field, mainly because of the typical fast dynamics of electrical systems.

Based on the model of the controlled system and a set of measured variables, this method calculates, at each sampling time T_s, the future values of the controlled variables for each of the switching combinations of the converter. This predictions are then evaluated into a cost function, which is minimized for obtaining the most suitable switching combination that accomplishes a set of control goals. Afterwards, the selected switching combination is applied at the beginning of the next sampling time. The main advantages, highlighted in the literature, of this controller are [38, 43, 44, 110]:

- Fast transient response compared to conventional linear controllers.
- Easy incorporation of different control goals in a single cost function.

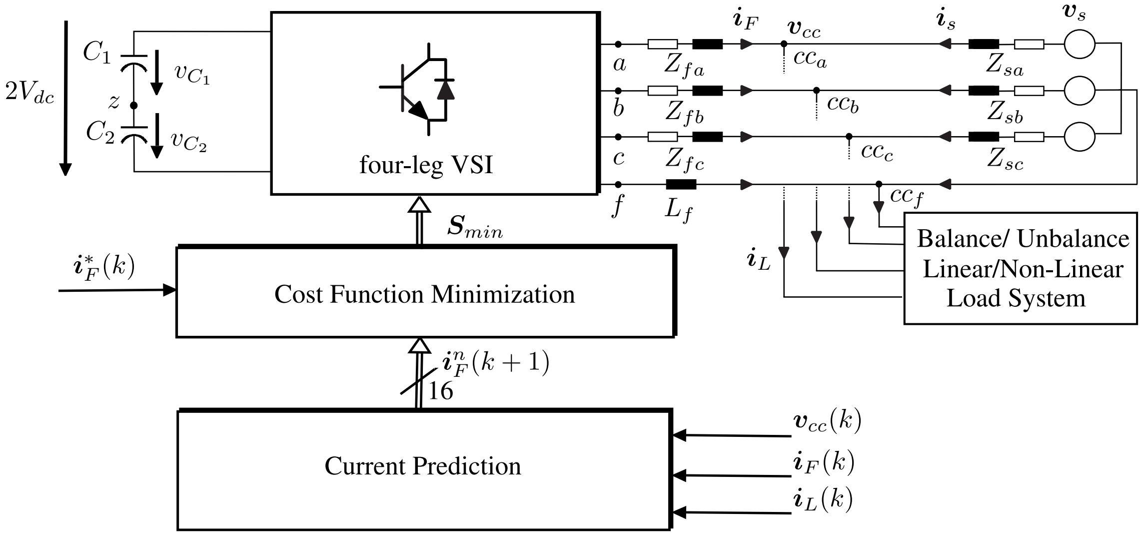

Figure 3.11: FS-MPC control Diagram for a two-level four-leg VSI used as an active filter. $\boldsymbol{i}_F$=$[i_{F_a}, i_{F_b}, i_{F_c}]$, $\boldsymbol{i}_s$=$[i_{s_a}, i_{s_b}, i_{s_c}]$, $\boldsymbol{i}_L$=$[i_{L_a}, i_{L_b}, i_{L_c}]$, $\boldsymbol{v}_{cc}$=$[v_{cc_{af}}, v_{cc_{bf}}, v_{cc_{cf}}]$.

- It exploits the discrete nature of the converter. Thereby, the cost function can be minimized by simply evaluating it with a finite set of switching combinations. This avoid complex multi-objective minimization problems.

Fig. 3.11 shows the control scheme implemented for a two-level four-leg VSI active filter [94]. The aim of this scheme is to control the current injected by the filter ($\boldsymbol{i}_F$) in order to compensate the harmonics and unbalances generated by the load current $\boldsymbol{i}_L$ and obtain sinusoidal grid currents $\boldsymbol{i}_s$. For this propose, at the beginning of each k^{th} sampling time, the grid voltages $\boldsymbol{v}_{cc}$, the filter currents $\boldsymbol{i}_F$ and load currents $\boldsymbol{i}_L$ are measured. Then, based on these measured variables and a discrete model of the system, implemented usually with backward or forward Euler discretization [113], 16 different currents can be predicted for each of the 16 switching combinations of the two-level four-leg converter. Each of these 16 predicted currents are denoted as $\boldsymbol{i}_F^n(k+1)$, where the index n denotes the n^{th} prediction. Thereafter, in order to track a the reference filter currents $\boldsymbol{i}_F^*(k)$, a cost function is evaluated for each of these 16 predictions and minimized to obtain the switching combination that perform the minimum error. The structure of the cost function is usually proposed as one- or two-norm errors, that is:

$$g_1^n = ||\boldsymbol{i}_F^* - \boldsymbol{i}_F^n||_1 = |i_a^* - i_a^n| + |i_b^* - i_b^n| + |i_c^* - i_c^n| \tag{3.25}$$

$$g_2^n = ||\boldsymbol{i}_F^* - \boldsymbol{i}_F^n||_2 = (i_a^* - i_a^n)^2 + (i_b^* - i_b^n)^2 + (i_c^* - i_c^n)^2 \tag{3.26}$$

Thus, the switching combination that minimizes the cost function, either g_1 or g_2, at each sampling time T_s is selected to be applied at the beginning in the following sampling time. This control action is denoted as $\boldsymbol{S}_{min}$ in the diagram of Fig. 3.11 and represents the states of each of the eight switches of the two-level four-leg VSI.

This control strategy have been applied in two level and three-level NPC VSIs based active filters and power suplies [19, 29, 30, 94, 114, 115]. Furthermore, it achieves fast tracking of current references and it also allows simple balance of the voltages on the dc-link just by incorporating an extra term in the cost function. However, it presents certain issues that still have not been overcome, such as:

- It performs a variable switching frequency, which can generate resonances with second-order output filters and produces unequally distributed power losses.
- The incorporation of additional control goals to the cost function entails a trade-off among several targets. The priority that the controller gives to each of these control tasks is based on a constant value, named weighting factors, that multiply each term. The selection of these weighting factors to obtain the best performance is still a matter of research and up to date, they are mainly obtained based on try an error or empirical procedures [116].
- The performance of the controller changes as the operation point of the converter changes. Thereby, for instance, when controlling a current through a load with a small inductance, the switching frequency of the devices increase considerably compared to a load which posses a slower dynamic. Same occurs when the amplitude of the controlled current changes. This variability can be an important issue, specially for system where the load dynamically changes, as usually required in four-wire applications [117].

Recent research on predictive control addresses this problem and uses a suitable modified cost function in order to avoid the empirical calculation of weighting factors [110, 118]. However, this requires an accurate model of the controlled system, available in electrical drives applications, but usually not available in four-wire applications.

3.2.4 Additional Control Strategies

Additional control algorithms have been also reported recently in the literature. In [17] the 16 switching combinations of the two-level four-leg VSI have been divided into two groups according to the polarity of the zero-sequence component of each switching combination. Thereby, the standard two-dimensional SVM is applied to each group of eight vectors. Although this allows modulation of the output voltages avoiding three-dimensional search. The compensation capability of the converter is not fully exploit.

In [27], each leg of a three-level four-leg converter, connected to an output *LC* filter, is decoupled and treated independently as three three-level buck converters. This simplify the modulation algorithm to single-phase converters, but reduces the utilization of the redundant vectors and also increase the output voltage harmonic distortion of the converter, as the modulation operates equivalently to a *Non-Redundant* sequence for the three-dimensional SVM method presented in Section 3.1.1.

In [28] a generalized PWM algorithm, similar to the carrier-based method presented in Section 3.2.2, for three-leg four-wire is proposed. Furthermore, by introduction of a shifting voltage term, it also allows its implementation in four-leg converters. This method is based on the *voltage-seconds* approximation and directly calculates the *duty cycles* for the switches of each leg avoiding vectorial representation of the switching states. This method is equivalent to the three-dimensional SVM algorithm for three-leg four-wire topologies. However, its implementation in four-leg multilevel converters have not been reported. Furthermore, important issues such as: utilization of different switching patterns, utilization of the dc-link or utilization of the redundant vectors for balancing the voltages on the dc-link capacitors in four-leg multilevel converters have not been yet reported. Moreover, it does not work in a three-dimensional space, which reduce flexibility of the algorithm and limits the implementation of more sophisticated control techniques for balancing the voltages on dc-link capacitors such as Virtual Space Vector PWM (VSVPWM) [69]. Additional modulation algorithms formulated in a general form for multi-leg converters, which could be potentially used in four-leg converters, have been reported in [119–122].

3.2.5 Discussion and Remarks

This chapter has summarized the most relevant control strategies for three-leg four-wire and four-leg VSIs. The three-dimensional SVM techniques, either in $\alpha\beta\gamma$ of *abc* coordinate frame, arise as the most flexible techniques that exploit all the features of four-leg converters. However, their complexity or impediment of working in an $\alpha\beta\gamma$ domain has encouraged the development of new alternative methods, as an effort for reducing the complexity of the SVM algorithms. Naturally, this simplification come usually together with restrictions that reduce the flexibility and capability of the converter. However, they can be good candidates for certain applications.

The following remarks can be concluded from the current state of the art for controlling converters in four-wire applications:

- Currently, the four-leg converters arise as the most suitable topology for four-wire applications. Compared to the three-leg four-wire topologies, four-leg converters provides a superior performance, allowing 15% more of dc-link voltage utilization and a larger range of compensation of zero-sequences. Additionally it does not require huge dc-link capacitors to provide circulation path to the neutral wire.

- The three-dimensional SVM technique together with the hysteresis PWM current control, both in $\alpha\beta\gamma$ coordinates, arise as the most mature and reliable techniques for controlling four-leg converters with fixed and variable switching frequency. The first present an extension of the standard SVM algorithm, providing extension of well known arrangement of switching sequences, power losses distribution and overmodulation methods. The second is also an extension of the typical hysteresis control in $\alpha\beta$ coordinates, which is even standard in commercial drive application, such a Direct Torque Control (DTC) [123]. The use of both techniques has been well reported for two-level converters. However, both of them have limitations for multilevel applications. The first require complex calculations and large number of tables, while the second limits the utilization of redundant vectors and produces a high switching frequency.

- The Carrier based SPWM used for standard three-leg converters can be directly used in three-leg four-wire converters. This a simple alternative to control these converters when no special requirements of switching sequences or harmonics spectrum has to be accomplished. For the best knowledge of the author, the implementation of this method in multilevel converters have not been reported. Nevertheless, the unbalanced nature of loads in four-wire applications and the limited use of the redundant vectors would complicates the balance of the voltages on the dc-link capacitors.

- The Carrier Based PWM technique developed for four-leg converters, presented in Section 3.2.2, arises as an interesting alternative for controlling two-level four-leg converters, as it is demonstrated that perform equivalent switching patterns as in the three-dimensional SVM. However, its limited use of the redundant switching combinations reduce the controllability over the voltages on the dc-link capacitors in multilevel applications [109] and become its main drawback.

- The three-dimensional SVM technique implemented in *abc* coordinates appears as the first technique that provides an easy extension to four-leg multilevel converters and also allows flexible utilization of the redundant vectors. However, it is still in a premature state and important issues such as: arrangement of switching sequences, elimination of selective harmonics or overmodulation methods have not been reported yet.

The development of a simple three-dimensional SVM algorithm in the $\alpha\beta\gamma$ frame suitable for multilevel converters is subject that still remains open and cover in this dissertation. A simple three-dimensional SVM algorithm in the $\alpha\beta\gamma$ is proposed and validated in a four-leg NPC VSI. Furthermore, this topology with the proposed SVM technique are implemented as a $400Hz$ power supply for aerospace applications.

CHAPTER 4

Resonant Controllers for Voltage Source Power Converters

Abstract: *This chapter presents the guidelines for designing resonant controllers for compensation of multiple harmonic components. First the Nyquist stability analysis is discussed and analyzed for single and multiple resonant controllers. Thereafter the importance of the approximation method used for discretization of resonant controllers and compensation of the computational delay when high order harmoncs are being compensated is discussed.*

In recent years, resonant controllers have arisen as an interesting alternative for directly controlling sinusoidal waveforms of arbitrary frequencies with zero steady-state error. These controllers are of particular interest in systems where several harmonic components have to be compensated. This is mainly because it avoids the implementation of multiple rotating dq-frames, obtained by using Park Transformation for each harmonic, and multiple Phase-Looked Loop (PLL) systems [6, 124]. Its implementation has been reported in several applications such as: Active Power Filters (APFs) [125–133], Uninterruptible Power Supplies (UPSs) for non-linear loads [21, 134–136], dynamic voltage restorers (DVRs) [137] , active rectifiers [138, 139], aerospace applications [140, 141] and grid connected converters for photovoltaic [142, 143] and wind energy systems [144–147].

The Fig. 4.1 shows the control scheme, based on resonant controllers, for the two most representative applications used for harmonics compensation in four-wire systems, i.e. an APF and a UPS for unbalanced and non-linear loads.

In the Fig. 4.1a the APF has been connected to a four-wire system via a first-order filter, which transfer function is given by:

$$P_1(s) = \frac{I_f(s)}{V_f(s) - V_{cc}(s)} = \frac{1}{L_f s + R_f} \tag{4.1}$$

where $I_f(s)$, $V_f(s)$ and $V_{cc}(s)$ are the representation in the frequency domain of $\boldsymbol{i}_F$, $\boldsymbol{v}_F$ and $\boldsymbol{v}_{cc}$

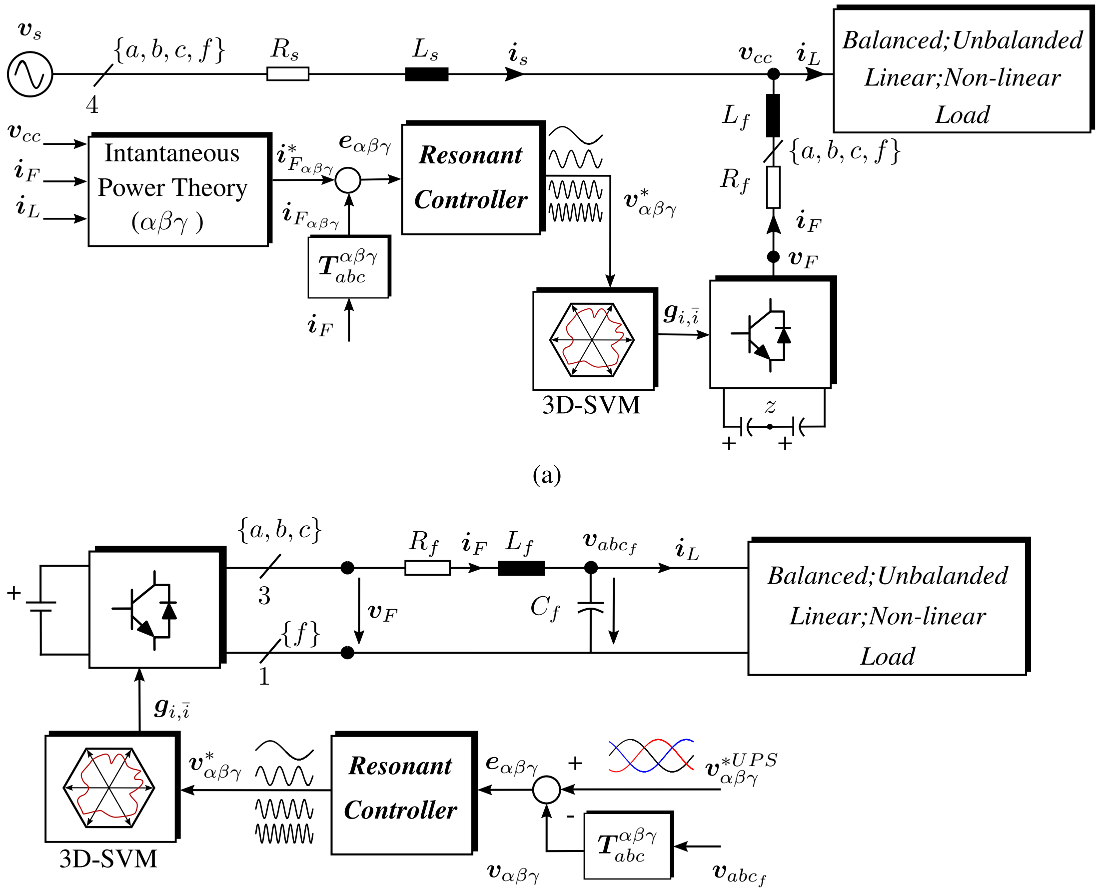

(b)

Figure 4.1: Control diagram for a (a) Active Power Filter and (b) and UPS for four-wire systems using Resonant Controllers. For (a) and (b): load currents $\boldsymbol{i}_L = [i_{La}, i_{Lb}, i_{Lc}]$, converter output currents $\boldsymbol{i}_F = [i_{Fa}, i_{Fb}, i_{Fc}]$, converter output voltages $\boldsymbol{v}_F = [v_{F_{af}}, v_{F_{bf}}, v_{F_{cf}}]$, reference voltages for SVM $\boldsymbol{v}^*_{\alpha\beta\gamma}=[v^*_\alpha, v^*_\beta, v^*_\gamma]$, trigger signals for the converter $\boldsymbol{g}_{i,\bar{i}}$. For (a): grid currents $\boldsymbol{i}_s=[i_{s_a}, i_{s_b}, i_{s_c}]$, common coupling voltages $\boldsymbol{v}_{cc}=[v_{cc_{af}}, v_{cc_{bf}}, v_{cc_{cf}}]$. For (b): output filtered voltages $\boldsymbol{v}_{abc_f}=[v_{af}, v_{bf}, v_{cf}]$, reference for the output filtered voltages in $\alpha\beta\gamma$ coordinates $\boldsymbol{v}^{*UPS}_{\alpha\beta\gamma}=[v^{*UPS}_\alpha, v^{*UPS}_\beta, v^{*UPS}_\gamma]$.

respectively.

The APF of Fig. 4.1a aims to control the converter output currents $\boldsymbol{i}_F$ to compensate the grid currents $\boldsymbol{i}_s$ from the unbalances and harmonic distortion produced by the load currents $\boldsymbol{i}_L$. For this propose, a set of resonant current controllers have to be designed to track each harmonic component of the reference current $\boldsymbol{i}^*_{F_{\alpha\beta\gamma}}$. This reference is given by an external controller [60] and is usually calculated by using the instantaneous power theory [100, 102]. Afterwards, the output of each resonant controller are added to provide a voltage reference $\boldsymbol{v}^*_{\alpha\beta\gamma}$ that is going to be synthesized by a power converter.

In Fig. 4.1b the control scheme for an UPS connected to an isolated four-wire system is presented. The UPS provides balanced and symmetric three-phase four-wire voltages ($\boldsymbol{v}_{abc_f}$) to an unbalanced and non-linear load, compensating the droop voltages across the filter, namely R_f and L_f. In order to control the voltages at the terminals of the output *LC* filter, a single-loop voltage resonant controller has been proposed in Fig. 4.1b. This single-loop voltage controller receives the voltage tracking error $\boldsymbol{e}_{\alpha\beta\gamma}$ and directly provides the reference voltages $\boldsymbol{v}^{*}_{\alpha\beta\gamma}$ to be synthesized by the power converter [148]. The required transfer function for designing a proper controller for a second-order system, namely the *LC* filter is given by

$$P_2(s) = \frac{V_{abc_f}(s)}{V_F(s)} = \frac{1}{L_f C_f s^2 + R_f C_f s + 1} \tag{4.2}$$

where $V_{abc_f}(s)$ represents the voltage at the loads terminals, i.e., $\boldsymbol{v}_{abc_f}$, and $V_F(s)$ is the voltage at the converter terminals, i.e., $\boldsymbol{v}_F$, in the frequency domain. Equivalently to the control scheme presented for the APF, a set of resonant controllers, each of them tuned for controlling one specific frequency, have to be designed when several voltage harmonics need to be compensated.

In order to design a proper resonant controller for each of the two presented application, its implementation for first- and second-order systems has to be analysed. This chapter presents an overview of the design of resonant controllers with multiple resonances applied to first- and second-order systems. This analysis covers the design of transient response of resonant controllers, stability margins and discretization for implementation in a real-time digital hardware. The design methods and stability considerations discussed in this chapter are later successfully validated in an experimental rig for an aerospace application presented in Chapter 6.

4.1 Multi-Resonant Controller Structures

According to recent literature, the most common structures for designing a resonant controller can be mainly summarized as follows [21, 128, 148, 149]: Resonant controller, Proportional Resonant controller, Vector Proportional Integral Resonant controller and Resonant controller with general lead-lag networks . These different structures basically differ in the number and positioning of the zeros of the controller, which allow to accomplish different dynamic performance requirements, maintaining an stable close-loop system. Their selection is mainly based on the application and the complexity of the plant.

The general form of a simple resonant controller in the s-domain can be represented as:

$$R(s) = \sum_{n=1}^{k} R_n(s) = \sum_{n=1}^{k} K_n \frac{s}{s^2 + \omega_n^2} \tag{4.3}$$

where K_n represents the gain and ω_n is the resonance frequency for the n^{th} resonant compensator $R_n(s)$. At the frequency ω_n, the controller $R_n(s)$ produces infinite gain in open-loop, which ensures zero steady-state error for tracking a reference signal at this frequency [150,151]. Therefore, the implementation of damping factors to increase the stability margin must be avoided, unless it is strictly necessary [60].

An extended structure can be implemented to control the phase-shift injected by each controller $R_n(s)$ around the frequency ω_n [125]:

$$R^c(s) = \sum_{n=1}^{k} R^c_n(s) = \sum_{n=1}^{k} K_n \frac{s\cos\vartheta_n - \omega_n \sin\vartheta_n}{s^2 + \omega_n^2} \tag{4.4}$$

Thereby, each controller $R_n^c(s)$ injects an angle of $\frac{\pi}{2}+\vartheta_n$ and $-\frac{\pi}{2}+\vartheta_n$ around each resonance frequency ω_n, giving an extra degree of freedom for the design of the controller. This structure is usually implemented for increasing the stability margins of a controller by compensating the phase-shift introduced by the plant at ω_n and calculated by

$$\vartheta_n = -\angle P_{1,2}(j\omega_n) \tag{4.5}$$

where $P_{1,2}(j\omega_n)$ represents either the first- or second-order plant $P_1(s)$ of (4.1) or $P_2(s)$ of (4.2) evaluated at ω_n. Note that for $\vartheta_n = 0$ the controller presented in (4.4) is equivalent to (4.3). Fig. 4.1 shows the open-loop Bode diagram of $R_1^c(s)$ designed for a resonance frequency of $\omega_1{=}100\pi$rad. Three different compensation angles, namely ϑ_1^1 ϑ_1^2 and ϑ_1^3, have been used for illustrating its effect over the phase of the controller. It is noted that for $\vartheta_1^1{=}0$, the resonant controller inject and angle of ±90° around 100πrad. Additionally, the magnitude of the controller is not affected by changing the compensation angle.

A proportional term K_P can be added to the resonant controllers presented in (4.3) and (4.4) to provide a faster transient response, giving also an additional degree of freedom for the design. This controller structure is known as Proportional Resonant (PR) Controller and is expressed as:

$$G(s) = K_p + \sum_{n=1}^{k} R_n(s) = K_p + \sum_{n=1}^{k} \left(K_n \frac{s}{s^2+\omega_n^2} \right) \tag{4.6}$$

$$G^c(s) = K_p + \sum_{n=1}^{k} R_n^c(s) = K_p + \sum_{n=1}^{k} \left(K_n \frac{s\cos\vartheta_n - \omega_n \sin\vartheta_n}{s^2+\omega_n^2} \right) \tag{4.7}$$

where $G(s)$ and $G^c(s)$ represent the PR controllers without and with control over the phase-shift injection, or also known as *delay compensation*.

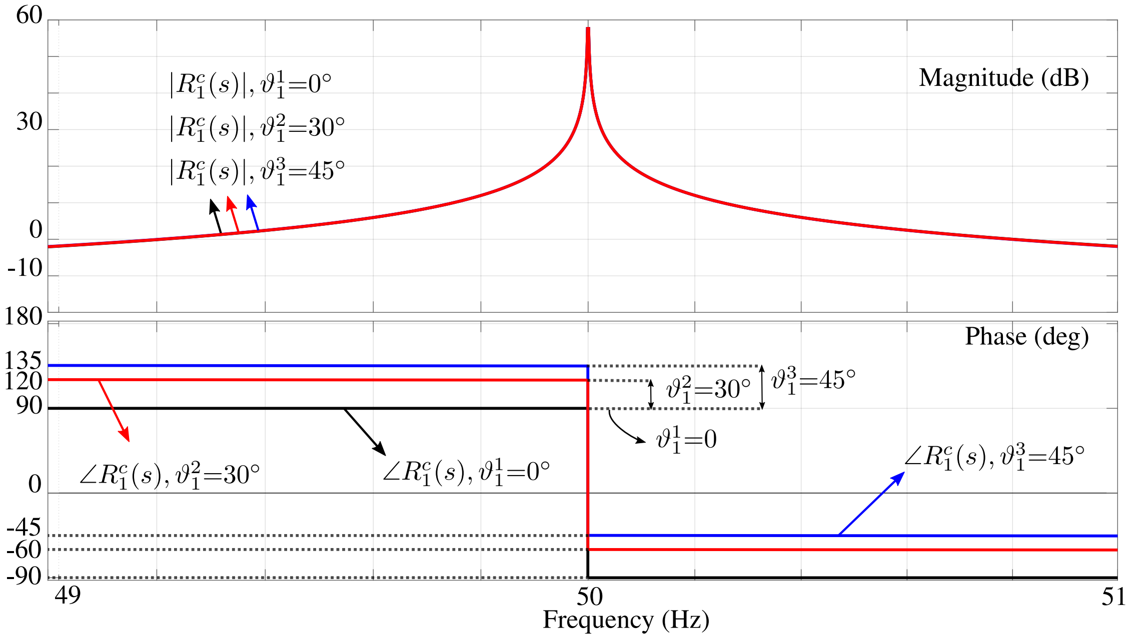

Figure 4.2: Bode plot for $R_1^c(s)=\frac{K_1(s\cos\vartheta_1-\omega_1\sin\vartheta_1)}{s^2+\omega_1^2}$ with $\omega_1{=}100\pi$rad., $K_1{=}10$ and three different compensation angles. $\vartheta_1^1{=}0°$,$\vartheta_1^2{=}30°$ and $\vartheta_1^3{=}45°$.

The structure presented in (4.7) represents the most suitable and flexible configuration for most of the applications of resonant controllers for power converters. However, a more general structure can be obtained introducing arbitrary number of lead-lag networks [21, 136]. This structure is represented as:

$$R_{Net}(s) = \sum_{n=1}^{k}\left(K_n\frac{s}{s^2+\omega_n^2}\cdot\prod_{i=1}^{k}\frac{s+a_i}{s+b_i}\right) \tag{4.8}$$

where $\{a_i, b_i\}\in\mathbb{R}$. This structure is more flexible and can be employed for complex plants, where the previous methods does not provide enough degree of freedom for achieving the control requirements. A particular structure implemented for first-order plants have gained attention lately in the literature and it is known as Vector Proportional Integral (VPI) Resonant Controller, given by [130, 131]

$$R^c_{VPI_n} = K_n\frac{(s\cos\vartheta_n-\omega_n\sin\vartheta_n)(sL_f+R_f)}{s^2+\omega_n^2} \tag{4.9}$$

where L_f and R_f are the parameters of a first-order filter. This structure allows phase compensation ϑ_n for the controlled frequency ω_n, and uses a lead network to cancel the dynamic of a first-order plant. It provides easy design and good performance, but it is very sensible to variations on the filter parameters. Thereby, errors in the estimation of real parameters can easily lead to instability or amplify considerably the noise in a real implementation [150, 151].

4.2 Multi-Resonant Controllers for First-Order Systems

The design of any controller must accomplish with three important principles: a) it must satisfy the dynamic close-loop requirements, b) it must provide enough stability margins to deal with parameters uncertainties, usually found in real implementations and c) it must be as simple as possible, to guarantee a successful implementation. Therefore, the methods and resonant controller structures presented and analysed in the following section are based on these three principles.

Fig. 4.3 shows the general control diagram for a set of k resonant controllers implemented for tracking k harmonic components presents in $Y^*(s)$ and applied to a general plant $P(s)$. Using $P(s)$ as the first-order filter $P_1(s)$ of (4.1), $Y^*(s)$=$I_f^*(s)$ and $Y(s)$=$I_f(s)$, the diagram of Fig. 4.3 represents the current control structure for a first-order filter (see Fig. 4.1a). With $I_f^*(s)$ and $I_f(s)$ as the reference and controlled current signals in frequency domain.

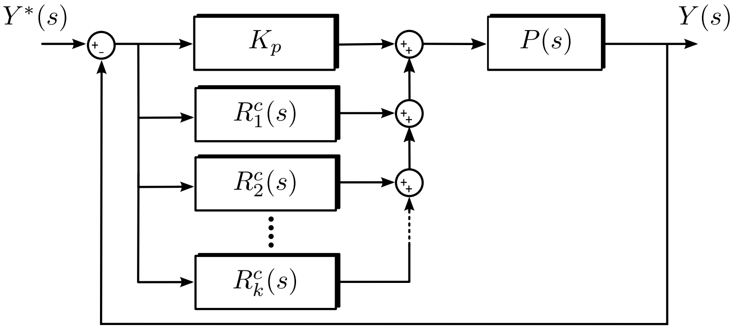

Figure 4.3: General close-loop control scheme for a proportional resonant controller with *delay compensation* ($G^c(s)$) applied to a plant $P(s)$.

For the sake of generality, the controller with angle compensation $G^c(s)$ of (4.7) has been selected for implementation in Fig. 4.3. However, as will be demonstrated, the compensation angle ϑ_n is usually not required and in most of the cases a PR controller $G(s)$ of (4.6), setting ϑ_n=0 in $G^c(s)$, provides enough flexibility for successfully controlling k sinusoidal current components of frequencies ω_n, for $n \in \{1, 2, .., k\}$.

4.2.1 Single-Resonant Controller Design

As a first approach, let us consider the resonant controller of (4.3) for compensation of only one fundamental current component of frequency ω_1 in a first-order plant $P_1(s)$. This controller is given by

$$G(s) = K_p + R_1(s) = K_p + K_1 \frac{s}{s^2 + \omega_1^2} \tag{4.10}$$

Due to the complex conjugate poles of a resonant controller $G(s)$, the design of its transient response using standard root-locus or bode methods provides usually an inaccurate approximation. However, by shifting $G(s)$ in the frequency domain from ω_1 to ω_0=0, this controller can be approximated to an equivalent standard Proportional Integral (PI) controller [124]. Thereby, each resonant controller $R_n(s)$ of (4.3) can be shifted in the frequency domain for placing its resonance frequency ω_n at ω_0=0 by using

$$R^{dc}(s) = R_n(s + j\omega_n) + R_n(s - j\omega_n) - R_{2n}(s) \tag{4.11}$$

where $R^{dc}(s)$ represents the controller $R_n(s)$ with its resonance frequency ω_n shifted to ω_0=0 and it is expressed as:

$$R^{dc}(s) = \frac{K_1}{s} \tag{4.12}$$

Equivalently, the controller $R^{dc}(s)$ can be shifted back to a desired resonance frequency ω_n by using:

$$R_n(s) = \frac{R^{dc}(s + j\omega_n) + R^{dc}(s - j\omega_n)}{2} \tag{4.13}$$

Thereby, using (4.11), the proportional resonant controller of (4.10) can be expressed as an equivalent PI controller as:

$$G^{dc}(s) = K_p + R^{dc}(s) = K_p + \frac{K_1}{s} \tag{4.14}$$

So that, the simple PI controller of (4.14) can be used for obtaining the gain parameters K_1 and K_p that accomplishes with a certain design criteria. The design can be accomplished by a root-locus analysis and then directly implement the gain parameters K_1 and K_p in (4.10) for controlling a signal of frequency ω_1. Fig. 4.4 shows the root-locus design for the controller $G^{dc}(s)$ of (4.14) and the first-order plant of (4.1). The close-loop poles have been placed to obtain a damping factor of ξ=0.54 and a settling time t_{set}=1.6ms.

Fig. 4.5 shows the time domain step-response for the implementation of both controllers, $G^{dc}(s)$ of (4.14) and the $G(s)$ of (4.10). Both controllers have been implemented to the same first-order plant $P_1(s)$ and with the same gains parameters K_p and K_1 which are obtained from the design of Fig. 4.4. As it can be seen, the transient step-response performed by the signal controlled by $G^{dc}(s)$, namely $i_f^{dc}(t)$, is equivalent to the step-response displayed by the sinusoidal signal controlled by $G(s)$, i.e. $i_f(t)$. The settling time for both signals is approximately $1.6ms$ and their overshoot $M_p \approx 1.25\%$. This is slightly larger than the 1.16% considered in the root-locus design of Fig. 4.4. This non-ideal response is explained by the influence of the extra zero incorporated in the close-loop transfer function of the system composed by $G^{dc}(s)$ and $P_1(s)$ [150, 151]. This close-loop function is expressed as:

$$\frac{I_f^{dc}(s)}{I_f^{*dc}(s)} = \frac{\frac{K_p}{L_f}(s + \frac{K_1}{K_p})}{s^2 + s(\frac{R_f + K_p}{L_f}) + \frac{K_1}{L_f}} \tag{4.15}$$

where $I_f^{*dc}(s)$ and $I_f^{dc}(s)$ are the direct-current reference and controlled signals in s-domain. The equivalent close-loop transfer function for a system composed by the proportional resonant controller $G(s)$ in (4.10) and $P_1(s)$ can be expressed as:

$$\frac{I_f(s)}{I_f^{*}(s)} = \frac{\frac{K_p}{L_f}(s^2 + \omega_1^2) + \frac{2K_1}{L_f}}{s(s^2 + \omega_1^2) + \frac{R_f + K_p}{L_f}(s^2 + \omega_1^2) + \frac{2K_1}{L_f}} \tag{4.16}$$

From simple inspection of (4.15) and (4.16) it can be noticed that substituting s=0 in (4.15) and s=$j\omega_1$ in (4.16) results in a perfect tracking of each reference signal with an unitary gain and without phase-shift errors. In order to minimize the effect of the extra zero of (4.15) over

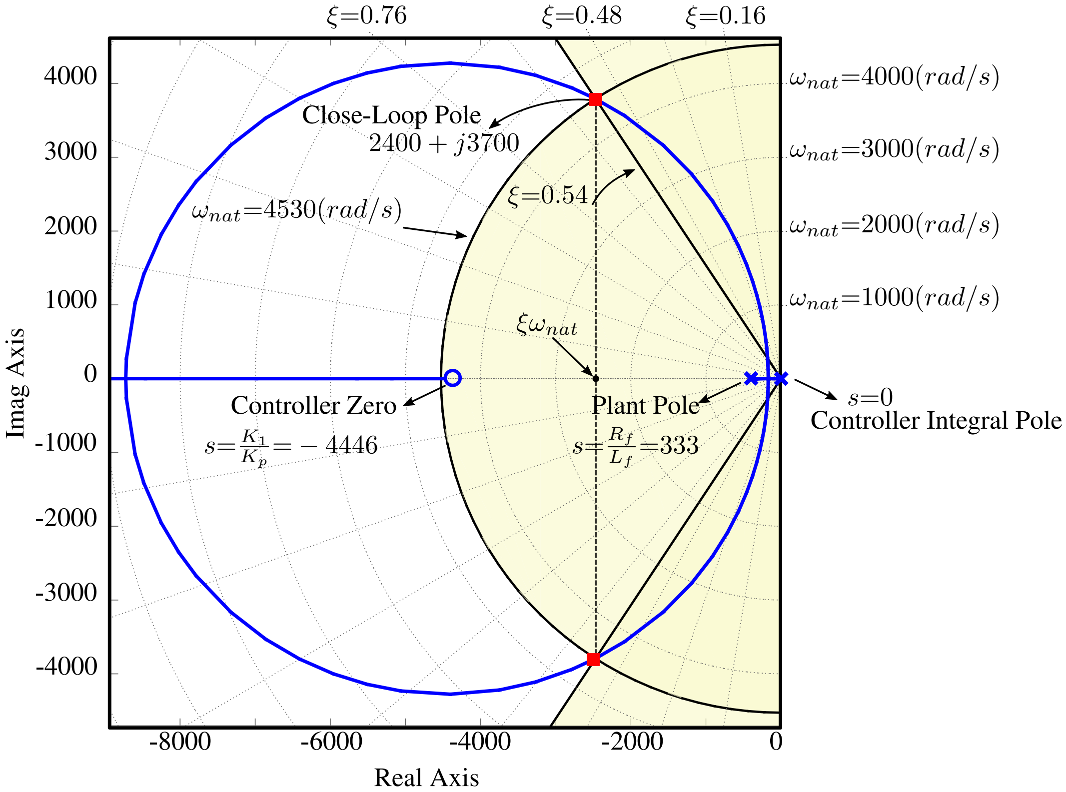

Figure 4.4: Root-Locus for a Proportional Integral controller $G^{dc}(s)=K_p+\frac{K_1}{s}$ and a first-order plant $P_1(s)=\frac{1}{L_f s+R_f}$, with parameters $R_f=1\Omega$ and $L_f=3mH$. The controller gains are $K_p=13.81$ and $K_1=61407$ for obtaining a close-loop response with settling time $t_{set}\approx 1.63ms$ and a maximum peak response of $M_p\approx 1.16\%$, namely damping factor $\xi\approx 0.54$ and natural frequency $\omega_{nat}\approx 4530$rad/s.

the close-loop transient response, the values of K_1 and K_p should be selected to place the zero $s=\frac{-K_1}{K_p}$ as far as possible from the real part of the complex conjugate close-loop poles showed in Fig. 4.4 [150, 151]. The real part of the complex conjugate close-loop poles can be expressed as $\xi\omega_{nat}$. Thereby, a good rule for considering negligible the effect of the extra zero over the transient response of the close-loop system is given by [150]:

$$\frac{K_1}{K_p}\geq 10|\xi\omega_{nat}| \tag{4.17}$$

It is important to mention that, in order to have a theoretical equivalent transient response for both controllers, i.e. transient response of a *dc* signal and of a sinusoidal signal of an arbitrary frequency ω_n, the input reference-step must excite the same frequencies in both controllers during the transient interval. This means, that for achieving a perfect equivalent transient response, the sinusoidal waveform should be equivalent to a constant step during the transient response. Although this is usually not achievable, a very good approximation is obtained when the designed settling time is relative small compared to the period of the controlled sinusoidal signal. Thus, an empirical good criteria for considering both transient responses approximately equivalent is to use

$$t_{set}\leq\frac{T_n}{4} \tag{4.18}$$

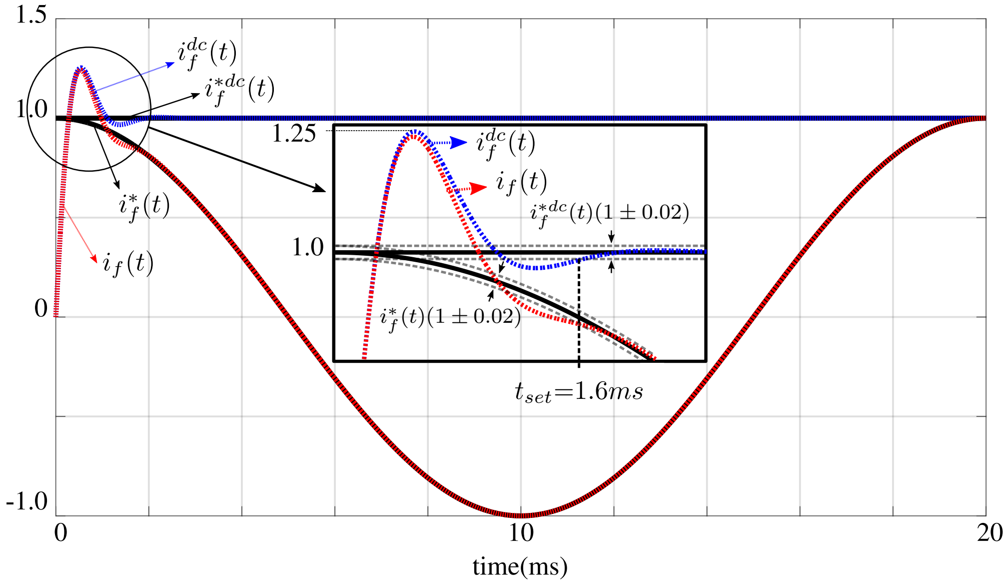

Figure 4.5: Time domain step-responses for a Proportional Resonant Controller $G(s)=K_p + \frac{K_1}{s^2+\omega_1^2}$ and a PI controller $G^{dc}(s)=K_p + \frac{K_1}{s}$ with K_p=13.81, K_1=61407 and ω_1=100πrad/s implemented in a plant $P_1(s)=\frac{1}{L_f s+R_f}$, with parameters $R_f=1\Omega$ and $L_f=3mH$. The overshoot for both responses approximately $M_p \approx 1.25\%$ with a settling time $t_{set} \approx 1.6ms$. $i_f(t)$, $i_f^*(t)$ $i_f^{dc}(t)$ and $i_f^{*dc}(t)$, represents the controlled and reference signals for the alternating and the equivalent *dc* currents.

where t_{set} is the settling time used in the design of $G^{dc}(s)$ and T_n is the period of the controlled sinusoidal signal of frequency ω_n.

In order to demonstrate this criteria, Fig. 4.6 shows the time response of a proportional resonant controller tuned at a frequency $\omega_3=300\pi rad/s$ and implemented with the same parameters K_p and K_1 used in Fig. 4.5. As it can be seen, the settling time is still equivalent to the *dc* response. However, the overshoot has decreased from 1.25 to 1.17, this is mainly because the designed settling time t_{set} represents now almost one quarter of the period of the reference signal, $T_3=6.\bar{6}ms$ and the sinusoidal reference waveform can no longer be considered as a constant step.

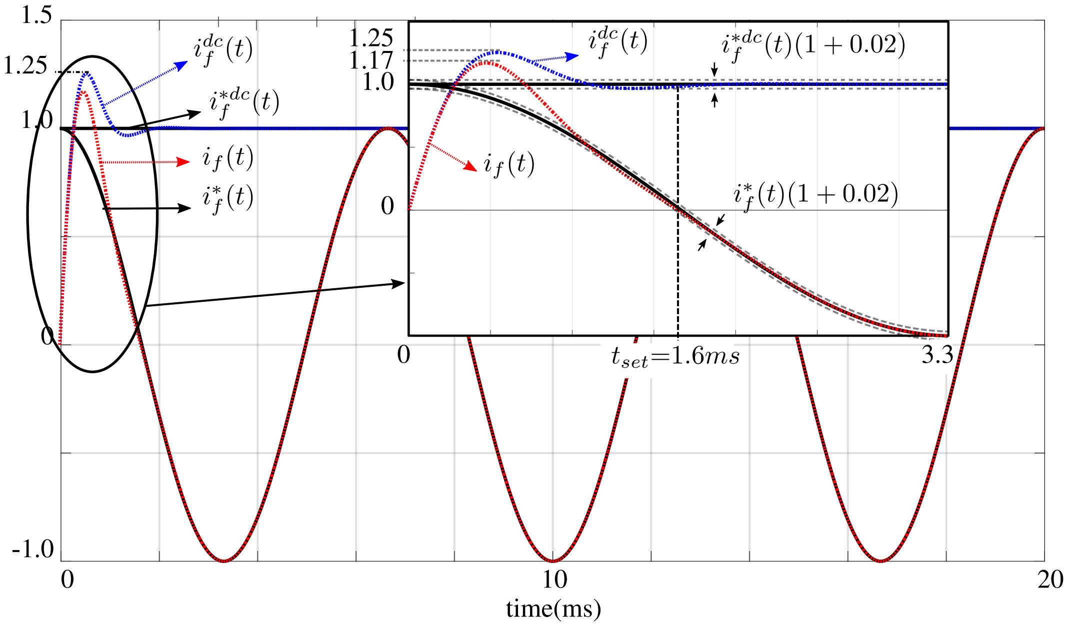

Figure 4.6: Time domain step-responses for a Proportional Resonant Controller $G(s)$=$K_p + \frac{K_3}{s^2+\omega_3^2}$ and a PI controller $G^{dc}(s)$=$K_p + \frac{K_3}{s}$ with K_p=13.81, K_3=61407 and ω_3=300πrad/s implemented in a plant: $P_1(s)$=$\frac{1}{L_f s+R_f}$, with parameters R_f=1Ω and L_f=3mH. The settling time for both responses is approximately t_{set}≈1.6ms. The overshoot for the sinusoidal response is approximately is $M_p \approx 1.17\%$, while for the *dc* response is approximately $M_p \approx 1.25\%$. $i_f(t)$, $i_f^*(t)$ $i_f^{dc}(t)$ and $i_f^{*dc}(t)$, represents the controlled and reference signals for the alternating and the equivalent *dc* currents.

4.2.2 Multi-Resonance Controller Design

The implementation of several resonant controllers in one transfer function, as presented in (4.7) and Fig. 4.3, leads to an unavoidable coupling effect among the controllers, which distort the transient response designed for each individual controller. For the sake of the analysis, a simple current resonant controller for compensation of two current harmonics at frequencies ω_1 and ω_3 can be used. This controller is given by

$$G(s) = K_p + R_1(s) + R_3(s) = K_p + K_1\frac{s}{s^2+\omega_1^2} + K_3\frac{s}{s^2+\omega_3^2} \tag{4.19}$$

Ideally, in a fully decoupled controller, the transient response produced by a resonant controller designed only for ω_1, as in Fig. 4.5, should keep unaltered after introducing a second resonant controller for controlling ω_3, as presented in (4.19). Likewise, the transient response performed by a resonant controller designed only for ω_3, as presented in Fig. 4.6, should be the same transient response performed by the controller $G(s)$ of (4.19), if the same parameters K_p and K_3 are used.

This ideal decoupled performance of each resonant controller is theoretically not achievable, mainly because the magnitude response of $R_1(s)$ (or equivalently $R_3(s)$) is not zero around ω_3 (or equivalently ω_1), generating a crossing effect. Thereby, the step response of $G(s)$ for a signal of frequency ω_1 (or equivalently ω_3) can be completely different to the individual response of $R_1(s)$ (or equivalently $R_3(s)$) if the controller $R_3(s)$ (or equivalently $R_1(s)$) possesses a considerable gain at this frequency. Additionally, the phase response interaction between $R_1(s)$ and $R_3(s)$ is also unavoidable and should be analysed. For this purpose, let us analyse the open-loop response of a system composed by $G(s)$ of (4.19) and a first order plant $P_1(s)$ of (4.1). It can be expressed as:

$$\begin{aligned} N_{1,3}(s) &= P_1(s)(K_p + R_1(s) + R_3(s)) \\ N_{1,3}(s) &= \frac{K_p}{L_f s + R_f} + K_1 \frac{s}{(s^2+\omega_1^2)(L_f s + R_f)} + K_3 \frac{s}{(s^2+\omega_3^2)(L_f s + R_f)} \end{aligned} \tag{4.20}$$

Fig. 4.7 shows the transfer functions for $P_1(s)(R_1(s) + R_3(s))$, $P_1(s)R_1(s)$ and $P_1(s)R_3(s)$. Each transfer function has been implemented using the same parameters obtained in the previous design (see Fig. 4.5) and considering $K_3{=}K_1$. As it can be seen from Fig. 4.7, the open-loop response of $(R_1(s) + R_3(s))P_1(s)$ possesses a negative infinite amplitude peak (zero absolute gain) at ω_q, which produces a step of 90° in its phase response. This abrupt change in the phase response results in an equivalent phase for $(R_1(s) + R_3(s))P_1(s)$ and $R_3(s)P_1(s)$ around ω_3. Similarly, $(R_1(s) + R_3(s))P_1(s)$ and $R_1(s)P_1(s)$ also posses same phase response around ω_1.

This similarity between the independent resonant controllers and the multi-resonant controller is subject to the selection of the gains of each controller, namely K_1 and K_3. Thereby, to obtain an approximated decoupled design, the following remarks, based on Fig. 4.7, should be considered:

- The adjustment of K_1 or K_3 moves the magnitude responses $|P_1(s)R_1(s)|$ or $|P_1(s)R_3(s)|$ upward or downward, while maintains the phase responses inalterable. This adjustment moves the intersection frequency ω_q, shifting the negative infinite gain peak of $P_1(s)(R_1(s)+R_3(s))$ and affecting the coupling of the controllers. Thereby, for instance, a high value of K_1 compared to K_3 moves ω_q towards ω_3. This results in a reduced gain of $|P_1(s)(R_1(s) + R_3(s))|$ for frequencies that approach to ω_3 from the left side, which can be prejudicial if the frequency of the controlled signal slightly variates in a small range.

- The selection of K_1 and K_3 should provide a phase band $\Delta\omega_q$ that generates an equivalent phase response for $\angle P_1(s)(R_1(s) + R_3(s))$ and $\angle P_1(s)R_1(s)$ (or equivalently $\angle P_1(s)R_3(s)$) around ω_1 (or equivalently ω_3) with a sufficient margin range. Thereby, for instance, a high value of K_1 compared to K_3 produces a very small phase band $\Delta\omega_q$ and the equivalence between $\angle P_1(s)(R_1(s) + R_3(s))$ and $\angle P_1(s)R_3(s)$ is valid only for a narrow band around ω_3. As it will be studied later, this can lead to stability problems.

Thus, for reducing the coupling effect of a set of k resonant controllers: $R_n(s)$ for $n \in \{1, 2, ..., k\}$. A good design criteria is to select the gains of each resonant controller K_n for placing the intersection frequency between $|P_1(s)R_n(s)|$ and $|P_1(s)R_{n+1}(s)|$, defined by ω_{q_n}, to a similar distance from ω_n and ω_{n+1}, ensuring a good margin $\Delta\omega_{q_n}$.

In order to proof the previous analysis, Fig. 4.8a shows the step response for the controller of (4.19), implemented with the same parameters used in Fig. 4.7. As it can be seen, firstly a sinusoidal step reference with a frequency ω_1 is implemented. Compared to Fig. 4.5, the transient response is slightly affected by the unavoidable coupling effect of both controllers, i.e. $R_1(s)$ and $R_3(s)$. However, the transient response can still be considered acceptable similar

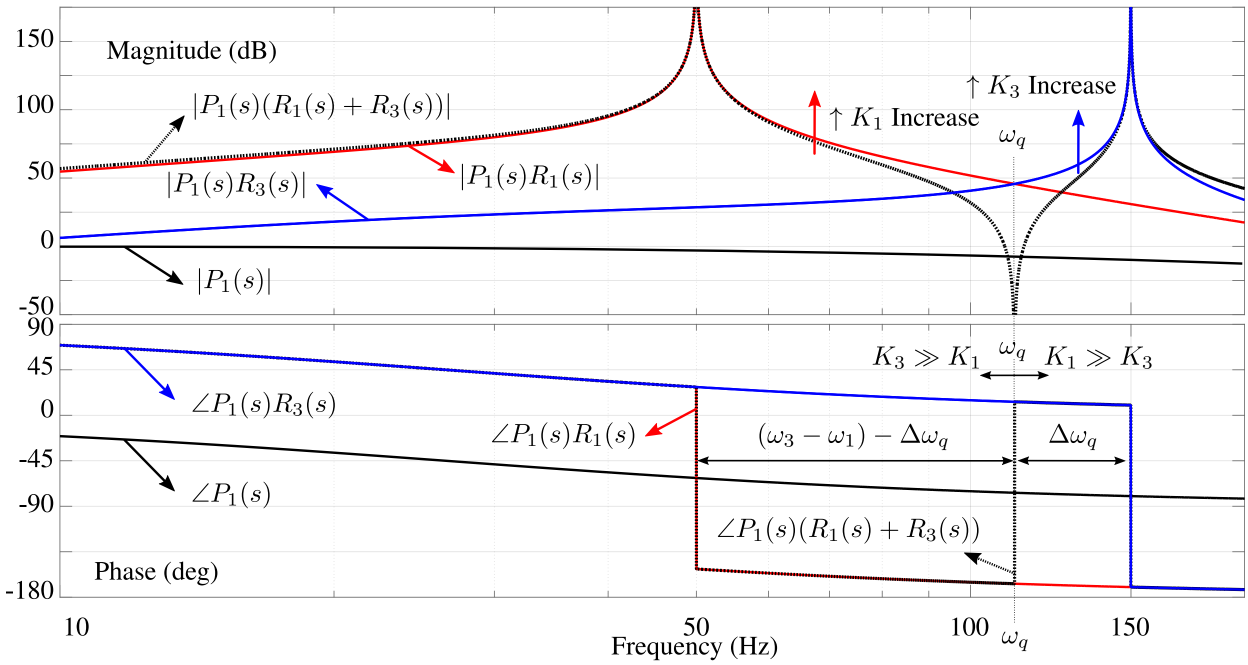

Figure 4.7: Bode diagram for the frequency response of $P_1(s)$, $P_1(s)(R_1(s)+R_3(s))$, $P_1(s)R_1(s)$, $P_1(s)R_3(s)$. With K_1=K_3=61407, ω_1=100πrad/s, ω_3=300πrad/s, L_f=$3mH$ and R_f=1.0Ω.

to the transient response obtained in Fig. 4.5. After $20ms$, a sinusoidal step reference with an amplitude of 20% and frequency ω_3 is introduced. The response has also increased its overshoot compared to its independent implementation showed Fig. 4.6. However, it still performs a reasonable similar transient response compared to Fig. 4.6.

Similarly, Fig. 4.8b shows the same procedure but increasing K_3 in ten times. As it can be seen, although K_1 have not been changed, the coupling effect dramatically affected its transient response. Naturally, the transient response for ω_3 the at $20ms$ has been also affected.

In general, the transient response of a multi-resonant controller is mainly determined by the resonant controller designed for the fundamental frequency ω_1, as the magnitude of the controlled signal at this frequency is usually much larger than the additional compensated components. Moreover, the additional gains K_n for the resonant compensators, $R_n(s)$ for $n \in \{2,..k\}$, can be selected to find a suitable trade-off between fast elimination of the steady-state error for the signal of frequency ω_n and to provide sufficient stability margins (as shown in the following section).

As an alternative solution to reduce the coupling effect of resonant controllers, a set notch filters can be implemented previous the input of each resonant controller $R_n^c(s)$ of Fig. 4.3. This can reduce the coupling affect among the k controllers $R_n(s)$ for $n \in \{1,2,..k\}$, as they only receive signals of frequency ω_n at which they are tuned. However, this increases the complexity of the controller. Additionally, the dynamic of the notch filters also interfere in the transient response of the controllers [152].

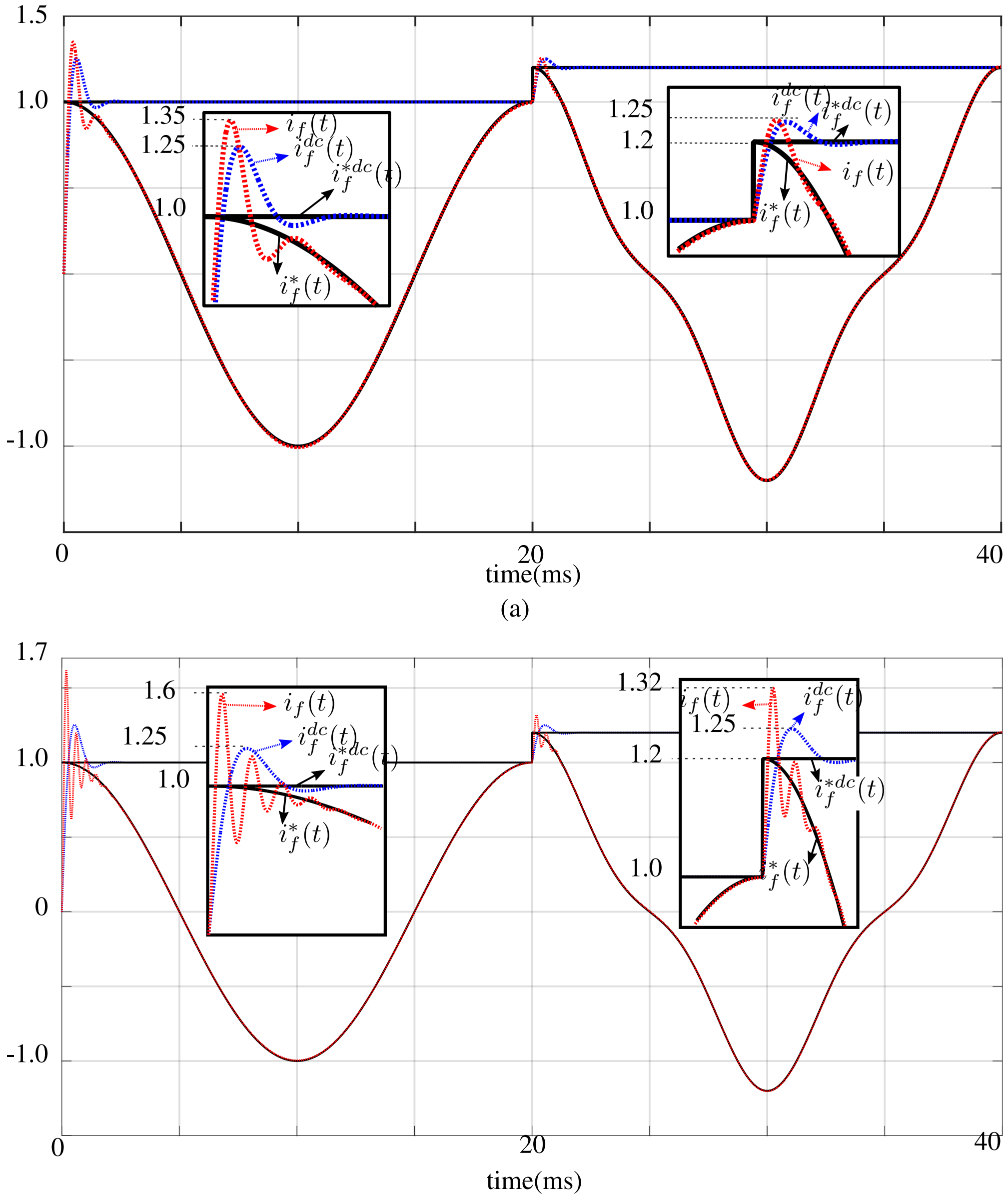

(a)

(b)

Figure 4.8: Time domain step-responses for a Proportional Resonant Controller $G(s){=}K_p + \frac{K_1}{s^2+\omega_1^2} + \frac{K_3}{s^2+\omega_3^2}$ and a PI controller $G^{dc}(s){=}K_p + \frac{K_1}{s}$ with (a) $K_p{=}13.81$, $K_1{=}K_3{=}61407$, $\omega_1{=}100\pi$rad/s and $\omega_3{=}300\pi$rad/s implemented in a plant: $P_1(s){=}\frac{1}{L_f s+R_f}$, with parameters $R_f{=}1\Omega$ and $L_f{=}3mH$ in (b) only $K_3{=}614070$ has been changed. $i_f(t)$, $i_f^*(t)$ $i_f^{dc}(t)$ and $i_f^{*dc}(t)$, represents the controlled and reference signals for the alternating and the equivalent *dc* currents.

4.2.3 Nyquist Stability Analysis

After obtaining the parameters that perform a desired transient response for a resonant controller with one or multiple resonances, its relative stability has to be studied to ensure a robust operation. Usually, the phase- and gain-margins obtained in a bode plot are enough indicators to proof the relative stability of a certain controller design. However, these parameters are only valid for open-loop responses that monotonically decay, which produces only one phase-margin and one gain-margin across the frequency spectrum. When resonant controllers are implemented, the bode magnitude response can cross the abscissa ($0dB$) multiple times, leading to multiple phase-margins. Likewise, the phase response perform a step of $180°$ for every resonance frequency, which can lead to several gain-margins. Thereby, typical phase- and gain-margins are not a reliable indicator for stability when resonant controllers are implemented. A more suitable and reliable indicator of relative stability margins is the reciprocal of the sensitivity peak, namely the minimum distance of a Nyquist plot to the critical instability point $(-1, 0j)$ [151].

In order to obtain a stable close-loop response, the Nyquist plot of the open-loop transfer function of a system should not enclose the point $(-1, 0j)$ in the complex plane [151]. Thus, the open-loop transfer function for a resonant controller implemented for compensation of a frequency ω_1 applied to a first-order plant is given by

$$N_1(s) = P_1(s)(K_p + R_1(s)) = \frac{K_p}{L_f s + R_f} + K_1 \frac{s}{(s^2 + \omega_1^2)(L_f s + R_f)} \tag{4.21}$$

In order to obtain the stability margins of $N_1(s)$, let us analyse the effect that each term of (4.21) has over the Nyquist diagram:

- Fig. 4.9a shows the Nyquist diagram of $K_p P_1(s)$, plotted for positive (in solid lines) and negative (in dotted lines) frequencies. Several curves are plotted to observe the effect of an increment in K_p. As it can be seen, for $\omega : 0 \rightarrow \infty$, the plot starts at the point $(\frac{K_p}{R_f}, 0j)$ with $\omega = 0$ and finishes at $(0, 0j)$ when $\omega \rightarrow \infty$. Due to the magnitude of $P_1(s)$ monotonically decreases to zero while its phase-response also decreases monotonically from $0°$ to $-90°$ (see Fig. 4.7), the Nyquist path does not present discontinuities, describing always a curve in the right side of the plane. Hence, an increment in K_p enlarge the curve, shifting the starting point to the right side of the plane. Thereby, the term $K_p P_1(s)$ shifts the open-loop Nyquist diagram of $N_1(s)$ to the stable region, pushing it away from the critical point $(-1, 0j)$.

- Fig. 4.9b shows the Nyquist of $P_1(s)R_1(s)$ for positive frequencies (the path for negative frequencies is symmetrically placed in the plane). From simple inspection of (4.21), the starting point of the Nyquist plot is $(0, 0j)$ for ω=0. Thereafter, the plot rapidly increases its magnitude being theoretically infinite when ω reaches ω_1 from the left side (ω_1^-). After ω is infinitesimally larger than ω_1, the magnitude starts to decrease and the phase have been shifted in $-180°$, which makes the curve appears from the other extreme of the diagram (see Fig. 4.7). After that, the magnitude slowly decreases to zero, arriving to the starting point $(0, 0j)$. As illustrated in Fig. 4.7, the phase-response of $P_1(s)R_1(s)$ is not affected by the term K_1 and it is only determined by the parameters of the plant L_f, R_f and the controlled frequency ω_1. Thereby, its starting angle (for ω=0) and arriving angle (for $\omega \rightarrow \infty$) are always $90°$ and $-180°$. However, a large value of K_1 maintains these starting and arriving angles for a larger range of frequencies. Although an increment of K_1 does not change the phase-response of $P_1(s)R_1(s)$, it influences the closeness of the curve to the point $(-1, 0j)$, when $\omega \rightarrow \infty$, affecting negatively the stability margin as shown in Fig. 4.9b. It is important to mention that the modification of K_p and K_1 correspondingly changes the transient response as discussed in the previous section.

- Fig. 4.9c and Fig. 4.9d shows the complete open-loop response for $N_1(s)$. Each diagram shows the effect of changing K_p or K_1 respectively. As it can be expected, an increment in K_p, maintaining K_1 constant, pushes the Nyquist plot away from the critical stability point $(-1, 0j)$, shifting also the starting point $\frac{K_p}{R_f}$. Contrary, an increment of K_1, maintaining K_p constant, pushes the Nyquist trajectory closer to the critical point $(-1, 0j)$, reducing the stability margin.

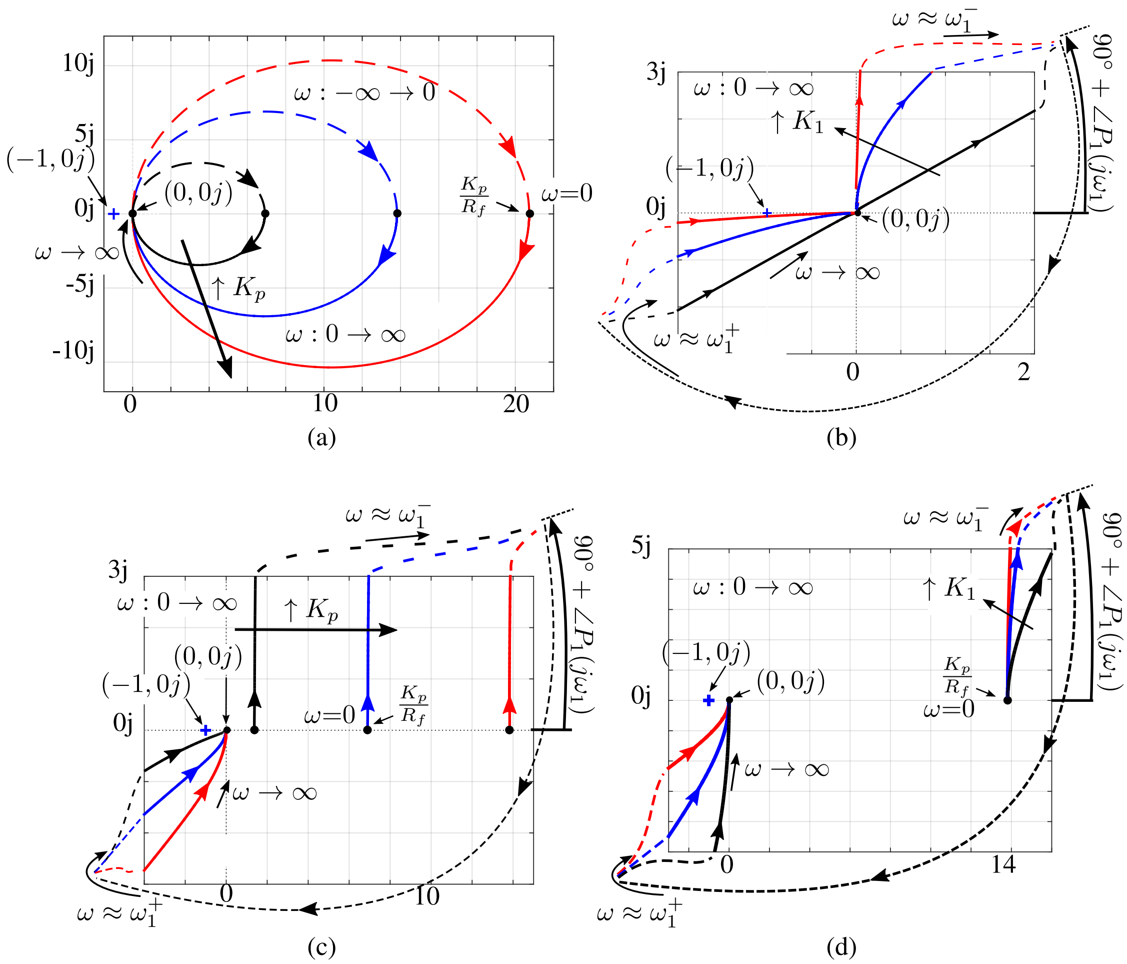

(a) (b) (c) (d)

Figure 4.9: Nyquist plot and analysis for the open loop responses of (a) $c_1 \cdot K_p P_1(s)$ for $c_1{=}\{0.5, 1.0, 1.5\}$, (b) $c_2 \cdot P_1(s)R_1(s)$ for $c_2{=}\{10^{-3}, 10^{-2}, 1\}$, (c) $P_1(s)(c_1 \cdot K_p + c_2 \cdot R_1(s))$ for $c_1{=}\{0.1, 0.5, 1.0\}$ and $c_2{=}1.0$ and (d) $P_1(s)(c_1 \cdot K_p + c_2 \cdot R_1(s))$ for $c_1{=}1.0$ and $c_2{=}\{0.1, 0.3, 1.0\}$. $K_p{=}13.81$, $K_1{=}61407$, $\omega_1{=}100\pi$rad/s, $R_f{=}1\Omega$ and $L_f{=}3mH$.

The Fig. 4.10 shows open-loop response of $N_1(s)$ with the same parameters listed in the caption of the Fig. 4.4. As it can be seen, the path starts at $(\frac{K_p}{R_f}, 0j) \approx (14, 0j)$ and tends to infinity with an asymptote of 47° as ω approaches to ω_1^-, describing the path marked by σ_a.

Thereafter, the curve appears from the other extreme of the plot, $180°$ behind, describing the path σ_b that converge to the point $(0, 0j)$ as ω approaches to infinity. The critical frequency ω_c and the phase-margin $PM_{N_1(s)}$ are also showed in the Fig. 4.10 by using a unitary circle. As the path does not describe any point with a phase of $180°$, the gain-margin is not depicted. The minimum distance between the critical point $(-1, 0j)$ and the Nyquist plot is defined as η and it represents the inverse of the sensitivity peak [151]. This index combine both, phase- and gain-margins in only one indicator. Thereby, a small value of η leads to small stability margins and the system can become easily unstable. Additionally, a small value of η leads to very underdamped transient responses [151].

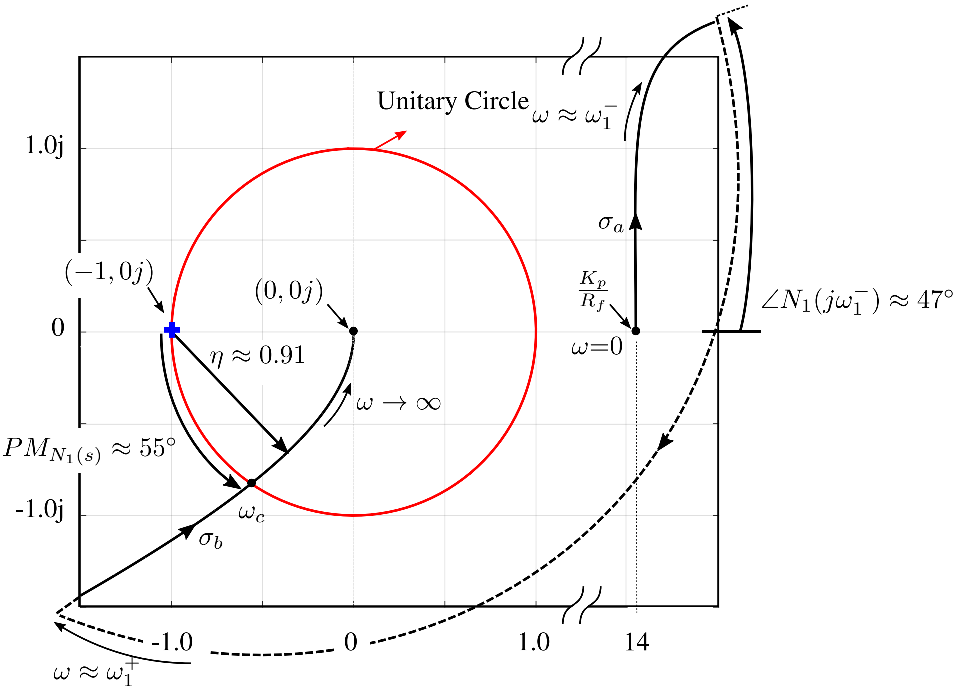

Figure 4.10: Nyquist diagram for the open-loop response $N_1(s)$ of (4.21). The implemented parameters are: R_f=1Ω, L_f=$3mH$, K_p=13.81, K_1=61407 and ω_1=100πrad/s. ω_c≈5800rad/s.

Fig. 4.11 shows the Nyquist diagram for a first-order plant and a resonant controller implemented with compensation two frequencies, namely the response of the open-loop function $N_{1,3}(s)$ presented in (4.20). Using the bode plot presented in Fig. 4.7, the diagram of Fig. 4.11 can be easily understood. Thereby, the plot starts again in $(\frac{K_p}{R_f}, 0j) \approx (14, 0j)$ for ω=0 and tends to infinity as ω approaches to ω_1^-, describing the path marked by σ_a. However, after accomplishing the $180°$ phase step, the path approaches again to $(\frac{K_p}{R_f}, 0j) \approx (14, 0j)$ through the path marked as σ_b (see Fig. 4.7). Thereafter, the path tends again to infinity as ω approaches to ω_3^- describing the path marked as σ_c to finally appears $180°$ behind, approaching to $(0, 0j)$ as denoted by the curve σ_d. Similarly to Fig. 4.10, the asymptote for ω_1^- is still $47°$, but a second asymptote is placed now as ω approaches to ω_3^- with an angle of $19°$. Generally, the incorporation of additional resonant controllers lead to the same number of additional asymptotes and $-180°$ turns in the Nyquist plot.

As it can be seen from Fig. 4.11, the incorporation of a second resonant controller has reduced the distance of the Nyquist plot to the critical point $(-1, 0j)$ from 0.91 to 0.71, reducing the stability margin. Consequently, the phase-margin have been also reduced. Generally, the incorporation of additional resonant controllers for compensation of higher order frequencies reduces this stability margin. So that, the gains of the resonant controllers K_n are usually readjusted to obtain a minimum reasonable stability margin. An empirical good estimation for the stability margin can be considered as $\eta \geq 0.4$.

Additionally, a change of plant parameters or gain of the controllers could lead to the path denoted as σ_b in Fig. 4.11 crosses the unitary circle, generating multiple phase- and gain-margins. This confirm that these are not reliable stability indicators and their consideration can lead to erroneous conclusions regarding the stability of the system [60].

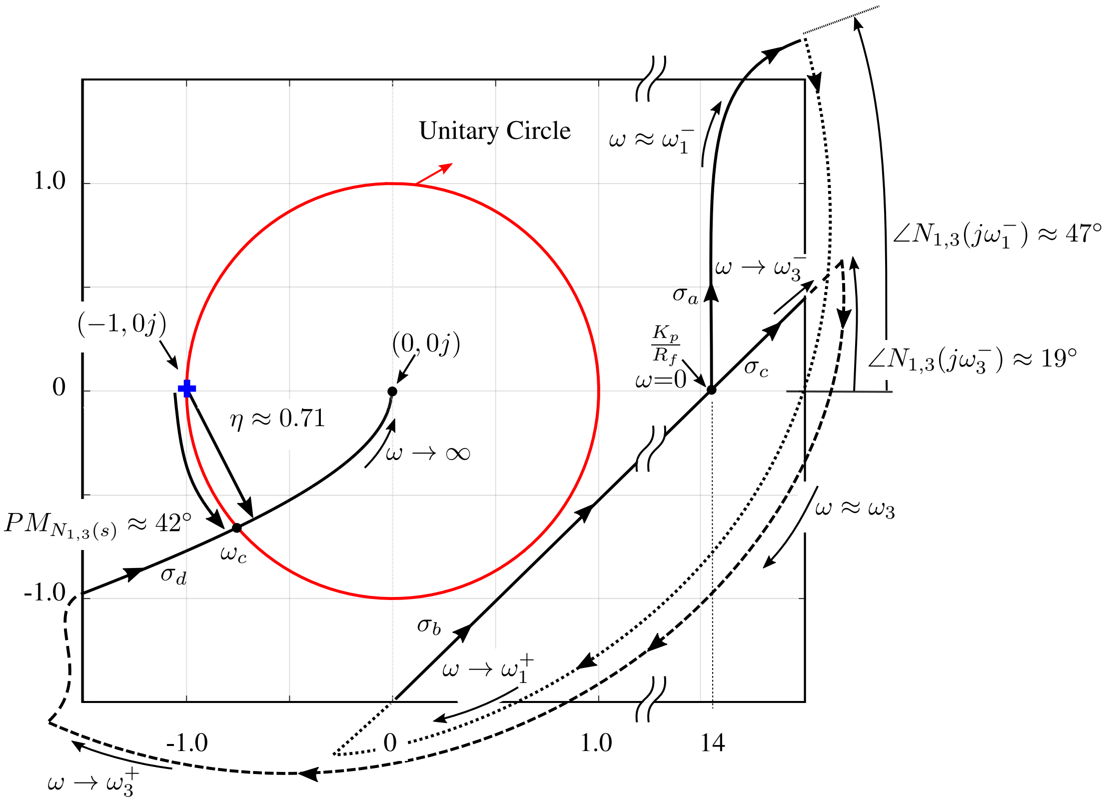

Figure 4.11: Nyquist diagram for the open-loop response $N_{1,3}(s)$. The implemented parameters are: R_f=1Ω, L_f=$3mH$, K_p=13.81, K_1=61407, K_3=61407, ω_1=100πrad/s and ω_3=300πrad/s.

In case that a readjustment of the controller gains K_1 or K_3 of (4.21) is required to increase the stability margin of a system. The new close-loop transient response can be estimated by obtaining the close-loop poles of the system using the equivalent PI controller for the resonant controller set at ω_1, as shown in Fig. 4.4. The modification of the gain parameters for the additional resonant controllers, i.e., K_3 should be selected to maintain them as decoupled as possible, as explained in the previous section. This is also valid for compensation of n different frequencies.

4.2.4 Resonant Controller with angle compensation

As it was presented in (4.7), a compensation angle ϑ_n can be introduced to each resonant controller, to manipulate the angle of the open-loop transfer function around each resonance frequency ω_n. Adjusting this angle, it is possible to shift the the asymptotes of the Nyquist plot when ω approaches to each of the resonance frequencies ω_n. In Fig. 4.10 it was shown that the Nyquist curve tends to infinite asymptotically with an angle of 47°, which also define the angle of the curve when it appears from the bottom of the plot, after rotating $-180°$, influencing the stability margin η. Thereby, using a proportional resonant controller with angle compensation as follows:

$$G^c(s) = K_p + K_1 \frac{s\cos\vartheta_1 - \omega_n \sin\vartheta_1}{s^2+\omega_n^2} \tag{4.22}$$

$$\vartheta_1 = -\angle P_1(s = j\omega_1) \tag{4.23}$$

permits the positioning of the asymptote angle at 90°, increasing the stability margin η. Fig. 4.12a shows the Nyquist diagram for implementation of this controller for a first-order plant. Its open-loop transfer function can be expressed as:

$$N_1^c(s) = P_1(s)G^c(s) = \frac{K_p}{L_f s + R_f} + \frac{K_1(s\cos\vartheta_1 - \omega_1\sin\vartheta_1)}{(L_f s + R_f)(s^2+\omega_1^2)} \tag{4.24}$$

where ϑ_1 has been selected as (4.23). As it can be seen from Fig. 4.12a, the starting point has been marked as κ_0, which from simple inspection of (4.24) can be expressed as:

$$\kappa_0 = \frac{K_p}{R_f} - \frac{K_1\sin\vartheta_1}{R_f\omega_1} \tag{4.25}$$

and must be placed at the right side of the critical point $(-1, 0j)$, which gives an insight for the selection of the values K_p and K_1. Consequently, the curve tends to infinite with an angle of 90° as ω approaches to ω_1^- to then appears from the bottom of the plot and converge to the origin with also an angle of 90°. Thereby, the stability margin η have been increased to 1.0, which produces a more robust controller against uncertainties and mismatches on the plant model and its parameters. However, this increment of stability is accomplished at expenses of an usually overdamped transient response. Note that the open-loop response illustrated in Fig. 4.12a possesses two phase margins, namely $PM^1_{N_1(s)}$ and $PM^2_{N_1(s)}$, which confirm that a typical bode analysis is not a suitable indicator for resonant controllers.

In order to obtain an approximation of the transient response performed by (4.22), its equivalent PI controller can be obtained using (4.11). This, equivalent controller centred at ω_0=0 can be expressed by

$$G^{c-dc}(s) = K_p + \frac{K_1\cos\vartheta_1}{s} \tag{4.26}$$

Using (4.26) and the first order plant $P_1(s)$ of (4.1), the close-loop poles of an equivalent *dc* system can be obtained and an approximated transient response can be estimated.

It is important to remark that the equivalence presented in (4.26) or (4.14) are useful simplifications for approximating the transient response of a resonant controller, when the desired settling time accomplishes (4.18) [153]. However, they do not represent neither the same close-loop nor the same open-loop systems. Although this equivalence can be useful for designing an approximated transient response, the stability analysis of both functions are not equivalent. Hence, a Nyquist stability analysis using the resonant controllers $G(s)$ of (4.6) or $G^c(s)$ of (4.7) must be accomplished for ensure stability.

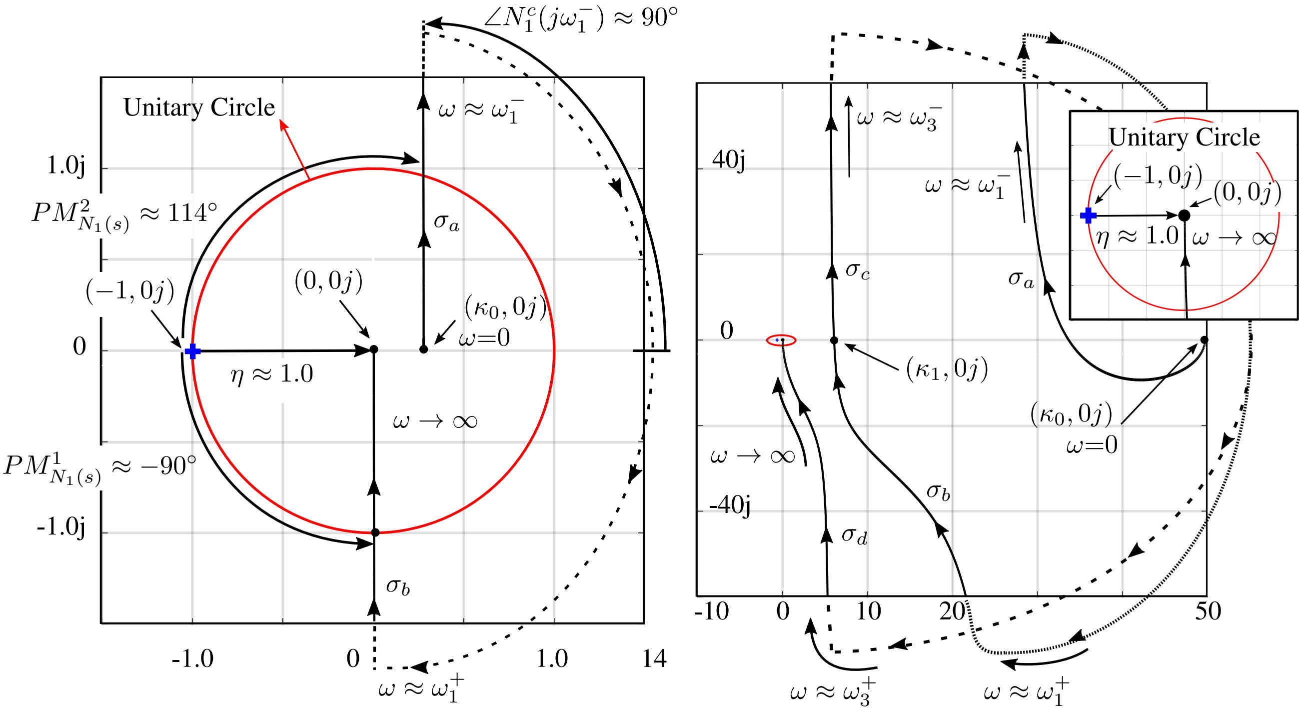

(a) (b)

Figure 4.12: Nyquist diagram for resonant controllers implemented with angle compensation. In (a) Nyquist diagram of (4.24) with parameters: K_p=13.81, K_1=6140.7, ω_1=100πrad/s, $\vartheta_1 \approx -47°$ and in (b) the Nyquist diagram of (4.27) with parameters: K_p=69.08, K_1=6140.7, K_3=6140.7, $\vartheta_1 \approx -47°$, $\vartheta_3 \approx -19°$, ω_1=100πrad/s and ω_3=300πrad/s. For both cases the plant parameters are: R_f=1Ω, L_f=3mH.

Fig. 4.12b shows the Nyquist diagram for compensation of two frequencies. Similarly to (4.24), its open-loop transfer function can be expressed as:

$$N^c_{1,3}(s) = \frac{K_p}{L_f s + R_f} + \frac{K_1(s\cos\vartheta_1 - \omega_1 \sin\vartheta_1)}{(L_f s + R_f)(s^2 + \omega_3^2)} + \frac{K_3(s\cos\vartheta_3 - \omega_3 \sin\vartheta_3)}{(L_f s + R_f)(s^2 + \omega_3^2)} \tag{4.27}$$

From simple inspection of (4.27), the initial point of the Nyquist plot $(\kappa_0, 0j)$ can be expressed as:

$$\kappa_0 = \frac{K_p}{R_f} - \frac{K_1 \sin\vartheta_1}{R_f \omega_1} - \frac{K_3 \sin\vartheta_3}{R_f \omega_3} \tag{4.28}$$

which have to be placed at the right side of the critical point $(-1, 0j)$. Starting from this point, the Nyquist path tends to infinity as ω approaches to ω_1^- with an asymptote of 90° (path σ_a) to then appears 180° behind (path σ_b) and again describes a semicircle rotation as ω approaches to ω_3^- (path σ_c), crossing the real axis again at the point $(\kappa_1, 0j)$. Finally, the path approaches to the point $(0, 0j)$ as ω tends to infinity (path σ_d). The upper right corner of Fig. 4.12b shows a closer view of the origin of the plane. As it can be seen, the path tends to the point $(0, 0j)$ with 90°, leading to a stability margin of η=1.

As it was seen in Fig. 4.12a, in order to avoid the enclosure of the critical point $(-1, 0j)$, the starting point of the Nyquist plot $(\kappa_0, 0j)$ has to accomplish with $\kappa_0 > -1$. However, when multiple resonant controllers are implemented, the Nyquist path crosses the real axis multiple times. This was observed in Fig. 4.12b, where the path also crosses the real axis at the point $(\kappa_1, 0j)$ because of a second compensated frequency. For ensuring stability, all these cross points must be placed at the right side of the critical point $(-1, 0j)$, which force to readjust the proportional gain K_p and the controllers gains K_n when several frequencies are compensated. The general expression for obtaining the initial point $(\kappa_0, 0j)$ for a controller designed for compensation of k different frequencies, is expressed as:

$$\kappa_0 = \frac{K_p}{R_f} - \sum_{n=1}^{k} \frac{K_n \sin \vartheta_n}{R_f \omega_n} \tag{4.29}$$

Thereby, depending of the compensated angles ϑ_n and the number of controllers, the values for K_p and K_n can be selected to ensure $\kappa_0 > -1$.

As demonstrated in Section 4.2.3, a resonant controller without compensation of the phase-shift introduced by the plant can successfully accomplishes a good stability margin and a proper transient response in a first-order plant. Thereby, although its implementation helps for increasing the stability margins, it is not strictly required for ensure stability.

The compensation angle become necessary mainly under the following two situations, which are correspondingly study in the following two section of this chapter:

- When the phase-shift introduced by the plant shifts the asymptotes of the Nyquist plots beyond $-90°$, which would generate a path that enclose the critical point $(-1, 0j)$. This can occurs in a second-order system, where the plant can introduce a phase-shift between 0° to $-180°$.

- Similarly, the Nyquist plot can enclose the critical point $(-1, 0j)$ when the computational time delay, introduced by digital computers in real implementation, represents more than more than $90°$ of a compensated signal. This usually occurs when high-order harmonics are being compensated.

4.3 Multi-Resonant Controllers for Second-Order Systems

Generally, the output voltages $\boldsymbol{v}_{abc_f}$ of a power supply connected to an output LC filter, as presented in Fig. 4.1b, can be regulated based on two different control structures:

- The first structure assumes that the voltage dynamic ($\boldsymbol{v}_{abc_f}$) is much slower that the current dynamic ($\boldsymbol{i}_F$) and divides the problem into two independent control-loops [151]. Thereby, an external voltage control-loop and an internal nested current control-loop are independently designed. In order to ensure proper operation, both controllers have to be decoupled. This usually achieved by tuning the internal nested current controller with a bandwidth around ten times higher than the bandwidth of the outer controller. The use of a nested control structure provides a simple design of the controllers, as the second-order plant is reduced to two first-order plants. Additionally, it also provides the advantage of a direct control over the current $\boldsymbol{i}_F$.

- When high-order voltage harmonics has to be compensated, the internal current controller of a nested control structure must perform a very fast dynamic response to maintain the internal and external control loops decoupled. This is usually not achievable, because the bandwidth of the internal current controller is physically limited in real implementation by the sampling time of the digital controllers and the switching frequency of the power converter [148, 154]. Additionally, when the dynamics of voltage and currents are similar, the nested controller can not be considerer decoupled, generating coupling effect and a poor performance. This issues can be solve by using a direct voltage control-loop, as presented in Fig. 4.1b. This control structure has gained attraction in aerospace applications, where fundamental frequencies between $400Hz$ to $800Hz$ has to be controlled and high-order harmonics have to be compensated [154, 155]. Thereby, the direct voltage control-loop has been selected for analysis in this chapter and will be later implemented in an aerospace application in Chapter 6.

The closed-loop control scheme presented in Fig. 4.3 can be used for representing the close-loop voltage control for the UPS presented in Fig. 4.1b. Consequently, from Fig. 4.3, $P(s)$ is expressed as $P_2(s)$ of (4.2), $Y(s)=V_f(s)$ and $Y^*(s)=V_f^*(s)$. Where $V_f(s)$ and $V_f^*(s)$ are the frequency domain representation of one phase of the controlled and reference output voltages, i.e. $\boldsymbol{v}_{\alpha\beta\gamma}$ and $\boldsymbol{v}_{\alpha\beta\gamma}^{*UPS}$ of Fig. 4.1b.

Fig. 4.13 shows the bode diagram for the second-order plant $P_2(s)$ designed with a resonance peak at approximately $2400Hz$. Unlike the bode diagram of the first-order plant presented in Fig. 4.7, a second-order plant generates an abrupt magnitude and phase change at f_{res}, which leads to a system that can easily become unstable, complicating the tuning of the multiple resonant controllers. Therefore, in order obtain a controller that provides larger stability margin, the resonant controller of (4.4), using $K_p=0$, arises as the most suitable alternative for controlling a second-order system. Hence, a resonant controller for controlling a fundamental voltage of $400Hz$ and compensation of a 5^{th} harmonic component of $2000Hz$ can be expressed as:

$$R^c(s)=R_1^c(s)+R_5^c(s)=K_1\frac{s\cos\vartheta_1-\omega_1\sin\vartheta_1}{s^2+\omega_1^2}+K_5\frac{s\cos\vartheta_5-\omega_5\sin\vartheta_5}{s^2+\omega_5^2} \tag{4.30}$$

$$\vartheta_1=-\angle P_2(j\omega_1) \tag{4.31}$$

$$\vartheta_5=-\angle P_2(j\omega_5) \tag{4.32}$$

The bode diagram for the open-loop transfer function composed by this resonant controller and the second-order filter $P_2(s)$ is also illustrated in Fig. 4.13. As it can be seen, its phase response is equal to $\pm 90°$ at each resonance frequency ω_1 and ω_5. This is because of the compensation angles $\vartheta_1\approx 1.5°$ and $\vartheta\approx 22°$ introduced in (4.30).

Hence, in order to obtain the stability margins of the close-loop system, a Nyquist analysis of the open-loop transfer function $P_2(s)R^c(s)$ is required. Let us first consider the implementation of only one resonant controller, namely only $R_1^c(s)$ of (4.30). Fig. 4.14a shows the Nyquist

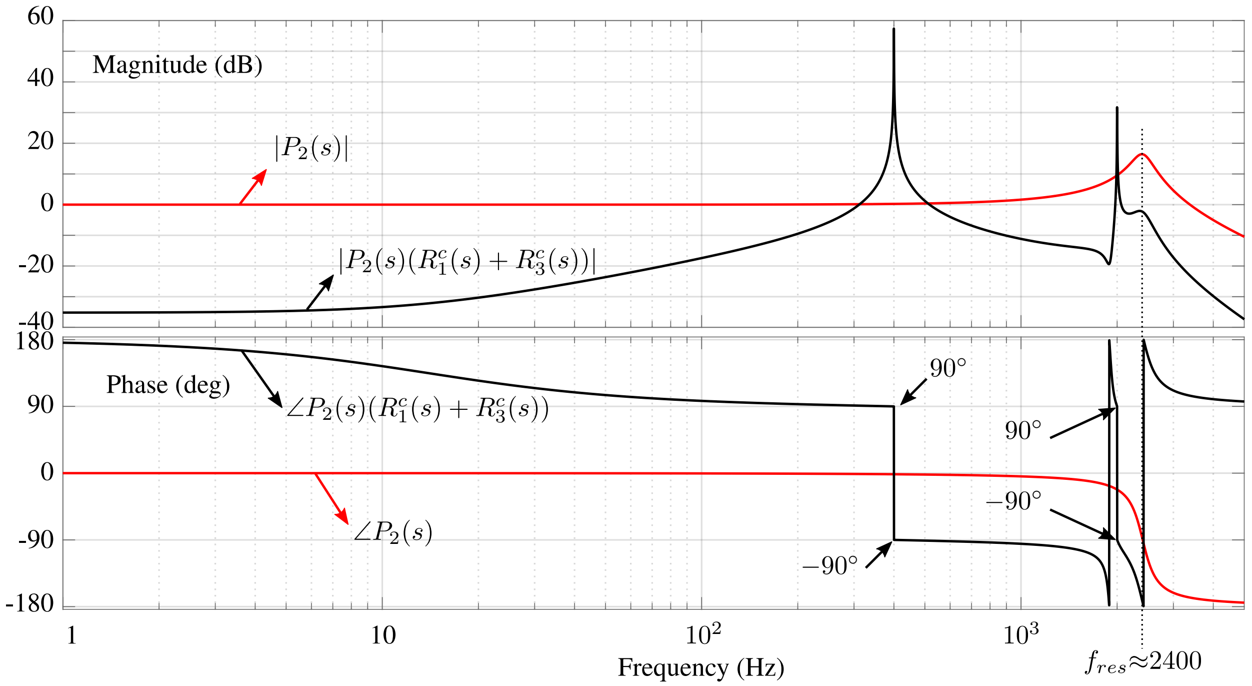

Figure 4.13: Bode diagram for the second-order plant $P_2(s)$ of (4.2) and the resonant controller $R^c(s){=}R_1^c(s)+R_5^c(s)$ of (4.30). The implemented parameters are: $L_f{=}219\mu H$, $R_f{=}0.5\Omega$, $C_f{=}20\mu F$, $\omega_1{=}800\pi$rad/s, $\omega_5{=}4000\pi$rad/s $K_1{=}1250$, $K_5{=}150$, $\vartheta_1 \approx 1.5°$, $\vartheta_5 \approx 22°$.

diagram of the open-loop function $R_1^c(s)P_2(s)$ for three different values of K_1. As expected, and zoomed at the upper left corner of Fig. 4.14a, the diagram starts at κ_0 for each of the different values of K_1. This initial point can be calculated in a general form as $(P_2(0j)R^c(0j))$, i.e.,

$$\kappa_0{=}-\sum_{n=1}^{k}\frac{K_n\sin\vartheta_n}{\omega_n} \tag{4.33}$$

Afterwards, the path tends to infinite with an angle of $90°$ (path σ_a), rotating $-180°$ to appear from the bottom of plot (path σ_b). However, instead of directly approaching to zero, as presented in Fig. 4.12a for a first-order filter, it performs a curve towards the critical point $(-1,0j)$. This curve is product of the damped resonance of the filter $P_2(s)$ at the frequency f_{res} (see Fig. 4.13). Therefore, in order to avoid an unstable close-loop operation, i.e., avoid the enclosure of the critical point $(-1,0j)$, the gain of the controller K_1 has to be limited. In Fig. 4.14a, the red line represents the Nyquist plot for a controller which gain produces an unstable operation, enclosing the point $(-1,0j)$. Thenceforth, the Nyquist path approaches to the origin $(0,0j)$, through the path denoted as σ_b.

Consequently, Fig. 4.14b shows the Nyquist diagram for the complete open-loop response $P_2(s)R^c(s)$ of (4.30), with compensation of the fundamental voltage of $400Hz$ and the 5^{th} voltage harmonic of $2000Hz$. Two different values of K_5 have been implemented to observe its influence on the Nyquist path. As usual, the plot starts at κ_0 for $\omega{=}0$ (κ_0^1 or κ_0^2 for each value of K_5), calculated as (4.33). Thereafter, the path describes the trajectory denoted as σ_a, approaching to infinity with an angle of $90°$ as ω approaches to ω_1^-. Consequently, the trajectory

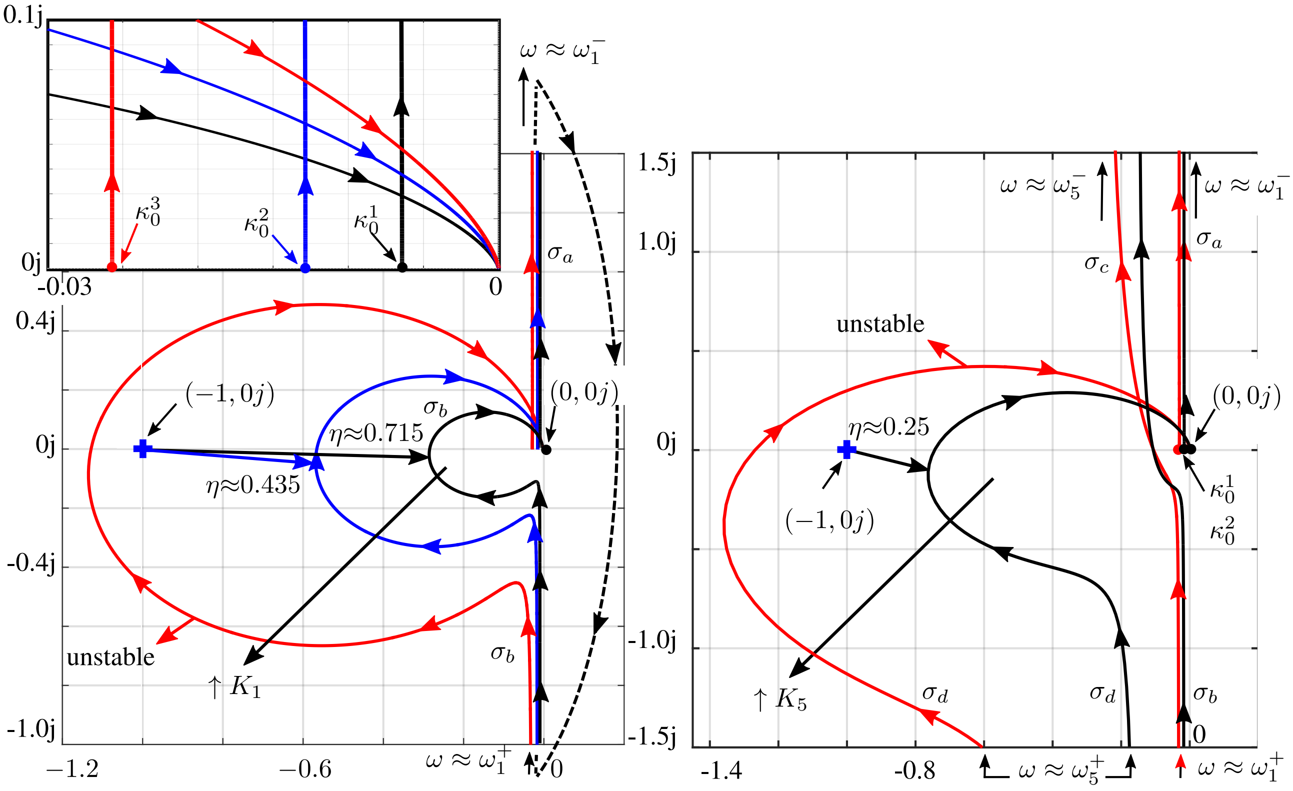

(a) (b)

Figure 4.14: Nyquist diagram for (a) $P_2(s)R_1^c(s)$ with K_1=$\{625, 1250, 2500\}$ and starting points in increasing order: κ_0^1= $-$ 0.0064, κ_0^2= $-$ 0.0129, κ_0^3= $-$ 0.0257 and for (b) $P_2(s)(R_1^c(s) + R_5^c(s))$ with K_1=1250, K_5=$\{150, 600\}$, $\vartheta_5 \approx 22°$ and starting points in increasing order: κ_0^1= $-$ 0.0171, κ_0^2= $-$ 0.0309. For both plots, L_f=219μH, R_f=0.5Ω, C_f=20μF, ω_1=800πrad/s, ω_5=4000πrad/s and $\vartheta_1 \approx 1.5°$.

rotates $-180°$ and appears from the bottom of the plot, denoted as σ_b. Then, it crosses the real axis and tends again to infinity with an angle of $90°$ (see Fig. 4.13) as ω approaches to ω_5^-, following the path described by σ_c. Thereafter, it appears again from the bottom of the plot, describing the characteristic curve produced by the resonance peak of the second-order filter, denoted as σ_d. Finally the path converge to the origin of the plot $(0, 0j)$. As it can be observed, the gain K_5 of the resonant controller $R_5^c(s)$ has to be limited to avoid enclosure of the critical point $(-1, 0j)$.

Note that in case of compensation of frequencies beyond f_{res}, the compensated angle dramatically increases. For instance, in case of compensation of component of frequency ω_7=$7\omega_1$, the required compensating angle is $\vartheta_7 \approx 153°$. Therefore, the compensation angle for this frequency become mandatory to accomplish an stable close-loop operation.

The value of K_1 usually determines the transient response of the system, because it defines the performance of the fundamental waveform. Thereby, as no proportional term is used, K_1 is usually selected as large as possible to obtain a fast transient response, but it has to be limited to avoid instability operation and to leave enough stability margin for incorporation of the the additional controllers, which gains parameters, K_5 in this example, pushes the Nyquist diagram to unstable operation.

The proximity of the Nyquist path to the critical point $(-1, 0j)$ in Fig. 4.14b is directly proportional to the magnitude of the resonant peak of $P_2(s)$ at f_{res}. Thereby, the natural damping resistance R_f present in the inductance L_f of $P_2(s)$ is very important for achieving an stable operation and consequently the proportional term K_p is usually not implemented for controlling second-order systems by using resonant controllers, as this term enlarge the path described by σ_b of Fig. 4.14a or σ_d of Fig. 4.14b, leading easily to instability. When the value of R_f is not large enough to ensure a proper stability margin, a virtual resistance R_f can be employed to enlarge the stability margins. This is known as virtual resistor or active damping method [99, 156, 157]. However, it produces a comparable effect to the reduction of the gain values of the resonant controllers K_n.

Eliminating the proportional term K_p permits the design of an stable and more robust close-loop system, but leads to an slower overdamped response, typical of pure integral controllers. However, this is not critical issue, as the gain of each resonant controller can be usually tuned high enough for achieving an acceptable transient performance, accomplishing with power quality standards. This has been proven in Chapter 6 through the implementation of a Ground Power Unit (GPU) for aerospace applications accomplishing with the military standard: *MIL-STD-704F Aircraft Electric Power Characteristics* [10].

The Fig. 4.15 shows the transient response for the stable controller designed in Fig. 4.14b. As it can be seen, the transient response for the fundamental frequency reference step has an small coupling effect with the 5^{th} harmonic component. However, it is rapidly eliminated after approximately one cycle ($2.5ms$). Thereafter, at time $10ms$ a second step reference for incorporation of 10% of 5^{th} harmonic component is performed. As it can be seen, after the transient response, the tracking error is eliminated after one to two cycles ($5ms$).

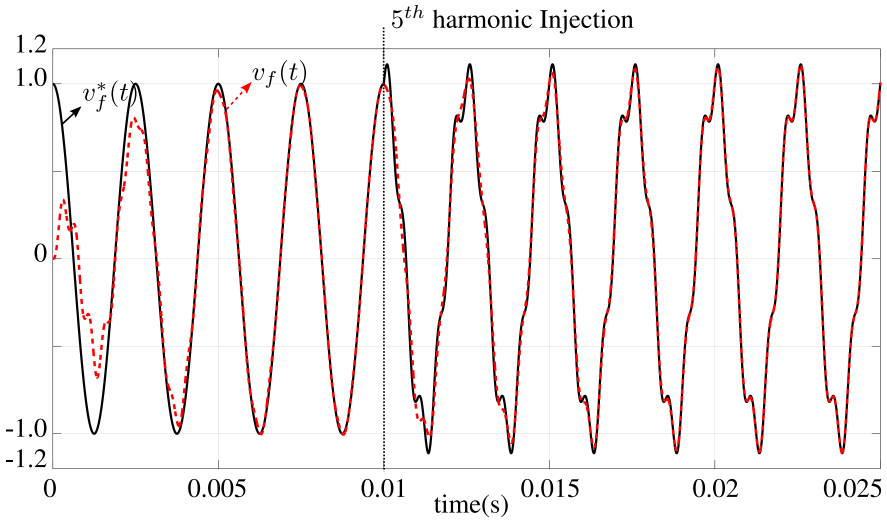

Figure 4.15: Transient response of a controlled voltage $v_f(t)$ for a second-order plant $P_2(s)$ and a resonant controller $R^c(s)$=$R^c_1(s)$ + $R^c_5(s)$ for compensation of fundamental $400Hz$ and fifth harmonic of $2000Hz$. The initial reference signal is equal to $v_f^*(t)$= $\cos(800\pi t)$ and at t=$10ms$ it become $v_f^*(t)$= $\cos(800\pi t) + 0.1\cos(4000\pi t)$. The parameters for the plant are: L_f=$219\mu H$, R_f=0.5Ω, C_f=$20\mu F$. The parameters for the controller are: ω_1=800πrad/s, K_1=1250, $\vartheta_1 \approx 1.5°$, ω_5=4000πrad/s, K_5=150, $\vartheta_5 \approx 22°$.

4.4 Implementation of Resonant Controllers in Digital Systems

In order to implement a controller in a digital system, its discretization and stability analysis in discrete-time is required. Fig. 4.16 shows the typical single-loop control structure implemented for controlling the discrete current or voltage variable represented as $Y(k)$. The discrete form of the n^{th} resonant controller with angle compensation presented in (4.4) are denoted as $R_n^c(z)$ for $n \in \{1, 2, .., k\}$. A power converter, used as actuator, is represented as constant gain and the computational calculation time required for computing the control algorithm in a digital system is represented as a single discrete-time delay T_s. A discrete-time representation for the continuous-time plant $P(s)$ of Fig. 4.3 can be obtained by its *Hold Equivalent* model $P(z)$.

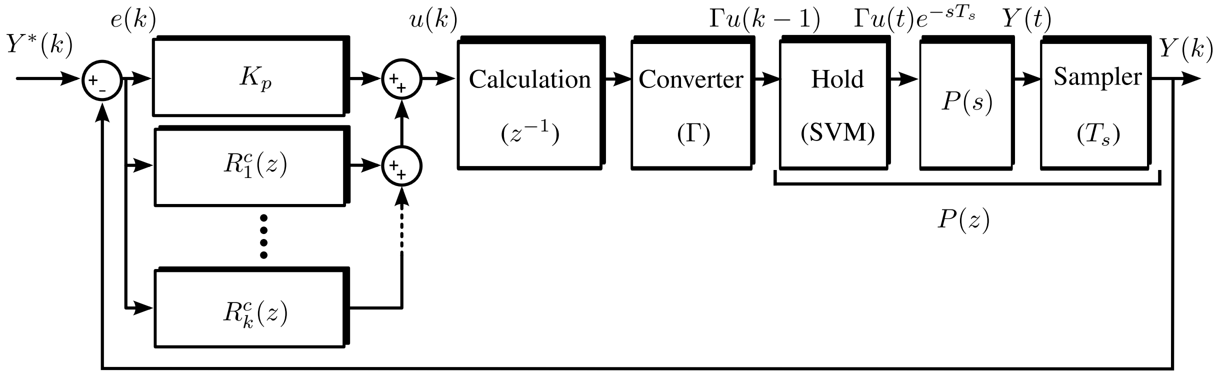

Figure 4.16: Discrete-time single-loop control structure for implementation of resonant controllers. $Y^*(k)$ and $Y(k)$ represents the reference and controlled discrete-time variables. $R_n^c(z)$ for $n = \{1, 2, .., k\}$ represent a resonant controller with delay compensation for compensation of a signal with frequency ω_n in discrete-time.

4.4.1 Summary of Discretization Methods

Several different discretization methods can be used for transforming a continuous-time system $X(s)$ into its equivalent discrete-time system $X(z)$. They can be summarized as follows [150, 151, 158]:

- *Numerical Integral Approximation:* This methods use a numerical approximation of the continuous derivative operator $s=\frac{d}{dt}$, for substituting it in $X(s)$ and obtaining the equivalent discrete-time system $X(z)$. The most common approximations are: Backward-Euler rule (4.34), Forward-Euler rule (4.35), Tustin or Trapezoidal rule (4.36) and Tustin with prewarping (4.37). Unlike Backward- or Forward-Euler rule, the Tustin approximation is the only that exactly maps the stability region of the continuous-time domain (left side of the *s-plane*) into the stability region of the discrete-time domain (unitary circumference) [150, 158]. For this reason, this is also known as bilinear transformation. Although Tustin approximation provides the advantage of an equivalent stability region for both, continuous- and discrete-time systems, it maps the complete continuous-time imaginary axis ($s=j\omega$) only into 0 to 2π, which leads to large approximation error for high-order frequencies. In order to overcome this problem, an extended method, namely Tustin with prewarping of (4.37), can be implemented. This method centered the approximation around ω_0. Thereby, it ensures that the continuous- and discrete-time systems behave approximately similar around this frequency (at ω_0 both system are equivalent).

$$X^{be}(z)= X(s)|_{s=\frac{z-1}{T_s}} \tag{4.34}$$

$$X^{fe}(z)= X(s)|_{s=\frac{z-1}{zT_s}} \tag{4.35}$$

$$X^{t}(z)= X(s)|_{s=\frac{2(z-1)}{T_s(z+1)}} \tag{4.36}$$

$$X^{tpw}(z)= X(s)|_{s=\frac{\omega_0(z-1)}{tan(\frac{\omega_0 T_s}{2})(z+1)}} \tag{4.37}$$

- *Hold Approximation:* This method has been presented in the diagram of Fig. 4.16. Thereby, a continuous time system $X(s)$, embedded into a discrete-time control structure, is preceded by a hold circuit which transform the discrete input signal into a continuous signal for $X(s)$. Thereafter, the output of $X(s)$ is sampled at T_s rate to be converted again in a discrete-time signal. This complete system represent the equivalent discrete-time function $X(z)$. The precision of the discrete representation depends on the order of hold circuit. Thereby, the most commonly implemented hold circuits are the zero-order hold (ZOH) and the firs-order hold (FOH) approximations. These approximations are described in (4.38) and (4.39) respectively, where $\mathcal{Z}$ represents the z-transform.

$$X^{zoh}(z)=\frac{(z-1)}{z}\mathcal{Z}\left\{\mathcal{L}^{-1}\left\{\frac{X(s)}{s}\right\}\right\} \tag{4.38}$$

$$X^{foh}(z)=\frac{(z-1)^2}{zT_s}\mathcal{Z}\left\{\mathcal{L}^{-1}\left\{\frac{X(s)}{s^2}\right\}\right\} \tag{4.39}$$

- *Zero-Pole matching Approximation:* By using the discrete *z-transform*, a continuous-time pole s_0 is related to a discrete-time pole z_0 as $z_0{=}e^{s_0 T_s}$, where T_s represents the implemented sampling time. Using this equivalence, the zeros of the continuous time system can be also mapped to the discrete-time system to obtain its equivalent discrete representation [150, 151, 158].

- *Other Approximations:* The impulse invariant approximation is also an alternative for discretization of continuous-time systems. In this approximation, the impulse response of the continuous-time system is obtained and then sampled to obtain its equivalent discrete impulse response. Thereby, a discrete-time representation of $X(s)$ is obtained as (4.40). Another alternative of discrete representation is the *delta-transform* presented in (4.41). This transformation uses an equivalent variable γ to represent the discrete-time equivalent model. This model has the advantage that is coherent with the continuous transfer function $X(s)$. Thus, a delta transfer function expressed as function of T_s approaches to its equivalent transfer function in the s-domain when T_s approaches to zero [151].

$$X^{imp}(z)=\mathcal{Z}\left\{\mathcal{L}^{-1}\left\{X(s)\right\}\right\} \tag{4.40}$$

$$X_{\delta}(\gamma)=T_s\; X(z)|_{z=T_s\gamma+1} \tag{4.41}$$

4.4.2 Discretization of First- and Second-Order Systems

In order to design a resonant controller in the z-domain, a discrete time representation of the controlled plant must be obtained. The control structure presented in Fig. 4.16 represents an hybrid system [151], where a discrete controller provides a reference actuation signal to a power converter, which synthesize this signal to finally provide it to a continuous plant $P(s)$. Thereby, it results convenient to discretize $P(s)$ by using hold approximations. Usually, input of the equivalent discrete time plant $P(z)$, $\Gamma u(k-1)$, is maintained as a constant value during each sampling period T_s and a PWM or SVM method is used to approximate this constant value $(u(k))$ during one period T_s. Therefore, the hold circuit of Fig. 4.16 is usually approximated by a zero-order hold (ZOH) [159]. Thereby, using (4.38) in the first order plant of (4.1), its equivalent discrete-time transfer function can be obtained by

$$P_1^{zoh}(z)=\frac{1-e^{-R_fT_s/L_f}}{R_f(z-e^{-R_fT_s/L_f})} \tag{4.42}$$

The similarity between the continuous-time plant and the discrete-time plant depends on the selected hold approximation. Thereby, an inappropriate selection of the hold method can negatively affect the discrete-time stability analysis of the close-loop system of Fig. 4.16. Fig. 4.18a illustrates the bode response for the first-order continuous-time plant $P_1(s)$ and its discretization by using zero- and first-order hold methods. These discrete-time equivalences are represented as $P_1^{foh}(z)$ and $P_1^{zoh}(z)$ respectively. As it can be seen, for high order frequencies, there is an important mismatch between the continuous-time plant $P_1(s)$ and its ZOH discretization $P_1^{zoh}(z)$. This difference is also illustrated in Fig. 4.18b in a Nyquist diagram. Thereby, unlike $P_1(s)$, that approaches to $(0, 0j)$ as ω tends to infinity, $P_1^{zoh}(z)$ and $P_1^{foh}(z)$ approaches to the negative and positive real axis respectively as ω tend to the Nyquist frequency $\omega_{nyq}=\pi f_s$.

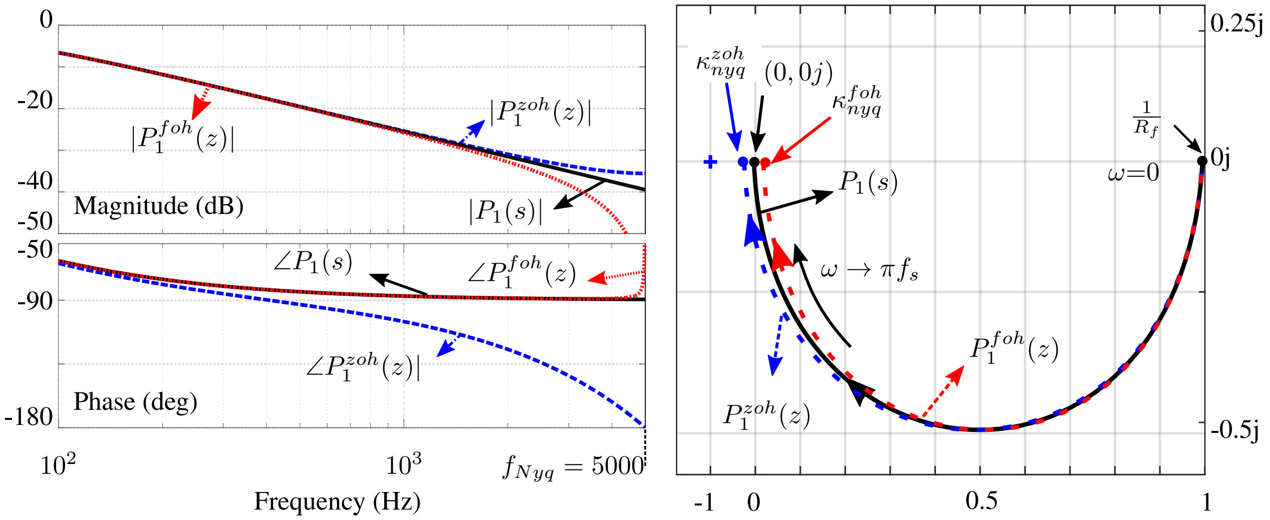

(a) (b)

Figure 4.17: (a) Bode and (b) Nyquist diagram for the continuous-time first-order plant $P_1(s)$ and its ZOH ($P_1^{zoh}(z)$) and FOH ($P_1^{foh}(z)$) equivalent discrete-time representations. Sampling time T_s=100μs (f_s=10kHz) and filter parameters are R_f=1Ω, L_f=3mH.

Using the ZOH discretization method of (4.38) to the second-order plant $P_2(s)$ of (4.2), its discrete form is given by

$$P_2^{zoh}(z)=1-\frac{z-1}{\sqrt{1-\xi^2}}\left(\frac{ze^{-\xi\omega_{nat}T_s}\sqrt{1-\xi^2}\sin\left(T_s\omega_{nat}\sqrt{1-\xi^2}-arcos(\xi)\right)}{z^2-2ze^{-\xi\omega_{nat}T_s}\cos\left(T_s\omega_{nat}\sqrt{1-\xi^2}\right)+e^{-2\xi\omega_{nat}T_s}}\right) \tag{4.43}$$

$$\omega_{nat}=\frac{1}{\sqrt{L_fC_f}} \tag{4.44}$$

$$\xi=\frac{R_f\sqrt{L_fC_f}}{2L_f} \tag{4.45}$$

where R_f, L_f and C_f are the parameters of the second-order filter. In order to compare the effect of the discretization on a second-order plant, Fig. 4.18a shows the bode diagram for discretization of the second order filter $P_2(s)$ of (4.2) by three different methods. As it can be seen, the FOH discretization ($P_2^{foh}(z)$) provides the best phase approximation, but it changes the magnitude response at ω_{res}. On the other hand, the ZOH discretization method produces the larger mismatch with the continuous-time plant, specially on the phase response. Additionally, the Tustin with prewarping discretization ($P_2^{tpw}(z)$) has been implemented to show that it provides the best approximation. This is because it approximates the function $P_2(s)$ around the prewarping frequency ω_0, set as the damped resonance frequency ω_{res} for this plant. This is confirmed in the Nyquist diagram presented in Fig. 4.18b, where the ZOH approximation even crosses the negative real axis, enclosing the critical instability point $(-1, 0j)$. Thus, it is possible that implementing an stable close-loop controller designed in the s-domain does not result in a stable operation in discrete-time real implementation and, so that, a discrete-time stability analysis is required previous the real implementation, specially when high-order frequencies, or frequencies close to the damped resonance ω_{res}, are being compensated.

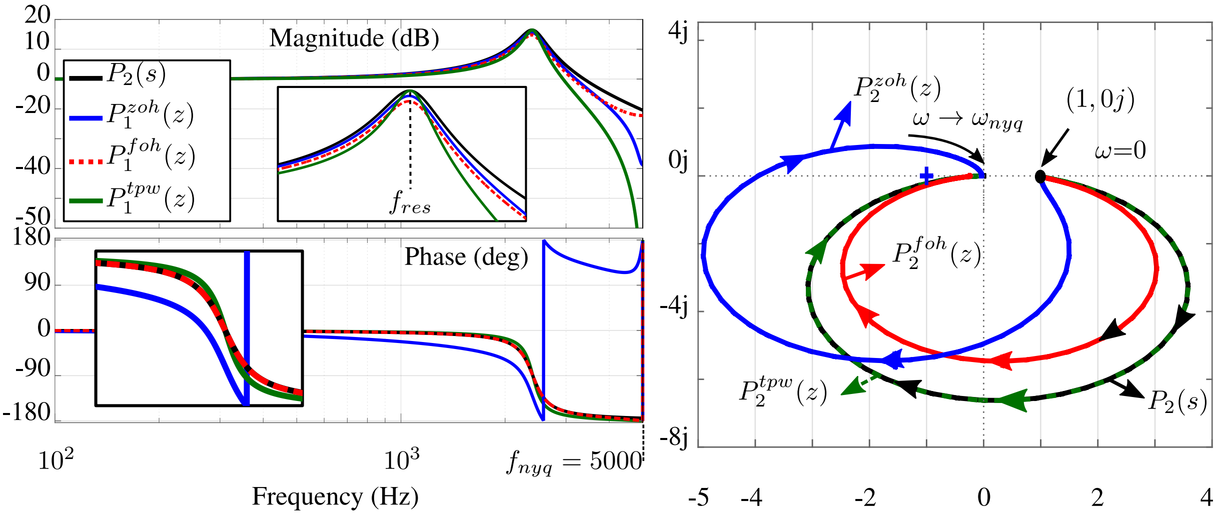

(a) (b)

Figure 4.18: (a) Bode and (b) Nyquist diagram for the second-order plant $P_2(s)$ and its ZOH ($P_2^{zoh}(z)$), FOH ($P_2^{foh}(z)$) and Tustin with prewarping ($P_2^{tpw}(z)$) with ω_0=Ω_{res} discretization. T_s=100μs (f_s=10kHz), R_f=0.5ω, L_f=219μH and C_f=20μF, ω_{res}=4800πrad/s.

4.4.3 Discretization of Resonant Controllers

In order to implement a resonant controller $R_n(s)$ of (4.3) or $R_n^c(s)$ of (4.4) in a digital system, its discretization has to fulfil two important requirements:

- The discretization method must not shift the resonant frequency ω_n of each resonant controller.
- In order to ensure zero steady-state error, the discretization method must maintain an infinite gain at the resonant frequency ω_n.

Among the methods presented in (4.34) to (4.41), the only methods that accomplish these restrictions are: ZOH, FOH, zero-pole matching, impulse invariant and Tustin with prewarping approximation [60]. Additionally, the methods Tustin with prewarping and FOH provide the best approximation overall the frequency spectrum, as it was illustrated in Fig. 4.18, and are specially suitable as discretization methods for resonant controllers [160].

Thereby, substituting the resonant controller $R(s)$ of (4.3) into the Tustin and FOH discretization methods of (4.37) and (4.39), the discrete representation of $R(s)$ is obtained and given by [149, 158, 161]:

$$R^{foh}(z) = \sum_{n=1}^{k} R_n^{foh}(z) = \sum_{n=1}^{k} K_n \frac{(1-\cos(\omega_n T_s))(1-z^{-2})}{\omega_n^2 T_s(1-2z^{-1}\cos(\omega_n T_s)+z^{-2})} \tag{4.46}$$

$$R^{tpw}(z) = \sum_{n=1}^{k} R_n^{tpw}(z) = \sum_{n=1}^{k} K_n \frac{\sin(\omega_n T_s)(1-z^{-2})}{2\omega_n(1-2z^{-1}\cos(\omega_n T_s)+z^{-2})} \tag{4.47}$$

where T_s is the discretization sampling time, ω_n is the resonance frequency of the n^{th} resonant controller, $R^{foh}(z)$ and $R^{tpw}(z)$ represent the discretized resonant controller implemented with FOH and Tusting with prewarping respectively. The prewarping frequency of $R^{tpw}(z)$ has been selected as the resonance frequency of each resonant controller ω_n.

Similarly, substituting the resonant controller with angle compensation $R^c(s)$ of (4.4) into the Tustin with prewarping and FOH discretization methods of (4.37) and (4.39), the discrete representation of $R^c(s)$ is obtained and given by [149, 158, 161] [1]:

$$\begin{aligned} R^{c-foh}(z) = \sum_{n=1}^{k} K_n & \frac{cos(\omega_n D_n T_s)(1-z^{-2})(1-cos(\omega_n T_s)))}{\omega_n^2 T_s(1-2z^{-1}cos(\omega_n T_s)+z^{-2})} \\ & - \frac{sin(\omega_n D_n T_s)\left[\omega_n T_s - sin(\omega_n T_s) + z^{-1}(2sin(\omega_n T_s) - 2\omega_n T_s cos(\omega_n T_s)) + z^{-2}(\omega_n T_s - sin(\omega_n T_s))\right]}{\omega_n^2 T_s(1-2z^{-1}cos(\omega_n T_s)+z^{-2})} \end{aligned} \tag{4.48}$$

$$R^{c-tpw}(z) = \sum_{n=1}^{k} K_n \frac{\frac{1}{2}(1-z^{-2})\cos(\omega_n D_n T_s)\sin(\omega_n T_s) - (1+2z^{-1}+z^{-2})\sin(\omega_n D_n T_s)\sin^2(\frac{\omega_n T_s}{2})}{\omega_n(1-2z^{-1}\cos(\omega_n T_s)+z^{-2})}, \tag{4.49}$$

---

[1] Note that the equation provided in [149, 161] for $R^{c-foh}(z)$ is not correct. The correct equation is presented in this section.

where $R^{c-foh}(z)$ and $R^{c-tpw}(z)$ represent the discretized resonant controller with delay compensation implemented with FOH and Tusting with prewarping respectively, T_s is the discretization sampling time and ω_n is the resonance frequency of the n^{th} resonant controller. The prewarping frequency of $R^{c-tpw}(z)$ has been selected as the resonance frequency of each resonant controller ω_n. The term D_n represents the number of samples for compensating the phase-shift introduced by the first- or second-order plant. Equivalently to ϑ_n of (4.4), D_n for the n^{th} resonant controller is given by:

$$D_n = \frac{-\angle P^{zoh}_{1,2}(z_n = e^{j\omega_n T_s})rad}{T_s \omega_n} \tag{4.50}$$

where $P^{zoh}_{1,2}(z_n = e^{j\omega_n T_s})$ represents the ZOH discrete-time representation of a first- or second-order plant evaluated at the resonance frequency z_n. Note that substituting $D_n=0$ in (4.48) and (4.49) leads to the expressions (4.46) and (4.47).

4.4.4 Computational Delay Compensation

Although the computational delay $z^{-1} = e^{-j\omega_n T_s}$, described in Fig. 4.16, is usually negligible for controlling signals of fundamental frequency $\omega_1 \leq 100Hz$ at standard sampling frequencies $f_s \geq 5kHz$. This delay becomes an important portion of the period of a compensated signal of frequency ω_n, when resonant controllers are implemented for compensation of high-order harmonics. Hence, for instance, a single delay T_s, at a sampling rate $f_s = 16.8kHz$, produces an equivalent phase-shift of $\vartheta^d_1 = 8.5°$ for compensation of a signal of fundamental frequency $\omega_1 = 400Hz$. Likewise, it represents a phase-shift of $\vartheta^d_{11} = 94°$ for compensation of a 11^{th} harmonic component.

In a Nyquist diagram, the phase-shift ϑ^d_n, generated by the computational delay to the n^{th} resonant controller $R^c_n(s)$, shifts the asymptote produced by the n^{th} resonance ω_n in an angle of ϑ^d_n. This may lead to a Nyquist path that encloses the point $(-1, 0j)$, generating an unstable close-loop system [148, 162]. In order to overcome this problem, the computational delay has to be compensated. Thus, to generate asymptotes at ±90° for each resonant frequency ω_n, the compensation angle ϑ_n of each controller $R^c_n(s)$ of (4.4) must be calculated as:

$$\vartheta_n = \vartheta^P_n + \vartheta^d_n \tag{4.51}$$

$$\vartheta^P_n = -\angle P_{1,2}(s = j\omega_n) \tag{4.52}$$

$$\vartheta^d_n = \omega_n T_s \tag{4.53}$$

where ϑ^P_n represents the angle for compensation of the phase-shift produced by the plant and ϑ^d_n is the compensation angle for a unitary computational delay T_s. Similarly, for a discrete resonant controller $R^{c-foh}(z)$ of (4.48) or $R^{c-tpw}(z)$ of (4.49), the compensation is achieved just by increasing D_n in one unit. Hence, the compensation term D_n is expressed as:

$$D_n = D^P_n + D^d_n = \frac{-\angle P^{zoh}_{1,2}(z_n = e^{j\omega_n T_s})rad}{T_s \omega_n} + 1 \tag{4.54}$$

where D^P_n is the compensation of the phase-shift produced by the discrete-time first- or second-order plant $P^{zoh}_{1,2}$ and D^d_n represents the compensation of the computational delay T_s. The discrete-time delay compensation D_n^d can be also selected as two sampling units in case that the digital hardware implementation introduces an additional delay [126].

4.4.5 Multi-Resonant Controller design in *z*-domain

In order to visualize the difference between a continuous-time and discrete-time controller design, Fig. 4.19a shows the open-loop Nyquist Diagram for a continuous-time and a discrete-time resonant controller for compensation of a fundamental $400Hz$ component and a 11^{th} harmonic signal of $4400Hz$ implemented in a second-order plant. Both resonant controllers, $R^c(s)$ of (4.4) and $R^{c-foh}(z)$ of (4.48), have been designed for compensation of the phase-shift introduced by the second-order plant $P_2(s)$ of (4.2) and $P_2^{zoh}(z)$ of (4.43) respectively and for compensation of the computational delay T_s.

Similarly to the Nyquist diagram presented in Fig. 4.14b , the Nyquist plot for the open-loop function $R^c(s)P_2(s)$ of Fig. 4.19a starts at κ_0, while for $R^{c-foh}(z)P_2^{zoh}(z)$ it starts at κ_0^{foh}, which can be obtained by simple inspection of (4.48) replacing $z{=}1$. Thereafter, both responses tends to infinity with an asymptote of 90° as ω approaches to ω_1^- (path denoted by σ_a), compensating the phase-shift introduced by the plant and the computational delay. Thenceforth, the Nyquist path appears from the bottom of the plot and describe the typical curve that approaches to the instability point $(-1, 0j)$ (path denoted by σ_b) produced by the damped resonance of the second order plant. Afterwards, both paths describe a trajectory towards the origin $(0, 0j)$, but before arriving to it they tends again to infinity as the frequency ω approaches to the second controlled frequency, i.e. ω_{11}. This path is marked as σ_c. Finally, the path appears again from the bottom of the plot to approach to the origin $(0, 0j)$ as ω tends to infinity for the continuous-time response and as ω tends to the Nyquist frequency πf_s for the discrete time equivalent response.

Fig. 4.19b shows the effect of eliminating the computational delay compensation for the resonant controller designed for the 11^{th} harmonic, i.e. $\vartheta_{11}^d{=}0$ and $D_{11}^d{=}0$ for the continuous- and discrete-time controller respectively. As expected, for frequencies $\omega < \omega_{11}$, the Nyquist diagram describe the same path as illustrated previously in Fig. 4.19a. However, as ω approaches to ω_{11}^-, the asymptote is not placed at 90° any more and, as discussed above, it has been shifted in 94° generating a path that enclose the critical point $(-1, 0j)$ and leading to an unstable close-loop system. Therefore, the delay compensation become neccesary in this case and must be implemented to avoid unstable operation.

It should be noticed that the selection of the compensation angles for placing the asymptotes at 90° in the Nyquist diagram does not represent a theoretical optimum value, which maximize stability margin η [60]. However, it is a very simple rule which provides satisfactory results for first- and second-order systems. Furthermore, due to the natural mismatch between the ideal model used for the controller design and the real model used in an experimental rig, some fine-tuning is usually necessary to exactly fulfil with the design specifications. Therefore, the presented method of setting the asymptotes to 90° is considered as a more simple and effective solution and will be implemented throughout this work.

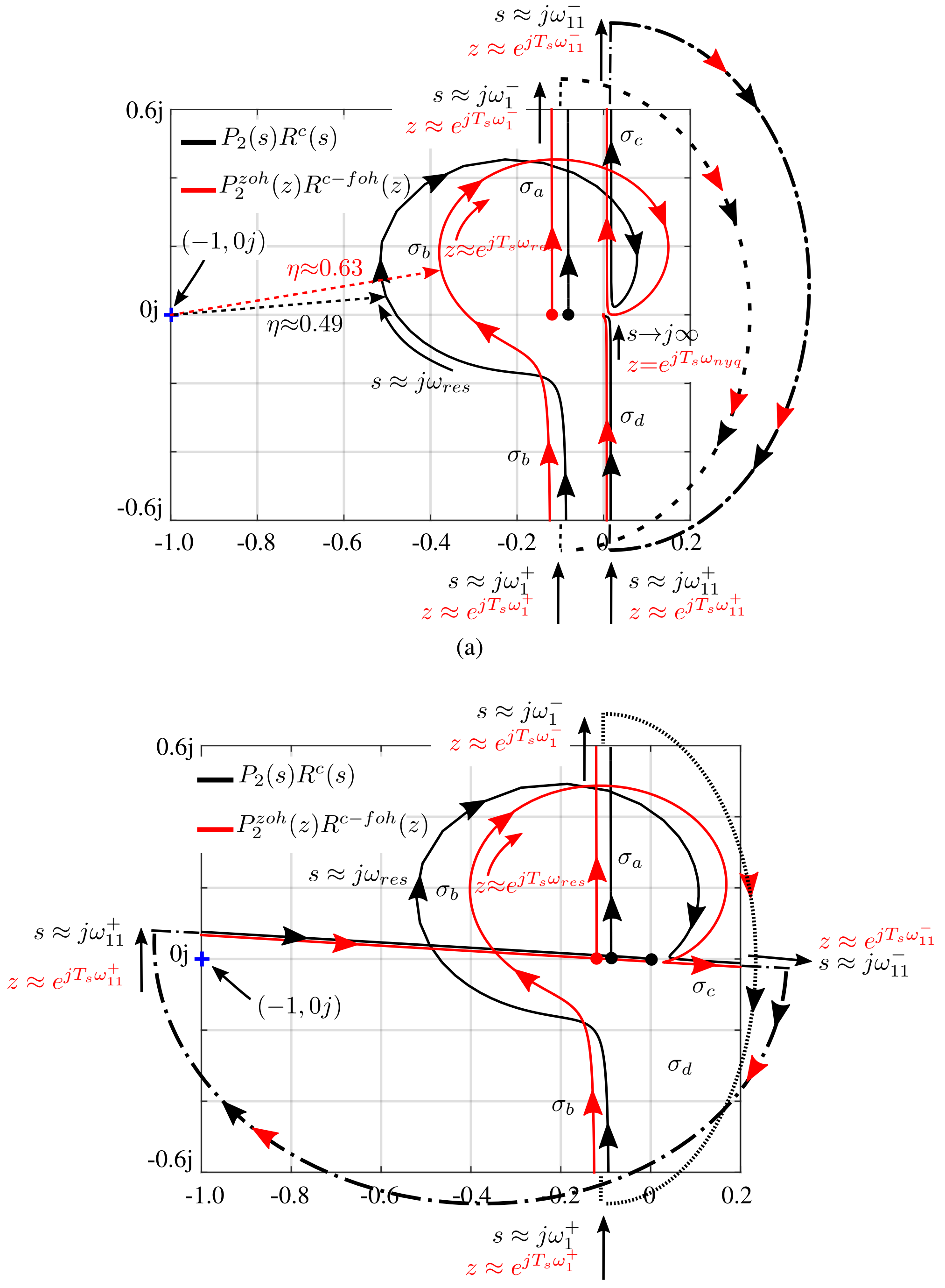

(a)

(b)

Figure 4.19: Nyquist diagram for the open-loop transfer function of a system composed by (black lines in (a) and (b)): a continuous resonant controller for compensation of first and eleventh harmonics, $R^c(s)=R_1^c(s) + R_{11}^c(s)$ of (4.4) and a second order plant $P_2(s)$ of (4.2) and (red lines in (a) and (b)): a discrete-time resonant controller for compensation of first and eleventh harmonics $R^{c-foh}(z)=R_1^{c-foh}(z)+R_{11}^{c-foh}(z)$ of (4.48) and discrete second-order plant $P_2^{zoh}(z)$ of (4.43). For (a) in $R^c(s)$: $\vartheta_1\approx1.48° + 8.5°\approx10°$,$\vartheta_{11}\approx173° + 94°\approx267°$, $K_1=1250$, $K_{11}=150$, $\omega_1=800\pi$rad/s, $\omega_{11}=8800\pi$rad/s. In $R^{c-foh}(z)$: $T_s=\frac{1}{16800}$, $D_1\approx0.7 + 1\approx1.7$, $D_{11}\approx2.3 + 1\approx3.3$, $K_1=1250$ and $K_{11}=150$, $\omega_1=800\pi$rad/s, $\omega_{11}=8800\pi$rad/s. For $P_2(s)$ and $P_2^{zoh}(z)$: $R_f=0.5\Omega$, $L_f=219mH$, $C_f=20\mu F$, $\omega_{ref}\approx4800\pi$rad/s. For (b) $\vartheta_{11}=\approx173°$ and $D_{11}\approx2.3$, the rest of the parameters have not been modified.

CHAPTER 5

Space Vector Modulation for a four-leg NPC Converter

Abstract: *This chapter proposes a three-dimensional space vector modulation in* $\alpha\beta\gamma$ *coordinates for a four-leg NPC converter. First, the modulation space is studied and a simple algorithm for selecting the voltage vectors and calculate its dwell time is proposed. Consequently, an analysis of the voltage fluctuations on the dc-link neutral-point voltage presented and explained by subdividing the modulation space into different regions based on the number of redundant vectors. This allows to estimate the ripple and oscillation frequency on the dc-link neutral-point for designing the dc-link capacitors operating under non-linear and unbalanced systems. Thereafter, the analysis of the harmonics content on the modulated waveforms and switching frequency of the devices under different switching sequences is also addressed. Finally, a new overmodulation scheme in a three-dimensional space is proposed. Unlike the standard saturation methods, this scheme maintains the reference vector path inside the modulation region avoiding the incorporation of additional undesirable harmonics into the modulated waveform, maximizing the utilization of the dc-link voltage.*

Different control algorithms have been proposed in the literature for controlling a four-leg converter, such as: predictive control [19, 29, 30], carrier-based PWM strategies [15, 26–28] and SVM algorithms in abc [18, 31] and $\alpha\beta\gamma$ coordinate frames [17, 32–37]. As discussed in Chapter 3, three-dimensional SVM in abc and $\alpha\beta\gamma$ coordinates arise as the most flexible and promising techniques for modulating the output voltages in a four-leg converter. Whereas its implementation in abc coordinates provides a fast vector identification, dwell-time calculation and easy extension to multi-level VSI, the three-dimensional SVM implemented $\alpha\beta\gamma$ provides decoupling of zero-sequence, which is essential for generating different switching patterns, e.g. even harmonics elimination, implementation of overmodulation algorithms and direct control of the zero-sequence component. Nevertheless, at least in its current state, the high number of calculation has limited the use of SVM in $\alpha\beta\gamma$ space only to two level VSI. This chapter proposes a three-dimensional SVM algorithm in $\alpha\beta\gamma$ coordinates that can be easily extended for multilevel converter. Additionally, it gives an extensively analysis of the use of redundant vectors for controlling the balance of the voltages on the dc-link capacitors and to generate different switching patterns. Finally a three-dimensional overmodulation method is introduced.

5.1 Four-leg Neutral Point Clamped Converter

A three-level NPC converter has considerable advantages compared to a conventional two-level converter. For instance, NPC converters can be connected to medium voltage systems without a power transformer being required [7] and they can operate with a relatively high effective switching frequency, reducing the total harmonic distortion at the grid/load side [24]. Moreover, for a similar application an NPC inverter requires smaller power filter when compared with a conventional two-level VSI [25]. In addition, lower *dv/dt* values, higher efficiency and less stress in the devices are also considered important advantages of the NPC converter over the conventional two-level topology.

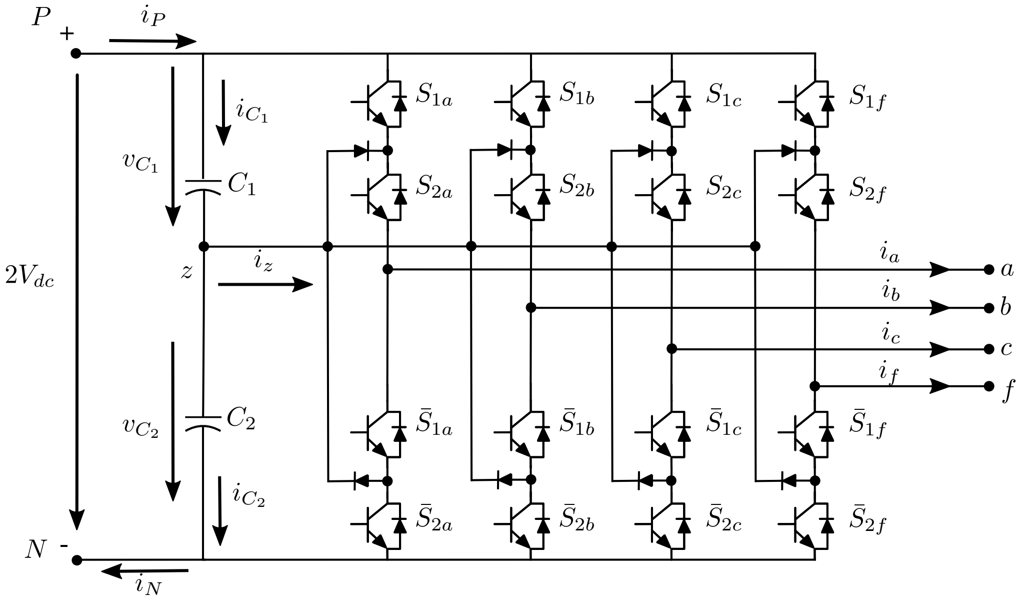

Figure 5.1: Electrical diagram for a four-leg NPC

Recently, two-level four-leg converters [109], [18], [20] and four-leg matrix converters [21], [90] have gained interest as solutions for applications where compensation of zero-sequence is necessary. However, when MV connection is required and/or high efficiency is desirable, the reduction of switching frequency along with an acceptable harmonic distortion become key issues which is usually unfeasible by conventional matrix converters or two-level VSI. By that, the application of four-leg NPC converters has been recently discussed in the literature [27, 29–31, 79, 94]. This topology is presented in Fig. 5.1 and is foreseen to be an interesting solution for MV systems where a path for the circulation of zero-sequence current is required, such as in isolated/grid connected Distributed Power Generation Systems (DPGSs), μGrids, active filters for distribution systems and high-power four-wire UPS as for instance for large data centers. Additionally, due to the higher effective switching frequency of its modulated waveforms compared to the switching frequency of each device. It become an attractive solution for aerospace applications, which require high fundamental frequencies, in the range of $400Hz$ to $800Hz$ [32,34,91,136].

5.2 Definition of the Space of Vectors

The four-leg NPC converter of Fig. 5.1 is composed of dc-link capacitors C_1 and C_2 and the switches per phase are S_{1x}, S_{2x} and $\bar{S}_{1x}$, $\bar{S}_{2x}$, where $x \in \{a, b, c, f\}$ and represents each leg of the inverter. Switches $\bar{S}_{1x}$, $\bar{S}_{2x}$ represent the complement of the switches S_{1x}, S_{2x} respectively. Each leg of the converter has three possible states $(S_{1x}, S_{2x}) \in \{(1,1),(0,1),(0,0)\}$. Thus, the four-leg NPC can perform 3^4=81 switching states. Moreover, the current through the neutral-point (i_z) is given by

$$i_z = \sum_{x=a,b,c,f} \bar{S}_{1x} S_{2x} i_x \tag{5.1}$$

In the rest of this work the poles a, b and c of each leg are referred as phases, while pole f is referred as the neutral wire/leg. In order to implement a SVM algorithm, first the space formed by the 81 combination must be analyzed. Thereby, in order to achieve decoupling of the zero-sequence component, the $\alpha\beta\gamma$ transformation presented in (2.14) has to be used. The 81 switching combinations and the reference vector in the $\alpha\beta\gamma$ coordinates can be expressed as follows:

$$\boldsymbol{v}^i_{\alpha\beta\gamma} = \boldsymbol{T}^{\alpha\beta\gamma}_{abc} \boldsymbol{v}^i_{abc} \tag{5.2}$$

$$\boldsymbol{v}^*_{\alpha\beta\gamma} = \boldsymbol{T}^{\alpha\beta\gamma}_{abc} \boldsymbol{v}^*_{abc} \tag{5.3}$$

$$\boldsymbol{v}^i_{abc} = [v^i_{af}, v^i_{bf}, v^i_{cf}] \tag{5.4}$$

$$\boldsymbol{v}^i_{\alpha\beta\gamma} = [v^i_{\alpha}, v^i_{\beta}, v^i_{\gamma}] \tag{5.5}$$

The vector $\boldsymbol{v}^i_{\alpha\beta\gamma}$ of (5.2) provides the $\alpha\beta\gamma$ representation of the phase-to-neutral voltages produced by the i^{th} switching combination $\boldsymbol{v}^i_{abc}$, with $i \in \mathbb{N} : [1, 81]$. Note, that each component of the vector $\boldsymbol{v}^i_{abc}$ in (5.4) has five possible states, normalized by half of the dc-link voltage (V_{dc}), i.e. {-2,-1,0,1,2}. Although the instantaneous value of the reference vector is commonly given directly in $\alpha\beta\gamma$ coordinates by an external controller, same transformation can be applied to the instantaneous reference vector in case it is given in *abc* coordinates, as shown in (5.3). Thus, $\boldsymbol{v}^*_{abc}$ and $\boldsymbol{v}^*_{\alpha\beta\gamma}$ contains the instantaneous components of the reference vector in abc and $\alpha\beta\gamma$ coordinates respectively.

After applying (5.2) to the 81 different switching combinations, 65 different vectors in the $\alpha\beta\gamma$ space, represented by $\boldsymbol{v}^i_{\alpha\beta\gamma}$, are generated. Its switching combinations are shown in Table C.1 and C.2 from Appendix C. These vectors are classified as follows: 14 redundant vectors, 50 non-redundant vectors and 1 zero vector with a triple redundancy. For convenience, Table C.1 and C.2 summarize this information with the following notation: the zero vector is represented as $\boldsymbol{v}^{0z}_{\alpha\beta\gamma}$, $\boldsymbol{v}^{0n}_{\alpha\beta\gamma}$ or $\boldsymbol{v}^{0p}_{\alpha\beta\gamma}$; redundant vectors are represented as $\boldsymbol{v}^{kn}_{\alpha\beta\gamma}$ or $\boldsymbol{v}^{kp}_{\alpha\beta\gamma}$, for

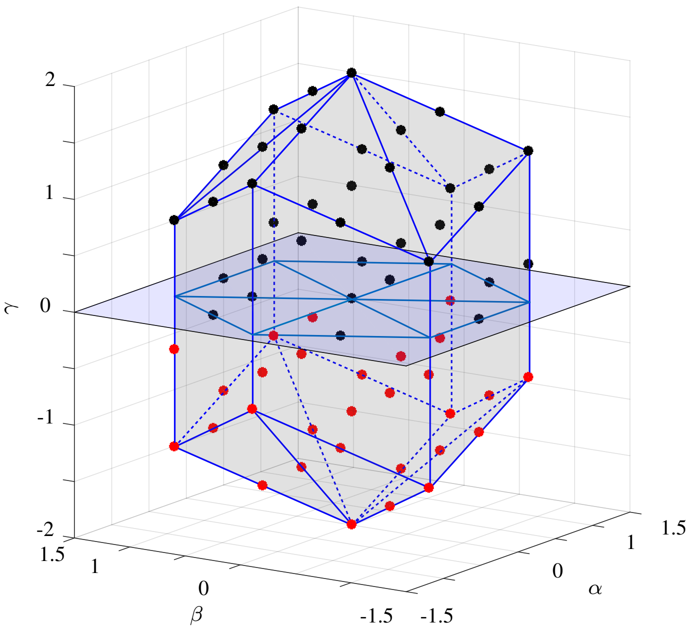

Figure 5.2: Representation of the 65 different vectors in the $\alpha\beta\gamma$ space for a four-leg NPC converter. Additionally, the external surface generated by the most distant vectors and the $\alpha\beta$ plane are shown.

$k \in \mathbb{N} : [1, 14]$, where the sub-index n or p distinguishes the relative positive or negative polarity of the output voltages respect to the neutral point z (see Fig. 5.1). Finally, $\boldsymbol{v}^k_{\alpha\beta\gamma}$ for $k \in \mathbb{N} : [15, 50]$ represent the non-redundant vectors.

The normalized voltages of each leg respect to the neutral point z, $\boldsymbol{v}^i_{abcf}$, the magnitude of each vector $\boldsymbol{v}^i_{\alpha\beta\gamma}$ and current through the NP generated by each switching combination $i_z(\boldsymbol{v}^i_{\alpha\beta\gamma})$ are also available in Table C.1 and C.2 as additional information. Furthermore, the vectors $\boldsymbol{v}^i_{\alpha\beta\gamma}$ are arranged in increasing order according to its magnitude. This emphasizes that eight different amplitudes are present. Hence, the normal classification of short, medium and long vectors, typically used for the three-leg NPC converter, is no longer applicable.

Once obtained the coordinates of the 65 different vectors, its position in the $\alpha\beta\gamma$ space must be studied in order to define the allowable modulation region. Fig. 5.2 shows the 65 different points in the $\alpha\beta\gamma$ space. For a better understanding, differentiation of black and red points are used to indicate whether the points are above or under the the $\alpha\beta$ plane. Furthermore, Fig. 5.2 shows the external surface of the polygon formed by the joint of the largest vectors (most distant points to the origin), which correspond to the complete allowable modulation region, where a reference vector can be linearly modulated.

Fig. 5.3 shows a top view of Fig. 5.2, as expected, the region formed by the projection of the 65 points onto the $\alpha\beta$ plane is the same as in a three-leg NPC converter. Additionally, each vertex of this region represents the projection of three, four or five of the 65 different vectors that share the same $\alpha\beta$ components. Similarly, Fig. 5.4 show the $\alpha\gamma$ and $\beta\gamma$ view of Fig. 5.2. Thereby, Fig. 5.2 to Fig. 5.4 provide full description of the three-dimensional location for the 65 vectors in the $\alpha\beta\gamma$ space.

As it was mentioned in Chapter 2, the modulation of a reference vector using the four nearest

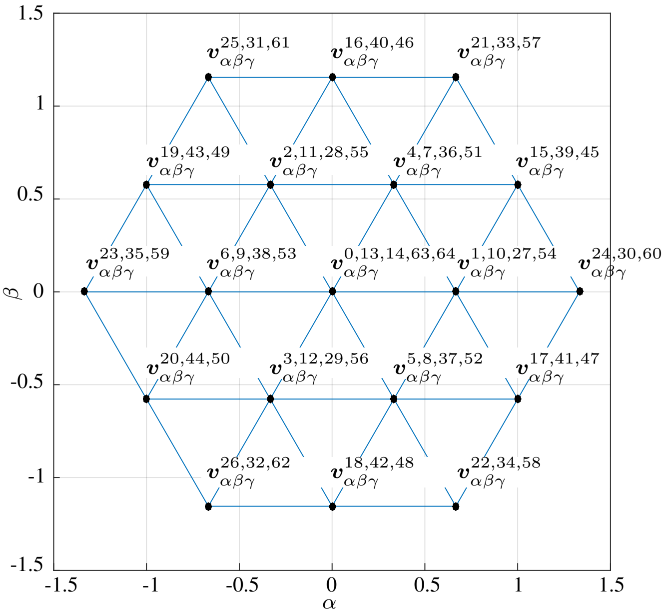

Figure 5.3: $\alpha\beta$ top view of the complete modulation region for a four-leg NPC converter.

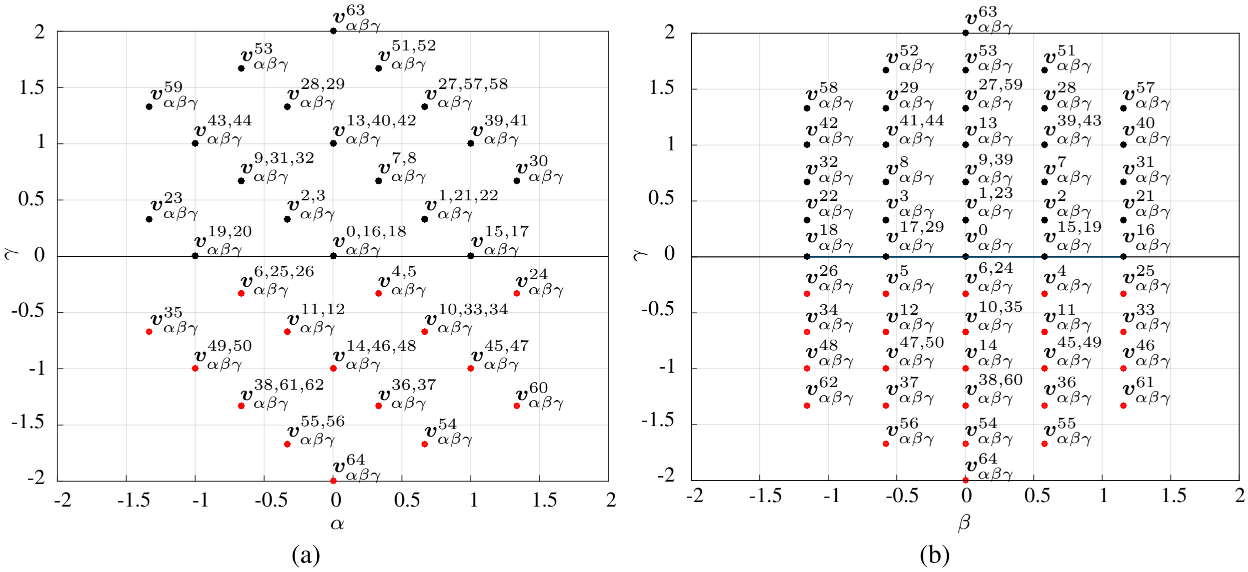

(a)

(b)

Figure 5.4: (a) $\alpha\gamma$ and (b) $\beta\gamma$ view of the complete modulation region for a four-leg NPC converter.

vectors that enclose it, yields to minimization of the number of switching commutations and harmonic distortion [50]. This is particularly important in multilevel converters, where low voltage harmonic distortion, low switching frequency and low power losses are typically demanded. Thus, the selection of these four vectors form the smallest region, i.e. a tetrahedron, that can contain the reference vector in the $\alpha\beta\gamma$ space and are ultimately the vectors to be used for accomplishing the modulation algorithm at each sampling time. Analyzing the region of Fig. 5.2, it can be concluded that it is form of 192 different tetrahedrons. However, each of this tetrahedrons are composed of a different number of redundant vectors. Thus, in order to understand how the modulation region is constructed, it is necessary to classify each tetrahedron based on the number of non-redundant vectors that they possess. Additionally, as it will be shown, this classification allows simple realization of different switching patterns and gives a perception of the control capability of the voltage over the dc-link capacitors.

Table 5.1 shows the classification for the different kind of tetrahedrons presents inside the modulation region of Fig. 5.2. The first column of this table shows the type of tetrahedron TT_n, where n represents the number of non-redundant vectors for each kind of tetrahedron. Thus, for instance, tetrahedrons of type 1 (TT_1) possesses one non-redundant vector and three redundant vectors. Additionally, the last column of this table shows that 24 tetrahedrons of this kind are found in the complete region of Fig. 5.2. Similarly, tetrahedrons of type 2 (TT_2) are composed of 2 redundant vectors and 2 non-redundant vectors and there are 48 of them in the entire modulation region.

Table 5.1: Tetrahedrons Classification

Tetrahedron Type (TT)	Redundant Vectors.	Non-Redundant Vectors	Zero Vectors	Total of Tetrahedrons
TT_0	3	0	1	24
TT_1	3	1	0	24
TT_2	2	2	0	48
TT_3	1	3	0	96

Fig. 5.5 shows the internal composition of the modulation space presented in Fig. 5.2. The complete region can be understood as being built up from different regions, each one forming a surface and enclosing the volume of the previous one.

The first region is formed from the 24 TT_0 (and has the zero vector as its center). Fig. 5.5a shows this first region, composed of all the redundant vectors (i.e $\boldsymbol{v}_0$ to $\boldsymbol{v}_{14}$). In addition, over the surface of the region generated by the TT_0, two TT_1 are depicted to highlight how the next region is formed. Therefore a TT_1 is formed by three redundant vectors (provided by the surface of the region in Fig. 5.5a) and another fourth vector (which must be a non-redundant because all the fifteen redundant vectors are forming the first region). All the 24 TT_1 form the second region, which is shown in Fig. 5.5b. Thereupon the TT_2 are formed based on the surface of the last region. Fig. 5.5c shows how this is accomplished for two TT_2. Thus, one TT_2 contains 2 redundant vectors and one non-redundant vector (provided by the surface generated by TT_1) and a fourth vector which must be non-redundant. The region formed by all the 48 TT_2 is depicted in Fig. 5.5d. Finally, and based on the same methodology, the 96 TT_3 are formed,

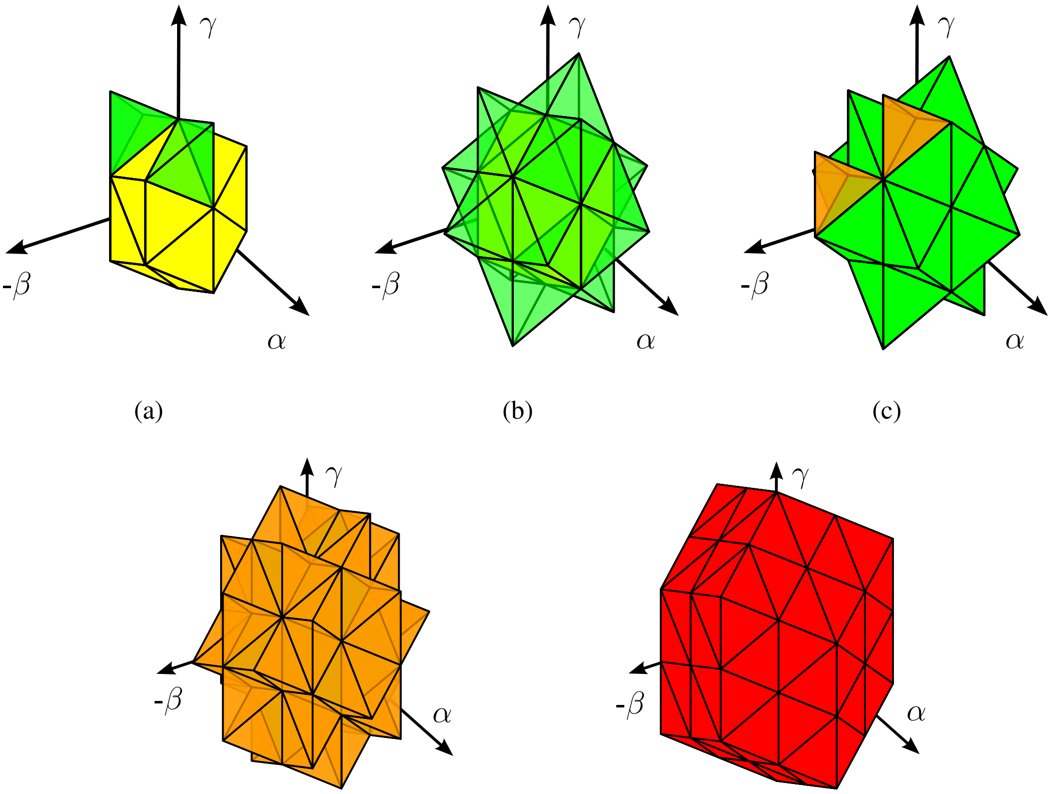

(a) (b) (c)

(d) (e)

Figure 5.5: Different tetrahedrons in the $\alpha\beta\gamma$ space for a four-leg NPC converter. In (a) the region formed by all the TT_0 and two TT_1, (b) region formed by all TT_1, (c) region formed by all the TT_1 and two TT_2, (d) region formed by all TT_2 and (e) region formed by all the TT_3.

which are shown in Fig. 5.5e. Clearly, this last external surface represents the same polygon showed previously in Fig. 5.2.

5.3 The Reference Vector in $\alpha\beta\gamma$ the Space

Regardless the application, a four-leg converter is typically used for compensation of the zero-sequence and/or harmonic components. Thereby, the components of the reference voltage vector that this kind of converters synthesize, either $\boldsymbol{v}^*_{\alpha\beta\gamma}$ or $\boldsymbol{v}^*_{abc}$, are usually non-sinusoidal and unbalanced three-phase system. In general, the components of $\boldsymbol{v}^*_{abc}$ can be balanced/unbalanced and/or sinusoidal/non-sinusoidal, which allows the reference vector $\boldsymbol{v}^*_{\alpha\beta\gamma}$ to describe any possible trajectory within the $\alpha\beta\gamma$ space. Let's consider a simple sinusoidal system in abc coordinates, which voltages $\boldsymbol{v}^*_{abc}$ can be expressed as:

$$v_{af}^*(t) = A\cos(\omega t + \phi_a) \tag{5.6}$$
$$v_{bf}^*(t) = B\cos(\omega t - \frac{2\pi}{3} + \phi_b) \tag{5.7}$$
$$v_{cf}^*(t) = C\cos(\omega t + \frac{2\pi}{3} + \phi_c) \tag{5.8}$$

This system represents a generalization of a symmetric and balanced three-phase system. Ideally, the magnitudes A, B and C are equal and the phases ϕ_a, ϕ_b and ϕ_c are equal, leading to the standard circle in the $\alpha\beta$ plane, which equations in $\alpha\beta\gamma$ coordinates are given by

$$v_{\alpha}^*(t) = m\cos(\omega t) \tag{5.9}$$
$$v_{\beta}^*(t) = m\cos(\omega t - \frac{\pi}{2}) \tag{5.10}$$
$$v_{\gamma}^*(t) = 0 \tag{5.11}$$

with m=A=B=C and ϕ_a=ϕ_b=ϕ_c=0. Thus, as presented in Chapter 2, m represents the magnitude of the reference vector, or also called modulation index and is the most important variable that define the path of the reference vector. Contrary, this definition is not longer valid for a non-balanced and/or non-symmetrical three-phase system, where $A \neq B \neq C$ and $\phi_a \neq \phi_b \neq \phi_c$. For this case, each component of the reference vector $\boldsymbol{v}_{\alpha\beta\gamma}^*$ can be expressed as:

$$v_{\alpha}^*(t) = m_{\alpha}\cos(\omega t + \phi_{\alpha}) \tag{5.12}$$
$$v_{\beta}^*(t) = m_{\beta}\cos(\omega t - \frac{\pi}{2} + \phi_{\beta}) \tag{5.13}$$
$$v_{\gamma}^*(t) = m_{\gamma}\cos(\omega t + \phi_{\gamma}) \tag{5.14}$$

From (5.12) to (5.14), the path described by the reference vector $\boldsymbol{v}_{\alpha\beta\gamma}^*$ depends no longer on one modulation index m, but on the indices m_α, m_β, m_γ and the phases ϕ_α ϕ_β and ϕ_γ.

Considering $m_\alpha \neq m_\beta$ and $m_\gamma \neq 0$, an unbalanced system is generated and the trajectory of the reference vector is not longer a circle in the $\alpha\beta$ plane, but an ellipse inclined in the γ axis. Fig. 5.6a illustrates a top view in the $\alpha\beta$ plane of the path described by a reference vector with modulation indices $m_\alpha = 1.0$, $m_\beta = 0.77$ and $m_\gamma = 0.17$ ($A = 0.95\frac{2}{\sqrt{3}}$, $B = 0.47\frac{2}{\sqrt{3}}$, $C = 0.85\frac{2}{\sqrt{3}}$) and ϕ_a=ϕ_b=ϕ_c=0°. From Fig. 5.6a, the elliptical path, and the selected triangles that enclose the reference vector at each sampling time, can be clearly distinguished. Likewise, Fig. 5.6b shows the elliptical path in the $\alpha\beta\gamma$ frame and the tetrahedrons that enclose the reference path at each sampling time.

Typically, in balanced systems, the modulation index m is limited to $m_{max} = \frac{2}{\sqrt{3}}$ to maintain the path described by the reference vector inside the modulation region in the $\alpha\beta$ plane. Nevertheless, for unbalanced system, three different indices have been defined, namely m_α, m_β and m_γ. In consequence, it is theoretically possible that one or two of them posses a magnitude larger than m_{max} as long as the others modulation indices are small enough to allow the reference vector path to remain inside the modulation region of Fig. 5.2.

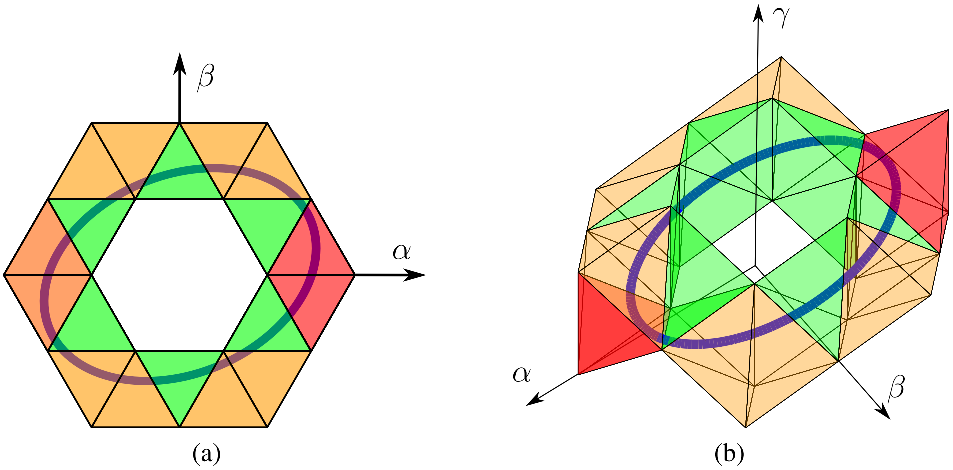

Figure 5.6: Voltage reference vector path for modulation indices $m_a = 0.95$,$m_b = 0.47$,$m_c = 0.85$, ϕ_a=ϕ_b=ϕ_c=0° in (a) the $\alpha\beta$ space and (b) the $\alpha\beta\gamma$ space.

Let's consider now that also harmonics have to be compensated. In that case, the components of the reference vector can be written in a general form as

$$v_\alpha^*(t) = \sum_{h=1}^{n} m_{\alpha_h} \cos\left(h \cdot \omega + \phi_{\alpha_h}\right) \tag{5.15}$$

$$v_\beta^*(t) = \sum_{h=1}^{n} m_{\beta_h} \cos\left(h \cdot \omega + \phi_{\beta_h}\right) \tag{5.16}$$

$$v_\gamma^*(t) = \sum_{h=1}^{n} m_{\gamma_h} \cos\left(h \cdot \omega + \phi_{\gamma_h}\right) \tag{5.17}$$

As it can be concluded from (5.15) to (5.17), in presence of harmonics compensation, unlimited different trajectories can be described by the reference vector. The purpose of the modulation is to synthesize each sampled values of this trajectory as accurate as possible maintaining the balance of the voltages on the dc-link capacitors. This can be successfully achieved as long as the path described by the reference vector remains inside the region presented in Fig. 5.2, as it will be shown in the following section. However, in case this path goes beyond the allowable modulation region, an algorithm to limit this trajectory must be implemented. This will be further study in section 5.6.

5.4 Synthesis of the Reference Vector

In the previous sections, the description of the three-dimensional modulation region in the $\alpha\beta\gamma$ space formed by a four-leg NPC converter was described. Furthermore, the characterization of a reference vector moving inside this space for an unbalanced and non-sinusoidal system was also introduced. In this section, an efficient algorithm for identification of the four nearest vectors that enclose the reference vector and calculation of their dwell times at each sampling time is presented. For this propose, it will be assume that the trajectory described by the reference vector $\boldsymbol{v}^{*}_{\alpha\beta\gamma}$ always reside inside the allowable modulation region of Fig. 5.2. Finally, the utilization of the redundant vectors to generate different switching patterns will be also addressed.

5.4.1 Tetrahedron Identification

For the sake of explanation, let us assume an instantaneous random value for the normalized reference vector in abc coordinates as $\underline{\boldsymbol{v}}^{*}_{abc}=[x,y,z]$, where $x;y;z \in \mathbb{R} : [-2,2]$ and its $\alpha\beta\gamma$ representation, $\underline{\boldsymbol{v}}^{*}_{\alpha\beta\gamma}$, is inside the modulation region of Fig. 5.2. The vectors $\underline{\boldsymbol{v}}^{s_1}_{\alpha\beta\gamma}$, $\underline{\boldsymbol{v}}^{s_2}_{\alpha\beta\gamma}$, $\underline{\boldsymbol{v}}^{s_3}_{\alpha\beta\gamma}$ and $\underline{\boldsymbol{v}}^{s_4}_{\alpha\beta\gamma}$ represent the four nearest vectors, generated by the converter, that enclose $\underline{\boldsymbol{v}}^{*}_{\alpha\beta\gamma}$. Additionally, $\underline{\boldsymbol{v}}^{s_1}_{abc}$, $\underline{\boldsymbol{v}}^{s2}_{abc}$, $\underline{\boldsymbol{v}}^{s_3}_{abc}$, $\underline{\boldsymbol{v}}^{s_4}_{abc}$ and $\underline{\boldsymbol{v}}^{s_1}_{abcf}$, $\underline{\boldsymbol{v}}^{s_2}_{abcf}$, $\underline{\boldsymbol{v}}^{s_3}_{abcf}$, $\underline{\boldsymbol{v}}^{s_4}_{abcf}$ represent the selected vectors in abc coordinates and the states for each leg of the converter respectively (see Table C.1).

The aim of a SVM algorithm is to identify these four vectors with their respective dwell-times with the minimum computational effort. Thereby, as (5.2) is a linear transformation, the seek of the four vectors that enclose the reference vector at each sampling time, denoted also as $\underline{\boldsymbol{v}}^{s_1-s_4}_{\alpha\beta\gamma}$ or $\underline{\boldsymbol{v}}^{s_1-s_4}_{abc}$, is equivalent for either abc or $\alpha\beta\gamma$ coordinate system. Nevertheless, the implementation of the modulation algorithm in $\alpha\beta\gamma$ coordinate system presents several advantages compared to its analogue abc reference frame, such as: a) avoid transformation from $\alpha\beta\gamma$ to abc coordinate system of the control references given by external controllers, b) direct control and visualization of the zero-sequence component, important in numerous applications [11, 13, 14, 32, 34, 98], c) simple implementation of overmodulation algorithms, specially important in power quality conditioners [26, 33], which is extensively discussed in section 5.6, d) straight implementation of even harmonics elimination, specially important in grid connected applications [54] and e) visualization, in the $\alpha\beta\gamma$ space, of the capability for balancing the voltage in the dc-link capacitors. Furthermore, as it will be shown later in this section, the $\alpha\beta\gamma$ coordinate system arrange the vectors in such a way that the identification of the tetrahedron can be reduced to the $\alpha\beta$ plane, avoiding three-dimensional search.

Considering that the transition between two adjacent vectors of the converter generates an unitary voltage step in only one phase of the converter (e.g. $\boldsymbol{v}^{1p}_{abc}$([1,0,0]) $\leftrightarrow$ $\boldsymbol{v}^{15}_{abc}$([1,0,-1])) (*minimum switching transition* principle). It can be affirmed that each component of $\underline{\boldsymbol{v}}^{*}_{abc}$ is contained between the components of the vectors $\underline{\boldsymbol{v}}_{0_{abc}}$ and $\underline{\boldsymbol{v}}_{0'_{abc}}$. Where, using the ***floor()*** function to each coordinate of $\underline{\boldsymbol{v}}^{*}_{abc}$, they can be obtained as:

$$\underline{\boldsymbol{v}}_{0_{abc}} = \boldsymbol{floor}\left(\underline{\boldsymbol{v}}^{*}_{abc}\right) \tag{5.18}$$

$$\underline{\boldsymbol{v}}_{0'_{abc}} = \underline{\boldsymbol{v}}_{0_{abc}} + [1,1,1] \tag{5.19}$$

Thus, these two vectors become the first two solutions of the four vectors $\underline{\boldsymbol{v}}^{s_1-s_4}_{abc}$(or its equivalent $\underline{\boldsymbol{v}}^{s_1-s_4}_{\alpha\beta\gamma}$). In order to find the two remaining vectors, Table 5.2 shows the six possible transition vectors, in abc and $\alpha\beta\gamma$ coordinates, that can be used to complete the sequence of four vectors. Note, that a transition from $\underline{\boldsymbol{v}}_{0_{abc}}$ to $\underline{\boldsymbol{v}}_{0'_{abc}}$ is also allowable, as it involves only one switching transition on the fourth leg of the converter, e.g. $\boldsymbol{v}_{10p}$ ([0,-1,-1] or [POOP]) $\leftrightarrow$ $\boldsymbol{v}_{10p}$ ([1,0,0] or [POOO]), in this case only the fourth leg has changed from positive state "P" to the zero state "O", i.e. adding a zero sequence component. This will be further discussed in the subsection 5.4.3 of this chapter.

Table 5.2: Vectors for Tetrahedron Selection in abc and $\alpha\beta\gamma$ coordinates

Transition vectors in abc coordinates	Transition vectors in $\alpha\beta\gamma$ coordinates
$\underline{\boldsymbol{v}}_{0_{abc}}=\underline{\boldsymbol{v}}^{s1}_{abc}=floor\ (\underline{\boldsymbol{v}}^{*}_{abc})+[0,0,0]$	$\underline{\boldsymbol{v}}_{0_{\alpha\beta\gamma}}=\underline{\boldsymbol{v}}^{s1}_{\alpha\beta\gamma}=\boldsymbol{T}^{\alpha\beta\gamma}_{abc}\underline{\boldsymbol{v}}^{s1}_{abc}+[0,0,0]$
$\underline{\boldsymbol{v}}_{1_{abc}}=\underline{\boldsymbol{v}}_{0_{abc}}+[1,0,0]$	$\underline{\boldsymbol{v}}_{1_{\alpha\beta\gamma}}=\underline{\boldsymbol{v}}_{0_{\alpha\beta\gamma}}+[\frac{2}{3},0,\frac{1}{3}]$
$\underline{\boldsymbol{v}}_{2_{abc}}=\underline{\boldsymbol{v}}_{0_{abc}}+[1,1,0]$	$\underline{\boldsymbol{v}}_{2_{\alpha\beta\gamma}}=\underline{\boldsymbol{v}}_{0_{\alpha\beta\gamma}}+[\frac{1}{3},\frac{\sqrt{3}}{3},\frac{2}{3}]$
$\underline{\boldsymbol{v}}_{3_{abc}}=\underline{\boldsymbol{v}}_{0_{abc}}+[0,1,0]$	$\underline{\boldsymbol{v}}_{3_{\alpha\beta\gamma}}=\underline{\boldsymbol{v}}_{0_{\alpha\beta\gamma}}+[-\frac{1}{3},\frac{\sqrt{3}}{3},\frac{1}{3}]$
$\underline{\boldsymbol{v}}_{4_{abc}}=\underline{\boldsymbol{v}}_{0_{abc}}+[0,1,1]$	$\underline{\boldsymbol{v}}_{4_{\alpha\beta\gamma}}=\underline{\boldsymbol{v}}_{0_{\alpha\beta\gamma}}+[-\frac{2}{3},0,\frac{2}{3}]$
$\underline{\boldsymbol{v}}_{5_{abc}}=\underline{\boldsymbol{v}}_{0_{abc}}+[0,0,1]$	$\underline{\boldsymbol{v}}_{5_{\alpha\beta\gamma}}=\underline{\boldsymbol{v}}_{0_{\alpha\beta\gamma}}+[-\frac{1}{3},-\frac{\sqrt{3}}{3},\frac{1}{3}]$
$\underline{\boldsymbol{v}}_{6_{abc}}=\underline{\boldsymbol{v}}_{0_{abc}}+[1,0,1]$	$\underline{\boldsymbol{v}}_{6_{\alpha\beta\gamma}}=\underline{\boldsymbol{v}}_{0_{\alpha\beta\gamma}}+[\frac{1}{3},-\frac{\sqrt{3}}{3},\frac{2}{3}]$
$\underline{\boldsymbol{v}}_{0'_{abc}}=\underline{\boldsymbol{v}}^{s4}_{abc}=\underline{\boldsymbol{v}}_{0_{abc}}+[1,1,1]$	$\underline{\boldsymbol{v}}_{0'_{\alpha\beta\gamma}}=\underline{\boldsymbol{v}}^{s4}_{\alpha\beta\gamma}=\underline{\boldsymbol{v}}_{0_{\alpha\beta\gamma}}+[0,0,1]$

From Table 5.2, and starting the sequence with $\underline{\boldsymbol{v}}_{0_{\alpha\beta\gamma}}$, the following sequences, ς_1 to ς_6, accomplish the *minimum switching transition* principle:

- $\varsigma_1:\underline{\boldsymbol{v}}_{0_{\alpha\beta\gamma}}-\underline{\boldsymbol{v}}_{1_{\alpha\beta\gamma}}-\underline{\boldsymbol{v}}_{2_{\alpha\beta\gamma}}-\underline{\boldsymbol{v}}_{0'_{\alpha\beta\gamma}}$
- $\varsigma_2:\underline{\boldsymbol{v}}_{0_{\alpha\beta\gamma}}-\underline{\boldsymbol{v}}_{3_{\alpha\beta\gamma}}-\underline{\boldsymbol{v}}_{2_{\alpha\beta\gamma}}-\underline{\boldsymbol{v}}_{0'_{\alpha\beta\gamma}}$
- $\varsigma_3:\underline{\boldsymbol{v}}_{0_{\alpha\beta\gamma}}-\underline{\boldsymbol{v}}_{3_{\alpha\beta\gamma}}-\underline{\boldsymbol{v}}_{4_{\alpha\beta\gamma}}-\underline{\boldsymbol{v}}_{0'_{\alpha\beta\gamma}}$
- $\varsigma_4:\underline{\boldsymbol{v}}_{0_{\alpha\beta\gamma}}-\underline{\boldsymbol{v}}_{5_{\alpha\beta\gamma}}-\underline{\boldsymbol{v}}_{4_{\alpha\beta\gamma}}-\underline{\boldsymbol{v}}_{0'_{\alpha\beta\gamma}}$
- $\varsigma_5:\underline{\boldsymbol{v}}_{0_{\alpha\beta\gamma}}-\underline{\boldsymbol{v}}_{5_{\alpha\beta\gamma}}-\underline{\boldsymbol{v}}_{6_{\alpha\beta\gamma}}-\underline{\boldsymbol{v}}_{0'_{\alpha\beta\gamma}}$
- $\varsigma_6:\underline{\boldsymbol{v}}_{0_{\alpha\beta\gamma}}-\underline{\boldsymbol{v}}_{1_{\alpha\beta\gamma}}-\underline{\boldsymbol{v}}_{6_{\alpha\beta\gamma}}-\underline{\boldsymbol{v}}_{0'_{\alpha\beta\gamma}}$

Hence, only one of these six sequences ς_1 to ς_6 contain the four vectors that enclose the reference $\underline{\boldsymbol{v}}^{*}_{\alpha\beta\gamma}$ at each sampling time. In order to identify the correct group of vectors, Fig. 5.7a and Fig. 5.7b show the cube formed by the eight vectors of Table 5.2 in abc and $\alpha\beta\gamma$ coordinates with a displaced origin located at $\underline{\boldsymbol{v}}_{0_{abc}}$ and $\underline{\boldsymbol{v}}_{0_{\alpha\beta\gamma}}$ respectively. The transformation of (5.2) rotates the cube of Fig. 5.7a up in 90°, placing $\underline{\boldsymbol{v}}_{0'_{\alpha\beta\gamma}}$ over $\underline{\boldsymbol{v}}_{0_{\alpha\beta\gamma}}$. Each cube is formed by six tetrahedrons, corresponding to the six possible switching sequences ς_1 to ς_6. For a better visual understanding, only three tetrahedrons are depicted with different colors inside each cube (the oder three are symmetrically placed). In order to identify the tetrahedron that contains $\underline{\boldsymbol{v}}^{*}_{abc}$ from 5.7a, six different planes that cross the cube of Fig. 5.7a must be generated and compared with $\underline{\boldsymbol{v}}^{*}_{abc}$ [18,31]. Unlike Fig. 5.7a, each vertex of the cube illustrated in Fig. 5.7b is placed according its zero sequence component. Thereby, only $\underline{\boldsymbol{v}}_{0_{\alpha\beta\gamma}}$ and $\underline{\boldsymbol{v}}_{0'_{\alpha\beta\gamma}}$ share the same $\alpha\beta$ values and are overlapped from a top view.

Fig. 5.8 show a top view of both cubes in a non-displaced origin reference frame. Unlike Fig. 5.8a, in Fig. 5.8b none of the six vectors, $\underline{\boldsymbol{v}}_{1_{\alpha\beta\gamma}}$ to $\underline{\boldsymbol{v}}_{6_{\alpha\beta\gamma}}$, is overlapped in the $\alpha\beta$ plane. Thereby, the simple calculation of ϕ, in Fig. 5.8b, provides straightforward identification of

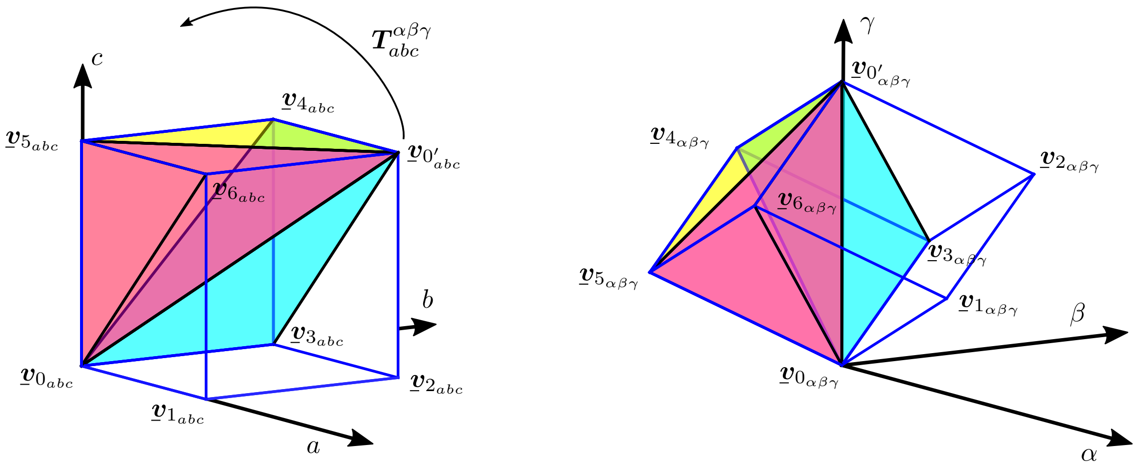

(a) (b)

Figure 5.7: Modulation region in the $\alpha\beta\gamma$ space for a four-leg NPC converter.

the two remaining vectors, $\underline{v}_{\alpha\beta\gamma}^{s2}$ and $\underline{v}_{\alpha\beta\gamma}^{s3}$, to complete the sequence $\underline{v}_{\alpha\beta\gamma}^{s1}$ to $\underline{v}_{\alpha\beta\gamma}^{s4}$ and the corresponding identification of the tetrahedron that contains $\underline{v}_{\alpha\beta\gamma}^{*}$. This reduces the search of the tetrahedron to a two-dimensional problem, same as for standard three-leg converters, avoiding three-dimensional computation. From Fig. 5.8a a light green region is observed in the upper half of the square. This color is obtained because of the superposition of the yellow and light blue tetrahedrons of Fig. 5.7a, which does not occurs in $\alpha\beta\gamma$ coordinate system as can be observed in Fig. 5.8b.

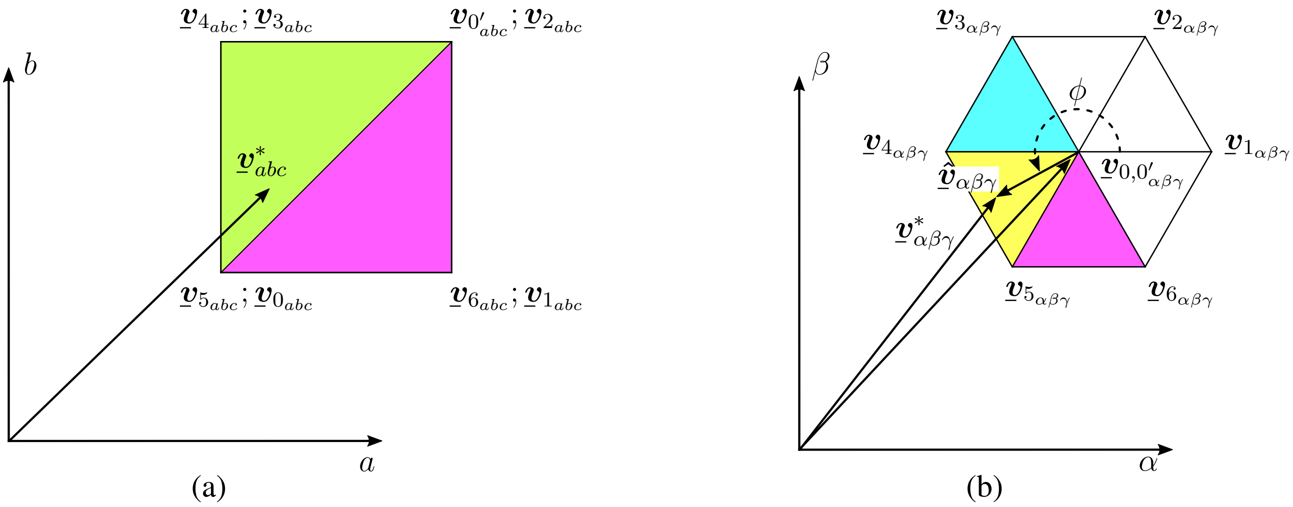

(a) (b)

Figure 5.8: Modulation region in the $\alpha\beta\gamma$ space for a four-leg NPC converter.

The following equations summarize the three required steps for selection of the tetrahedron when the reference vector is given in $\alpha\beta\gamma$ coordinate:

$$\underline{\boldsymbol{v}}_{0_{\alpha\beta\gamma}} = \boldsymbol{T}_{abc}^{\alpha\beta\gamma} \left[\boldsymbol{floor} \left(\boldsymbol{T}_{\alpha\beta\gamma}^{abc} \, \underline{\boldsymbol{v}}^{*}_{\alpha\beta\gamma} \right) \right] \tag{5.20}$$

$$\hat{\underline{\boldsymbol{v}}}_{\alpha\beta\gamma} = \underline{\boldsymbol{v}}^{*}_{\alpha\beta\gamma} - \underline{\boldsymbol{v}}_{0_{\alpha\beta\gamma}} \tag{5.21}$$

$$\phi = tan^{-1} \left(\frac{\hat{\underline{v}}_{\beta}}{\hat{\underline{v}}_{\alpha}} \right) \tag{5.22}$$

Finally, the selection of the vectors can be obtained based on ϕ as shown in Table 5.3.

Table 5.3: Selected Sequence of Vectors

ϕ	$\underline{\boldsymbol{v}}^{s_1-s_4}_{\alpha\beta\gamma}$
$\phi \in \left[0, \frac{\pi}{3}\right[$	$\underline{\boldsymbol{v}}_{0\alpha\beta\gamma} - \underline{\boldsymbol{v}}_{1\alpha\beta\gamma} - \underline{\boldsymbol{v}}_{2\alpha\beta\gamma} - \underline{\boldsymbol{v}}_{0'\alpha\beta\gamma}$
$\phi \in \left[\frac{\pi}{3}, \frac{2\pi}{3}\right[$	$\underline{\boldsymbol{v}}_{0\alpha\beta\gamma} - \underline{\boldsymbol{v}}_{2\alpha\beta\gamma} - \underline{\boldsymbol{v}}_{3\alpha\beta\gamma} - \underline{\boldsymbol{v}}_{0'\alpha\beta\gamma}$
$\phi \in \left[\frac{2\pi}{3}, \pi\right[$	$\underline{\boldsymbol{v}}_{0\alpha\beta\gamma} - \underline{\boldsymbol{v}}_{3\alpha\beta\gamma} - \underline{\boldsymbol{v}}_{4\alpha\beta\gamma} - \underline{\boldsymbol{v}}_{0'\alpha\beta\gamma}$
$\phi \in \left[\pi, \frac{4\pi}{3}\right[$	$\underline{\boldsymbol{v}}_{0\alpha\beta\gamma} - \underline{\boldsymbol{v}}_{4\alpha\beta\gamma} - \underline{\boldsymbol{v}}_{5\alpha\beta\gamma} - \underline{\boldsymbol{v}}_{0'\alpha\beta\gamma}$
$\phi \in \left[\frac{4\pi}{3}, \frac{5\pi}{3}\right[$	$\underline{\boldsymbol{v}}_{0\alpha\beta\gamma} - \underline{\boldsymbol{v}}_{5\alpha\beta\gamma} - \underline{\boldsymbol{v}}_{6\alpha\beta\gamma} - \underline{\boldsymbol{v}}_{0'\alpha\beta\gamma}$
$\phi \in \left[\frac{5\pi}{3}, 2\pi\right[$	$\underline{\boldsymbol{v}}_{0\alpha\beta\gamma} - \underline{\boldsymbol{v}}_{6\alpha\beta\gamma} - \underline{\boldsymbol{v}}_{1\alpha\beta\gamma} - \underline{\boldsymbol{v}}_{0'\alpha\beta\gamma}$

Note that, from Table 5.2, the vectors $\boldsymbol{v}_{1\alpha\beta\gamma}$ to $\boldsymbol{v}_{6\alpha\beta\gamma}$ are always calculated based on $\boldsymbol{v}_{0\alpha\beta\gamma}$. Therefore, they do not need to be saved in any look-up table. Additionally, it should be noticed that from Table 5.3 the vectors $\underline{\boldsymbol{v}}^{s_1}_{abc}$ to $\underline{\boldsymbol{v}}^{s_4}_{abc}$ or $\underline{\boldsymbol{v}}^{s_1}_{abcf}$ to $\underline{\boldsymbol{v}}^{s_4}_{abcf}$ can be equivalently obtained.

5.4.2 Dwell time Calculation

Once the four stationary vectors, $\underline{\boldsymbol{v}}^{s_1}_{\alpha\beta\gamma}$ to $\underline{\boldsymbol{v}}^{s_4}_{\alpha\beta\gamma}$, or equivalently written as $\underline{\boldsymbol{v}}^{s_1-s_4}_{\alpha\beta\gamma}$, are obtained using (5.22) and Table 5.3, their dwell times must be calculated. The dwell time for each of the selected stationary vectors basically define the duty-cycle time (on-state or off-state time) for each of the switches of the converter during a sampled period T_s. Thereby, a reference vector can be synthesized as an average value using the selected vectors over T_s. Defining d_1, d_2, d_3 and d_4 as the dwell times for each of the selected vectors $\underline{\boldsymbol{v}}^{s_1-s_4}_{\alpha\beta\gamma}$, their normalized values can be obtained from:

$$\sum_{n=1}^{4} \underline{\boldsymbol{v}}^{s_n}_{\alpha\beta\gamma} d_n = \underline{\boldsymbol{v}}^{*}_{\alpha\beta\gamma} \tag{5.23}$$

From (5.23), an inverse matrix operation is required for calculating the dwell times. However, based on Table 5.3, only six different sequence combinations can be generated for enclosing the reference vector $\underline{\boldsymbol{v}}^{*}_{\alpha\beta\gamma}$. If this sequences are referred to the vector $\underline{\boldsymbol{v}}_{0\alpha\beta\gamma}$, only six matrices are required to calculate the dwell-times in all the space and the inversion of the matrices is avoided. Thereby, subtracting $\underline{\boldsymbol{v}}_{0\alpha\beta\gamma}$ to each vector of (5.23), the calculation of the dwell times can be easily obtained using $\hat{\underline{\boldsymbol{v}}}_{\alpha\beta\gamma}$ and ϕ, from (5.21) and (5.22), as:

$$\begin{bmatrix} d_2 \\ d_3 \\ d_4 \end{bmatrix} = \boldsymbol{D_n} \begin{bmatrix} \underline{\hat{\boldsymbol{v}}}_\alpha \\ \underline{\hat{\boldsymbol{v}}}_\beta \\ \underline{\hat{\boldsymbol{v}}}_\gamma \end{bmatrix} \tag{5.24}$$

$$d_1 = 1 - d_2 - d_3 - d_4 \tag{5.25}$$

where, $\boldsymbol{D}_n$ is a 3x3 matrix that takes six different values depending on the selected sequence, i.e. ϕ. Thereby, based on Table 5.2, $\boldsymbol{D}_n$ can be expressed as:

$$\boldsymbol{D}_1 = \begin{bmatrix} \frac{3}{2} & -\frac{\sqrt{3}}{2} & 0 \\ 0 & \sqrt{3} & 0 \\ -\frac{1}{2} & -\frac{\sqrt{3}}{2} & 1 \end{bmatrix} \qquad \phi \in \left[0, \frac{\pi}{3}\right[\tag{5.26a}$$

$$\boldsymbol{D}_2 = \begin{bmatrix} -\frac{3}{2} & \frac{\sqrt{3}}{2} & 0 \\ \frac{3}{2} & \frac{\sqrt{3}}{2} & 0 \\ -\frac{1}{2} & -\frac{\sqrt{3}}{2} & 1 \end{bmatrix} \qquad \phi \in \left[\frac{\pi}{3}, \frac{2\pi}{3}\right[\tag{5.26b}$$

$$\boldsymbol{D}_3 = \begin{bmatrix} 0 & \sqrt{3} & 0 \\ -\frac{3}{2} & -\frac{\sqrt{3}}{2} & 0 \\ 1 & 0 & 1 \end{bmatrix} \qquad \phi \in \left[\frac{2\pi}{3}, \pi\right[\tag{5.26c}$$

$$\boldsymbol{D}_4 = \begin{bmatrix} 0 & \sqrt{3} & 0 \\ -\frac{3}{2} & \frac{\sqrt{3}}{2} & 0 \\ 1 & 0 & 1 \end{bmatrix} \qquad \phi \in \left[\pi, \frac{4\pi}{3}\right[\tag{5.26d}$$

$$\boldsymbol{D}_5 = \begin{bmatrix} -\frac{3}{2} & -\frac{\sqrt{3}}{2} & 0 \\ \frac{3}{2} & -\frac{\sqrt{3}}{2} & 0 \\ -\frac{1}{2} & \frac{\sqrt{3}}{2} & 1 \end{bmatrix} \qquad \phi \in \left[\frac{4\pi}{3}, \frac{5\pi}{3}\right[\tag{5.26e}$$

$$\boldsymbol{D}_6 = \begin{bmatrix} \frac{3}{2} & \frac{\sqrt{3}}{2} & 0 \\ 0 & -\sqrt{3} & 0 \\ -\frac{1}{2} & \frac{\sqrt{3}}{2} & 1 \end{bmatrix} \qquad \phi \in \left[\frac{5\pi}{3}, 2\pi\right[\tag{5.26f}$$

$$\tag{5.26g}$$

The diagram of Fig. 5.9 summarizes the proposed methodology for achieving a SVM in $\alpha\beta\gamma$ coordinate frame for a four-leg NPC converter. It shows that after two steps it is possible to identify the sequence of vectors $\underline{\boldsymbol{v}}_{\alpha\beta\gamma}^{s_1-s_4}$ (or their equivalents $\underline{\boldsymbol{v}}_{abc}^{s_1-s_4}$; $\underline{\boldsymbol{v}}_{abcf}^{s_1-s_4}$) that enclose the reference $\underline{\boldsymbol{v}}_{\alpha\beta\gamma}^*$. Likewise, the calculation of their corresponding dwell-times, d_1 to d_4, can be easily obtain based basically only on the calculation of $\underline{\boldsymbol{v}}_{0\alpha\beta\gamma}$.

Although this methodology is proposed and implemented for a four-leg NPC converter in this work, the generality of the algorithm enables its implementation in any topology where the zero-sequence component has to be controlled and a three-dimensional SVM algorithm is needed.

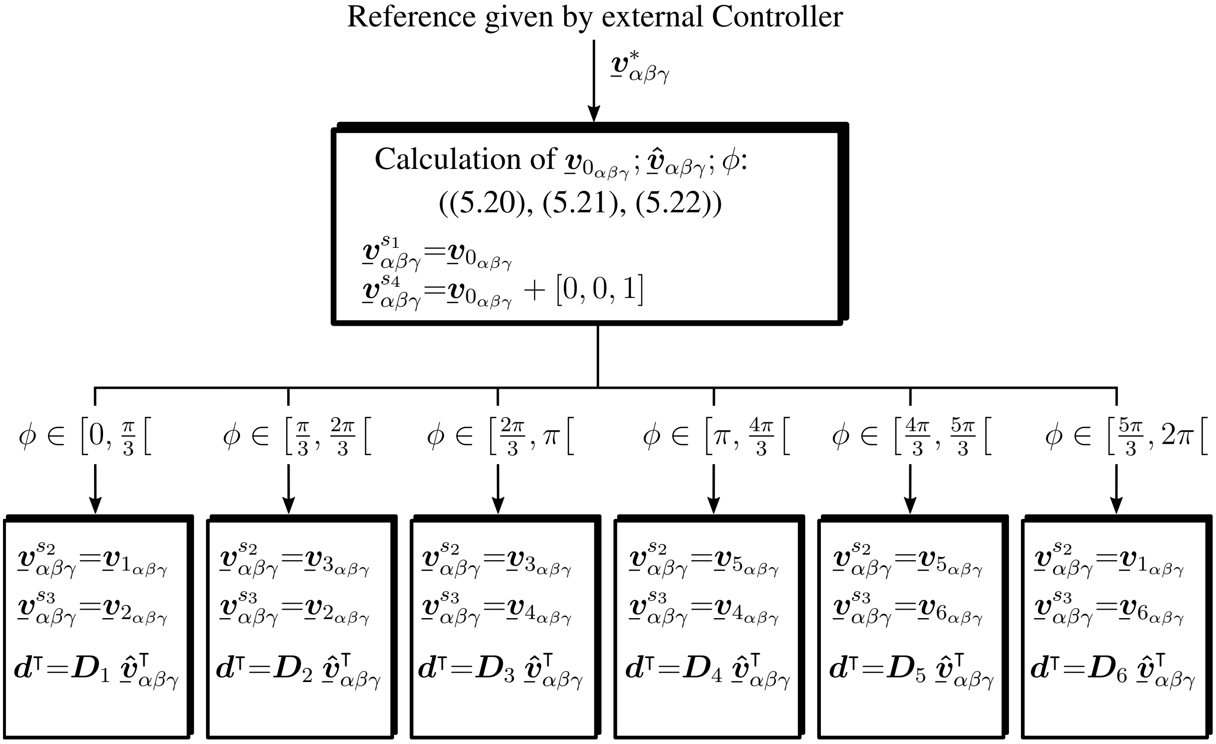

Figure 5.9: General diagram for a three-dimensional SVM. $\boldsymbol{d}^{\mathsf{T}}$ denotes the transpose of the vector $\boldsymbol{d}=[d_2, d_3, d_4]$. The dwell time d_1 is obtained as $d_1=1-d_2-d_3-d_4$; $\forall\,\phi$.

5.4.3 Switching Patterns for a four-leg NPC converter

After the stationary vectors and their dwell times have been obtained, a proper switching pattern that arrange these vectors during the sampling time T_s has to be defined. The selection of this pattern, also known as switching sequence, is always a trade-off between the number of commutations, i.e. power losses, and the accuracy of tracking of a reference signal, i.e. current or voltage ripple. Therefore, the selection between different patterns mostly depends on the application.

As presented in Chapter 2 and 3, for a two-level inverter, either three- or four-leg, zero-vectors are always available at each sampled period, which along with the active vectors synthesize a reference. Hence, two important categories of switching sequences were defined, i.e. *Single-Redundancy Sequence* and *Non-Redundancy Sequence*. They mainly differ in the number of zero-vector redundancies used in the modulation [163], [50].

For a n-level NPC converter, either three or four leg, not only the harmonic spectrum has to be considered when designing a switching pattern, but also the capability to balance the voltage on the dc-link capacitors. Thus, the *Non-Redundancy Sequence* is not a suitable alternative, as it seriously limits the dc-link voltage balance capability. Furthermore, not only the zero-vector possesses redundancy, but also several different active vectors leading to several different possible switching combinations, which quantity depends on the number of legs and levels of the converter. Thereby, typically for 3 or 5 level three-leg converters, a preset look-up table containing the switching sequences to be implemented in each region of the modulation space is arranged (see Chapter 2).

For the best knowledge of the author, the definition of switching patterns implemented in a four-leg NPC converter has not been yet explored, which presents a more difficult challenge, as the high number of tetrahedrons makes impracticable the use of preset look-up tables and an algorithm for determining this sequences has to be developed.

In this section, a simply algorithm which avoids the use of tables for obtaining the correct sequence is presented. Additionally, two relevant switching patterns, named *Full-Redundancy Sequence* and *Single-Redundancy Sequence*, for the three-level four-leg NPC converter are proposed. The first proposed switching pattern employs all possible redundancies of the selected vectors, while the second uses only one redundant vector during each sampling period. This two different patterns, offer different features regarding the switching frequency of each device and controllability of the NP current i_z. Thereby, they can be selected according to the application. As a general condition for both proposed patterns, only one device is switched on and a second device, from the same leg, is switched off during the transition from one switching combination to another. This accomplishes the already defined *minimum switching transition* principle.

5.4.3.1 Full Redundancy Switching Pattern

This switching sequence makes use of all the available switching combinations, i.e. redundant vectors, at each sampled period T_s. The use of all redundancies of the stationary vectors increase the controllability over the NP current of the four-leg NPC converter, which results in a better control over the voltage in the dc-link capacitors. Additionally, it can increase the equivalent switching frequency of the modulated waveform, which reduce the size of output filters.

Let us consider the two different tetrahedrons, TT_1 and TT_2, which vectors ($\underline{\boldsymbol{v}}_{\alpha\beta\gamma}^{s_1-s_4}$) are shown in Table 5.4 and arranged in a descending order respect to their γ coordinate. In order to select a suitable switching sequence, each vector is shown with their respective positive and negative redundancies (as non-redundant vectors possess only one switching combination, they use the entire row). To generate a switching sequence that uses all the available switching combinations, first a pivot vector has to be selected.

Table 5.4: Sequence of the Switching Vectors

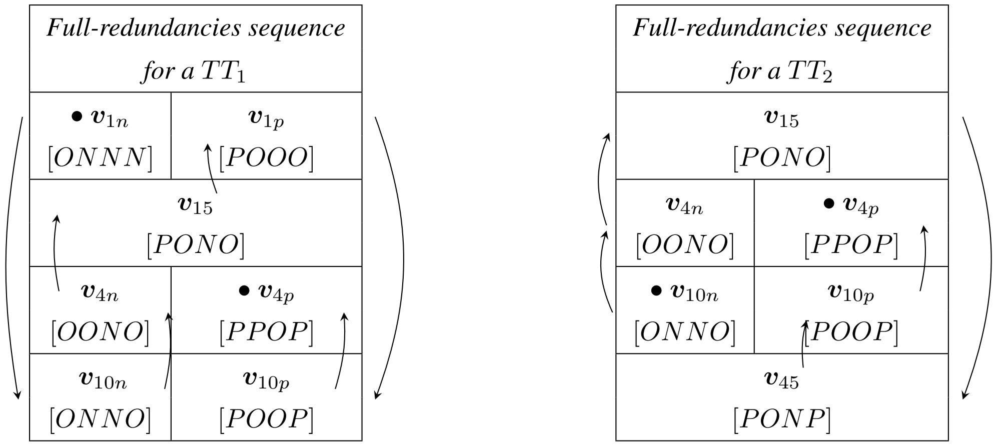

Full-redundancies sequence for a TT_1	
• $\boldsymbol{v}_{1n}$ $[ONNN]$	$\boldsymbol{v}_{1p}$ $[POOO]$
$\boldsymbol{v}_{15}$ $[PONO]$	
$\boldsymbol{v}_{4n}$ $[OONO]$	• $\boldsymbol{v}_{4p}$ $[PPOP]$
$\boldsymbol{v}_{10n}$ $[ONNO]$	$\boldsymbol{v}_{10p}$ $[POOP]$

Full-redundancies sequence for a TT_2	
$\boldsymbol{v}_{15}$ $[PONO]$	
$\boldsymbol{v}_{4n}$ $[OONO]$	• $\boldsymbol{v}_{4p}$ $[PPOP]$
• $\boldsymbol{v}_{10n}$ $[ONNO]$	$\boldsymbol{v}_{10p}$ $[POOP]$
$\boldsymbol{v}_{45}$ $[PONP]$	

The pivot vector of the sequence is always selected as the vector that possesses the largest number of positive(P)/negative(N) states (marked as •). Thus, starting from this pivot vector, a

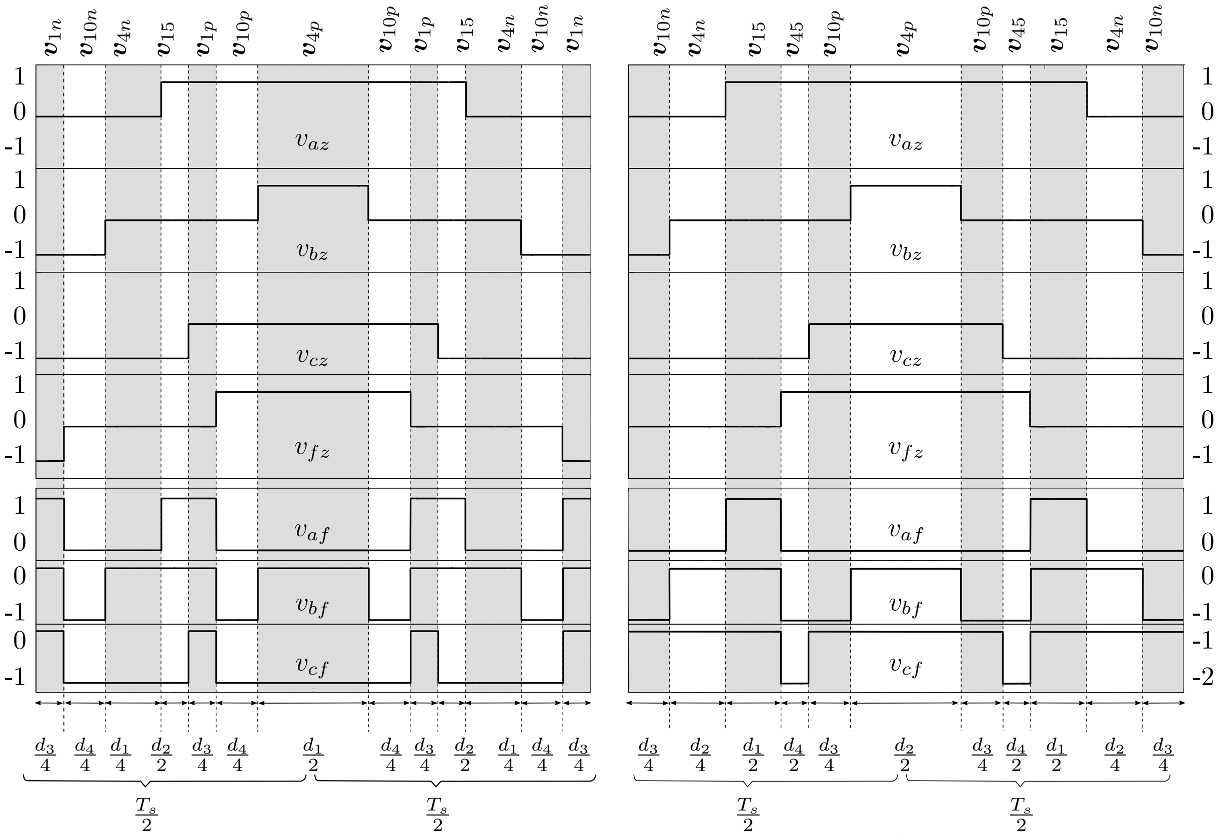

(a) (b)

Figure 5.10: Switching commutation for each leg of the four-leg NPC converter and the phase-to-neutral output voltages using *Full-Redundancy Symmetric n-type* sequence for: (a) pattern using a TT_1 formed by $\{\boldsymbol{v}_1, \boldsymbol{v}_{15}, \boldsymbol{v}_4, \boldsymbol{v}_{10}\}$ and (b) a TT_2 formed by $\{\boldsymbol{v}_{15}, \boldsymbol{v}_4, \boldsymbol{v}_{10}, \boldsymbol{v}_{45}\}$.

descending/ascending direction must be followed until each vector has been transitioned once. Thereby, depending on the selected pivot vector, two possible sequences can be selected. When the selected pivot vector posses the largest number of positive states, the sequence is called *p-type* sequence. Similarly, a sequence starting with the pivot vector that posses the largest number of negative states is defined as *n-type* sequence.

The arrows of Table 5.4 show the *n-type* sequence for each tetrahedron. This sequence is then mirrored in one sampled time T_s to symmetrically align the pattern, generating the *Full Redundancy Symmetric n-type* sequences as depicted in Fig. 5.10.

From Fig. 5.10a it can be noticed that the TT_1, composed of 3 redundant vectors and one non-redundant vector, generates a sequence composed of seven different vectors. Likewise, the sequence generated by a tetrahedron TT_2, illustrated in Fig. 5.10b, is arranged by using only six vectors. Using this switching pattern, different switching frequencies per device are generated depending on the different tetrahedrons that enclose the reference vector over one fundamental path.

In Chapter 2, a methodology to obtain the switching frequency per device was presented. Hence, in (2.31) a general expression for calculation of the per-device average switching frequency over a fundamental period T_1 was presented and is rewritten here for convenience as

$$\bar{f}_{dev_i} = \bar{f}^s_{dev_i} + f^f_{dev_i} \tag{5.27}$$

where $\bar{f}^{s}_{dev_i}$, presented in (2.32), represents the average switching frequency of the i^{th} device over the Λ sampling times T_s contained in one fundamental period T_1. The term $f^{f}_{dev_i}$, presented (2.33), represents the extra switching commutations (k_i), for the i^{th} switching device, generated during the transition from one sampling time to another over one fundamental period T_1. For convenience these expressions are rewritten here as

$$\bar{f}^{s}_{dev_i} = \sum_{n=1}^{\Lambda} \frac{f^{s_n}_{dev_i}}{\Lambda} \tag{5.28}$$

$$f^{f}_{dev_i} = \frac{k_i}{2} f_1, \tag{5.29}$$

From the sequences presented in Fig. 5.10, it can be noticed that some phase voltages, i.e. $v_{iz}\ i \in \{a, b, c, f\}$, posses only two transitions during one sampling time, e.g v_{az} and v_{cz} in Fig. 5.10a, while other phases posses four transitions, e.g v_{bz} and v_{fz} in Fig. 5.10a. The phase voltages modulated with four transitions require that all the four devices of one leg are switched on and off in one sampling time. Differently, when only two transitions are involved, two switches in one leg are switched on and off in one sampling time (see Fig. 2.13).

Thus, for instance, for the sampling interval showed in Fig. 5.10a, the switching frequency for each device of phases a and c are obtained as

$$f^{s_n}_{dev_{\bar{S}_{1a,1c}}} = f^{s_n}_{dev_{S_{1a,1c}}} = f_s \tag{5.30}$$

$$f^{s_n}_{dev_{\bar{S}_{2a,2c}}} = f^{s_n}_{dev_{S_{2a,2c}}} = 0 \tag{5.31}$$

Similarly for phases b and f of Fig. 5.10a, the switching frequency perform by each device is given by

$$f^{s_n}_{dev_{\bar{S}_{1b,1f}}} = f^{s_n}_{dev_{S_{1b,1f}}} = f_s \tag{5.32}$$

$$f^{s_n}_{dev_{\bar{S}_{2b,2f}}} = f^{s_n}_{dev_{S_{2b,2f}}} = f_s \tag{5.33}$$

By that, the average switching frequency of each device over one fundamental period T_1 is determined by the number of voltage transitions used in each leg of the converter at each sampling time. Consequently, this is determined by the type of tetrahedrons selected over T_1 and summarized as follows:

- In a TT_0: All four legs of the converter posses four voltage transitions. Therefore, for a reference vector that moves close to the origin of the modulation region and its trajectory only select TT_0 (see Fig. 5.5a), the switching frequency for each device would be equal to f_s.

- In a TT_1: Two legs of the converter posses four voltage transitions and two legs posses two voltage transitions.

- In a TT_2: One leg of the converter possesses four voltage transitions while three legs posses two voltage transitions.
- In a TT_3: All four legs of the converter posses only two voltage transitions. Therefore, for a ac reference vector that moves around the boundaries of the modulation region and its trajectory selects only TT_3 (see Fig. 5.5e), the switching frequency per device would be equal to $\frac{f_s}{2}$.

As a result, using *Full Redundancy Symmetric* switching pattern, the switching frequency of each device will be determined by the type of tetrahedrons that the reference path involves in one fundamental cycle. Although this frequency can be different for each device of the converter and its exact calculation depends on every path described by the reference vector, neglecting f^f_{dev}, it can be bounded by:

$$\frac{f_s}{2} < \bar{f}_{dev_i} < f_s \tag{5.34}$$

Therefore, the use of this switching pattern is most suitable for applications where the switching frequency of the devices is not critically limited and a better harmonic distortion of the controlled signal together with high controllability and less ripple over the current through the NP of the converter is desirable.

5.4.3.2 Single Redundancy Switching Pattern

Although the previous switching sequences provides good controllability for balancing voltages over the dc-link capacitors. It produces high and unequal switching frequencies for each device of the converter, which in some applications may be unacceptable. In order to reduce and equally distribute the switching frequency among all the devices, a method that uses only one redundancy is presented in this section.

At least one redundancy is required, as it allows the control over the NP current i_z. Thereby, only the redundancies of the redundant vector with the largest dwell time, i.e. with the highest influence over the NP current, is implemented at each sample time. The sequence pattern is based on the same algorithm explained in the previous section. However, the pivot vector is not selected based on the number of positive(P)/negative(N) states, but it is the redundant vector with the largest dwell time. Consequently, starting from this vector, a *n-* or *p-type* sequence can be generated and the sequence stops once it reaches the redundancy of this pivot vector. Thus, for instance, for the TT_1 of Table 5.4 and using $\boldsymbol{v}_{10p}$ as the pivot vector, the *p-type* sequence is: $\boldsymbol{v}_{10p}, \boldsymbol{v}_{1p}, \boldsymbol{v}_{15}, \boldsymbol{v}_{4n}, \boldsymbol{v}_{10n}$. Using $\boldsymbol{v}_{4n}$ as the pivot vector, the correct *n-type* sequence is: $\boldsymbol{v}_{4n}, \boldsymbol{v}_{15}, \boldsymbol{v}_{1p}, \boldsymbol{v}_{10p}, \boldsymbol{v}_{4p}$. This last sequence is shown in Fig. 5.11a, where only two voltage transitions per leg are employed at each sampling time. Similarly, Fig. 5.11b shows the *n-type* sequence for the TT_2 of Table 5.4 using also $\boldsymbol{v}_{4n}$ as the pivot vector. Comparing Fig. 5.10 with Fig. 5.11 the reduction and evenness of the switching frequency at each leg is evident. Thereby, regardless of the path described by the reference vector, neglecting f^f_{dev} and considering that *ac* signals are being modulated, the switching frequency per device over a fundamental cycle is given by:

$$\bar{f}_{dev} = \frac{f_s}{2} \tag{5.35}$$

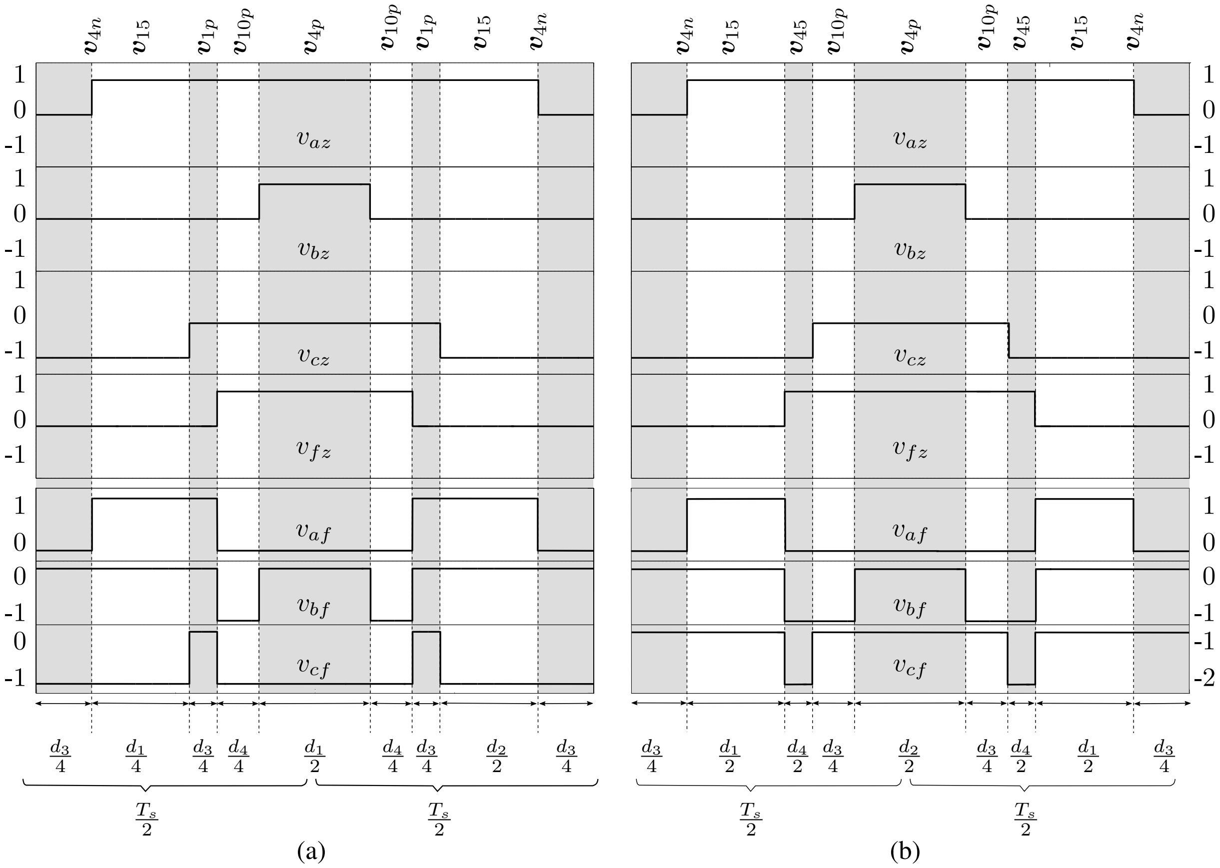

Figure 5.11: Switching commutation

Therefore, under this pattern the switching frequency for each device is nearly constant and will be increased only by the small term f_{dev}^{f}, which has to be determined by every different reference path.

5.5 Voltage balance of the dc-link Capacitors

In order to complete the SVM algorithm for the four-leg NPC converter, a strategy to balance the dc-link capacitors must be defined. Different techniques to balance the voltages on the dc-link capacitors for the three-leg NPC converters have been reported in the literature. These methods were presented in Chapter 2 and were mainly categorized as: active control, passive control and hysteresis control [66], [53], [164]. In this work an active control methodology for a four-leg NPC is described, as it will be later implemented in an experimental rig. Thereby, the dwell times for the redundant vectors are calculated in order to track a reference NP current, $\bar{i}_z^*$, which is provided by an external *PI* controller (see Fig. 2.20).

Using (5.1), the NP current i_z generated by each of the four vectors that form the selected tetrahedron, i.e. $\boldsymbol{v}_{\alpha\beta\gamma}^{s1}$, $\boldsymbol{v}_{\alpha\beta\gamma}^{s2}$, $\boldsymbol{v}_{\alpha\beta\gamma}^{s3}$ and $\boldsymbol{v}_{\alpha\beta\gamma}^{s4}$, can be calculated. Thus, the averaged NP current in one sample time T_s can be expressed as

$$\bar{i}_z = \sum_{i=1}^{4} \lambda_i \cdot d_i \cdot i_{z_i}\left(\boldsymbol{v}^{s_i}_{\alpha\beta\gamma}\right) \tag{5.36}$$

Where $i_{z_i}\left(\boldsymbol{v}^{s_i}_{\alpha\beta\gamma}\right)$ represents the current through the NP generated by $\boldsymbol{v}^{s_i}_{\alpha\beta\gamma}$ (calculated as (5.1)). In case $\boldsymbol{v}^{s_i}_{\alpha\beta\gamma}$ possesses redundancies, then the current produced by the positive redundancy is used in (5.36). Consequently, d_i are the dwell times for each of the selected vectors calculated in (5.24). Furthermore, λ_i is known as the sub-modulation index and represent the time proportion between the positive and negative redundancies of a redundant vector. The calculation of λ_i is limited to $\lambda_i \in [-1, 1]$ and is calculated to obtain an averaged NP current $\bar{i}_z$ equal to the external reference i_z^*. Due to (5.36) is a general representation, the sub-modulation index λ_i must be set to 1 for non-redundant vectors

The number of unknown indices λ_i to be calculated in (5.36) depends on the available redundant vectors. Thus, when the *Single-Redundancy Symmetric* switching pattern is used, only one index λ_i needs to be calculated at each sample time, which can be directly obtained using (5.36).

On the other hand, for *Full-Redundancy Symmetric* switching pattern, the number of indices λ_i to be calculated in (5.36) can be greater than one, which entails infinite number of solutions for each λ_i. Thereby, in order to solve this equation, the following method is used:

- Firstly, only the λ_i for the redundant vector with the largest dwell time is obtained, while the others indices λ_i are equaled to 0.
- In case that after the first calculation the condition $\bar{i}_z{=}i_z^*$ is not fulfilled, i.e. the first sub-modulation is saturated to 1 or -1. The sub-modulation index λ_i for the redundant vector with the second largest dwell time is included into the equation and calculated. Similarly to the first step, the rest of the indices λ_i are equaled to 0.
- The same process continue until the condition $\bar{i}_z{=}i_z^*$ is fulfilled or no more redundant vectors are available.

This strategy minimize the number of sub-dwell times equal to zero, which can produce undesirable switching transitions.

Once the sub-modulation index λ_i have been calculated, the sub-dwell times d_{i_p} and d_{i_n} have to be obtained. Equation (5.37) shows the calculation of d_{i_p} and d_{i_n} based on λ_i. The sub-dwell times d_{i_p} and d_{i_n} represent the dwell time for the positive and negative redundancies of a redundant vector respectively.

$$\left.\begin{aligned} d_{i_p} &= (1+\lambda_i)\cdot \tfrac{d_i}{2} \\ d_{i_n} &= (1-\lambda_i)\cdot \tfrac{d_i}{2} \\ |\lambda_i| &\leq 1 \end{aligned}\right\} \quad i \in \{1,2,3,4\} \tag{5.37}$$

5.6 Overmodulation Limitation

Previously in this chapter it has been assumed that the reference vector always resides inside the modulation region presented in Fig. 5.2. Although this assumption is usually true during normal operation, under special circumstances such as: transients, overload for short periods of time or excessive compensation of harmonic content, the reference vector can be beyond the limits of this space. In Chapter 2, the conventional methods for overmodulation were presented. These overmodulation methods are intend for electrical drives, where boosting the fundamental component of the modulated waveform is achieved at expenses of incorporation of non-characteristic low order harmonics. The incorporation of these non expected low order harmonics can be acceptable in drive application. However, for power conditioner, where the compensation of harmonics content is one of the main objectives, this can cause serious problems, such as: excitation of resonances in output filters or loads, phase shift of the compensated harmonics, which can produce malfunction of the close-loop controllers, or increment of the harmonic distortion of the controlled signal beyond of the standards requirements. Therefore, a method for limiting the reference vector without introducing extra harmonics and achieving maximum utilization of the dc-link voltage is required. For the best knowledge of the author, this issue have not been reported in the literature, where most of the authors either saturate the reference vector to the limits of the modulation region, to a unitary circle or assume a dc-link voltage large enough to always be able to modulate any reference vector [26, 33, 59].

The increment in the number of levels of a converter only subdivide the modulation region in more and smaller sub-regions, introducing more available vectors inside a region and allowing a finer tracking of a controlled signal. However, the external boundaries of the modulation region is exclusively defined by the dc-link voltage level. Thereby, as the study of overmodulation strategies only involve the boundaries of a modulation space. It can be said that this study is independent of the number of levels of the converter and only regards whether the modulation is achieved in $\alpha\beta$ or $\alpha\beta\gamma$ space.

5.6.1 Overmodulation Limitation in $\alpha\beta$ plane

Three-leg converters are usually intend to work with three phases and no consideration of unbalances or zero sequence components. Therefore, its zero sequence, or γ axis, is usually neglected and a modulation is achieved in the $\alpha\beta$ plane. In order to limit the reference vector without introducing additional harmonic components and maximizing the utilization of the dc-link voltage, a constant gain has to used to limit the trajectory of the reference vector to the point that its trajectory is tangent to the boundaries of the modulation region. To achieve this, let us represent the reference vector for a power conditioning converter as:

$$\boldsymbol{v}^*_{\alpha\beta} = \boldsymbol{v}^*_{f_{\alpha\beta}} + \boldsymbol{v}^*_{h_{\alpha\beta}}, \tag{5.38}$$

where the reference vector $\boldsymbol{v}^*_{\alpha\beta}$ has been separated into its fundamental component $\boldsymbol{v}^*_{f_{\alpha\beta}}$ and its harmonic component $\boldsymbol{v}^*_{h_{\alpha\beta}}$, which contains all the harmonic components to be later modulated by the converter.

Fig. 5.12 shows the decomposition of $\boldsymbol{v}^*_{\alpha\beta}$ into $\boldsymbol{v}^*_{f_{\alpha\beta}}$ and $\boldsymbol{v}^*_{h_{\alpha\beta}}$ for a reference vector placed beyond the boundaries of the modulation region in the $\alpha\beta$ plane (it is assumed that $\boldsymbol{v}^*_{f_{\alpha\beta}}$ is inside

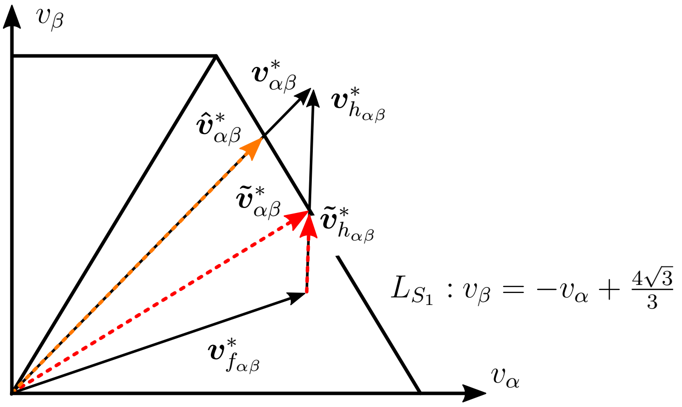

Figure 5.12: Limitation for the reference vector represented in the first quadrant of the modulation region in the $\alpha\beta$ plane.

the modulation region). Additionally, $\hat{\boldsymbol{v}}^*_{\alpha\beta}$ represents the typical saturation of the reference vector, where $\boldsymbol{v}^*_{\alpha\beta}$ is limited to the border of the hexagon. Otherwise, the proposed method limits $\boldsymbol{v}^*_{\alpha\beta}$ to $\tilde{\boldsymbol{v}}^*_{\alpha\beta}$ by limiting the harmonic component $\boldsymbol{v}^*_{h_{\alpha\beta}}$ to $\tilde{\boldsymbol{v}}^*_{h_{\alpha\beta}}$ by

$$\tilde{\boldsymbol{v}}^*_{h_{\alpha\beta}} = \eta \cdot \boldsymbol{v}^*_{h_{\alpha\beta}}, \tag{5.39}$$

and η represent a constant value that limits $\boldsymbol{v}^*_{h_{\alpha\beta}}$ to maintain the reference path inside the modulation region. Thus, $\tilde{\boldsymbol{v}}^*_{\alpha\beta}$ is obtained as the addition of the limited vector $\tilde{\boldsymbol{v}}^*_{h_{\alpha\beta}}$ and the fundamental component $\boldsymbol{v}^*_{f_{\alpha\beta}}$. In order to obtain η, the intersection between $\boldsymbol{v}^*_{h_{\alpha\beta}}$ and the boundary line of each sector has to be calculated. The equations that define the borders for each sector (L_{S_1} to L_{S_6}) are described as:

$$L_{S_1}: \quad v_\beta = -v_\alpha + \frac{4\sqrt{3}}{3} \tag{5.40}$$

$$L_{S_2}: \quad v_\beta = \frac{2\sqrt{3}}{3} \tag{5.41}$$

$$L_{S_3}: \quad v_\beta = v_\alpha + \frac{4\sqrt{3}}{3} \tag{5.42}$$

$$L_{S_4}: \quad v_\beta = -v_\alpha - \frac{4\sqrt{3}}{3} \tag{5.43}$$

$$L_{S_5}: \quad v_\beta = -\frac{2\sqrt{3}}{3} \tag{5.44}$$

$$L_{S_6}: \quad v_\beta = v_\alpha - \frac{4\sqrt{3}}{3} \tag{5.45}$$

The intersection point between one of these straights and the reference vector $\boldsymbol{v}^*_{h_{\alpha\beta}}$ provides the vector $\tilde{\boldsymbol{v}}^*_{\alpha\beta}$. Thereby, η can be easily calculated as

$$\eta = \frac{|\tilde{\boldsymbol{v}}^*_{\alpha\beta} - \tilde{\boldsymbol{v}}^*_{f_{\alpha\beta}}|}{|\boldsymbol{v}^*_{h_{\alpha\beta}}|} \tag{5.46}$$

This procedure is performed at every sampling time, where η is overwritten always that a smaller value is found. Thereby, after a cycle, only one constant value is used to limit the reference vector.

Let us consider as example the following reference vector, for compensation of 7^{th} harmonic:

$$v_{af}^{*} = \frac{2\sqrt{3}}{3}\left[0.9\sin\left(\omega t\right) + 0.2\sin\left(7\omega t\right)\right] \tag{5.47}$$

$$v_{bf}^{*} = \frac{2\sqrt{3}}{3}\left[0.9\sin\left(\omega t - \frac{2\pi}{3}\right) + 0.2\sin\left(7\omega t - 7\frac{2\pi}{3}\right)\right] \tag{5.48}$$

$$v_{cf}^{*} = \frac{2\sqrt{3}}{3}\left[0.9\sin\left(\omega t + \frac{2\pi}{3}\right) + 0.2\sin\left(7\omega t + 7\frac{2\pi}{3}\right)\right] \tag{5.49}$$

Applying the Clarke transformation of (5.3) in (5.47) to (5.49), the reference vector $\boldsymbol{v}_{\alpha\beta}^{*}$ is obtained and depicted in Fig. 5.13. Fig. 5.13b shows the reference vector $\boldsymbol{v}_{\alpha\beta}^{*}$ and the vector $\hat{\boldsymbol{v}}_{\alpha\beta}^{*}$, which represents the path saturated by the borders of the allowable modulation region. On the other hand, in Fig. 5.13a, the vector $\tilde{\boldsymbol{v}}_{\alpha\beta}^{*}$ represents the path obtained by the proposed limitation. It can be clearly seen, that the limited curve described by $\tilde{\boldsymbol{v}}_{\alpha\beta}^{*}$ remains inside and tangent to the boundaries of the modulation region, this confirm that the dc-link voltage is being fully utilized.

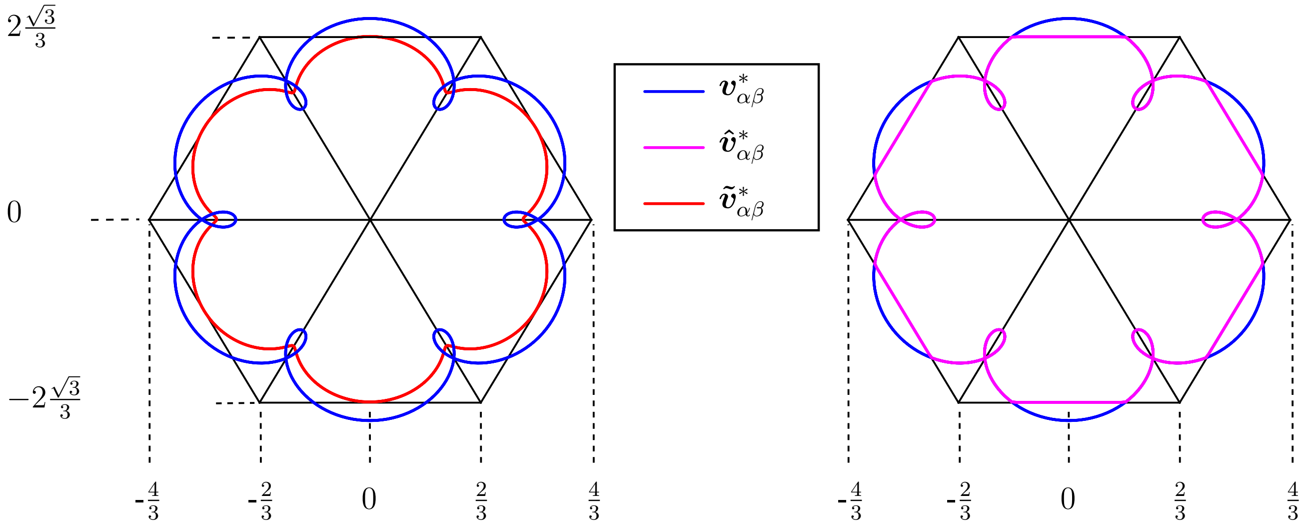

(a) (b)

Figure 5.13: (a) Reference vector $\boldsymbol{v}_{\alpha\beta}^{*}$ and the limited reference $\tilde{\boldsymbol{v}}_{\alpha\beta}^{*}$, with $\eta \approx 0.5$. In (b) $\hat{\boldsymbol{v}}_{\alpha\beta}^{*}$ represents the limitation of the reference vector by saturation of the trajectory to the borders of the modulation region.

Fig. 5.13 shows the Fast Fourier Transformation (FFT) for the α and β components of $\boldsymbol{v}_{\alpha\beta}^{*}$,

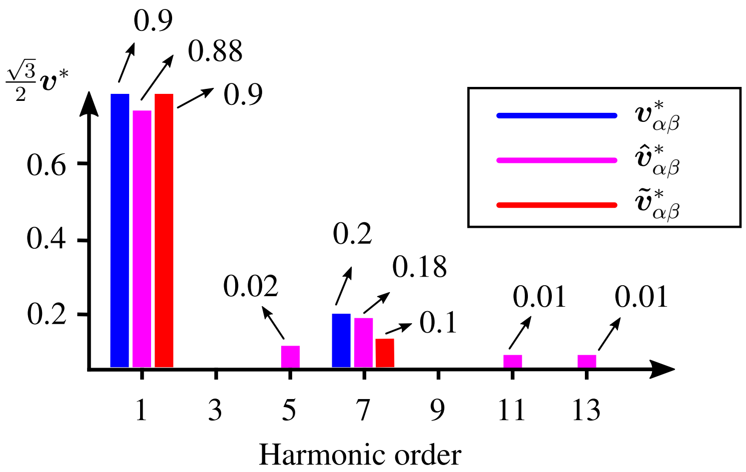

Figure 5.14: Magnitude of the harmonic components for the vectors $\boldsymbol{v}^*_{\alpha\beta}$, $\hat{\boldsymbol{v}}^*_{\alpha\beta}$ and $\tilde{\boldsymbol{v}}^*_{\alpha\beta}$. The shift phases for each component are: $\{\angle v^*_{\alpha_1}, \angle v^*_{\alpha_7}, \angle\hat{v}^*_{\alpha_1}, \angle\hat{v}^*_{\alpha_7}, \angle\tilde{v}^*_{\alpha_1}, \angle\tilde{v}^*_{\alpha_7}\}$=0°, $\{\angle v^*_{\beta_1}, \angle v^*_{\beta_7}, \angle\hat{v}^*_{\beta_1}, \angle\hat{v}^*_{\beta_7}, \angle\tilde{v}^*_{\beta_1}, \angle\tilde{v}^*_{\beta_7}\}= -90°$. Additionally, for $\hat{\boldsymbol{v}}^*_{\alpha\beta}$: $\angle\hat{v}^*_{\alpha_5}$=0°, $\angle\hat{v}^*_{\alpha_{11}}$=0°, $\angle\hat{v}^*_{\alpha_{13}}$=180° and $\angle\hat{v}^*_{\beta_5}$=90°, $\angle\hat{v}^*_{\beta_{11}}$=90°, $\angle\hat{v}^*_{\beta_{13}}$=90°.

$\hat{\boldsymbol{v}}^*_{\alpha\beta}$ and $\tilde{\boldsymbol{v}}^*_{\alpha\beta}$. As the system is balanced and symmetric, the magnitude of the harmonic components of the α and β waveforms for each of the above mentioned vectors are identical and they differ only on their shift phases. Likewise, this harmonic spectrum also represents the harmonic content of the reference voltages in abc coordinates.

From Fig. 5.14 it is clearly observed that the proposed method does not incorporate additional harmonics to the limited waveform. However, it increase the error in tracking the 7^{th} harmonic. Thus, $\tilde{\boldsymbol{v}}^*_{\alpha\beta}$ represents the maximum feasible trajectory to track the reference vector without incorporation of additional harmonics.

One additional issue has to be considering before implementing this method. As showed in Fig. 5.12, in order to limit the harmonic vector $\boldsymbol{v}^*_{h_{\alpha\beta}}$ the correct border, i.e. sector, has to be selected to then intersect $\boldsymbol{v}^*_{h_{\alpha\beta}}$ with one of the straights presented in (5.40) to (5.45). Intuitively the same sector of $\boldsymbol{v}^*_{\alpha\beta}$ is firstly used. However, as shown in Fig. 5.15, around the corners of each sector it is feasible that the sector of $\boldsymbol{v}^*_{\alpha\beta}$ differs with the sector where $\boldsymbol{v}^*_{h_{\alpha\beta}}$ has to be intersected. This would lead to a limited reference vector which resides out of the modulation region. In order to overcome this problem, after calculating $\tilde{\boldsymbol{v}}^*_{h_{\alpha\beta}}$, it is verify that $\tilde{\boldsymbol{v}}^*_{\alpha\beta}$ belongs to the modulation region. In case it resides out of the modulation region, then $\tilde{\boldsymbol{v}}^*_{h_{\alpha\beta}}$ is recalculated using the boundary of closest adjacent sector.

To conclude, the diagram of Fig. 5.16 summarizes the proposed method for limiting the reference vector without incorporation of additional harmonics. For now it has been considered that the fundamental vector $\boldsymbol{v}^*_{f_{\alpha\beta}}$ is placed inside the allowable modulation region previous to the limitation of $\boldsymbol{v}^*_{h_{\alpha\beta}}$. However, $\boldsymbol{v}^*_{f_{\alpha\beta}}$ could also be placed beyond the boundaries of the modulation region, which will be analyzed in the following subsection.

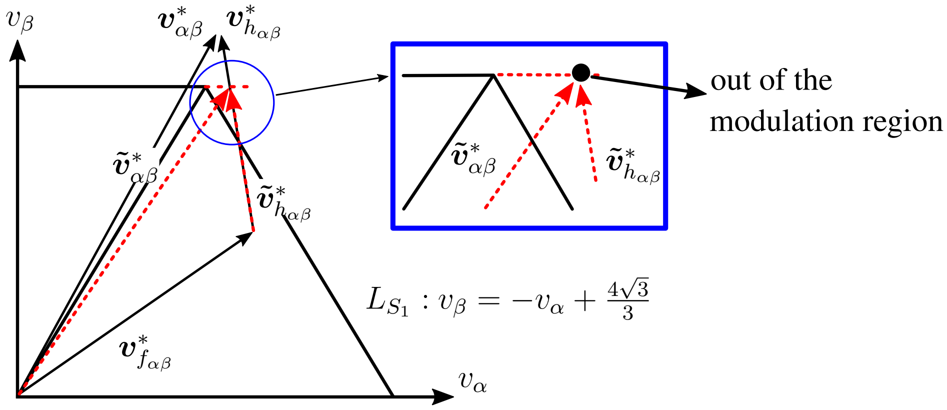

Figure 5.15: Representation of a false selection of sector for limiting $\boldsymbol{v}^*_{h_{\alpha\beta}}$. $\boldsymbol{v}^*_{\alpha\beta}$ belongs to sector II. However $\boldsymbol{v}^*_{h_{\alpha\beta}}$ should be limited with the border of sector I.

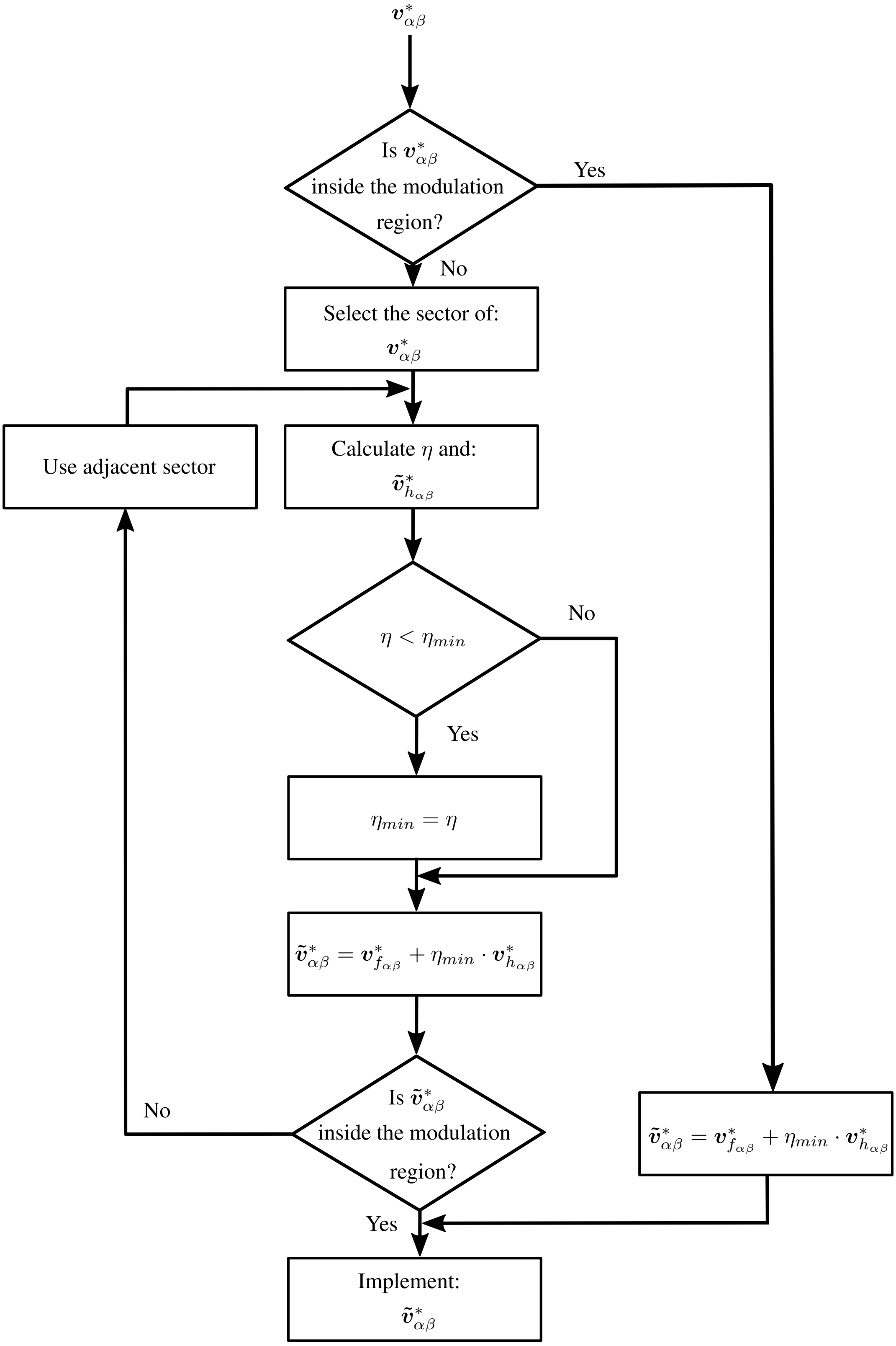

Figure 5.16: Diagram for the proposed Overmodulation limitation in the $\alpha\beta$ space. Initial value for η_{min} is equal to one.

5.6.2 Overmodulation Limitation in $\alpha\beta\gamma$ Space

Although, for simplicity, the proposed overmodulation methodology was introduced for balanced and symmetric systems in the $\alpha\beta$ plane, its real potential is exploited for unbalanced and non-symmetric systems.

When an overmodulation algorithm wants to be implemented in a power conditioner, two important conditions has to be accomplished. Firstly, it is important to avoid incorporation of additional harmonics on the reference vector, as they can produce undesirable resonances, specially when they are connected with second or third order systems. Secondly, as it was presented in Chapter 4, when these extra harmonic coincide with one of the components compensated by a close-loop controller, it will trigger a false compensation, which could lead to overamplification of the compensated signal. Moreover, the phase shift of each reference harmonic component must remain unalterable after the overmodulation algorithm, as a mismatch in the phase shift between the reference signal and the real modulated signal could also produce overamplification of the compensated signal, generating trip of the overvoltage or overcurrent protections. This is specially important for compensation of high order harmonics as presented in Chapter 4.

Extending the method presented in subsection 5.6.1, to the $\alpha\beta\gamma$ space, the reference vector presented in (5.38) can be expressed as

$$\boldsymbol{v}^*_{\alpha\beta\gamma} = \boldsymbol{v}^*_{f_{\alpha\beta\gamma}} + \boldsymbol{v}^*_{h_{\alpha\beta\gamma}} + \boldsymbol{v}^*_{zs_{\alpha\beta\gamma}}, \tag{5.50}$$

where $\boldsymbol{v}^*_{\alpha\beta\gamma}$ is the reference vector in the $\alpha\beta\gamma$ space, which is decomposed into its fundamental component $\boldsymbol{v}^*_{f_{\alpha\beta\gamma}}$, harmonic components $\boldsymbol{v}^*_{h_{\alpha\beta\gamma}}$ and the zero sequence components $\boldsymbol{v}^*_{zs_{\alpha\beta\gamma}}$, which represents the compensated harmonics that only posses values on the γ axis.

In Fig. 5.17a the $\alpha\beta\gamma$ space of Fig. 5.2 is redrawn with a reference vector inside the region. In Fig. 5.17a the decomposition of $\boldsymbol{v}^*_{\alpha\beta\gamma}$ into its three components is presented. For a better understanding, Fig. 5.17b shows a top view of Fig. 5.17a. As expected, the zero sequence vector $\boldsymbol{v}^*_{zs_{\alpha\beta\gamma}}$ is represented simply as a point in the $\alpha\beta$ plane.

Similarly to the previously explained methodology, the aim is to restrict $\boldsymbol{v}^*_{\alpha\beta\gamma}$ to the $\alpha\beta\gamma$ space shown in Fig. 5.17 by limiting each of its components. Thereby, the limited reference vector can be expressed as

$$\tilde{\boldsymbol{v}}^*_{\alpha\beta\gamma} = \tilde{\boldsymbol{v}}^*_{f_{\alpha\beta\gamma}} + \tilde{\boldsymbol{v}}^*_{h_{\alpha\beta\gamma}} + \tilde{\boldsymbol{v}}^*_{zs_{\alpha\beta\gamma}} \tag{5.51}$$

$$\tilde{\boldsymbol{v}}^*_{f_{\alpha\beta\gamma}} = \xi \cdot \boldsymbol{v}^*_{f_{\alpha\beta\gamma}} \tag{5.52}$$

$$\tilde{\boldsymbol{v}}^*_{h_{\alpha\beta\gamma}} = \eta \cdot \boldsymbol{v}^*_{h_{\alpha\beta\gamma}} \tag{5.53}$$

$$\tilde{\boldsymbol{v}}^*_{zs_{\alpha\beta\gamma}} = \tau \cdot \boldsymbol{v}^*_{zs_{\alpha\beta\gamma}}, \tag{5.54}$$

where ξ, η and τ are constant values. Thus, first ξ is obtained limiting the fundamental vector, $\boldsymbol{v}^*_{f_{\alpha\beta\gamma}}$, to the allowable modulation region. Consequently, calculating η the harmonic vector $\boldsymbol{v}^*_{h_{\alpha\beta\gamma}}$ is also limited. Finally, $\boldsymbol{v}^*_{zs_{\alpha\beta\gamma}}$ is limited calculating τ. In order to intersect each component with the boundaries of the allowable modulation region, the equations for the surface planes that form the polygon presented in Fig. 5.17a must be obtained. The six lateral boundaries of this polygon are formed by the γ extension of the six straights that form the hexagonal

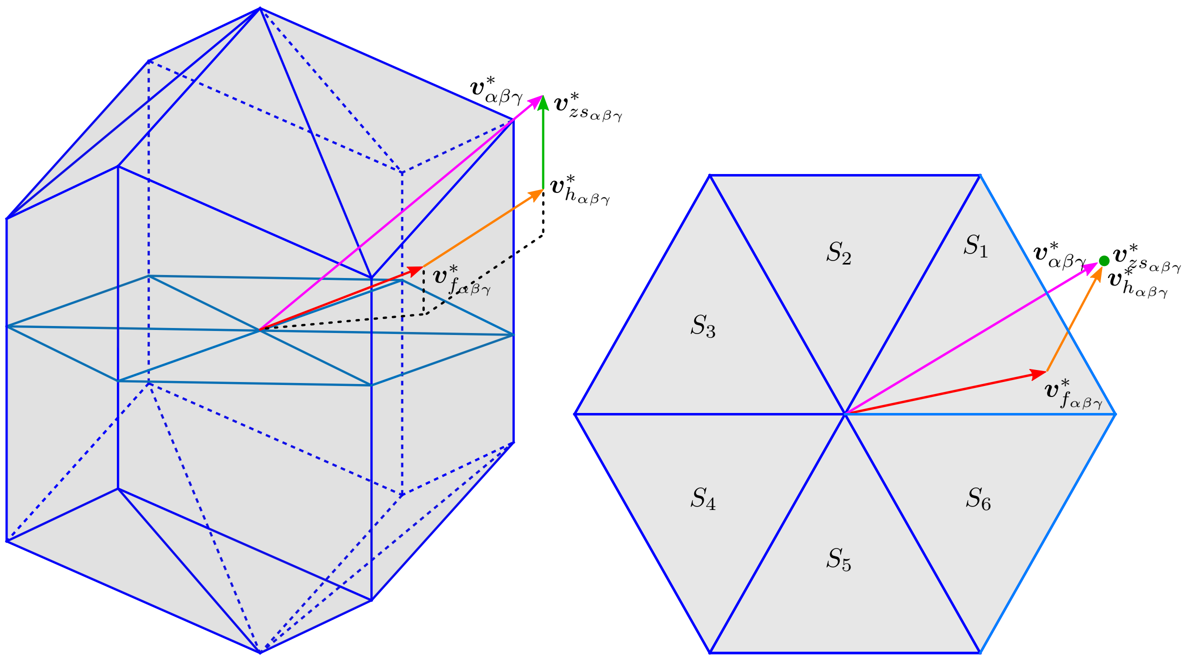

(a) (b)

Figure 5.17: (a) Reference vector $\boldsymbol{v}^*_{\alpha\beta\gamma}$ in the $\alpha\beta\gamma$ space decomposed into its fundamental, harmonics and zero sequence components ($\boldsymbol{v}^*_{f_{\alpha\beta\gamma}}$, $\boldsymbol{v}^*_{h_{\alpha\beta\gamma}}$, $\boldsymbol{v}^*_{zs_{\alpha\beta\gamma}}$). In (b) a top view of this figure.

modulation region of Fig. 5.17b. By that, same equations presented in (5.40) to (5.45) can be used for represent these surfaces. Additionally, the polygon is bounded at the top and bottom by three different planes. Each of these planes are placed above or below of different pairs of sectors according to Fig. 5.17b as follows:

Top boundary planes:

Sector S_1 and S_6, P_1: $$v_\gamma = 2 - v_\alpha \tag{5.55}$$

Sector S_2 and S_3, P_2: $$v_\gamma = 2 + \frac{v_\alpha}{2} - \frac{\sqrt{3}}{2}v_\beta \tag{5.56}$$

Sector S_4 and S_5, P_3: $$v_\gamma = 2 + \frac{v_\alpha}{2} + \frac{\sqrt{3}}{2}v_\beta \tag{5.57}$$

Bottom boundary planes:

Sector S_1 and S_2, P_4: $$v_\gamma = -2 + \frac{v_\alpha}{2} + \frac{\sqrt{3}}{2}v_\beta \tag{5.58}$$

Sector S_3 and S_4, P_5: $$v_\gamma = -2 - v_\alpha \tag{5.59}$$

Sector S_5 and S_6, P_6 : $$v_\gamma = -2 + \frac{v_\alpha}{2} - \frac{\sqrt{3}}{2}v_\beta \tag{5.60}$$

In order to calculate ξ, η and τ, first the fundamental vector $\boldsymbol{v}^{*}_{f_{\alpha\beta\gamma}}$ is intersected with the corresponding plane. The intersection point is defined as $\boldsymbol{v}^{int}_{f_{\alpha\beta\gamma}}$ and ξ is obtained as

$$\xi{=}\frac{|\tilde{\boldsymbol{v}}^{int}_{f_{\alpha\beta\gamma}}|}{|\boldsymbol{v}^{*}_{f_{\alpha\beta\gamma}}|} \tag{5.61}$$

If the fundamental vector has to be limited, it automatically defines $\eta{=}0$. However, usually the dc-link voltage is designed to avoid this condition and ξ is commonly equal to 1. Additionally, ξ can be virtually limited to a smaller value to provide a margin for compensation of harmonics components. Thereafter, with $\xi{=}1$, the intersection of $\boldsymbol{v}^{*}_{h_{\alpha\beta}}$ with its corresponding plane is achieved and defined as $\boldsymbol{v}^{int}_{h_{\alpha\beta}}$. Thereby, η is obtained as

$$\eta{=}\frac{|\boldsymbol{v}^{int}_{h_{\alpha\beta\gamma}} - \xi\boldsymbol{v}^{*}_{f_{\alpha\beta\gamma}}|}{|\boldsymbol{v}^{*}_{h_{\alpha\beta\gamma}}|} \tag{5.62}$$

Finally, using the limited fundamental and harmonic components, $\tilde{\boldsymbol{v}}^{*}_{f_{\alpha\beta\gamma}}$ and $\tilde{\boldsymbol{v}}^{*}_{h_{\alpha\beta\gamma}}$, the intersection point of the the zero-sequence component $\boldsymbol{v}^{*}_{zs_{\alpha\beta\gamma}}$ with one of the top or bottom planes is defined as $\boldsymbol{v}^{int}_{zs_{\alpha\beta\gamma}}$ and τ is calculated as

$$\tau{=}\frac{v^{int}_{zs_{\gamma}} - \xi v^{*}_{f_{\gamma}} - \eta v^{*}_{h_{\gamma}}}{v^{*}_{zs_{\gamma}}} \tag{5.63}$$

Due to the zero-sequence vector $\boldsymbol{v}^{*}_{zs_{\alpha\beta\gamma}}$ possesses only γ component, only the γ component of the fundamental and harmonic vectors are used in (5.63).

5.7 Experimental Rig

The experimental rig used to validate the three-dimensional SVM proposed in this Chapter is illustrated in Fig 5.18 (load is not shown). It is mainly composed of a control platform and the power electronics interface, based on the four-leg NPC converter presented in Fig. 5.20. The control platform is based on a Pentium-System board (2Gb RAM host PC with a 3.2GHz Pentium processor running the Arch-Linux operating system) and an FPGA board. This Pentium system runs the algorithm in real time using the Real Time Application Interface (RTAI) for Linux and is connected to the FPGA board by means of an ISA-bus. The FPGA board receives the measured states, implements over-voltage and over-current protection, implements the commutation with the Pentium Processor, implements $2\mu s$ dead time for each IGBT and sends the control signals to the IGBTs. Furthermore, the gate-signals are sent through optical fibers from the FPGA board to the four-leg NPC .

A more detailed view of the power electronics interface is illustrated in Fig. 5.19. For completeness, the output second order *LC* filter is shown as it will be used in the next chapter. Moreover, voltage and current measurements boards are also depicted. The current measurement board is based on a $60A$, $2MHz$ bandwidth, Sensitec CMS3015 current sensor. The voltage measurement board is based on $500V$ voltage transducer LEM LV25-P.

Fig. 5.20 shows a more detailed view of the four-leg NPC converter. It is based on the Microsemi IGBT-APTGL60TL120T3G, $60A$ and $1200V$, with a heat sink designed for up to around $6kW$. The drive circuit for each of the four leg of the converter, the dc-link capacitors and the fiber optics signals coming from the control platform can be clearly identify. The dc voltage is provided by a dc power supply, Heiden EA PS 81000-30, $1kV$, $30A$.

The experimental data has been acquired using a Textronix DPO 3024 Digital Phosphor Osciloscope, 200MHz, 1GS/s.

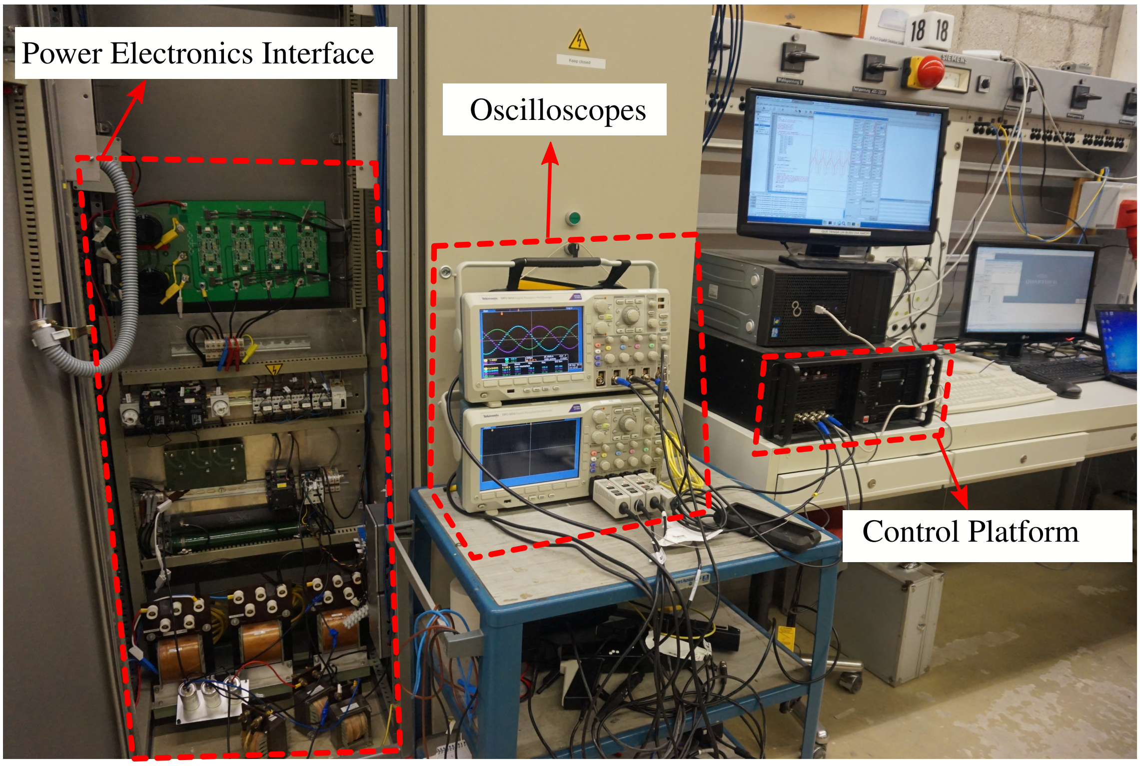

Figure 5.18: Complete view of a 6kW experimental rig for a four-leg NPC converter.

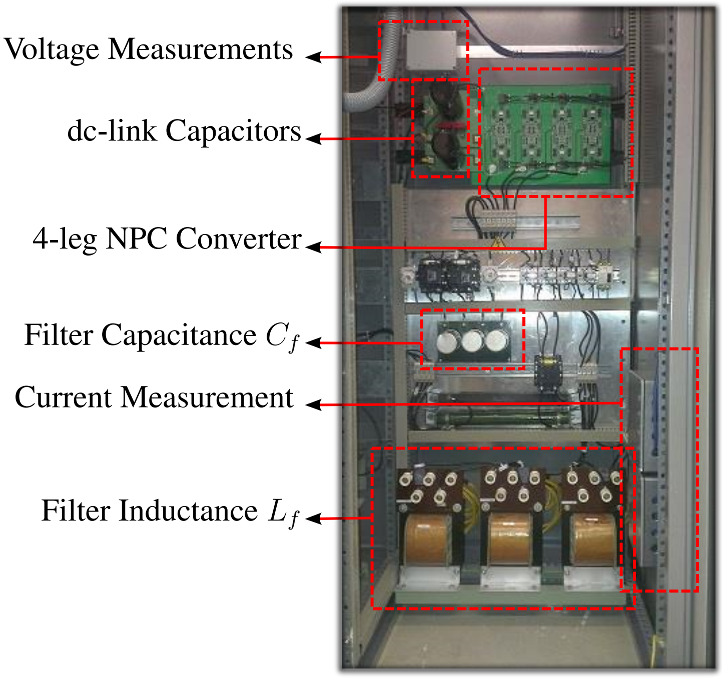

Figure 5.19: Power electronic interface and measurements boards for a 6kW experimental rig based on a four-leg NPC converter.

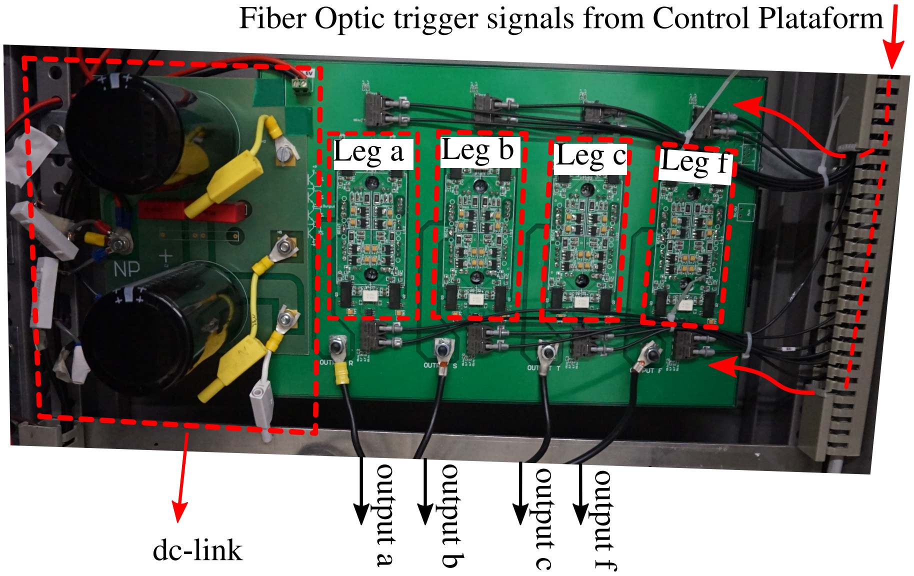

Figure 5.20: Power electronics board and dc-link interface for a four-leg NPC converter.

5.8 Experimental Assessment

In order to validate the proposed three-dimensional SVM and the overmodulation algorithm presented in this chapter, this section is divided in three parts. Firstly, the proposed three-dimensional SVM algorithm is tested in a four-leg NPC converter. The algorithm is implemented in open-loop and in open circuit under different scenarios to show the effectiveness of the algorithm. Secondly, the control over the dc-link voltage is analyzed under different unbalanced and non-linear loads. Finally, the proposed overmodulation algorithm is also tested under different conditions.

5.8.1 Three-dimensional SVM

In order to proof the good performance of the three-dimensional SVM, two important criteria has to be analyzed. First, the output voltage must be able to precisely modulate each of the harmonic components present at the reference waveform, accomplishing with their phase and magnitude. Secondly, the modulated waveforms must accomplish with the *minimum switching transition* principle, generating a proper pulse pattern, which reduces the harmonic distortion and switching losses.

Fig. 5.21 shows the output phase-to-neutral voltages for the four-leg NPC converter presented in Fig. 5.1 implemented with *Single-Redundancy Symmetric* switching pattern (see Section 5.4.3.2), which produces an approximately constant switching frequency under any condition. No load have been connected to the terminals of he converter. The reference for each phase of Fig. 5.21 has been selected as

$$v_{af}^{*}=\frac{270}{2}\frac{2}{\sqrt{3}}0.95\cos(100\pi t) \tag{5.64}$$

$$v_{bf}^{*}=\frac{270}{2}\frac{2}{\sqrt{3}}0.95\cos(100\pi t-\frac{2\pi}{3}) \tag{5.65}$$

$$v_{cf}^{*}=\frac{270}{2}\frac{2}{\sqrt{3}}0.95\cos(100\pi t+\frac{2\pi}{3}) \tag{5.66}$$

$$\tag{5.67}$$

Moreover, the dc-link voltage and sampling frequency are set to (see Fig. 5.1)

$$2V_{dc}=270V \tag{5.68}$$

$$f_s=6kHz \tag{5.69}$$

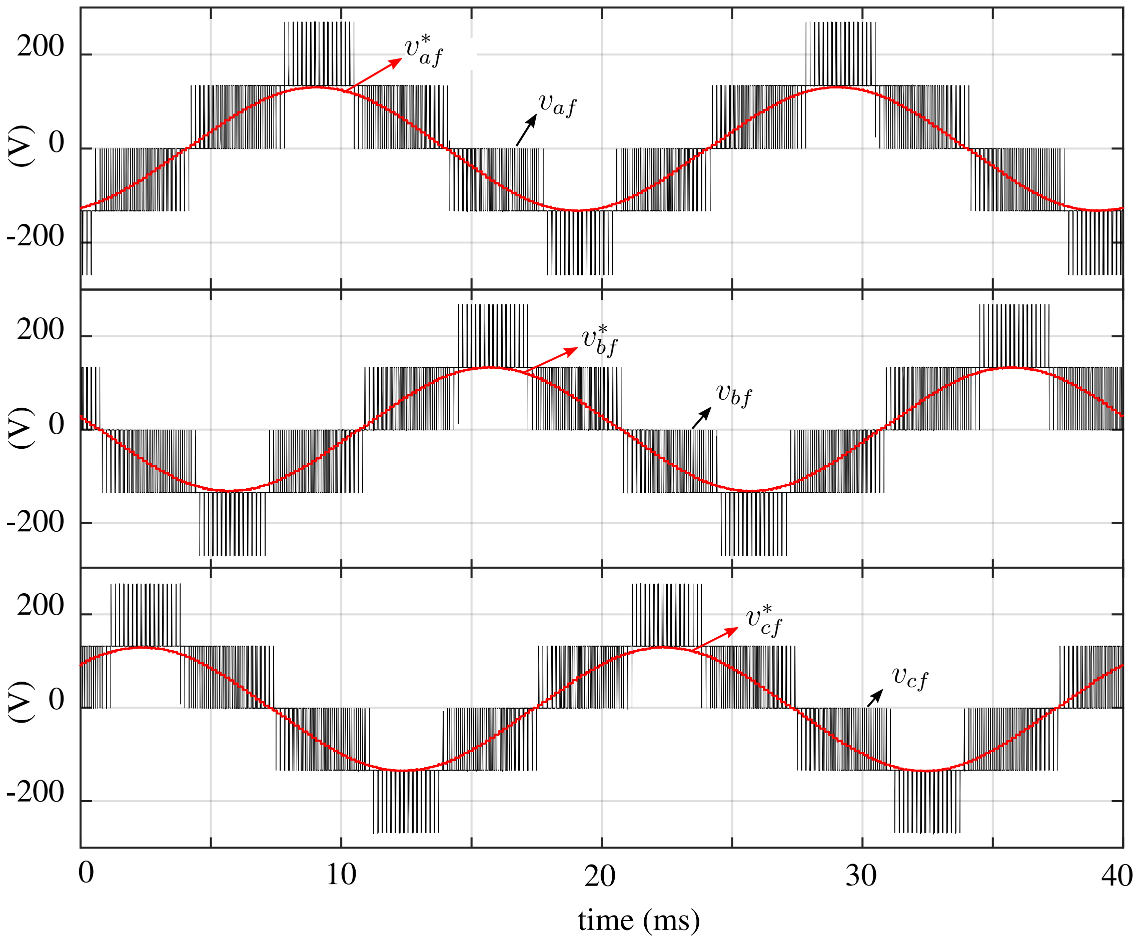

Figure 5.21: Output voltages v_{af},v_{bf} and v_{cf} for a four-leg NPC converter with their respective references v_{af}^*,v_{bf}^* and v_{cf}^* in red.

From Fig. 5.21 it can be observed that because of the fourth leg of the converter, five levels are generated at the output phase-to-neutral voltages. This reduces the *THD*$_v$, permit full utilization of the dc-link voltage and allows minimization of the output filter. The harmonic spectrum of v_{af} is shown in Fig. 5.22. Clearly, the first group of predominant harmonics are around $6kHz$. Additionally, the fundamental component is exactly modulated with a peak magnitude of $\frac{270}{2}\frac{2}{\sqrt{3}}0.95 \approx 153.5V$.

Fig. 5.23 shows the output voltages for each phase (leg) of the converter. As it can be seen, the fourth leg has to modulate a third harmonic in order to boost the phase-to-neutral output voltages and fully utilize the dc-link voltage. From Fig. 5.23, the switching frequency of each device of the four-leg NPC converter presented in Fig. 5.1 can be obtained. Thereby, for each leg of the converter, the switching transitions performed during the positive semi-cycle of the modulated waveform define the switching frequency of S_{1i} (and its complementary switch $\bar{S}_{1i}$), while the switching transitions performed during the negative semi-cycle define the switching frequency of S_{2i} (and its complementary switch $\bar{S}_{2i}$) for $i \in \{a, b, c, f\}$. Thereby, according to (5.27) and using the data provided by Fig. 5.23, the switching frequency for each device of the converter are given by

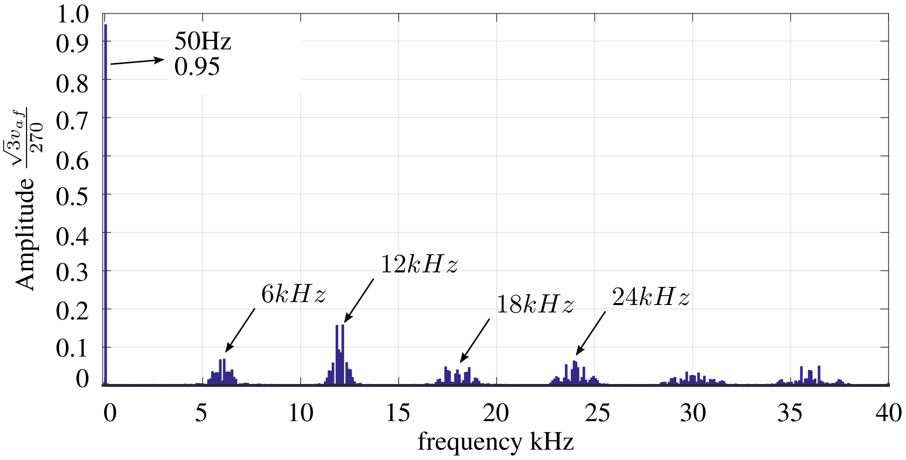

Figure 5.22: FFT for v_{af} of Fig. 5.21. The amplitude has been normalized by $\frac{270}{\sqrt{3}}$.

$$f_{S_{1a}}{=}f_{S_{1b}}{=}f_{S_{1c}}{=}f_{S_{1f}}{=}3000Hz \tag{5.70}$$

$$f_{S_{2a}}{=}f_{S_{2b}}{=}f_{S_{2c}}{=}3000+50{=}3050Hz \tag{5.71}$$

$$f_{S_{2f}}{=}3000+150{=}3150Hz \tag{5.72}$$

As expected, the switching frequency for each device is around half of the sampling frequency ($f_s{=}6kHz$). Hence, although the average switching frequency defined by the *Single Redundancy Symmetric* switching pattern at each sampling time is always $3kHz$, the transition between tetrahedrons generates an extra switching commutation during the negative semi-cycle, which is noticed as an increment in $50Hz$ in the switches S_{2a}, S_{2b} and S_{2c} and $150Hz$ in S_{2f}. However, this is an small quantity compared to the average switching frequency of $3kHz$, defined by the sampling frequency $f_s{=}6kHz$.

Fig. 5.24 shows a closer view of Fig. 5.21 around $21ms$. The alignment and fixed switching frequency of the *Single Redundancy Symmetric* switching pattern is clearly identify at each sampling time T_s.

In order to evaluate the modulation algorithm under a general case. The following unbalanced and non-sinusoidal references are used for modulation

$$v_{af}^*{=}\frac{270}{\sqrt{3}}\left(0.9\cos(\omega t)+0.1\cos(3\omega t)+0.1\cos(5\omega t)\right) \tag{5.73}$$

$$v_{bf}^*{=}\frac{270}{\sqrt{3}}\left(0.9\cos(\omega t-\frac{2\pi}{3})+0.1\cos(5\omega t+\frac{2\pi}{3})+0.15\cos(7\omega t-\frac{2\pi}{3})\right) \tag{5.74}$$

$$v_{cf}^*{=}\frac{270}{\sqrt{3}}\left(0.8\cos(\omega t+\frac{2\pi}{3})+0.15\cos(7\omega t+\frac{2\pi}{3})+0.1\cos(11\omega t-\frac{2\pi}{3})\right) \tag{5.75}$$

Fig. 5.25 shows the phase-to-neutral output voltages v_{af}, v_{bf} and v_{cf} with their respective references. The same sampling frequency ($f_s{=}6kHz$) and dc-link voltage ($270V$) of the previous

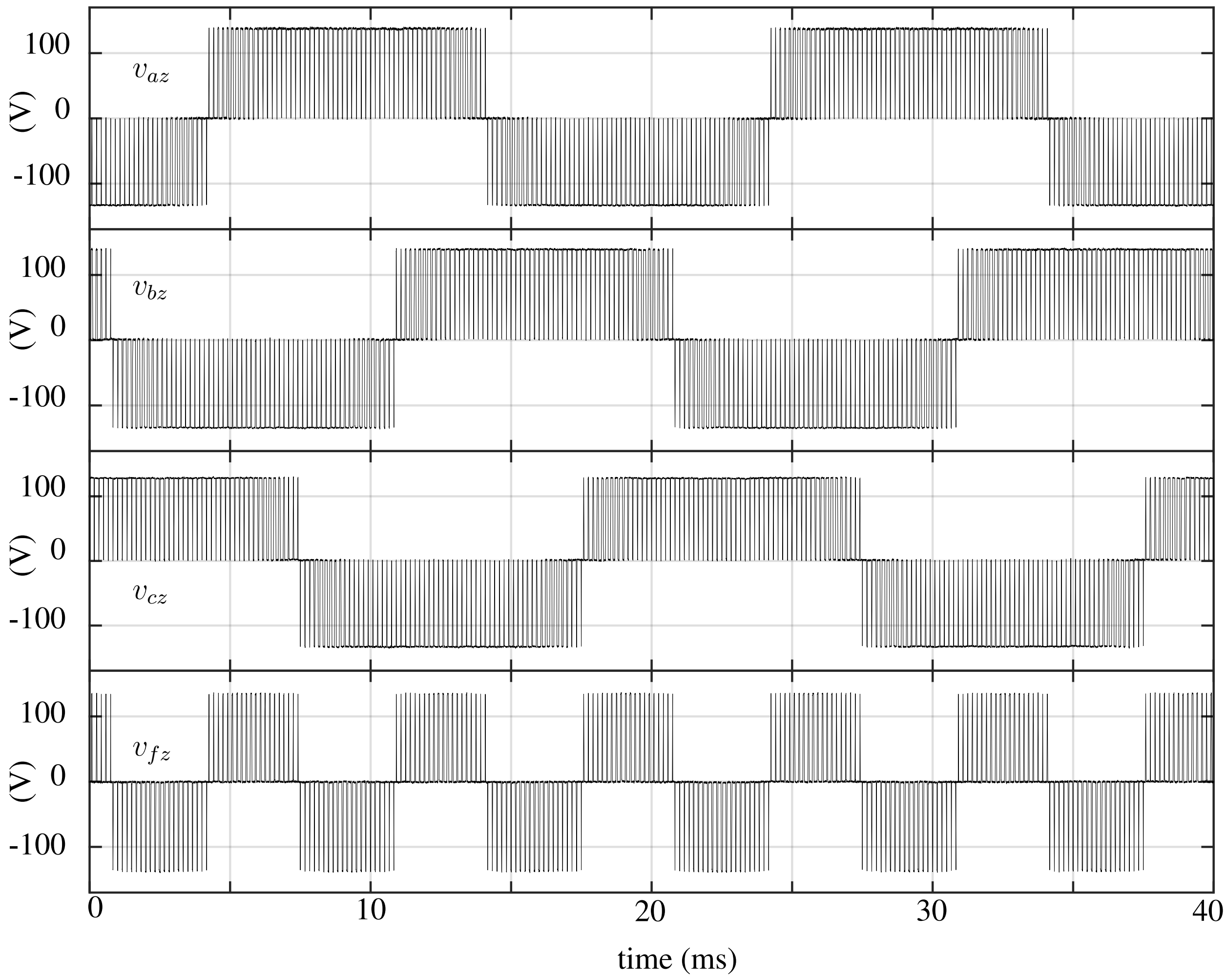

Figure 5.23: Output phase voltages v_{az}, v_{bz}, v_{cz} and v_{fz} for the voltages presented in Fig. 5.21. Sampling frequency f_s=$6kHz$, dc-link voltage 270 V.

example has been implemented. As it can be seen, each modulated waveform follows precisely their references. Fig. 5.26 shows the FFT analysis for each of the modulated waveforms. It can be clearly noticed that each of the modulated waveforms perfectly track their harmonic references presented in (5.73) to (5.75).

Additionally, Fig. 5.27 shows the phase voltages for each leg of the converter. Unlike Fig. 5.23, the modulated voltage v_{fz} of Fig. 5.27 does not represent an ideal third harmonic, but it has been modified to track each of the different harmonics in each leg of the converter. Similarly to the previous example, from Fig. 5.27 the switching frequency of each device of the converter can be calculated as follows

$$f_{S_{1a}}{=}f_{S_{1b}}{=}f_{S_{1c}}{=}f_{S_{1f}}{=}3000Hz \tag{5.76}$$

$$f_{S_{2a}}{=}f_{S_{2b}}{=}f_{S_{2c}}{=}3000+50{=}3050Hz \tag{5.77}$$

$$f_{S_{2f}}{=}3000+150{=}3250 \tag{5.78}$$

It can be noticed that the incorporation of additional harmonics slightly modified the switch-

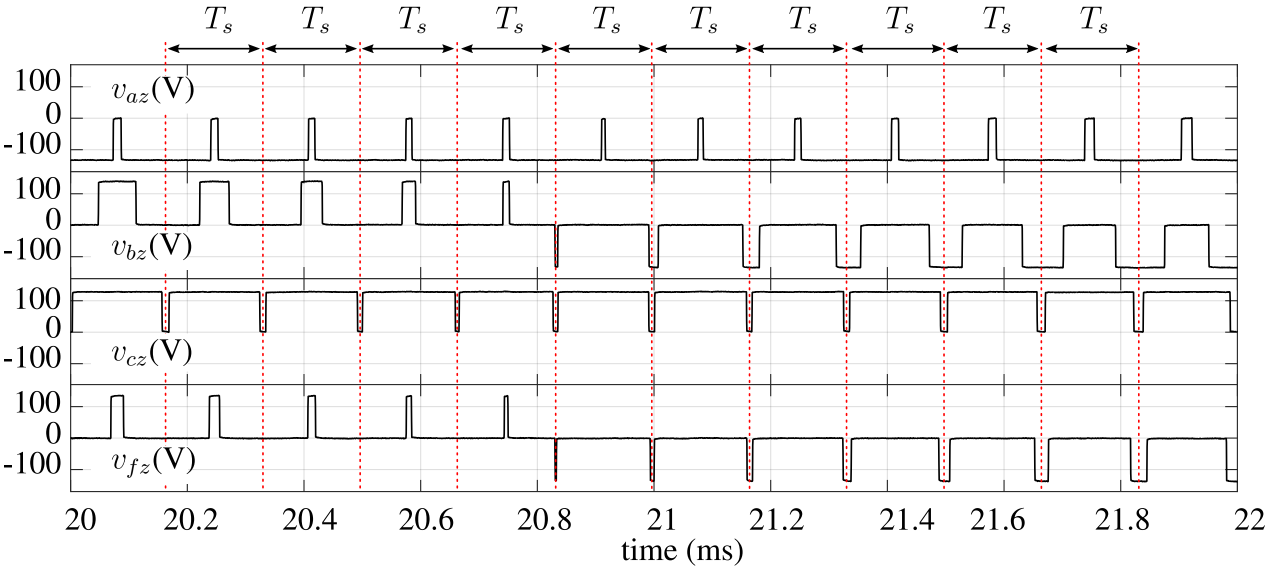

Figure 5.24: Closer view of the output phase voltages v_{az}, v_{bz}, v_{cz} and v_{fz} presented in Fig. 5.21. Sampling frequency f_s=$6kHz$, dc-link voltage 270 V.

ing frequency compared to the previous example presented in (5.70) to (5.72). The deviation of the switching frequency is caused by the modification of the path described by the reference vector. Thereby, additional commutations are incorporated when the reference vector changes between the different tetrahedrons. However, its deviation is still negligible compared to the average switching frequency defined by the *Single Redundancy Symmetric* switching pattern, i.e. $3kHz$.

As presented in Chapter 2, alternating every 60° in the $\alpha\beta$ plane between *positive* and *negative Single Redundancy Symmetric* switching pattern allows the elimination of even order harmonics harmonic components. Thereby, simply dividing the $\alpha\beta\gamma$ space in the same manner, elimination of even order harmonics can be also achieved for modulation of symmetric waveforms in a four-leg NPC converter. Fig. 5.28 shows the output waveform for modulation of a sinusoidal balanced reference with and without implementation of even order harmonics. Likewise, Fig. 5.29 shows their respective harmonic spectrum.

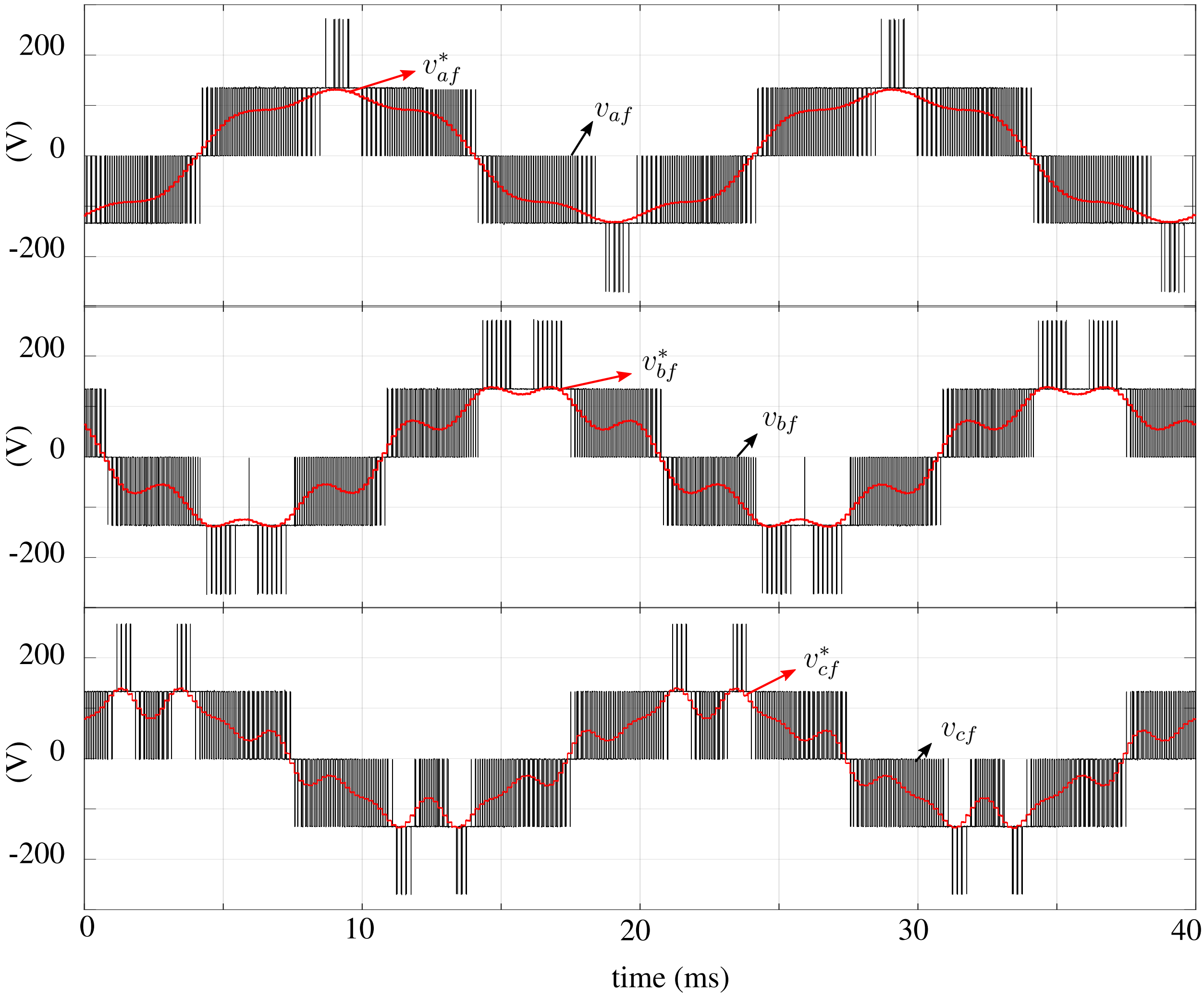

Figure 5.25: Output voltages v_{af},v_{bf} and v_{cf} for a four-leg NPC converter with their respective references v_{af}^*,v_{bf}^* and v_{cf}^* in red for unbalanced and non-sinusoidal references. Sampling frequency f_s=$6kHz$, dc-link voltage 270 V.

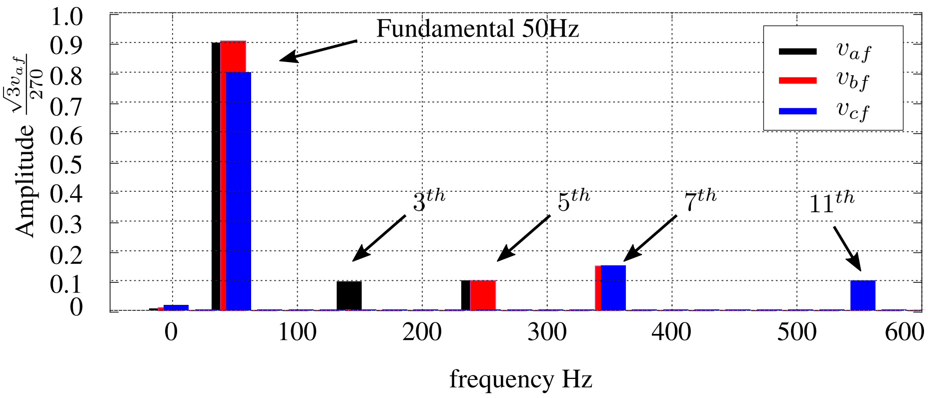

Figure 5.26: FFT for the phase-to-neutral voltages v_{af}, v_{bf} and v_{cf} of Fig. 5.21. The amplitude has been normalized by $\frac{270}{\sqrt{3}}$.

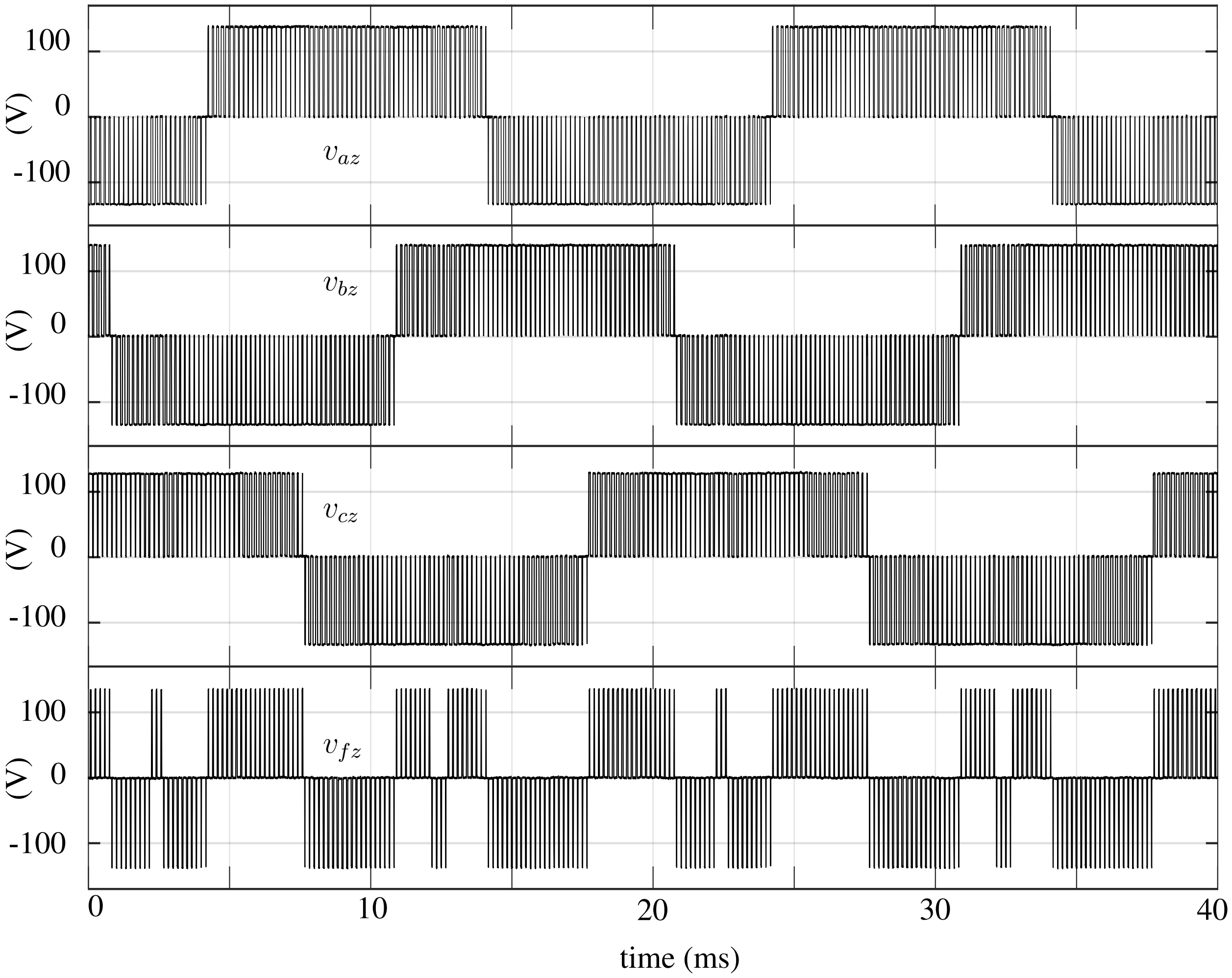

Figure 5.27: Output phase voltages v_{az}, v_{bz}, v_{cz} and v_{fz} for the voltages presented in Fig. 5.25. Sampling frequency f_s=$6kHz$, dc-link voltage 270 V.

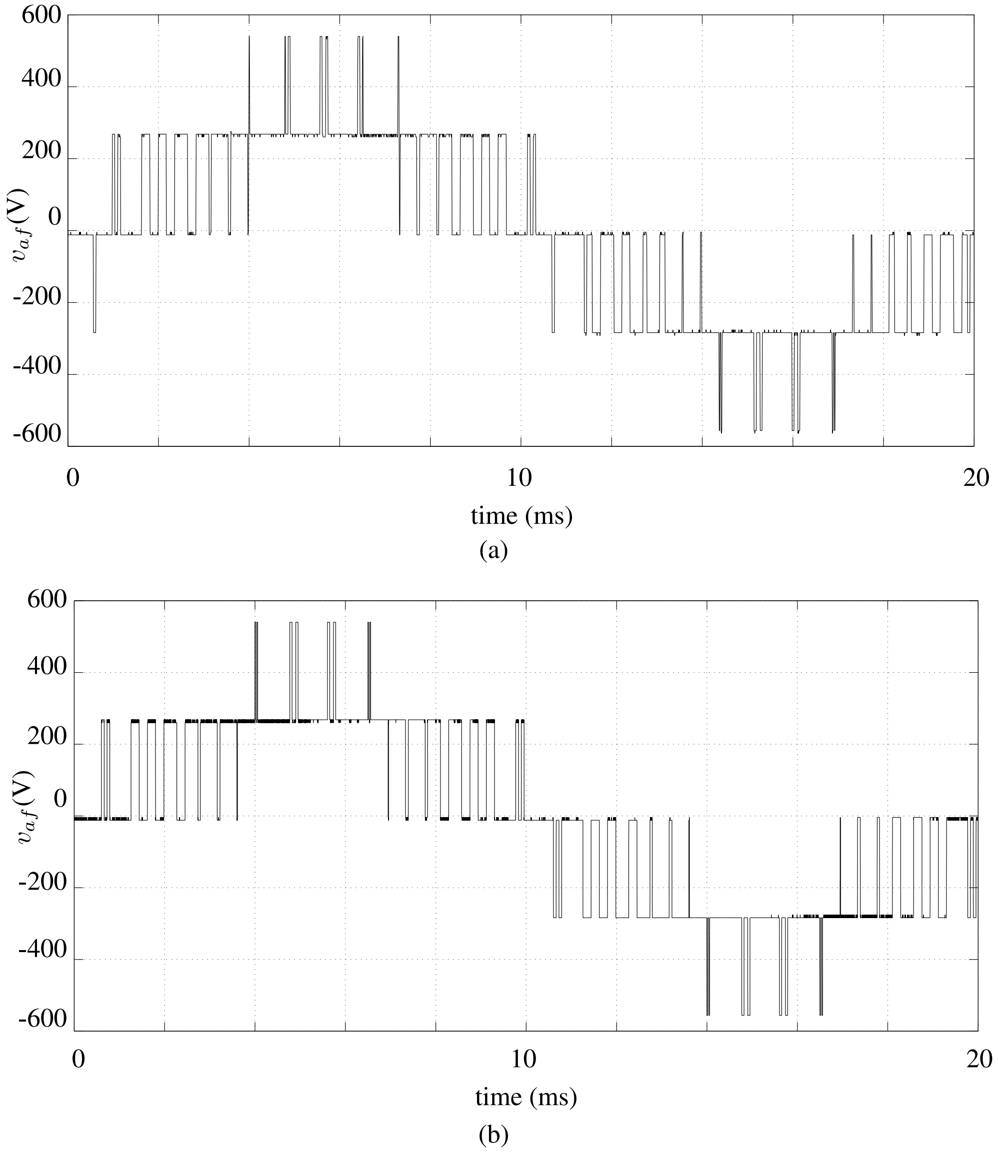

Figure 5.28: Experimental assessment of three-dimensional SVM for a four-leg NPC (a) v_{af} without even-harmonic eliminations and (b) v_{af} with even-harmonic elimination. Measurements are with the load disconnected, $f_{SVM} = 1200Hz$, $m = 0.95$ and $V_{dc} = 545V$.

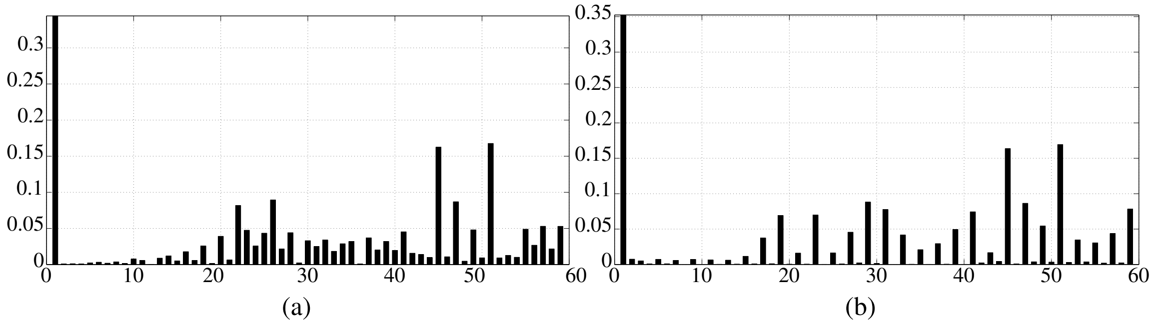

Figure 5.29: Normalized amplitude of harmonic components based on 50Hz fundamental frequency. The FFT for the waveform of (a) Fig.5.28a and (b) Fig. 5.28b.

5.8.2 dc-link Voltage Balance

The balance of the voltages on the capacitors C_1 and C_2, presented in Fig. 5.1, can be considered an issue of primary importance when controlling a NPC converter. The unbalance of these voltages generate an unequal voltage distribution across the semiconductors of the converter, which directly yields to a failure condition. In order to analyze the control capability of a four-leg NPC converter, the active control presented in Section 5.5 of this Chapter and the *Single Redundancy Symmetric* switching pattern have been implemented.

Fig. 5.30 shows the hardware scheme used for testing the voltage balance capability.

Fig. 5.31 shows the voltages v_{C_1} and v_{C_2} under three different load conditions. The voltage references, modulated in open-loop, for each phase-to-neutral voltage are given by

$$v_{af}^{*}=\frac{270}{\sqrt{3}}0.9\cos(\omega t) \tag{5.79}$$

$$v_{bf}^{*}=\frac{270}{\sqrt{3}}0.9\cos(\omega t-\frac{2\pi}{3}) \tag{5.80}$$

$$v_{cf}^{*}=\frac{270}{\sqrt{3}}0.9\cos(\omega t+\frac{2\pi}{3}) \tag{5.81}$$

$$\tag{5.82}$$

From Fig. 5.31, two steps marked as t_i and t_c can be observed. First, at t_i, the three-dimensional modulation algorithm is initialized and implemented without active control over the voltages v_{C_1} and v_{C_2}. Under this condition, the dwell-times for each redundant vector is equally divided at every sampling time T_s. At t_c, the active control algorithm is activated, using (5.36) and (5.37) to calculate the dwell-times for each redundancy of the only redundant vector used in the implemented *Single Redundancy Symmetric* switching pattern.

In Fig. 5.31a, a balanced RL three-phase load has been connected (rectifier not connected, see Fig. 5.30). As it can be seen, before the initialization of the modulation algorithm (at t_i), the voltages v_{C_1} and v_{C_2} are almost balanced (initial condition). However after t_i, due to the transient response of the line currents generated by the initialization of the control algorithm, the voltages settle in an unbalanced condition. This phenomena is expected, because the implemented algorithm does not have any feedback of the voltages v_{C_1} or v_{C_2}. At t_c, the active control for balancing v_{C_1} and v_{C_2} has been incorporated (see Fig. 2.20 of Chapter 2 for visualization of the external control loop). Clearly, the voltages tends to a balanced condition around $134V$. A closer view of v_{C_1} and v_{C_2} is also provided in Fig. 5.31a, where the typical oscillation of three times the fundamental frequency can be observed. Fig. 5.31b and Fig. 5.31c represent the same analysis explained above, but with unbalanced load conditions. In Fig. 5.31b, phase c has been disconnected and in Fig. 5.31c, phase b and c have been disconnected. As it can be appreciated, and similarly to Fig. 5.31a, after t_i the voltages settle in an unbalanced condition (initial condition is now unbalanced). However, after the incorporation of active control at t_c, the voltages tends to a balanced condition. This can be better observed in Fig. 5.32, where the difference between v_{C_1} and v_{C_2} has been plotted. As it can be observed, before activating the active control to balance the voltages in the capcitors at t_c, the difference $v_{C_1}-v_{C_2}$ oscillates around a displaced center, while after t_c they oscillate around zero.

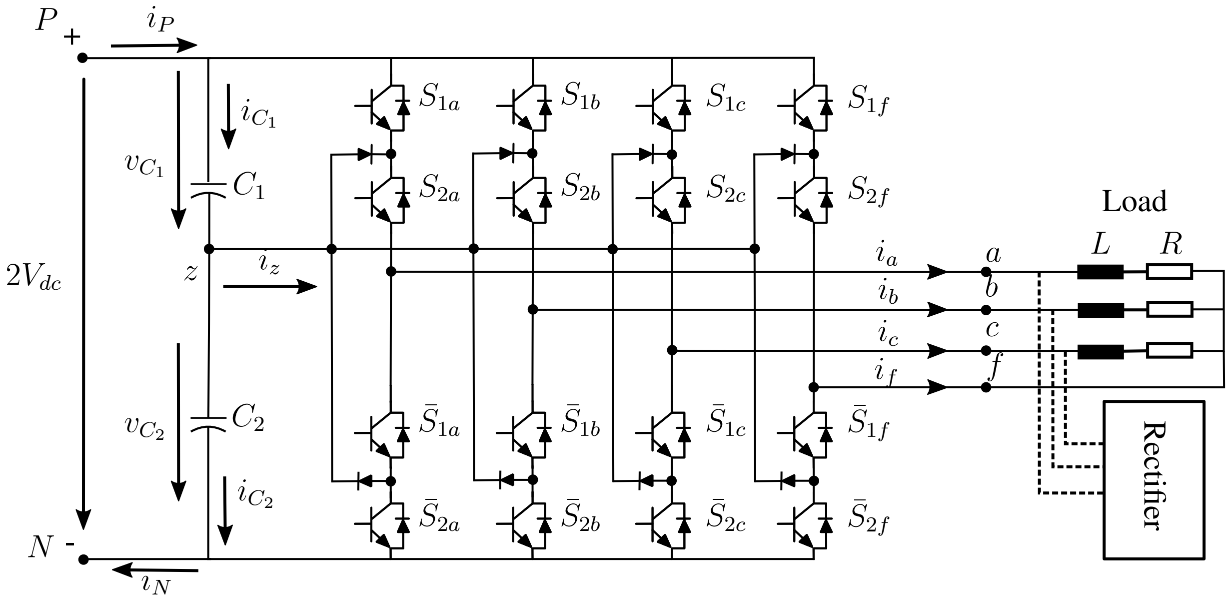

Figure 5.30: Representation of the hardware scheme of a four-leg NPC converter connected to a general RL linear load and a non-linear load.

From 5.31 and Fig. 5.32 it is evident that the ripple magnitude and the oscillation shape of v_{C_1} and v_{C_2} is determined by the load conditions, i.e. by the neutral-point current i_z. Thereby, as a general rule, the more balance is the load, i.e. smaller neutral-point current i_z, the smaller ripple is achieved into the dc-link voltage oscillation.

Fig. 5.33 shows the voltages v_{C_1} and v_{C_2} for the same load conditions presented in Fig. 5.31, but with the incorporation of a parallel three-phase rectifier as shown in Fig. 5.30. Thus, in 5.33a the three phase RL load is connected, in 5.33b the RL load of phase c has been disconnected and in 5.33c the RL load of phases b and c has been disconnected. As mentioned before, the incorporation of additional current harmonics have changed the voltage ripple and voltage shape compared to Fig. 5.31. However, the voltages v_{C_1} and v_{C_2} are still unbalanced before the incorporation of the active control at t_c. Fig. 5.34 and Fig. 5.35 shows the lines and neutral currents for each condition. This shows the capability of the converter to handle zero-sequence components maintaining the voltage balance on the dc-link capacitors.

In order to proof the voltage balance capability under modulation of non-sinusoidal waveforms, i.e. the selection of different type of tetrahedrons, the phase-to-neutral references have been modified to

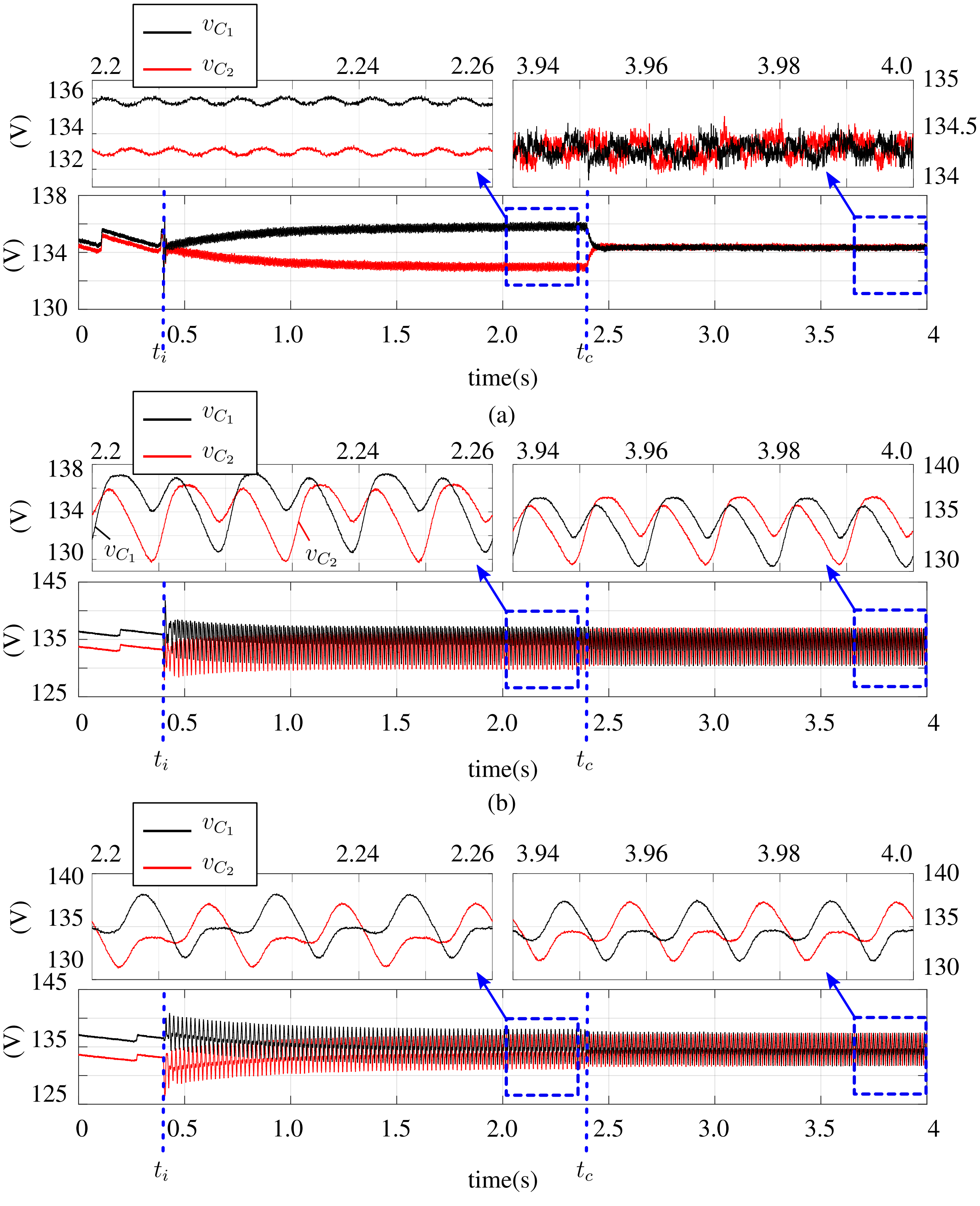

(a)

(b)

(c)

Figure 5.31: Control impact over the dc-link voltages v_{C_1} and v_{C_2} for (a) balanced three-phase load R=30Ω, L=22mH, (b) phase c has been disconnected, (c) phase b and c has been disconnected.

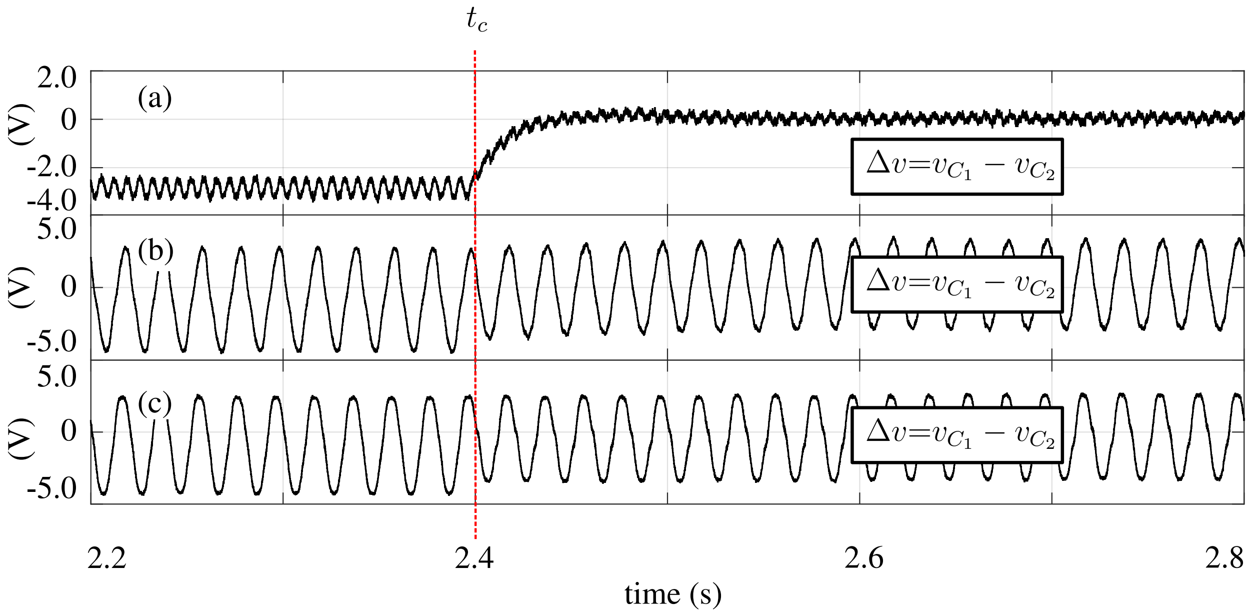

Figure 5.32: Difference $v_{C_1} - v_{C_2}$ for each of the three cases (a), (b) and (c) (same order), illustrated in Fig. 5.31.

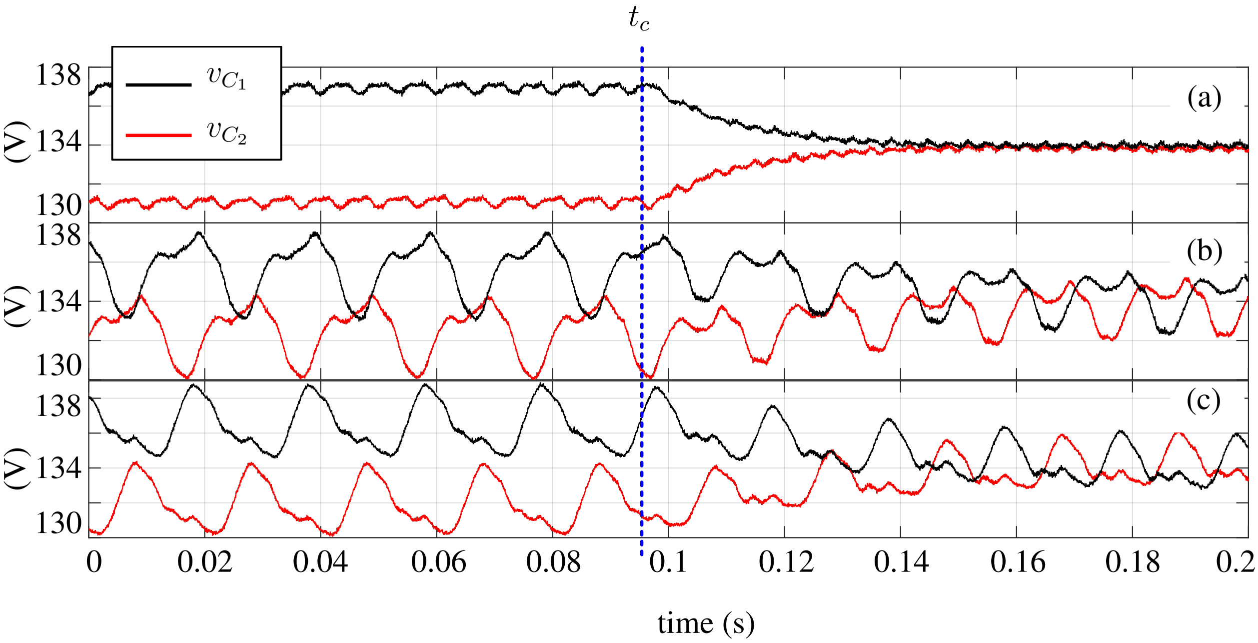

Figure 5.33: Control impact over the dc-link voltages v_{C_1} and v_{C_2} for (a) balanced three-phase load R=30Ω, L=22mH and a three-phase rectifier with load R_{rec}=60 (in parallel)(b) RL load of phase c has been disconnected, (c) RL load of phase b and c has been disconnected.

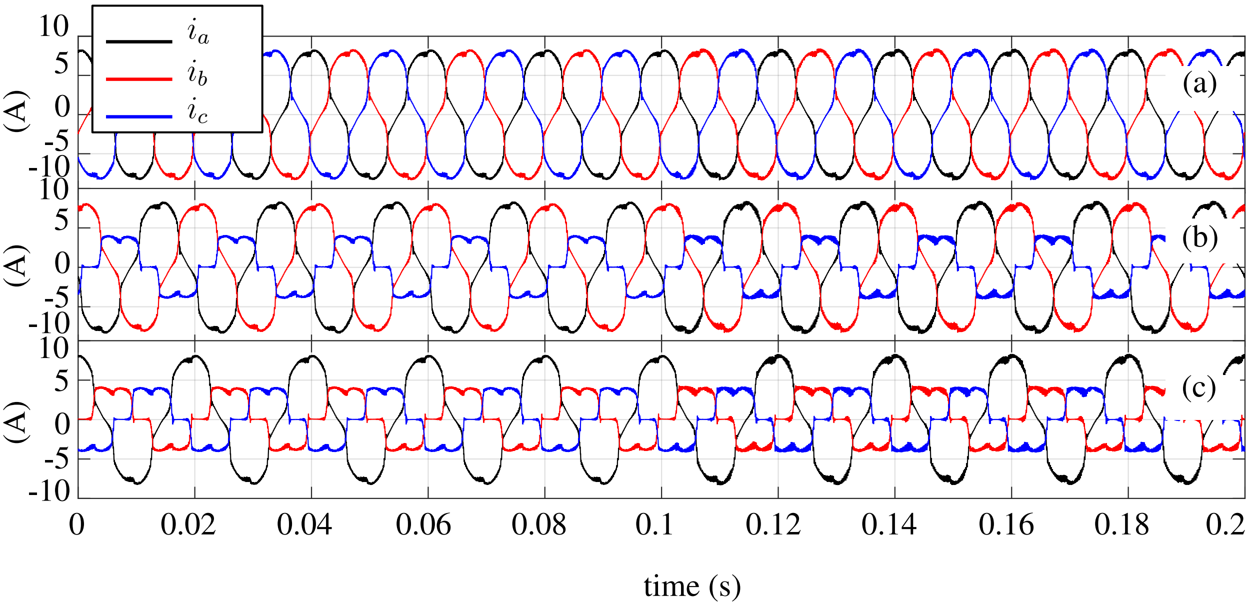

Figure 5.34: Line currents i_a, i_b and i_c for (a) balanced three-phase load R=30Ω, L=22mH and a three-phase rectifier with load R_{rec}=60 (in parallel)(b) RL load of phase c has been disconnected, (c) RL load of phase b and c has been disconnected.

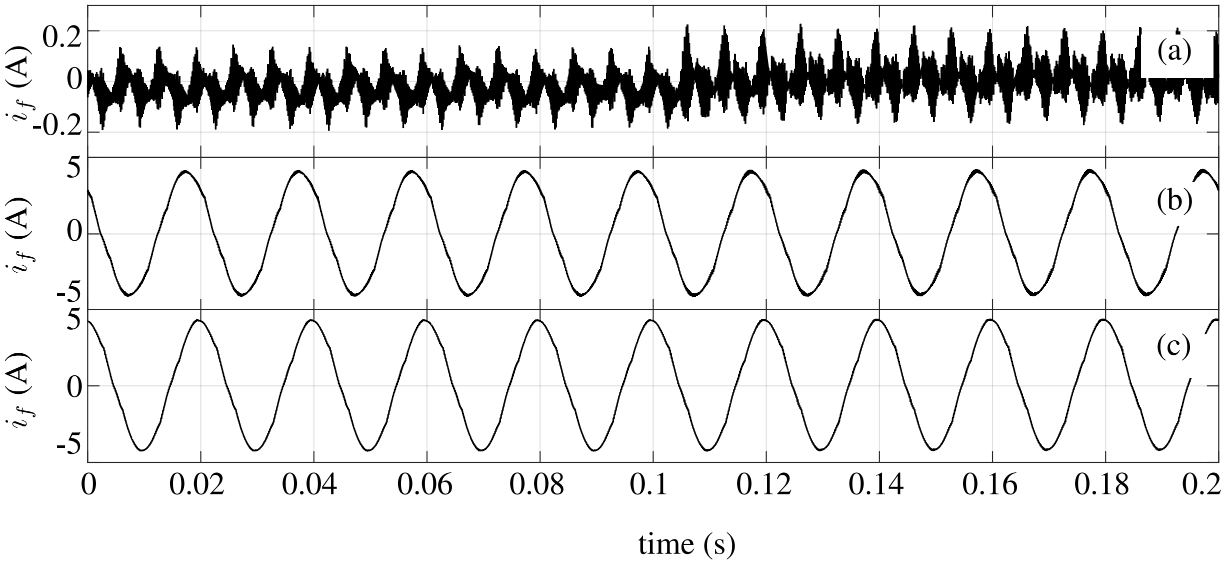

Figure 5.35: Neutral current i_f for (a) balanced three-phase load R=30Ω, L=22mH and a three-phase rectifier with load R_{rec}=60 (in parallel) (b) RL load of phase c has been disconnected, (c) RL load of phase b and c has been disconnected.

$$v_{af}^{*}{=}\frac{270}{\sqrt{3}}\left(0.9\cos(\omega t)+0.7\cos(3\omega t)+0.1\cos(5\omega t)+0.3\cos(9\omega t)\right) \tag{5.83}$$

$$v_{bf}^{*}{=}\frac{270}{\sqrt{3}}\left(0.9\cos(\omega t-\frac{2\pi}{3})+0.7\cos(3\omega t)+0.1\cos(5\omega t+\frac{2\pi}{3})+\right. \tag{5.84}$$
$$\left. 0.15\cos(7\omega t-\frac{2\pi}{3})+0.3\cos(9\omega t)\right)$$

$$v_{cf}^{*}{=}\frac{270}{\sqrt{3}}\left(0.8\cos(\omega t+\frac{2\pi}{3})+0.7\cos(3\omega t)+0.15\cos(7\omega t+\frac{2\pi}{3})+\right. \tag{5.85}$$
$$\left. 0.3\cos(9\omega t)+0.1\cos(11\omega t-\frac{2\pi}{3})\right)$$

Fig. 5.36 shows the voltages v_{C_1} and v_{C_2} for modulation of the non-sinusoidal references of (5.83) to (5.85) implemented with the same RL load and three-phase rectifier presented in Fig. 5.33. It can be noticed that, the incorporation of several different harmonics into the reference vector, does not present a limitation for accomplishing the balance of the dc-link voltages. By that, regardless of the reference vector path, the balance of the voltages is always possible as long as the currents does not posses a dc component. This is basically explained because ac line currents generate an ac current through the neutral-point of the converter, i.e. i_z. This leads to a natural oscillation of the voltages v_{C_1} and v_{C_2} around an arbitrary point, as it has been shown, avoiding divergence. Fig. 5.37 and Fig. 5.38 show the line and neutral currents for the corresponding cases presented in Fig. 5.36. As it can be seen from Fig. 5.38 the converter is capable of handling non-sinusoidal currents through the fourth leg with similar magnitudes to the line currents. This emphasis that the fourth leg should not be designed with smaller nominal rates. Unless the line current harmonics are strictly restricted.

To illustrate the limitation of the balance over the dc-link voltages v_{C_1} and v_{C_2}, a diode connected in series with the RL load of phase a has been implemented as shown in Fig. 5.39.

Fig. 5.40a and Fig. 5.40b show the voltages v_{C_1} and v_{C_2} after the activation of the modulation algorithm, occurred at t_i, with and without active control of the voltages v_{C_1} and v_{C_2} respectively. As it can be seen, in Fig. 5.40b the hardware protection has been tripped, set at $|v_{C_1}-v_{C_2}|{=}20V$. Thereby, the incorporation of a dc component in i_a force the utilization of an active control algorithm to achieve balancing of the dc-link voltages. This is because the dc component of i_a is also present in the neutral-point current i_z. By that, the natural oscillation of the voltages v_{C_1} and v_{C_2} around an arbitrary value when the dwell-times of the redundant vector are equally divided is not achievable. Thus, the active control algorithm must compensate the dc component introduced by i_a.

Although the balancing of the voltages v_{C_1} and v_{C_2} was achieved in 5.40a, the active control of the dc-link voltages does not ensure the successful voltage balancing when line currents posses dc component. This is shown in Fig. 5.40c, where increasing the magnitude of the voltage references, i.e. reducing the dwell-time of the only redundant vector, also produce trip of the voltage protection. Thereby, the balancing of the voltages can be only achieved when the dwell-time of the redundant vector over one fundamental cycle is large enough for compensating the dc-component introduced by i_a.

This can be explained looking at Fig. 5.5, where it was shown that a reference vector that moves around the center of the modulation region possesses a larger voltage balance capability,

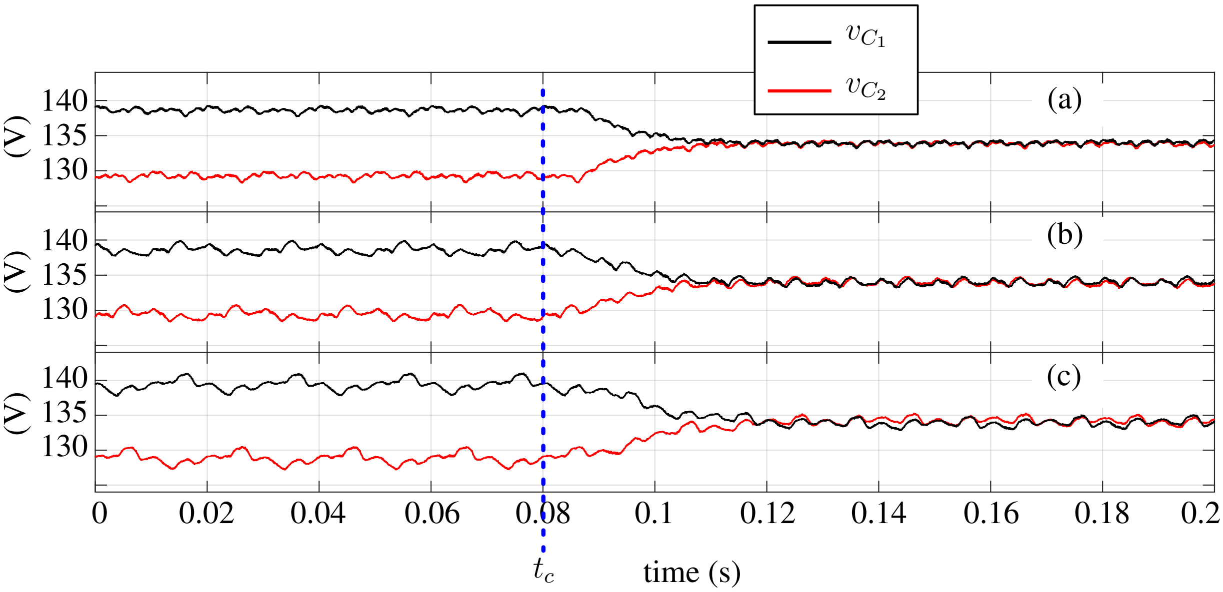

Figure 5.36: Control impact over the dc-link voltages v_{C_1} and v_{C_2} under non-sinusoidal modulated voltages for (a) balanced three-phase load R=30Ω, L=22mH and a three-phase rectifier with load R_{rec}=60 (in parallel)(b) RL load of phase c has been disconnected, (c) RL load of phase b and c has been disconnected.

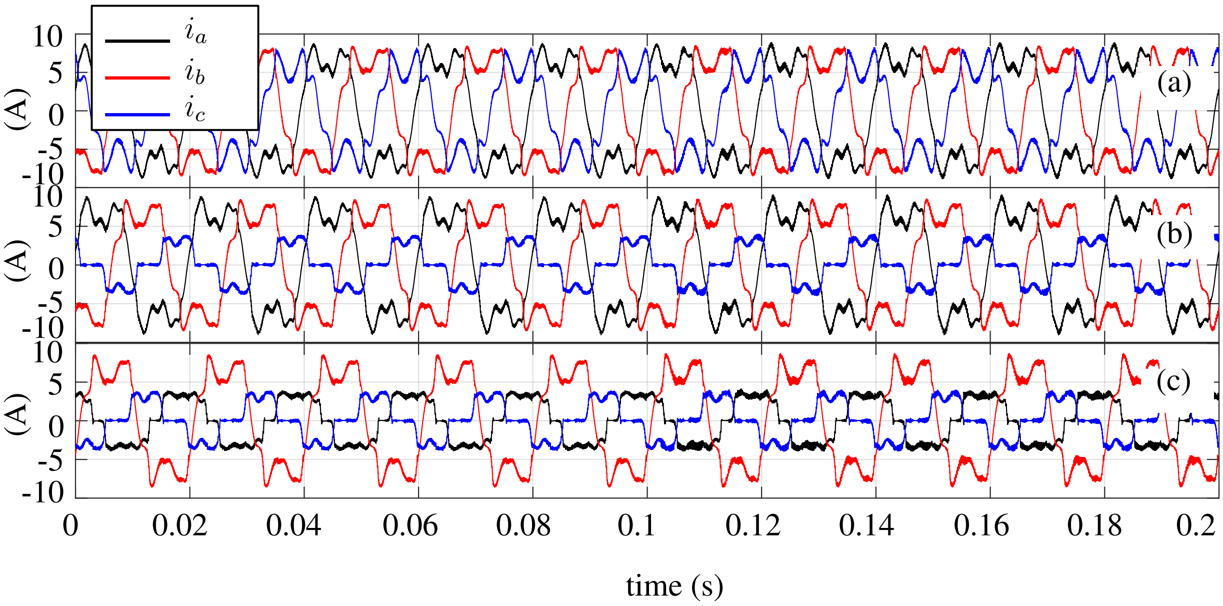

Figure 5.37: Line currents i_a, i_b and i_c under non-sinusoidal modulated voltages for (a) balanced three-phase load R=30Ω, L=22mH and a three-phase rectifier with load R_{rec}=60 (in parallel)(b) RL load of phase c has been disconnected, (c) RL load of phase b and c has been disconnected.

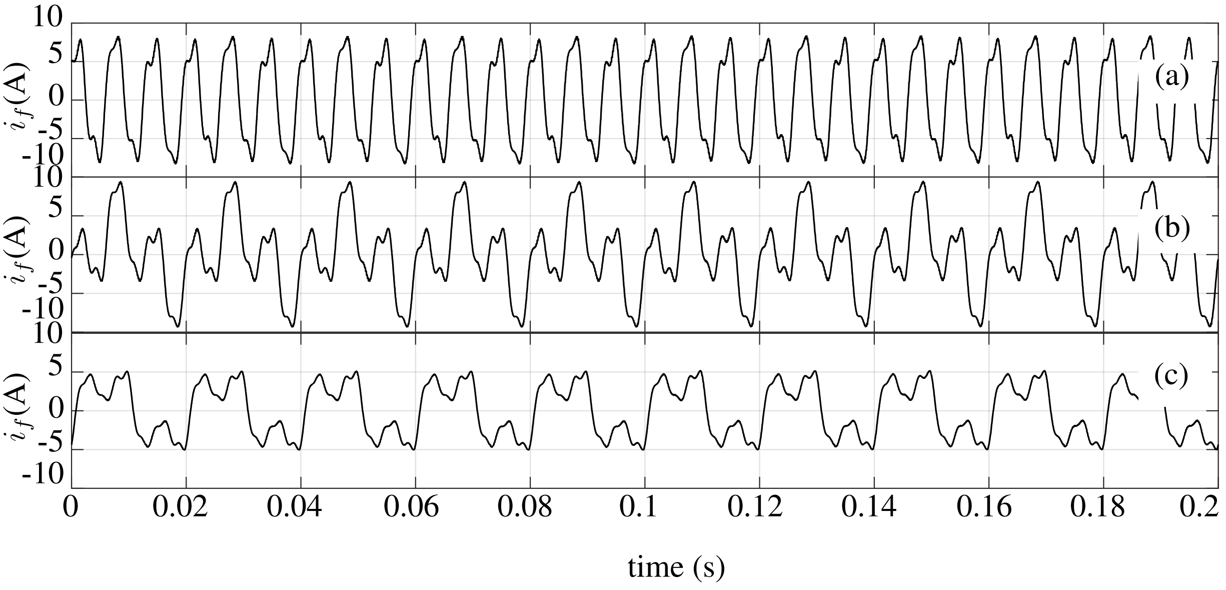

Figure 5.38: Neutral current i_f under non-sinusoidal modulated voltages for (a) balanced three-phase load R=30Ω, L=22mH and a three-phase rectifier with load R_{rec}=60 (in parallel) (b) RL load of phase c has been disconnected, (c) RL load of phase b and c has been disconnected.

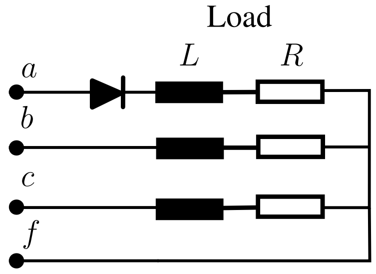

Figure 5.39: Non-linear load for generating dc component in phase a.

because every vector posses redundancy. However, when its path moves around the borders of the modulation region, using the TT_3 tetrahedrons, the voltage balance capability is reduced, as these tetrahedrons posses only one redundant vector. Additionally, the closer is the reference path to the outer boundaries, the harder become the voltage balancing because the dwell-time of the only redundant vector, used in every sampling time T_s, is reduced. Fig. 5.41 and Fig. 5.42 show the line and neutral currents i_a, i_b, i_c and i_f for each case presented in Fig. 5.40.

A more critical case occurs when only the load of phase a is connected. Similarly to Fig. 5.40, Fig. 5.43 shows the dc-link voltages v_{C_1} and v_{C_2} under three different cases. In Fig. 5.43a and Fig. 5.43b the modulation algorithm has been implemented with and without active control of the dc-link voltages respectively. As it can be seen, the balance is still possible, but the active control of the dc-link voltages is necessary. Although the compensation of the voltages can still be achieved, the threshold of divergence is smaller compared to Fig. 5.40. Thereby, for a single phase load, the voltages already diverge with a reference amplitude of $0.7\frac{2}{\sqrt{3}}$. It is caused because the dwell-time of the only redundant vector is not enough for compensate the dc component generated by i_a. Fig. 5.43 shows the line current i_a (same as i_f) for each case illustrated in Fig. 5.44.

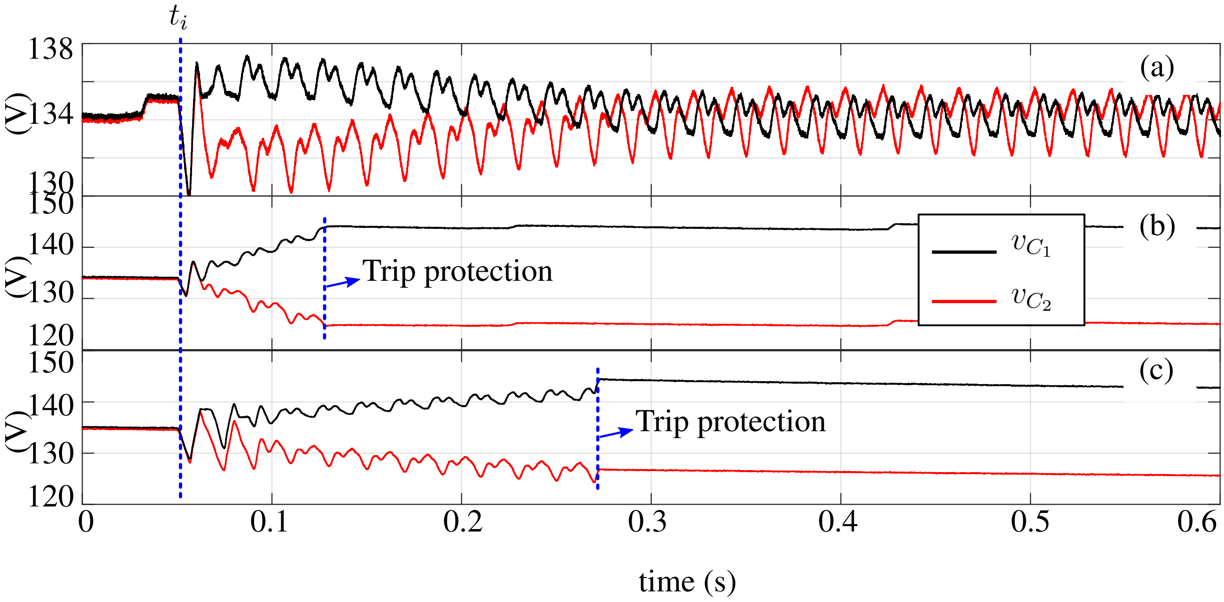

Figure 5.40: Control over dc-link voltages v_{C_1} and v_{C_2} under sinusoidal modulated voltages, and a balanced three-phase load R=30Ω, L=22mH with a series diode in phase a. In (a) active control for balancing v_{C_1} and v_{C_2} is implemented and the voltage references posses an amplitude $|v^*_{af}|$=$|v^*_{bf}|$=$|v^*_{cf}|$=$\frac{2}{\sqrt{3}}0.9$, (b) same references but without active control of v_{C_1} and v_{C_2}, (c) active control for balancing v_{C_1} and v_{C_2} is implemented and the references posses an amplitude $|v^*_{af}|$=$|v^*_{bf}|$=$|v^*_{cf}|$=$\frac{2}{\sqrt{3}}0.95$.

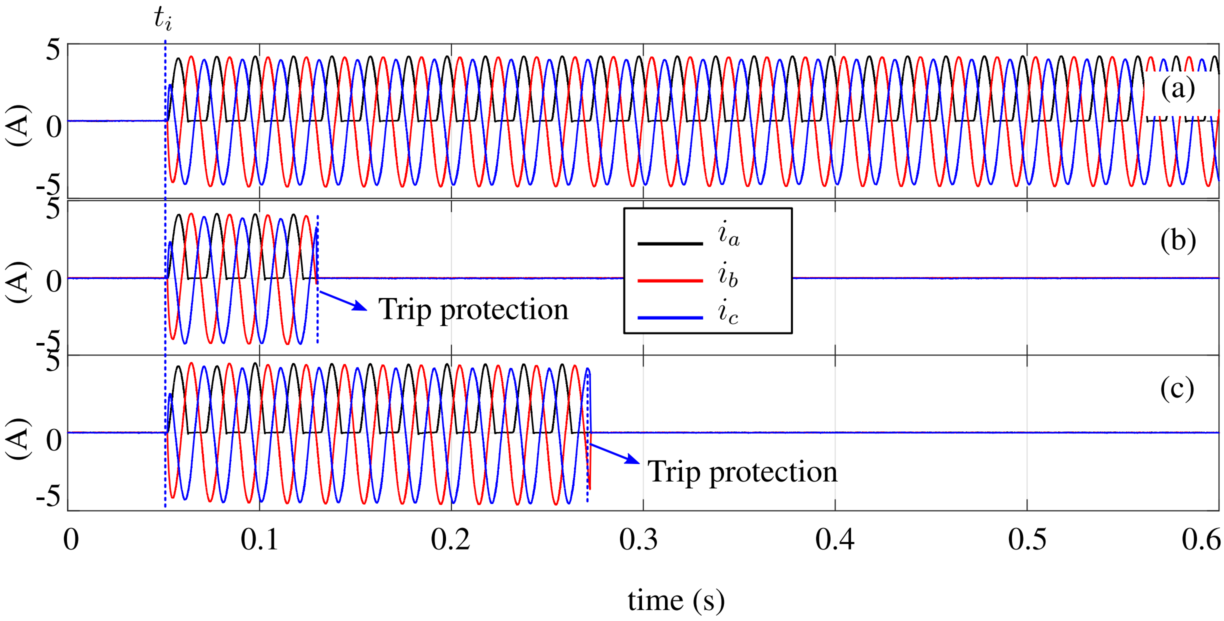

Figure 5.41: Line currents i_a, i_b and i_c for each case (a), (b) and (c) of Fig. 5.40 respectively.

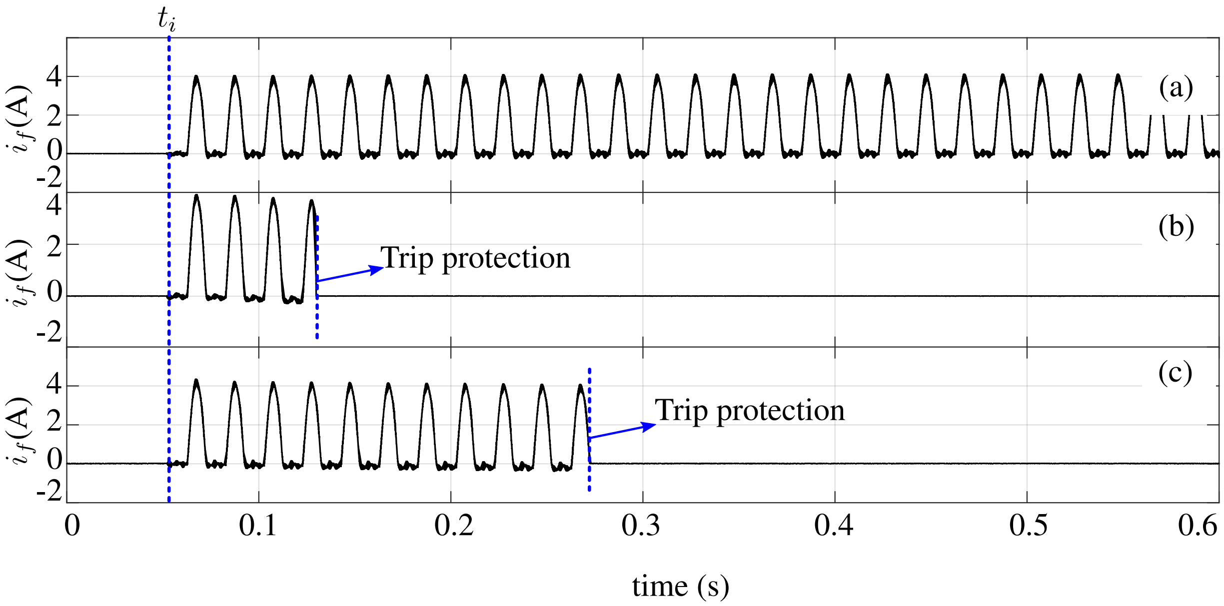

Figure 5.42: Neutral current i_f for each case (a), (b) and (c) of Fig. 5.40 respectively.

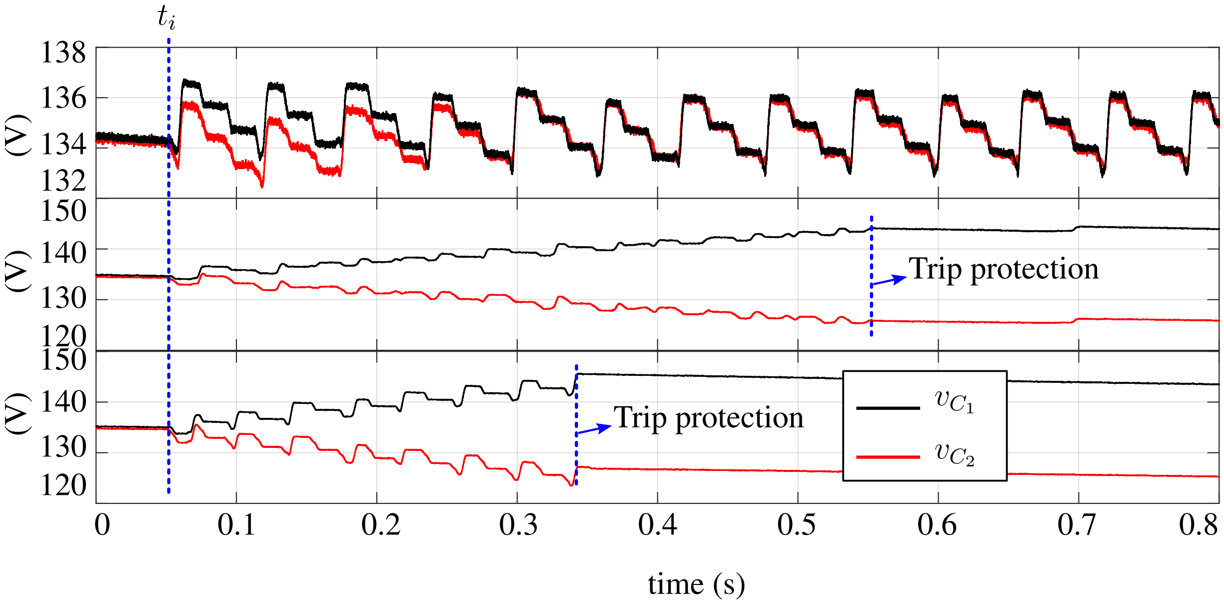

Figure 5.43: Control over dc-link voltages v_{C_1} and v_{C_2} under sinusoidal modulated voltages, and a single-phase load connected R=30Ω, L=22mH with a series diode connected in phase a. In (a) active control for balancing v_{C_1} and v_{C_2} is implemented and the voltage references posses an amplitude $|v^*_{af}|$=$|v^*_{bf}|$=$|v^*_{cf}|$=$\frac{2}{\sqrt{3}}0.5$, (b) same references but without active control of V_{C_1} and V_{C_2}, (c) active control for balancing v_{C_1} and v_{C_2} is implemented and the references posses an amplitude $|v^*_{af}|$=$|v^*_{bf}|$=$|v^*_{cf}|$=$\frac{2}{\sqrt{3}}0.7$.

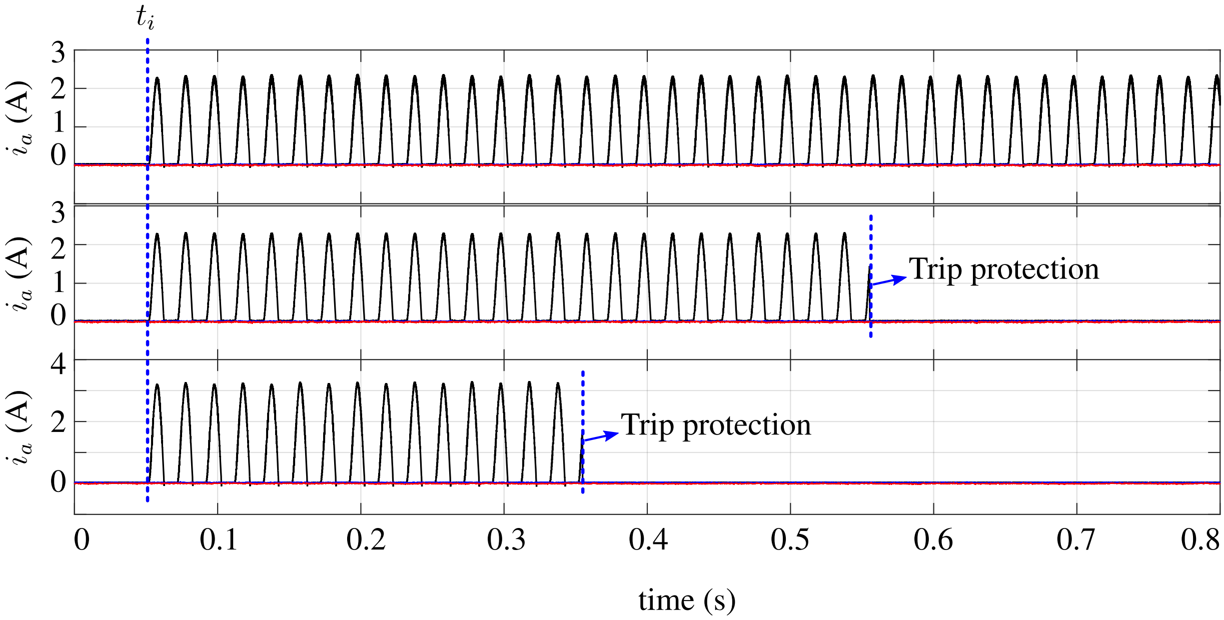

Figure 5.44: Line current i_a for each case (a), (b) and (c) of Fig. 5.43

5.8.3 Overmodulation

In order to analyze the overmodulation algorithm presented in Section 5.6, an arbitrary reference vector which path is beyond the borders of the allowable modulation region is generated. This reference is limited to the allowable modulation space by the proposed overmodulation method and then provided to the three-dimensional SVM to finally be modulated by the four-leg NPC converter in open-circuit. By analyzing the harmonic spectrum of the modulated output voltages, the effectiveness of the proposed method can be studied. For the analysis, the three-dimensional SVM modulation has been implemented with a sampling frequency of $f_s{=}12kHz$ and with the *Single Redundancy Symmetric* switching pattern. The algorithm for balancing the voltages on the dc-link capacitors has not been implemented and the dwell-times for both redundancies of the redundant vector have been equally divided.

Let us consider the components of a general reference vector $\boldsymbol{v}^*_{abc}{=}(v^*_{af}, v^*_{bf}, v^*_{cf})$, for compensation until the 11^{th} odd harmonics, as follows:

$$v^*_{af} = \frac{2}{\sqrt{3}} \sum_{i=1,3,5,7,9,11} a_i \sin\left(i \cdot \omega t + \phi_{a_i}\right) \tag{5.86}$$

$$v^*_{bf} = \frac{2}{\sqrt{3}} \sum_{i=1,3,5,7,9,11} b_i \sin\left(i \cdot \omega t + \phi_{b_i}\right) \tag{5.87}$$

$$v^*_{cf} = \frac{2}{\sqrt{3}} \sum_{i=1,3,5,7,9,11} c_i \sin\left(i \cdot \omega t + \phi_{c_i}\right) \tag{5.88}$$

The general form of equations (5.86) to (5.88) represent the typical waveforms modulated by a four-leg converter for compensating unbalanced and non-symmetric waveforms, where several single phase loads are connected to the different phases of the converter.

As first example, consider the reference vector shown in the first column of Table 5.5, composed of three unbalanced, but symmetric fundamental components. In order to limit this vector to the allowable modulation region, the proposed overmodulation algorithm and the standard algorithm that saturates the reference vector to the borders of polygon have been implemented in the experimental setup of Fig. 5.18.The second and third column of Table 5.5 show the harmonic components of the output voltages of the converter after limiting the reference vector by the proposed algorithm, i.e. $\tilde{\boldsymbol{v}}^*_{\alpha\beta\gamma}$, and the vector limited by the boundaries of the polyhedron, represented as $\hat{\boldsymbol{v}}^*_{\alpha\beta\gamma}$. The vectors have been expressed in abc coordinates and its components are measured at the output terminals of the four-leg NPC converter in open-circuit. Unlike $\hat{\boldsymbol{v}}^*_{\alpha\beta\gamma}$, the proposed limitation method does not add any additional harmonic component to the limited reference.

Table 5.5: Limitation for unbalanced fundamental reference vector. For $\tilde{\boldsymbol{v}}^*_{\alpha\beta\gamma}$, the limiting factors are: $\xi \approx 0.87$, η=1.0 and τ=1.0.

$H.Order$	$\frac{\sqrt{3}}{2}\boldsymbol{v}^*_{abc}\,(\cdot 100)$	$\frac{\sqrt{3}}{2}\tilde{\boldsymbol{v}}^*_{abc}\,(\cdot 100)$	$\frac{\sqrt{3}}{2}\hat{\boldsymbol{v}}^*_{abc}\,(\cdot 100)$
1^{st}	$[90\angle 0°, 110\angle 240°, 120\angle 120°]$	$[78\angle 0°, 96\angle 240°, 104\angle 120°]$	$[89\angle 0.6°, 105\angle 238.4°, 114\angle 121°]$
3^{rd}	$[0\angle 0°, 0\angle 0°, 0\angle 0°]$	$[0\angle 0°, 0\angle 0°, 0\angle 0°]$	$[1\angle 219.4°, 4\angle 91°, 3\angle -71.9°]$
5^{th}	$[0\angle 0°, 0\angle 0°, 0\angle 0°]$	$[0\angle 0°, 0\angle 0°, 0\angle 0°]$	$[0\angle 0°, 3\angle 82.8°, 3\angle 264.9°]$
7^{th}	$[0\angle 0°, 0\angle 0°, 0\angle 0°]$	$[0\angle 0°, 0\angle 0°, 0\angle 0°]$	$[1\angle 156.8°, 1\angle 77.8°, 2\angle -63.7°]$
9^{th}	$[0\angle 0°, 0\angle 0°, 0\angle 0°]$	$[0\angle 0°, 0\angle 0°, 0\angle 0°]$	$[1\angle 217.3°, 0\angle 0°, 1\angle 41.1°]$
11^{th}	$[0\angle 0°, 0\angle 0°, 0\angle 0°]$	$[0\angle 0°, 0\angle 0°, 0\angle 0°]$	$[0\angle 0°, 1\angle -78.1°, 1\angle 119.7°]$

Fig. 5.45 shows the path described by the original reference vector $\boldsymbol{v}^*_{\alpha\beta\gamma}$, the limited vector $\tilde{\boldsymbol{v}}^*_{\alpha\beta\gamma}$ and for $\hat{\boldsymbol{v}}^*_{\alpha\beta\gamma}$ in the $\alpha\beta\gamma$ space and the $\alpha\beta$ plane. Unlike $\hat{\boldsymbol{v}}^*_{\alpha\beta\gamma}$, the path described by $\tilde{\boldsymbol{v}}^*_{\alpha\beta\gamma}$ is also an ellipse, similar to the original reference $\boldsymbol{v}^*_{\alpha\beta\gamma}$, but it remains inside the allowable modulation region, being tangent to its interior borders. This yields to a limited reference $\tilde{\boldsymbol{v}}^*_{\alpha\beta\gamma}$, which maximize the utilization of the dc-link voltage without introducing additional harmonics components or phase shift on the controlled signals (see Table 5.5). Additionally, Fig. 5.46 shows a reconstruction of the output voltages for both limitation methods using only the first eleven harmonic components of Table 5.5. As it can be seen, although the proposed method reduces the amplitude of the sinusoidal references, it avoids the high distortion produced by the standard method saturating the reference to the borders of the polygon.

Fig. 5.47 shows the output voltages for the same conditions presented in Table 5.5, but connecting an output LC filter at the terminals of the four-leg NPC converter. Similarly to Fig. 5.46, the effectiveness of the proposed method can be clearly appreciated.

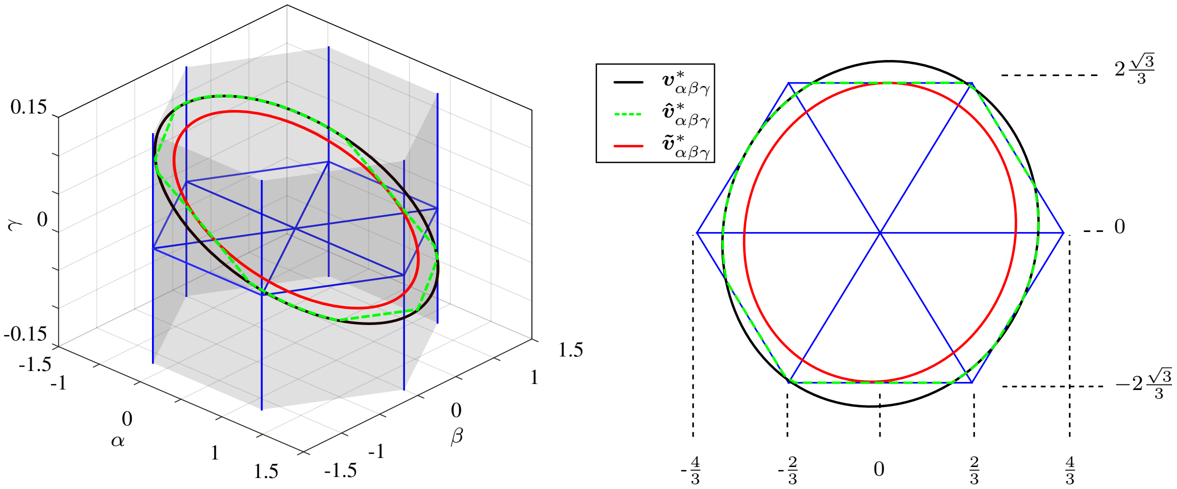

(a) (b)

Figure 5.45: (a) Path described by $\boldsymbol{v}^*_{\alpha\beta\gamma}$, $\tilde{\boldsymbol{v}}^*_{\alpha\beta\gamma}$ $\hat{\boldsymbol{v}}^*_{\alpha\beta\gamma}$ in the $\alpha\beta\gamma$ space for a sinusoidal unbalanced reference and (b) a top view of this figure.

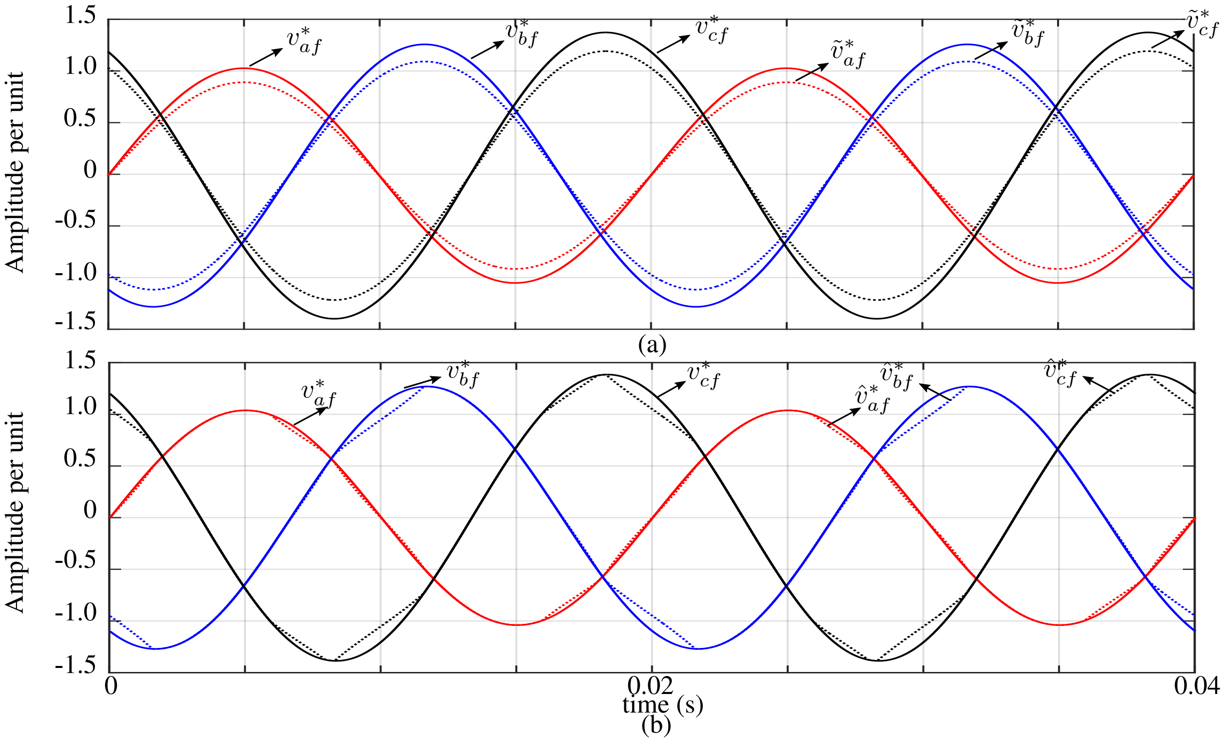

Figure 5.46: Reconstruction of output voltages using the first eleventh harmonics components for (a) the reference vector $\boldsymbol{v}^*_{abc}$ and its limitation $\tilde{\boldsymbol{v}}^*_{abc}$ inside the $\alpha\beta\gamma$ space. In (b) the saturation $\hat{\boldsymbol{v}}^*_{abc}$ is depicted.

In some works the idea of limiting the $\alpha\beta$ space by a circle, instead of using the natural hexagon, is extended to four-leg converters using a cylinder for limiting the modulation space in the $\alpha\beta\gamma$ space [33]. Although this idea is effective for balanced and symmetric systems, it is not an effective solution for unbalanced systems, as saturating the reference by a circular boundary produces same effects as saturating the reference by the borders of the polygon, i.e. incorporation of additional harmonics and phase shift of the controlled components.

Adding a fifth harmonic to the reference vector of Table 5.5, Table 5.6 is obtained. Comparing the second column of Table 5.6 with the second column of Table 5.5, not only the tracking of the fifth harmonic is achieved, but also a larger compensation for the fundamental component is possible. This is achieved because the vector generated by the fifth harmonic, i.e. $\boldsymbol{v}^*_{h_{\alpha\beta\gamma}}$, possesses opposite direction to the fundamental vector $\tilde{\boldsymbol{v}}^*_{f_{\alpha\beta\gamma}}$, when the later goes beyond the borders of the polygon, pushing the path showed in Fig. 5.45 towards the origin of the space. This is shown in Fig. 5.48, where the incorporation of the fifth harmonic allows a better utilization of the modulation space. Table 5.7 presents the same reference vector, but modifying the phase shift of the fifth harmonics. In this case, the vector $\boldsymbol{v}^*_{h_{\alpha\beta\gamma}}$ contributes to generate a path beyond the allowable modulation region. Therefore, the fundamental waveform is again limited as in Table 5.5 and the fifth harmonic is not fully compensated. However, for both cases, the proposed method does not produce additional harmonics or phase shift in the modified reference vector.

Let us now consider another example where not only fifth harmonic is compensated but also eleventh harmonic. Table 5.8 shows this example. Again $\boldsymbol{v}^*_{f_{\alpha\beta\gamma}}$ has been limited as originally in

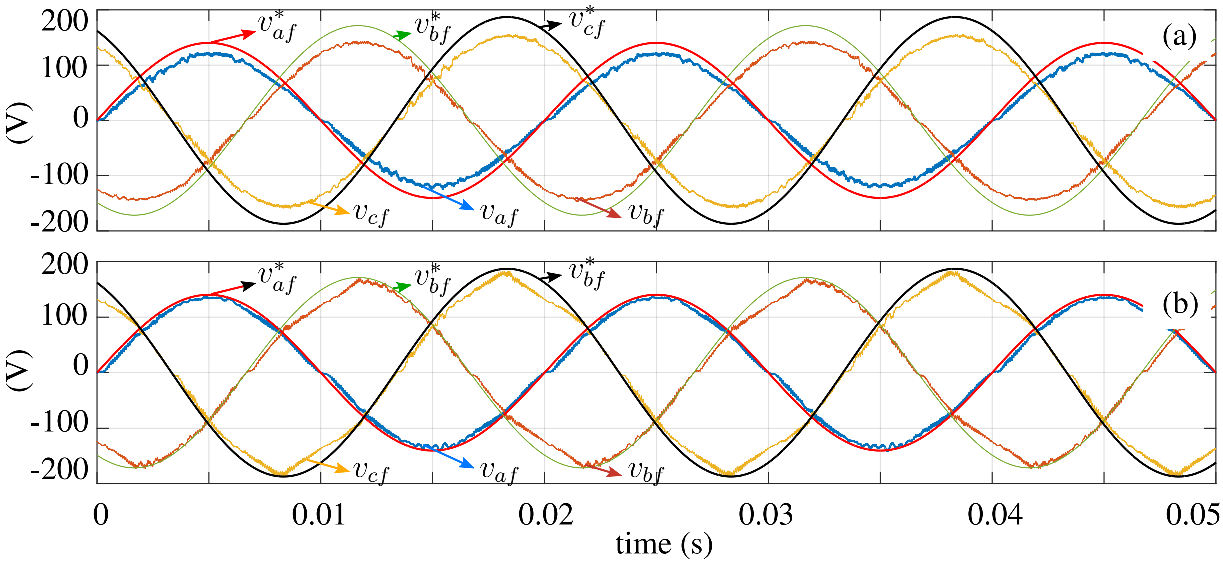

Figure 5.47: Output voltages using (a) the proposed overmodulation method ($\tilde{\boldsymbol{v}}_{abc}^*$) and (b) saturating the reference to the border of the allowable modulation region ($\hat{\boldsymbol{v}}_{abc}^*$) of a four-leg NPC converter connected with an output LC filter, L=210μH, C=20μF. Sampling frequency f_s=12kHz and *Single Redundancy Symmetric* switching pattern.

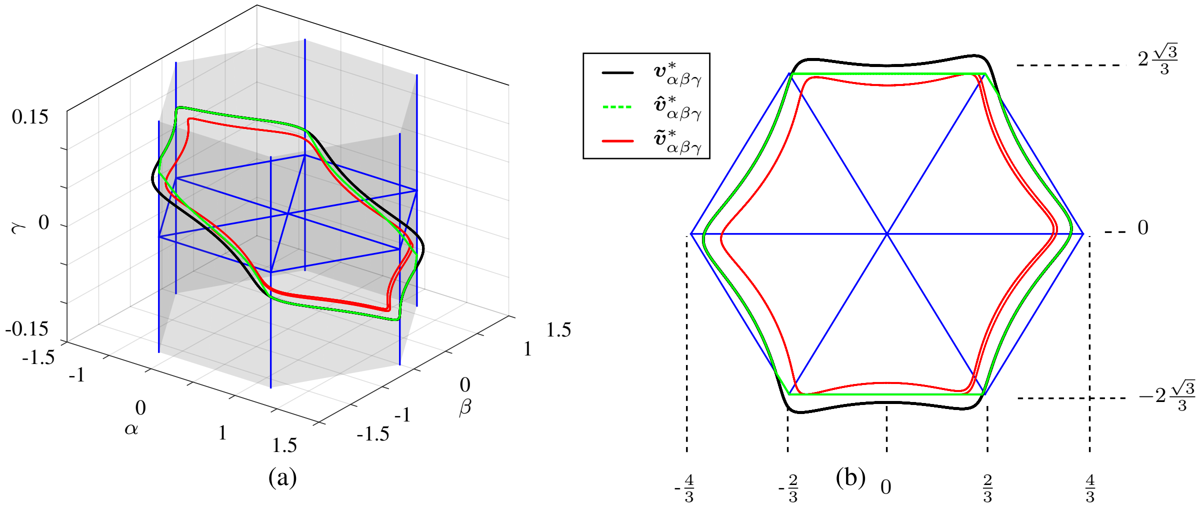

(a)

(b)

Figure 5.48: (a) Path described by $\boldsymbol{v}_{\alpha\beta\gamma}^*$, $\tilde{\boldsymbol{v}}_{\alpha\beta\gamma}^*$ $\hat{\boldsymbol{v}}_{\alpha\beta\gamma}^*$ in the $\alpha\beta\gamma$ space for a sinusoidal unbalanced reference with incorporation of fifth harmonic, in (b) a top view of this figure.

Table 5.6: Limitation for unbalanced fundamental reference vector and fifth harmonics. For $\tilde{\boldsymbol{v}}^*_{\alpha\beta\gamma}$, the limiting factors are: $\xi \approx 0.89$, η=1.0 and τ=1.0.

$H.Order$	$\frac{\sqrt{3}}{2}\boldsymbol{v}^*_{abc}$ $(\cdot 100)$	$\frac{\sqrt{3}}{2}\tilde{\boldsymbol{v}}^*_{abc}$ $(\cdot 100)$	$\frac{\sqrt{3}}{2}\hat{\boldsymbol{v}}^*_{abc}$ $(\cdot 100)$
1^{st}	$[90\angle 0°, 110\angle 240°, 120\angle 120°]$	$[80\angle 0°, 98\angle 240°, 107\angle 120°]$	$[89\angle 0.3°, 106\angle 238.7°, 115\angle 121°]$
3^{rd}	$[0\angle 0°, 0\angle 0°, 0\angle 0°]$	$[0\angle 0°, 0\angle 0°, 0\angle 0°]$	$[2\angle 179°, 2\angle 83.8°, 3\angle -54.3°]$
5^{th}	$[10\angle 0°, 10\angle 120°, 10\angle 240°]$	$[10\angle 0°, 10\angle 120°, 10\angle 240°]$	$[9\angle -2.2°, 9\angle 119°, 9\angle 243.4°]$
7^{th}	$[0\angle 0°, 0\angle 0°, 0\angle 0°]$	$[0\angle 0°, 0\angle 0°, 0\angle 0°]$	$[0\angle 0°, 2\angle -79.1°, 2\angle 92.6°]$
9^{th}	$[0\angle 0°, 0\angle 0°, 0\angle 0°]$	$[0\angle 0°, 0\angle 0°, 0\angle 0°]$	$[1\angle 8.8°, 1\angle 266.7°, 1\angle 112.8°]$

Table 5.7: Limitation for unbalanced fundamental reference vector and fifth harmonics. For $\tilde{\boldsymbol{v}}^*_{\alpha\beta\gamma}$, the limiting factors are: $\xi \approx 0.87$, η=0.9 and τ=1.0.

$H.Order$	$\frac{\sqrt{3}}{2}\boldsymbol{v}^*_{abc}$ $(\cdot 100)$	$\frac{\sqrt{3}}{2}\tilde{\boldsymbol{v}}^*_{abc}$ $(\cdot 100)$	$\frac{\sqrt{3}}{2}\hat{\boldsymbol{v}}^*_{abc}$ $(\cdot 100)$
1^{st}	$[90\angle 0°, 110\angle 240°, 120\angle 120°]$	$[78\angle 0°, 96\angle 240°, 104\angle 120°]$	$[88\angle 0.4°, 104\angle 238.5°, 113\angle 121°]$
3^{rd}	$[0\angle 0°, 0\angle 0°, 0\angle 0°]$	$[0\angle 0°, 0\angle 0°, 0\angle 0°]$	$[3\angle 210°, 3\angle 66.8°, 2\angle -52.8°]$
5^{th}	$[10\angle 90°, 10\angle 180°, 10\angle -84°]$	$[9\angle 90°, 9\angle 180°, 9\angle -84°]$	$[8\angle 90.9°, 7\angle 175.6°, 9\angle 259.4°]$
7^{th}	$[0\angle 0°, 0\angle 0°, 0\angle 0°]$	$[0\angle 0°, 0\angle 0°, 0\angle 0°]$	$[1\angle 72.9°, 3\angle -10.5°, 3\angle 193.4°]$
9^{th}	$[0\angle 0°, 0\angle 0°, 0\angle 0°]$	$[0\angle 0°, 0\angle 0°, 0\angle 0°]$	$[1\angle 107.6°, 0\angle 0°, 1\angle -81°]$
11^{th}	$[0\angle 0°, 0\angle 0°, 0\angle 0°]$	$[0\angle 0°, 0\angle 0°, 0\angle 0°]$	$[1\angle 199.3°, 1\angle 224.6°, 1\angle 32.8°]$
13^{th}	$[0\angle 0°, 0\angle 0°, 0\angle 0°]$	$[0\angle 0°, 0\angle 0°, 0\angle 0°]$	$[0\angle 0°, 1\angle 211°, 0\angle 0°]$

Table 5.5. Additionally, compared to Table 5.6 or Table 5.7, $\boldsymbol{v}^*_{h_{\alpha\beta\gamma}}$ has increased its magnitude and η is limited now to $\eta \approx 0.4$. Additionally, from the third column of Table 5.8, it is evident that the phase shift for the compensated components have been highly deviated.

From the modulation space of a four-leg NPC presented in Fig. 5.2, it can bee seen that a four-leg converter is able to compensate large zero sequence components. This is demonstrated in Table 5.9, where a large third-order zero sequence component is introduced to the reference vector, which has been fully compensated without affecting the compensation of fifth harmonic.

As definition, a zero sequence component is generated when the three abc reference signals posses the same amplitude and phase shift. Thereby, its $\alpha\beta$ components are zero and it possesses only a γ component (represented as $\boldsymbol{v}^*_{zs_{\alpha\beta\gamma}}$). This usually occurs in a balanced system by: 3^{th}, 9^{th}, 15^{th}, etc, harmonic components. However, in an unbalanced system, where the loads at each phase of the converter are different, it seldom occurs. Thus, in unbalanced systems, even the typical zero sequences systems such as: 3^{th}, 9^{th} or 15^{th} posses not only γ component, but also $\alpha\beta$ components. Under this condition, they are treated as any other harmonic, belonging to the vector $\boldsymbol{v}^*_{h_{\alpha\beta\gamma}}$. Table 5.10 shows an example of this situation, where the amplitudes for the third harmonic of the reference vector are different for each phase. Comparing the second

Table 5.8: Limitation for unbalanced fundamental reference vector, fifth and eleventh harmonics. For $\tilde{\boldsymbol{v}}^*_{\alpha\beta\gamma}$, the limiting factors are: $\xi \approx 0.87$, η=0.4 and τ=1.0.

$H.Order$	$\frac{\sqrt{3}}{2}\boldsymbol{v}^*_{abc}\,(\cdot 100)$	$\frac{\sqrt{3}}{2}\tilde{\boldsymbol{v}}^*_{abc}\,(\cdot 100)$	$\frac{\sqrt{3}}{2}\hat{\boldsymbol{v}}^*_{abc}\,(\cdot 100)$
1^{st}	$[90\angle 0°, 110\angle 240°, 120\angle 120°]$	$[78\angle 0°, 96\angle 240°, 104\angle 120°]$	$[87\angle 0.5°, 104\angle 238.5°, 113\angle 120.9°]$
3^{rd}	$[0\angle 0°, 0\angle 0°, 0\angle 0°]$	$[0\angle 0°, 0\angle 0°, 0\angle 0°]$	$[2\angle 207.9°, 3\angle 76.4°, 2\angle -46.5°]$
5^{th}	$[10\angle 90°, 10\angle 180°, 10\angle -84°]$	$[4\angle 90°, 4\angle 180°, 4\angle -84°]$	$[7\angle 92.7°, 7\angle 171.8°, 9\angle 258.5°]$
7^{th}	$[0\angle 0°, 0\angle 0°, 0\angle 0°]$	$[0\angle 0°, 0\angle 0°, 0\angle 0°]$	$[2\angle 85.4°, 3\angle -20.2°, 3\angle 190.7°]$
9^{th}	$[0\angle 0°, 0\angle 0°, 0\angle 0°]$	$[0\angle 0°, 0\angle 0°, 0\angle 0°]$	$[1\angle 128.4°, 1\angle 64.8°, 0\angle 0°]$
11^{th}	$[5\angle 16.4°, 7\angle 127.5°, 4\angle 25.2°]$	$[2\angle 16.4°, 3\angle 127.5°, 1\angle 25.2°]$	$[3\angle 20.4°, 5\angle 141.3°, 1\angle 268.1°]$
13^{th}	$[0\angle 0°, 0\angle 0°, 0\angle 0°]$	$[0\angle 0°, 0\angle 0°, 0\angle 0°]$	$[1\angle 16.3°, 2\angle 259.5°, 2\angle 112°]$

column of Table 5.9 with Table 5.10 it can be seen that the third harmonics is not longer treated as a zero sequence component, but it is limited as any other component of $\boldsymbol{v}^*_{h_{\alpha\beta\gamma}}$.

Table 5.9: Limitation for unbalanced fundamental reference vector, fifth harmonics and 90% of third order zero sequence component. For $\tilde{\boldsymbol{v}}^*_{\alpha\beta\gamma}$, the limiting factors are: $\xi \approx 0.87$, η=0.9 and τ=1.0.

$H.Order$	$\frac{\sqrt{3}}{2}\boldsymbol{v}^*_{abc}\,(\cdot 100)$	$\frac{\sqrt{3}}{2}\tilde{\boldsymbol{v}}^*_{abc}\,(\cdot 100)$	$\frac{\sqrt{3}}{2}\hat{\boldsymbol{v}}^*_{abc}\,(\cdot 100)$
1^{st}	$[90\angle 0°, 110\angle 240°, 120\angle 120°]$	$[78\angle 0°, 96\angle 240°, 104\angle 120°]$	$[88\angle 0.4°, 104\angle 238.5°, 113\angle 121°]$
3^{rd}	$[90\angle 0°, 90\angle 0°, 90\angle 0°]$	$[90\angle 0°, 90\angle 0°, 90\angle 0°]$	$[88\angle -0.9°, 91\angle 1.8°, 91\angle -0.9°]$
5^{th}	$[10\angle 90°, 10\angle 180°, 10\angle -84°]$	$[9\angle 90°, 9\angle 180°, 9\angle -84°]$	$[8\angle 90.9°, 7\angle 175.6°, 9\angle 259.4°]$
7^{th}	$[0\angle 0°, 0\angle 0°, 0\angle 0°]$	$[0\angle 0°, 0\angle 0°, 0\angle 0°]$	$[1\angle 72.9°, 3\angle -10.5°, 3\angle 193.4°]$
9^{th}	$[0\angle 0°, 0\angle 0°, 0\angle 0°]$	$[0\angle 0°, 0\angle 0°, 0\angle 0°]$	$[1\angle 107.6°, 0\angle 0°, 1\angle -81°]$
11^{th}	$[0\angle 0°, 0\angle 0°, 0\angle 0°]$	$[0\angle 0°, 0\angle 0°, 0\angle 0°]$	$[1\angle 199.3°, 1\angle 224.6°, 1\angle 32.8°]$
13^{th}	$[0\angle 0°, 0\angle 0°, 0\angle 0°]$	$[0\angle 0°, 0\angle 0°, 0\angle 0°]$	$[0\angle 0°, 1\angle 211.3°, 0\angle 0°]$

Table 5.10: Limitation for balanced fundamental reference vector, third, fifth and eleventh harmonics. For $\tilde{\boldsymbol{v}}^*_{\alpha\beta\gamma}$, the limiting factors are: $\xi \approx 1.0$, $\eta \approx 0.35$ and τ=1.0.

$H.Order$	$\frac{\sqrt{3}}{2}\boldsymbol{v}^*_{abc}$ $(\cdot 100)$	$\frac{\sqrt{3}}{2}\tilde{\boldsymbol{v}}^*_{abc}$ $(\cdot 100)$	$\frac{\sqrt{3}}{2}\hat{\boldsymbol{v}}^*_{abc}$ $(\cdot 100)$
1^{st}	$[90\angle 0°, 90\angle 240°, 90\angle 120°]$	$[90\angle 0°, 90\angle 240°, 90\angle 120°]$	$[88\angle 0°, 87\angle 239.1°, 86\angle 120°]$
3^{rd}	$[20\angle 0°, 10\angle 0°, 10\angle 0°]$	$[7\angle 0°, 3\angle 0°, 3\angle 0°]$	$[19\angle -1.7°, 10\angle 3.1°, 11\angle 0.3°]$
5^{th}	$[20\angle 90°, 10\angle 180°, 10\angle -84°]$	$[7\angle 90°, 3\angle 180°, 3\angle -84°]$	$[19\angle 83.2°, 10\angle 165.3°, 12\angle 264°]$
7^{th}	$[10\angle 0°, 30\angle 240°, 40\angle 120°]$	$[3\angle 0°, 10\angle 240°, 14\angle 120°]$	$[9\angle 4.4°, 27\angle 238.4°, 36\angle 122.6°]$
9^{th}	$[0\angle 0°, 0\angle 0°, 0\angle 0°]$	$[0\angle 0°, 0\angle 0°, 0\angle 0°]$	$[1\angle 173.2°, 1\angle 115.4°, 2\angle -31.7°]$
11^{th}	$[0\angle 0°, 0\angle 0°, 0\angle 0°]$	$[0\angle 0°, 0\angle 0°, 0\angle 0°]$	$[2\angle -53.7°, 2\angle 96.1°, 1\angle 180°]$
13^{th}	$[0\angle 0°, 0\angle 0°, 0\angle 0°]$	$[0\angle 0°, 0\angle 0°, 0\angle 0°]$	$[1\angle 145.2°, 3\angle 59.1°, 3\angle 254°]$

5.9 Discussion and Final Remarks

This chapter provided a comprehensive analysis of the three-dimensional SVM for a four-leg NPC converter. The experimental results presented in this chapter are intended to validate the proposed techniques to synthesize the output voltages of a four-leg NPC converter, including the balance of the voltages in dc-link capacitors. Therefore, they are mostly implemented in open-loop control and some of them in open circuit. An implementation of these algorithms under a closed-loop control is presented in the next chapter for an aerospace application.

The following remarks summarizes the contributions of this chapter, which can be also considered as contributions to the state of the art in this matter:

- A simple algorithm for achieving a space vector modulation in $\alpha\beta\gamma$ coordinates was proposed and experimentally validated. The algorithm reduces the complexity of the three dimensional search of tetrahedrons to only two dimensions, based on a simple three steps algorithm. Due to the generality of the proposed algorithm, it can be also applicable in further topologies, where control of the zero sequence is required.

- An algorithm for determining a suitable switching pattern for a four-leg NPC converter, considering the voltage balance of the dc-link capacitors was also addressed. An experimental validation of a switching pattern using a single redundant vector at each sampling time for achieving a nearly constant switching frequency for each device of the converter was successfully implemented and tested under different unbalanced and non-sinusoidal references.

- Using the proposed algorithm for generating the switching pattern, an active method for balancing the voltages on the dc-link capacitor was successfully implemented. It was showed that the ripple of the voltages in each of the dc-link capacitors is directly proportional to the unbalance level of the load. Additionally, the shape and frequency of the ripple of these voltages is defined by the line currents and is not restricted to be a sinusoidal of three times the fundamental frequency as in a three-leg NPC converter. Furthermore, a limitation for balancing the dc-link voltages occurs when a dc component is introduced in any of the line currents. This dc component is transfer to the NP current i_z, which makes the dc-link voltages diverge unless the dwell times of the redundant vectors are large enough to compensate this dc component over one fundamental cycle.

- An overmodulation algorithm for limiting a reference vector without introducing additional harmonics or phase shift on the reference values was presented in this section. This algorithm effectively limit a reference vector within the modulation range either in an $\alpha\beta$ plane or $\alpha\beta\gamma$ space, maximizing the utilization of the dc-link voltage. For this propose, the utilization of $\alpha\beta\gamma$ coordinates is very useful, as it makes easy to identify when the reference vector is out of the allowable modulation space.

CHAPTER 6

A four-leg NPC Converter as a Gound Power Supply

Abstract: *This chapter shows the utilization of a four-leg NPC converter as a Ground Power Unit (GPU) for aerospace applications. The fourth leg of the converter allows to handle unbalanced and non-linear loads presents in an aircraft. Furthermore, the multilevel nature of a four-leg NPC converter enables the reduction of the switching frequency in each device of the converter, which is crucial in this application due to the high* $400Hz$ *fundamental frequency. Additionally, it also allows compensation of higher order harmonic compared to two-level topologies. The resonant controllers described in Chapter 4 and the three-dimensional SVM algorithm with voltage balance of the dc-link capacitors presented in Chapter 5 have been implemented to successfully achieve control of a GPU compensating up to the eleventh harmonic component.*

In the last decades, the aircraft industry has faced a tremendous development in the technology used for communication, services and control systems within an aircraft [165], [166]. Electronic devices have played a fundamental role in this growth, leading to a more complex and sophisticated electrical system within the plane. The supply of electrical energy has to fulfill stringent power quality and safety regulations [10], [167]. By that, typical voltage levels within an aircraft have changed in the last decades, first $28Vdc$ was used [168]. However, nowadays and because of the higher power range and incorporation of sophisticated electronic devices, the standards typically establish a phase-to-neutral voltage level of $115Vrms$ at $400Hz$ [10]. The operation of an aircraft can be divided into two modes: ground and flight operation mode [168]. During flight operation mode, oil is used to drive the turbines, which are used to provide the aircraft with electrical energy. When the aircraft is landing and turbines are slowing down (ground operation mode), the electricity is provided to the aircraft by an Auxiliary Power Unit (APU), located normally at the rear of the aircraft. However, once the plane has landed, the use of the APU is restricted to avoid noise and pollution. Thereby, a Ground Power Unit (GPU) is connected to the aircraft instead. This connection was normally coordinated by operators to

(a) (b)

Figure 6.1: (a) Power Electronics based GPU and (b) Diesel operated GPU.

first shut down the APU and then connect the GPU to the aircraft. Nonetheless, in the last generation of commercial aircrafts (Boing 777, MD-11, Airbus 360) power transfer is achieved without interruptions and no previous disconnection of the APU is required, this is known as non-break power transfer (NBPT) [169]. Although GPUs have been for decades based on motor-generation system [168], this configuration is being replaced by static power converters, which provides more reliability, better power quality, better performance, lower price, lower maintenance and higher efficiency, becoming an standard solution for this application. Fig. 6.1 shows a typical solid state based and a diesel operated GPU connected to an aircraft.

The electrical system of an aircraft can be considered as a three-phase, four-wire unbalanced system, where different loads are connected to each of the phase-neutral voltages. Therefore, a GPU is designed as a four-wire power supply with phase-to-neutral voltages of $115Vrms$, $400Hz$ and with a power operation range between 30-$200kVA$, being $90kVA$ the most typical power rate. Furthermore, a 100% overload for $1s$ is usually required [169].

Fig. 6.2 shows the standard solution for a power electronics based GPU [154]. Three H-bridges, sharing the same dc-link, are used to control independently each of the output phase-to-neutral voltages. This allows to compensate the unbalanced drop voltages presents in the output filter, giving full controllability at the output of the converter. An alternative configuration reported in the literature uses transformers to add the output voltages of several inverters, generating an steeped output waveform [170]. Although this configuration offers good THD_v and low switching frequency, its controllability is complicated and the high number of elements reduce its reliability. Recently, new topologies such as matrix converters have been implemented in the literature as GPU [23,155,171]. This topology performs good power quality and does not require dc-link capacitors, which entails a compact design and higher reliability. However, it requires a high number of switches and high switching frequencies per device, which is its main drawback. By that, a four-leg NPC converter arises as a promising new solution for implementation of GPUs. The fourth leg provides an extra path to control zero-sequences components. Moreover, the topology reduces the switching frequency of each device com-

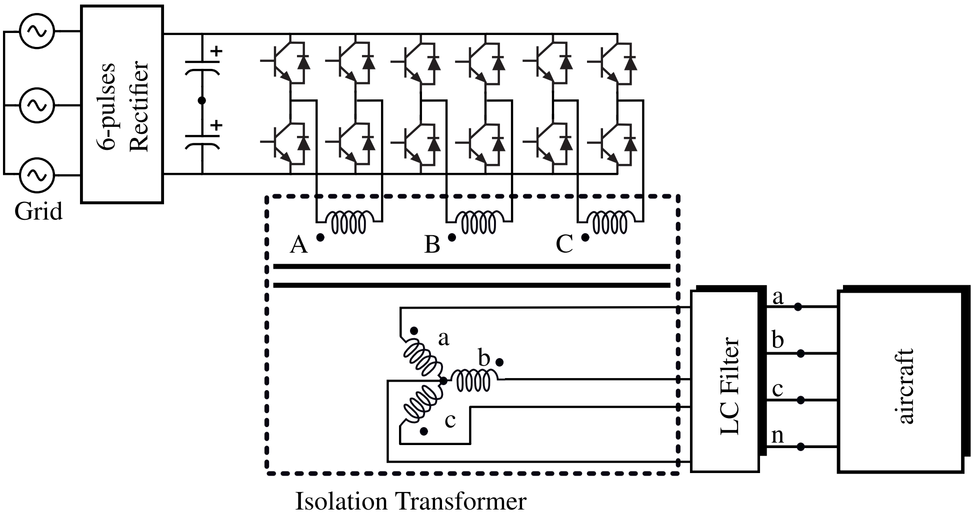

Figure 6.2: Six legs converter used as standard solution for a four-wired, 400 Hz Ground Power Unit. An isolation transformer could be required to avoid ground loops between the input grid and the load. A second order LC power filter is used at the aircraft side.

pared with a standard solution, allowing a higher efficiency, higher sampling rate and higher harmonics compensation [172]. Furthermore, the higher number of levels at the output voltage allows to use a smaller output filter and therefore a less bulky solution with lower reactive power consumption.

Standard Uninterruptible Power Supplies (UPS) for $50/60Hz$ operate at switching frequencies between $2-12kHz$. The high rate between the fundamental and the switching frequency allows to successfully implement several control schemes, such as: nested *d-q* controllers, resonant controllers, repetitive and predictive controllers [90, 135, 148, 173, 174]. When a $400Hz$ GPU is designed, the use of a $2kHz$ switching frequency is not longer an alternative, because the ratio between the fundamental component and switching frequency is dramatically reduced. Therefore, in this application the switching frequency has to be typically around $10-15kHz$ and even higher when harmonic compensation is required. Moreover, because of the high bandwidth required for the inner current loop used in double-loop nested controllers, this kind of controllers are not practically implementable and the use of single-loop voltage controllers have been preferred for this application. By that, in [169] a robust single-loop strategy has been proposed to control the output voltage of a GPU. However, although it achieves good performance under linear loads, it is not capable of compensating harmonic distortion under no-linear loads.

The necessity of providing harmonic compensation presents a new challenge for GPUs, originated from the large incorporation of electronic devices within an aircraft. Thereby, because of its easy implementation and high performance, recently resonant controllers have arisen as a competitive solution to control UPSs [21, 129, 133, 154, 155, 171]. In [154] a resonant controller have been proposed as a solution for a standard two-level, $400Hz$ GPU. The implementation includes third $(1200Hz)$, fifth $(2000Hz)$ and seventh $(2800Hz)$ harmonic compensation. Nonetheless, in GPU applications ($400Hz$ and $90kVA$), the two-level nature of the converter limits higher harmonics compensation because of the physical limitation of the switching devices. This problem has been overcame by the proposed multilevel topology, where regulation of the fundamental $400Hz$ voltage signal as well as compensation of the third, fifth, seventh, ninth and eleventh harmonic components are successfully achieved. Furthermore, special considerations such as sensitivity peak and discretization method must be taken into consideration during the controller design for ensuring stability and fast transient response when high order harmonics wants to be compensated [60,149,151]. This was extensively discussed in Chapter 4 and is implemented in the following sections.

6.1 Ground Power Unit Controller Design

Fig. 6.3 shows the proposed solution for a $400Hz$, $110Vrms$ GPU, where the aircraft is represented as a linear/non-linear, balanced/unbalanced load. A small output LC filter, designed with a resonance at $2.4kHz$, is connected to the output of the converter. A single-loop resonant controller is implemented to control the output voltages of the GPU, compensating third, fifth, seventh, ninth and eleventh harmonics. The three-dimensional SVM algorithm along with the overmodulation method proposed in Chapter 5 are used to synthesize the output voltages. Furthermore, using the redundant vectors of the four-leg NPC and the measurement of the dc-link voltages and output currents, a Proportional-Integral controller is implemented to balance the voltages on the dc-link capacitors.

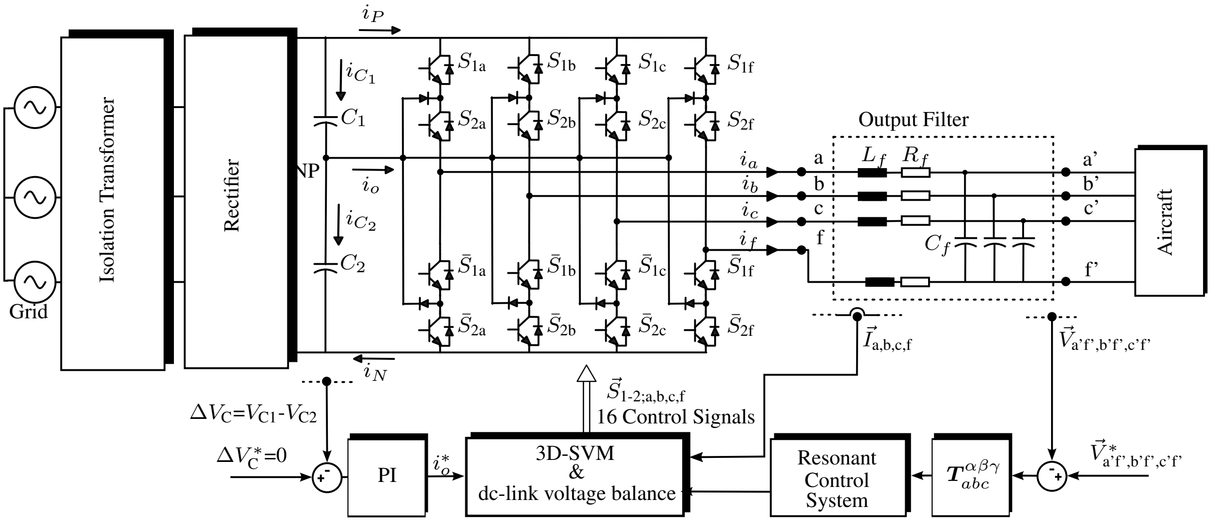

Figure 6.3: Control scheme for the proposed four-leg NPC used as GPU. An small output LC filter is used to obtain $400Hz$ sinusoidal output voltages. R_f represents the series resistance, L_f is the filter inductance and C_f is the capacitor of the filter. L_f=$425\mu H$, C_f=$10\mu F$ and R_f=0.4Ω.

6.1.1 Resonant Controller Design

The second-order transfer function that represents the output LC filter of Fig. 6.3 is given by

$$P(s) = \frac{V_o(s)}{V_i(s)} = \frac{1}{L_f C_f s^2 + R_f C_f s + 1} \tag{6.1}$$

where $V_o(s)$ and $V_i(s)$ represent the output and input voltages of the LC filter. As it was introduced in Chapter 4, the general form of a suitable resonant controller able to compensate the time delay introduced by the real time controller and the phase shift introduced by the LC filter of (6.1) is given by

$$R^c(s) = \sum_{n=1,3,..,11} R_n^c(s) = \sum_{n=1}^{k} K_n \frac{s\cos\vartheta_n - \omega_n \sin\vartheta_n}{s^2 + \omega_n^2} \tag{6.2}$$

where K_n represents the gain, ω_n is the resonance frequency and ϑ_n is the compensation angle for each of the n^{th} resonant compensators.

In order to implement (6.2) in a real-time digital platform, a discrete-time representation of the system must be obtained. The diagram of Fig. 6.4 shows the discrete-time close loop control structure.

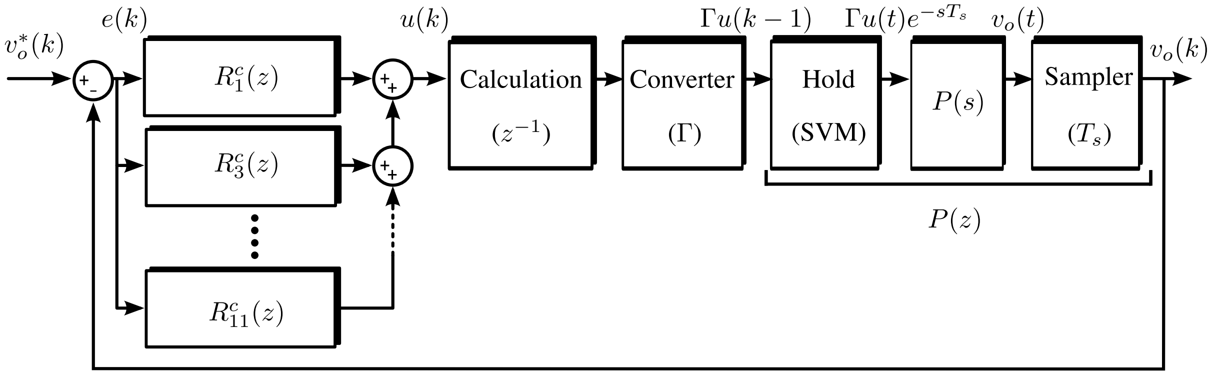

Figure 6.4: Discrete-time single-loop control structure for implementation of resonant controllers. $v_o^*(k)$ and $v_o(k)$ represents the reference and controlled discrete-time output voltages. $R_n^c(z)$ for $n = \{1,3,5,7,9,11\}$ represent a resonant controller with delay compensation for compensation of a signal with frequency ω_n in discrete-time, with ω_1=800πrad/s.

The computational delay has been represented as one sampling time delay and the converter as a constant gain Γ. Additionally, the plant is discretized by using a ZOH approximation. This discretization is presented in (6.3) and obtained using (4.43) with f_s=$16.8kHz$ and the parameters given in Fig. 6.3.

$$P^{zoh}(z) = \frac{0.38z + 0.37}{z^2 - 1.19z + 0.94} \tag{6.3}$$

The selection of the discretization method used in a resonant controller plays a fundamental role for the stability of the system. By that, Tusting with Prewarping (TPW) and First Order Hold (FOH) approximations are the most suitable discretization methods, as they maintain the resonance frequency and its infinite gain unalterable (see Chapter 4). Thus, the FOH discrete form of the controller presented in (6.2) is given by

$$R^{c-foh}(z) = \sum_{n=1,3,..,11} R_n^{c-foh}(z) = \sum_{n=1}^{k} K_n \frac{cos(\omega_n D_n T_s)(1-z^{-2})(1-cos(\omega_n T_s)))}{\omega_n^2 T_s (1-2z^{-1}cos(\omega_n T_s)+z^{-2})} \tag{6.4}$$

$$-\frac{sin(\omega_n D_n T_s)\left[\omega_n T_s - sin(\omega_n T_s) + z^{-1}(2sin(\omega_n T_s) - 2\omega_n T_s cos(\omega_n T_s)) + z^{-2}(\omega_n T_s - sin(\omega_n T_s))\right]}{\omega_n^2 T_s (1-2z^{-1}cos(\omega_n T_s)+z^{-2})}$$

where T_s is the discretization sampling time, K_n represents the gain and ω_n is the resonance frequency for each of the n^{th} resonant compensators. Equivalently to ϑ_n of (6.2), D_n in (6.4) is the number of samples to be compensated by the n^{th} resonant controller and is given by

$$D_n = \frac{-\angle P^{zoh}(z_n = e^{j\omega_n T_s})rad}{T_s \omega_n} + 1.0 \tag{6.5}$$

where $P^{zoh}(z_n = e^{j\omega_n T_s})$ is the ZOH discrete-time LC filter given in (6.3), evaluated at the resonance frequency z_n and the unitary term is for compensating the computational delay.

Table I shows the phase shift introduced by the plant and the equivalent phase shift generated by the computational time delay T_s for each of the compensated frequencies. The values are expressed for the continuous and discrete-time representations, using a sampling frequency of $f_s = 16.8kHz$.

Table I: Angle Compensation ϑ_n and D_n for $\omega_{1,3,5,7,9,11}$

ω_n rad/s	-$\angle P(j\omega_n)$	-$\angle P^{zoh}(z_n = e^{j\omega_n T_s})$	-$\angle e^{-j\omega_n T_s}$	ϑ_n	D_n
$\omega_1 = 2\pi \cdot 400$	0.59°	4.87°	8.57°	9.16°	1.56
$\omega_3 = 2\pi \cdot 1200$	2.27°	15.13°	25.71°	27.98°	1.58
$\omega_5 = 2\pi \cdot 2000$	8.69°	30.11°	42.85°	51.54°	1.70
$\omega_7 = 2\pi \cdot 2800$	167.42°	197.11°	60°	227.42°	4.28
$\omega_9 = 2\pi \cdot 3600$	175.59°	214.11°	77.14°	252.73°	3.77
$\omega_{11} = 2\pi \cdot 4400$	177.18°	224.21°	94.28°	271.46°	3.37

For the sake of explanation, before displaying the complete design for the six resonant controllers, only compensation of the fundamental component ($400Hz$) is analyzed. Thereby, Fig. 6.5 shows the discrete-time Bode and Nyquist diagrams for the open-loop transfer function of the control scheme of Fig. 6.4. The resonant controller of (6.4) has been implemented for $n=1$ and with the compensation term D_1 of Table I. Furthermore, the discrete-time representation of the second order plant of (6.3) has been used.

Fig. 6.5a shows that the angle of the open-loop transfer function at ω_1 is set to ±90°. This improves the stability margin of the close-loop system and it is achievable because of the compensation term D_1 introduced in the resonant controller. This can be also observed in the Nyquist diagram of Fig. 6.5b, where the path marked as σ_1 shows the trajectory tending to infinity with an angle of $\xi_1 = 90°$ for $\omega \approx \omega_1^-$. Likewise, the path marked as σ_2 shows the trajectory for $\omega \approx \omega_1^+$, which is also parallel to the imaginary axis, with $\xi_1 = -90°$. Consequently, before the path tends to the origin of the plane ($\omega \rightarrow \omega_{nyq}$), it describes a curve which approaches to the critical point $(-1, 0j)$. This path is generated by the resonance of the LC filter (ω_c) and mainly define the minimum distance between the point $(-1, 0j)$ and the Nyquist curve, i.e. the inverse of the sensitivity peak η. The gain of the controller K_1 can be selected to adjust η in the Nyquist diagram. By that, K_1 is tuned to select a good trade off between stability margin and transient response. The path marked with dotted line represents the Nyquist diagram for negative frequencies, which is symmetrically placed respect to the path depicted for positive frequencies.

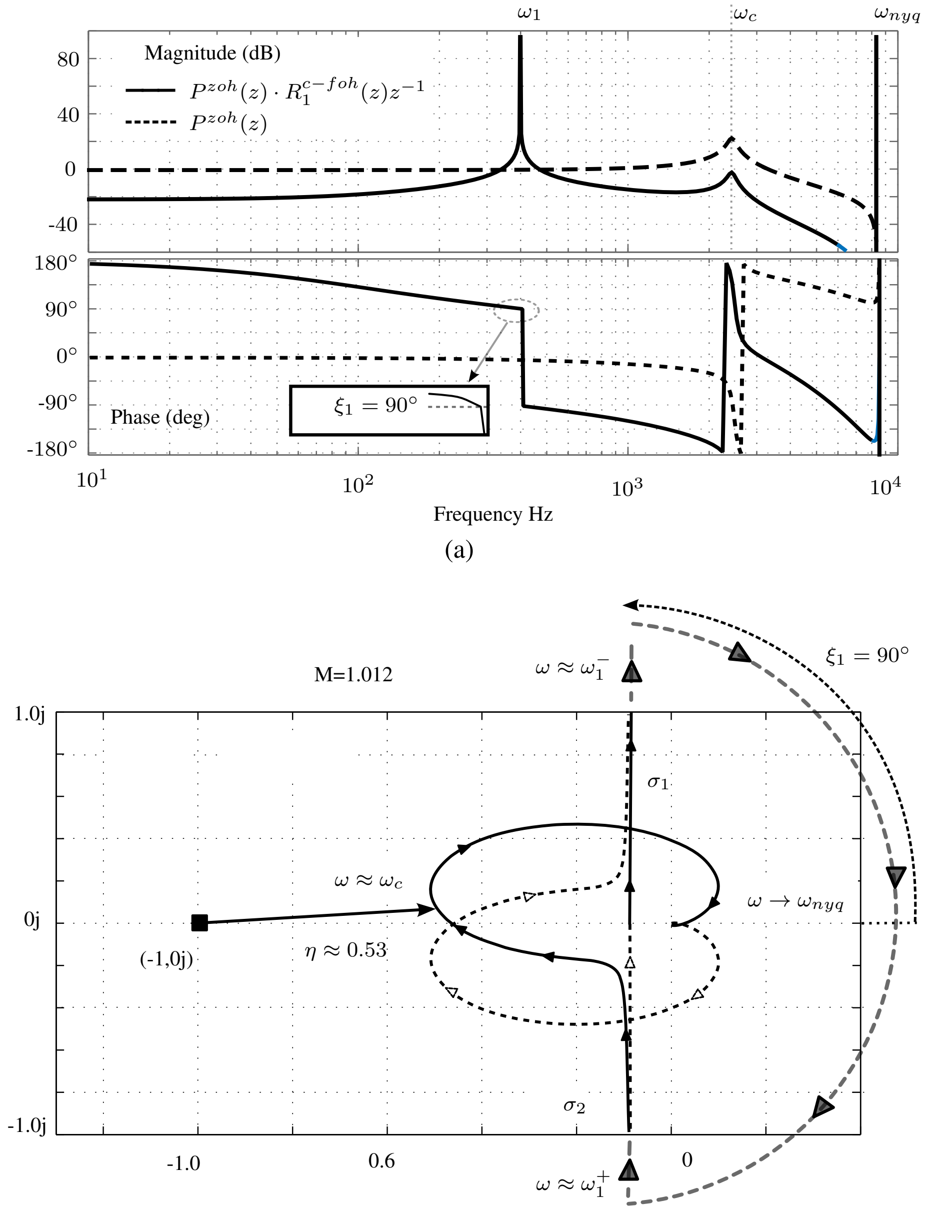

(a)

(b)

Figure 6.5: (a) Bode and (b) Nyquist diagram for the open-loop system $H(z) = R_1^{c-foh}(z)P^{zoh}(z)z^{-1}$. $T_s = 1/16800$ s, $R_f = 0.4\ \Omega$, $L_f = 425\ \mu$H and $C_f = 10\ \mu$F. $\omega_c = 2\pi \cdot 2400$ rad/s, Nyquist frequency $\omega_{nyq}{=}\frac{2\pi \cdot 16800}{2}$ rad/s. For $R_1^{c-foh}(z)$: D_1=1.28, $\omega_1 = 800\pi$ rad/s, $K_1 = 850$. In (b) Nyquist response for positive and negative frequencies (dotted lines) is shown.

Fig. 6.6 shows the discrete Bode and Nyquist diagram for the final design. This includes the compensation of the fundamental $400Hz$ component and compensation up to the eleventh odd harmonic components. The six parameters D_n of Table I have been used for implementation of the complete resonant controller of (6.4). Similarly to Fig. 6.5a, the Bode diagram of Fig. 6.6a possesses six peaks at each of the resonant frequencies $\omega_{1,3,5,7,9,11}$. The phase shift introduced by the LC filter and computational delay have been compensated in the controller for each of resonance frequencies. Thereby, a phase of $\pm 90°$ around $\omega_{1,3,5,7,9,11}$ is obtained. This is illustrated in Fig. 6.6b, where each of the resonance frequencies generates a path that tends to infinity with $90°$ and then appears $180°$ forward from the bottom of the graph. Thereby, the paths σ_1 and σ_2 are associated to the fundamental frequency ω_1. Consequently, each of the following pairs of paths, i.e. $\sigma_{3,4}$, $\sigma_{5,6}$, $\sigma_{7,8}$, $\sigma_{9,10}$ and $\sigma_{11,12}$, are associated with each of the five compensated harmonics, i.e. $\omega_{3,5,7,9,11}$. It can be noticed that between path σ_6 and σ_7 (between the fifth $(2.0kHz)$ and seventh $(2.8kHz)$ harmonic) the trajectory approaches to the critical point $(-1, 0j)$. As mentioned before, this is generated by the resonance of the LC filter, placed at approximately $2.4kHz$, which present the main limitation for increasing the gain of the controllers $(K_{1,3,5,7,9,11})$.

Compared to Fig. 6.5b, in Fig. 6.6b the gain K_1 for the fundamental controller has been notoriously reduced from 850 to 150. However, a similar value for the inverse of the sensitivity peak η is obtained in the Nyquist diagram. This reduction is explained due to the incorporation of the additional controllers, which gains also contribute to expand the Nyquist trajectory towards the critical point $(-1, 0j)$. Thus, the gains for each of the harmonic compensators, i.e. $K_{3,5,7,9,11}$, have been selected to achieve a good trade off between a safe stability margin and a fast transient response. Although these parameters are firstly designed by a theoretical approach a fine tuning is usually necessary during real implementation to achieve the desired performance. The following chapter presents an experimental validation of this controller implemented under several different scenarios.

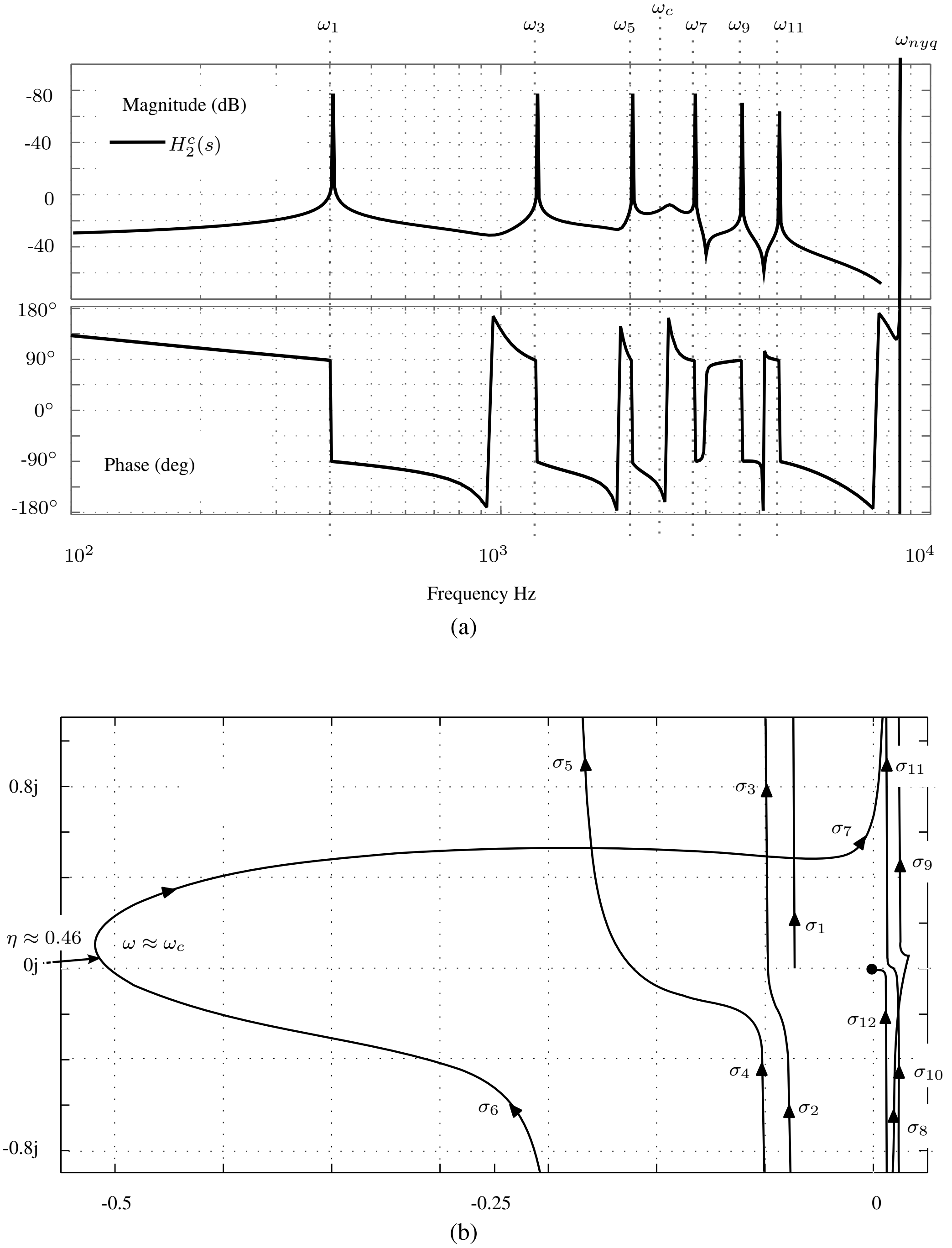

(a)

(b)

Figure 6.6: (a) Bode and (b) Nyquist diagram for the open-loop system $H(z) = R^{c-foh}(z)P^{zoh}(z)z^{-1}$. $T_s = 1/16800$ s, $R_f = 0.4\ \Omega$, $L_f = 425\ \mu$H and $C_f = 10\ \mu$F. $\omega_c = 2\pi \cdot 2400$ rad/s, Nyquist frequency $\omega_{nyq}=\frac{2\pi\cdot 16800}{2}$ rad/s. For $R^{c-foh}(z)$: K_1=150, $K_{3,9,11}$=100, $K_{5,7}$=50 D_n and ω_n from Table I.

6.2 Experimental Results

In order to validate the proposed four-leg NPC topology and the resonant controller design as a suitable solution for a GPU. The diagram of Fig. 6.3 has been implemented in the experimental rig presented in Fig. 5.18. The aircraft of Fig. 6.3 has been replaced by several linear/non-linear, balanced/unbalanced loads. Table II shows the different experimental parameters used on the consecutive experimental results. The three-dimensional SVM has been implemented with a switching frequency of f_s=$16.8kHz$ and with the *Single-Redundancy Symmetric* switching pattern throughout this section. Furthermore, the overmodulation method presented in Chapter 6.1.1 and the active balance of the voltages on the dc-link capacitors have been also implemented.

Table II: General Parameters of the Implemented Systems

Parameter	Value	Parameter	Value
C_1	$3300\,\mathrm{uF}$	Z	$10\,\Omega\,;2\,mH$
C_2	$3300\,\mathrm{uF}$	Z_1	$10\,\Omega\,;2\,mH$
V_{dc}	$325-430\,\mathrm{V}$	Z_2	$14\,\Omega\,;2\,mH$
C_f	$10\,\mathrm{uF}$	Z_3	$17\,\Omega\,;2\,mH$
L_f	$425\,\mathrm{uH}$	Single/Three-phase Full Wave	$220\,uF\,;60\,\Omega$
f_{sw}	$16.8\,\mathrm{kHz}$	Diode Bridge Rectifier	

6.2.1 Steady-State Performance

Using the controller designed in Section 6.1.1 for compensation of up to the eleventh odd harmonics and the parameters of the first column of Table II. Fig. 6.7 shows the performance of the proposed system of Fig. 6.3 under balanced operation, using Z of Table II as the load for each of the phases of the converter ($2.5kW$ approximately). As it can be seen, under this situation the voltages and currents posses very low distortion, even considering the small output LC filter and the high fundamental frequency. The output voltages posses an output effective value of $110Vrms$, frequency of $400Hz$ and a harmonic distortion below 1.2%, calculated using the first 50 harmonics of each output voltages. The theoretical voltage required in the dc-link of the four-leg NPC converter to modulate output phase-to-neutral voltages with a magnitude of $110Vrms$ is given by

$$2V_{dc}{=}110\sqrt{2}\sqrt{3} \approx 270Vdc \tag{6.6}$$

However, in order to provide enough voltage to compensate the drop voltages present on the LC filter. This value has been increased in the experimental rig to $325Vdc$. The balanced nature of the load avoids the generation of neutral current. Thus, for this case, i'_f=0, reducing the losses of the fourth leg to a negligible value.

Fig. 6.8 shows the unbalanced operation of the converter, using Z_1, Z_2 and Z_3 as loads for the output phase-to-neutral voltages of the converter: $v_{a'f'}$, $v_{b'f'}$ and $v_{c'f'}$ respectively. The power consumption of each branch are approximately: $0.95kW$, $0.65kW$ and $0.75kW$ respectively. As it can be seen, the controller successfully compensates the different magnitudes of drop voltages

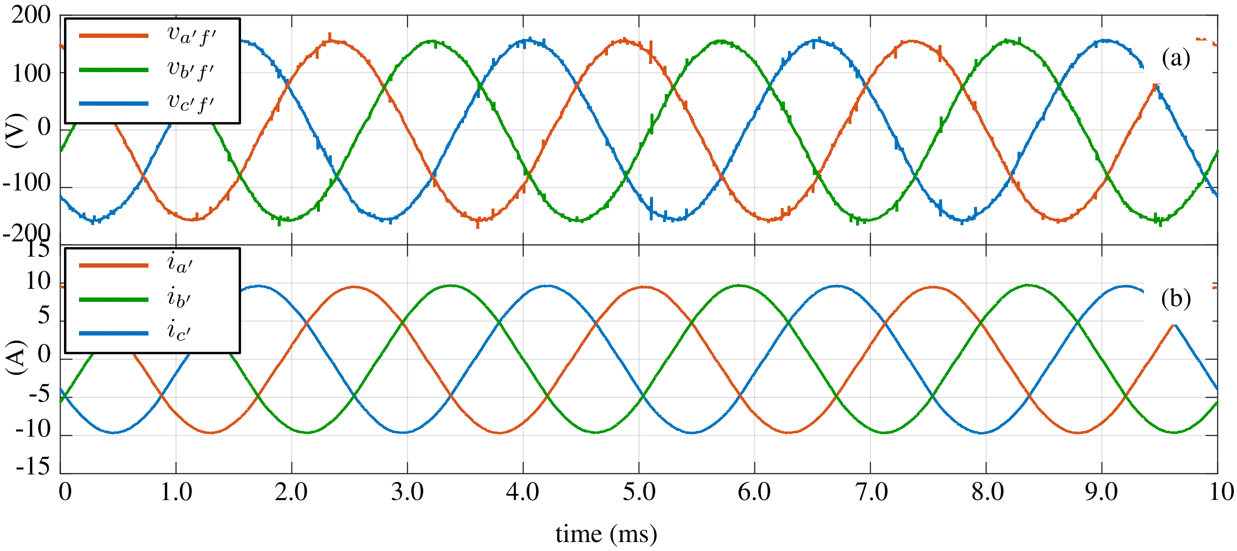

Figure 6.7: (a) Output voltages $v_{a'f'}$, $v_{b'f'}$ and $v_{c'f'}$ and (b) output currents $i_{a'}$, $i_{a'}$, $i_{c'}$ for a GPU under balanced linear load with load equal to Z. Sampling frequency of f_s=$16.8kHz$. *THD*$_{v_{a'f'}}$=1.11%, *THD*$_{v_{b'f'}}$=1.11% and *THD*$_{v_{c'f'}}$=1.12%.

on each phase of the filter, maintaining the output voltages balanced with an effective value of $110Vrms$ and frequency of $400Hz$. Moreover, the voltage harmonic distortion of each voltage is less than 2%, which is very good considering the small output filter and the small rate between the fundamental and the switching frequency. In addition, it successfully accomplished with the maximum allowable voltage harmonic distortion of 5% stated in military standards [10]. Furthermore, from Fig. 6.8b, the converter is able to handle a zero sequence current, i.e. i'_f, that possesses a higher magnitude than the line current i'_c and similar magnitude to $i_{a'}$ and $i_{b'}$. This remarks the fact that the fourth leg of the converter does not have to be designed with a reduced nominal power rate.

In order to evaluate the performance of the proposed topology and control strategy under non-linear loads, a three-phase full wave diode bridge rectifier with a RC load at the *dc* side is connected at the output of the GPU (see Table II). Fig. 6.9 shows the output voltages and currents using the balanced load (Z) and the $1.2kW$ three-phase full wave diode bridge rectifier of Table II. As described above, odd harmonics until the 11^{th} component have been compensated. As it can be seen, although the currents are very distorted, the output voltages remains with a low harmonic distortion, with a total voltage harmonic distortion below 3.0%. Additionally, their effective value and frequency are successfully regulated to $110Vrms$ and $400Hz$. In order to provide enough voltage for compensation of harmonic components, the dc-link voltage has been increased to $420Vdc$. Due to the connected rectifier does not produce zero sequence current and the linear load is balanced, the neutral current i'_f is negligible and is not depicted. Fig. 6.10 shows the reference voltages generated by the controller, which subsequently are synthesized by the three-dimensional SVM algorithm. Clearly, the reference voltage is far from an ideal sinusoidal. However, this is the required waveform to compensate the voltage drop produce by the distorted current circulating through the filter inductance L_f to subsequently obtain a sinusoidal load voltage.

Fig. 6.11 shows the output voltages under the same conditions of Fig. 6.9, but with com-

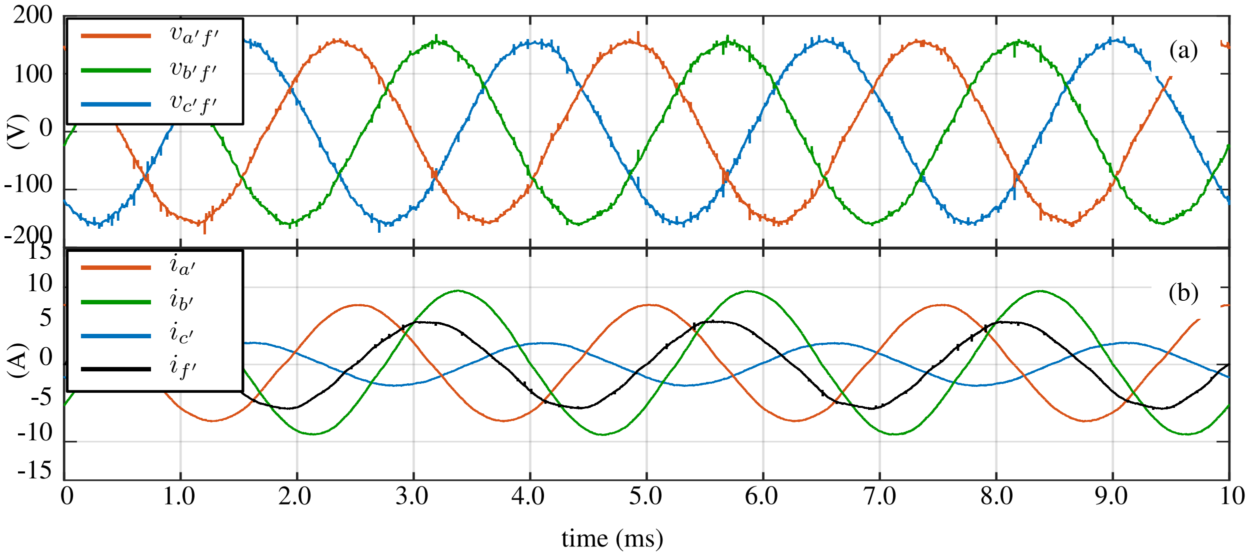

Figure 6.8: a) Output voltages $v_{a'f'}$, $v_{b'f'}$ and $v_{c'f'}$ and (b) output currents $i_{a'}$, $i_{a'}$, $i_{c'}$ for a GPU under unbalanced linear load with load equal to Z_a, Z_b and Z_c. Sampling frequency of f_s=$16.8kHz$. *THD*$_{v_{a'f'}}$=1.8%, *THD*$_{v_{b'f'}}$=1.9% and *THD*$_{v_{c'f'}}$=1.9%.

pensation of only fundamental $400Hz$ component. Although the fundamental component of these output voltages are still regulated to $110Vrms$ and $400Hz$, the total harmonic distortion is approximately 10%, which does not fulfill the maximum 5% required by the standards [10]. By that, the compensation of high order harmonics is mandatory to provide suitable output voltages.

Fig. 6.12 shows the performance of the GPU under an unbalanced linear load and the three-phase diode bridge rectifier of Table II. Thereby, even under unbalanced situation the output voltages are properly regulated and with a harmonic distortion below 3.3%. Additionally, the zero-sequence current generated by the linear unbalanced load is also depicted in Fig. 6.12c.

Finally, Fig. 6.13 shows the performance of the proposed GPU connected to a $0.4kW$ the single-phase full wave diode bridge rectifier and to the unbalanced linear load (Z_1, Z_2, Z_3) of Table II. As the single-phase full wave diode bridge rectifier introduces a distorted zero sequence component, the neutral current is not sinusoidal and contains the harmonics generated by the rectifier. This current also contains some even harmonics which are not compensated by the controller. Thereby, although the total harmonic distortion of the output voltages is still below the required 5% the phase where the single.phase rectifier is connected possesses a higher harmonic distortion.

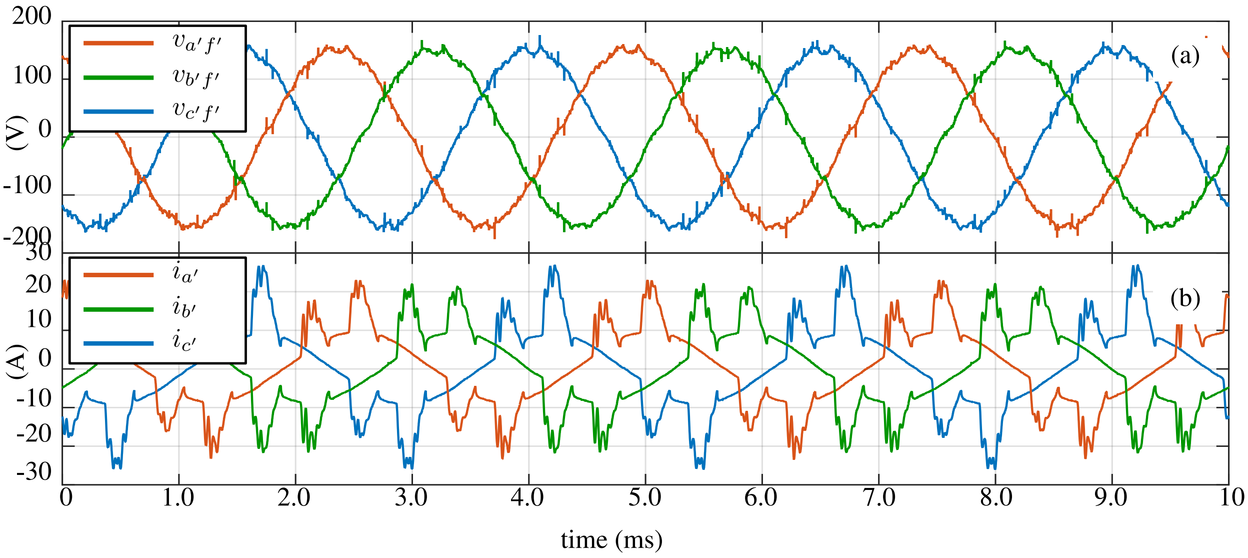

Figure 6.9: (a) Output voltages $v_{a'f'}$, $v_{b'f'}$ and $v_{c'f'}$ and (b) output currents $i_{a'}$, $i_{a'}$, $i_{c'}$ for a GPU connected to a balanced linear load (Z) and the three-phase rectifier of Table II. Sampling frequency of f_s=$16.8kHz$. *THD*$_{v_{a'f'}}$=2.8%, *THD*$_{v_{b'f'}}$=3.0% and *THD*$_{v_{c'f'}}$=3.0%.

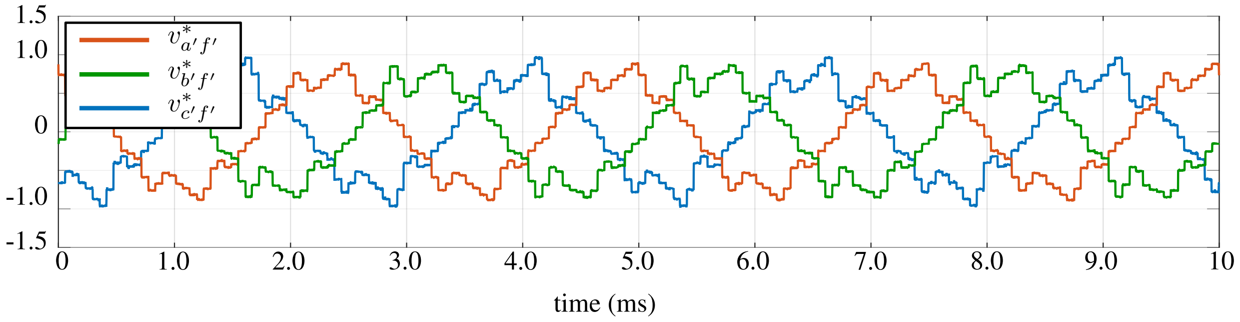

Figure 6.10: Reference voltages $v^*_{a'f'}$, $v^*_{b'f'}$ and $v^*_{c'f'}$ for a GPU connected to a balanced linear load (Z) and the three-phase rectifier of Table II.

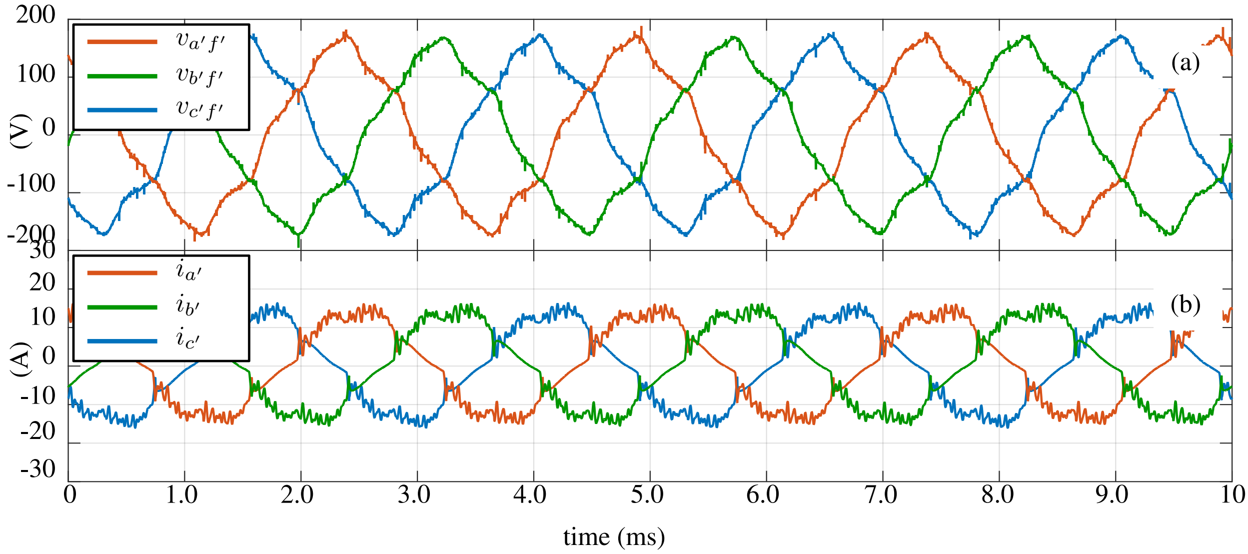

Figure 6.11: a) Output voltages $v_{a'f'}$, $v_{b'f'}$ and $v_{c'f'}$ and (b) output currents $i_{a'}$, $i_{a'}$, $i_{c'}$ for a GPU connected to a balanced linear load (Z_1, Z_2 and Z_3) and the three-phase rectifier of Table II. Compensation of only fundamental $400Hz$ component. Sampling frequency of f_s=$16.8kHz$. *THD*$_{v_{a'f'}}$=9.7%, *THD*$_{v_{b'f'}}$=9.8% and *THD*$_{v_{c'f'}}$=9.5%.

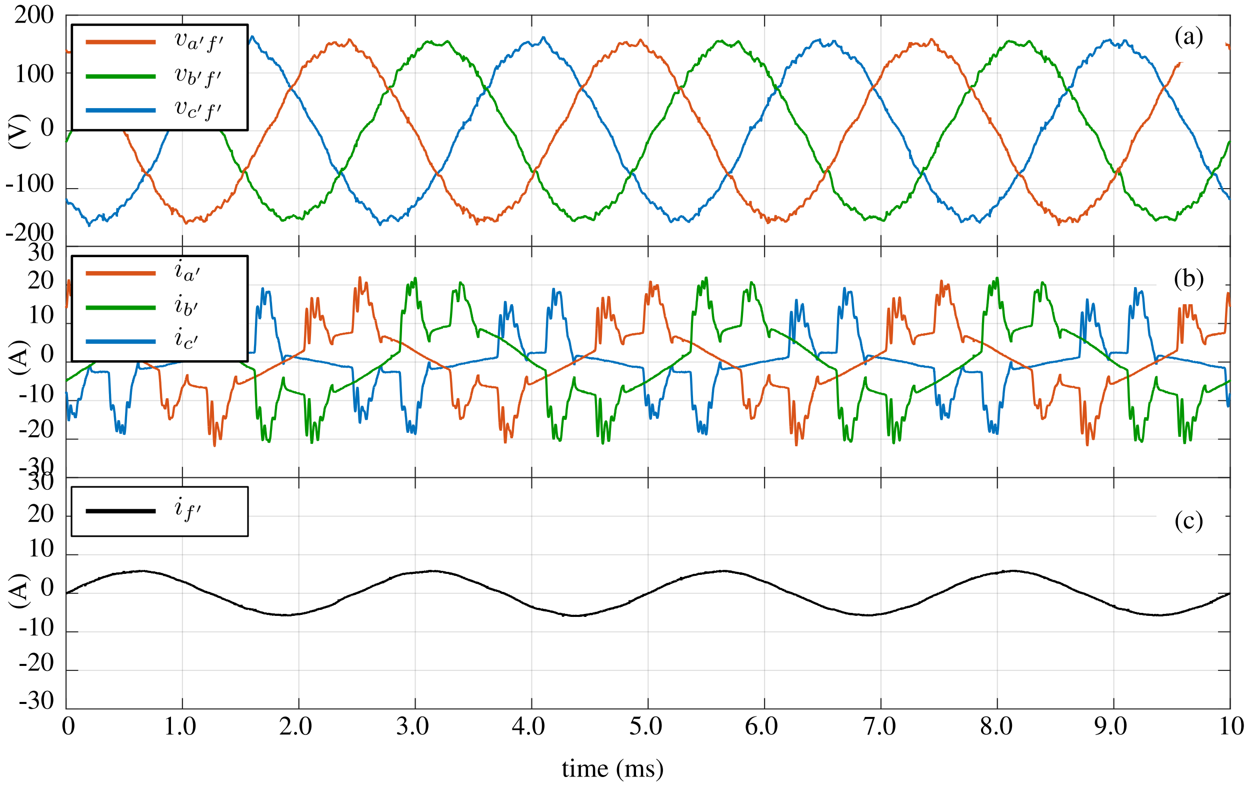

Figure 6.12: (a) Output voltages $v_{a'f'}$, $v_{b'f'}$ and $v_{c'f'}$ and (b) output currents $i_{a'}$, $i_{a'}$, $i_{c'}$ (c) $i_{f'}$ for a GPU connected to a unbalanced linear load (Z_1, Z_2 and Z_3) and the three-phase rectifier of Table II. Sampling frequency of f_s=$16.8kHz$. *THD*$_{v_{a'f'}}$=3.3%, *THD*$_{v_{b'f'}}$=3.1% and *THD*$_{v_{c'f'}}$=3.3%.

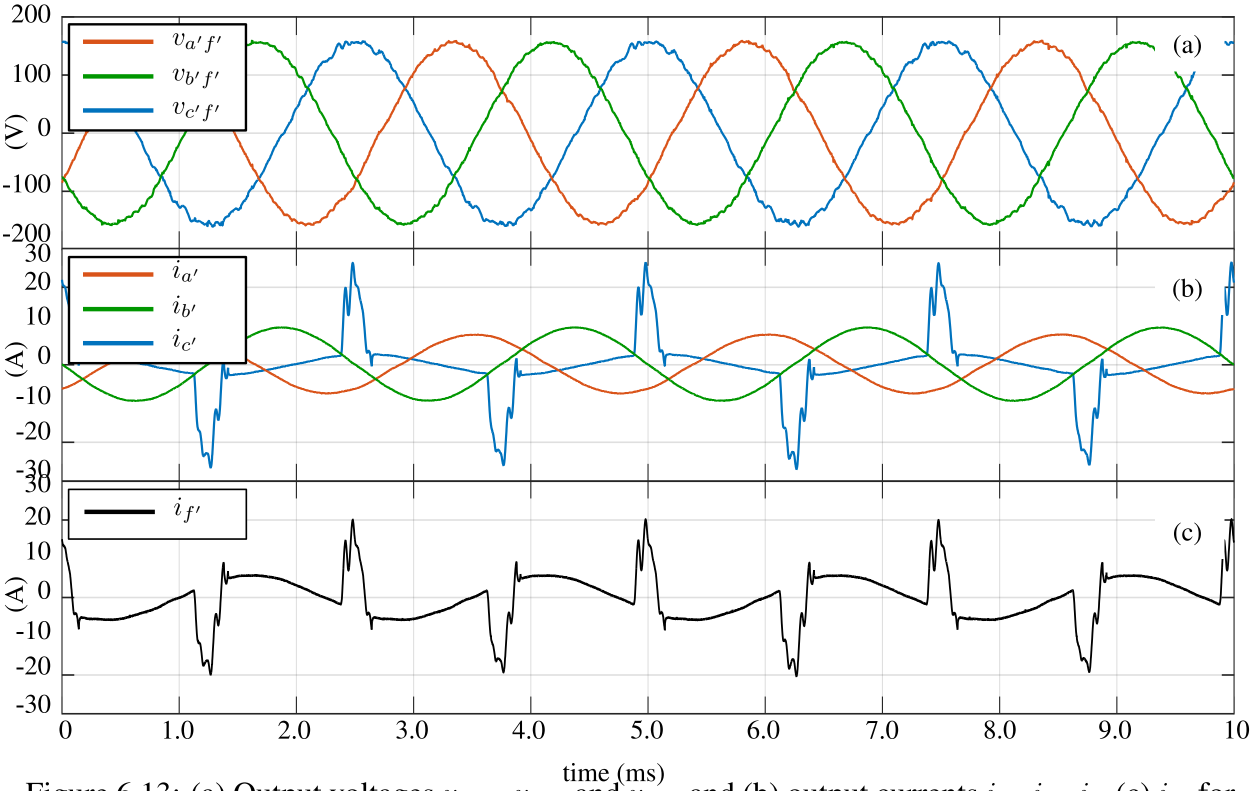

Figure 6.13: (a) Output voltages $v_{a'f'}$, $v_{b'f'}$ and $v_{c'f'}$ and (b) output currents $i_{a'}$, $i_{a'}$, $i_{c'}$ (c) $i_{f'}$ for a GPU under unbalanced linear load (Z_1, Z_2 and Z_3) and the single-phase rectifier of Table II. Sampling frequency of f_s=$16.8kHz$. *THD*$_{v_{a'f'}}$=2%, *THD*$_{v_{b'f'}}$=1.6% and *THD*$_{v_{c'f'}}$=2.7%

6.2.2 Transient Performance

Although the steady-state condition represents the most important operation mode of a GPU, its transient response must also accomplish with certain requirements. In this section it is demonstrated that the proposed solution provides an excellent transient response under different conditions and accomplishes with standards requirements tested in critical conditions.

Fig. 6.14 shows the performance of the GPU for disconnection of a balanced load ($2.8kW$). A three-phase mechanical switch has been connected to the load and opened at t_0. As it can be seen, the output voltages return to a sinusoidal condition after approximately 2 cycles, i.e. $5ms$.

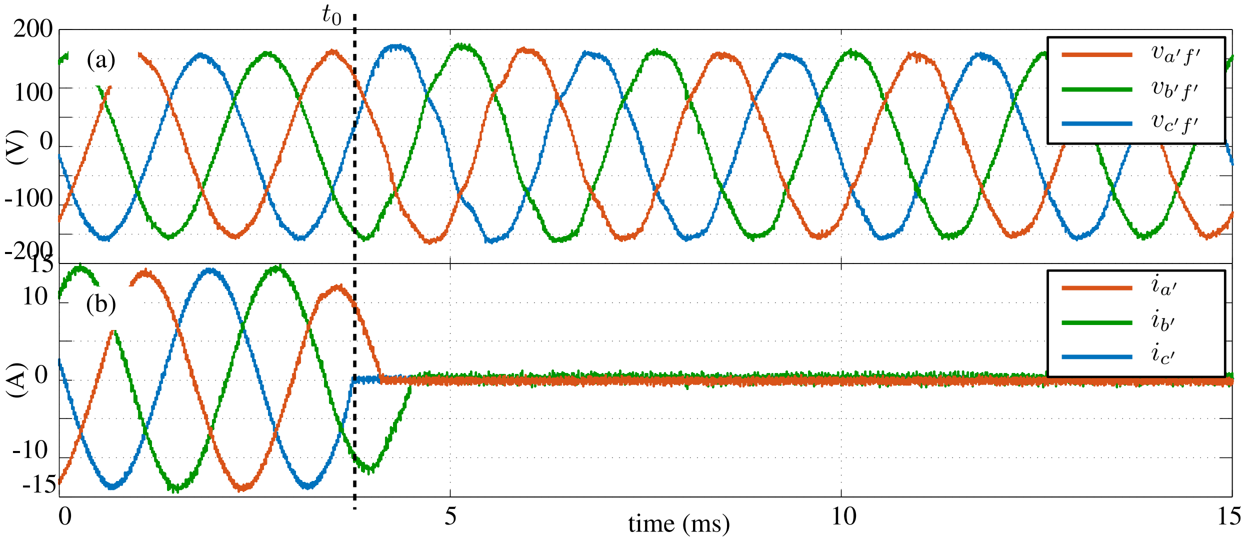

Figure 6.14: (a) Output phase-to-neutral voltages $v_{a'f'}$, $v_{b'f'}$, $v_{c'f'}$ and (b) line currents i'_a, i'_b and i'_c for disconnection of balanced load of $2.8kW$.

Fig. 6.15 illustrates the transient from an unbalance operation to a full balanced load. A three-phase mechanical switch has been connected to incorporate load at t_0. As it can be observed, the output voltages are almost not affected by the load impact.

Fig. 6.16 shows the regulation of the voltages on the dc-link capacitors from an open circuit condition to the full $2.8kW$ balanced linear load. The voltage deviation is less than $5V$, converging to its reference after around $100ms$. This validates the effectiveness of the voltage balance algorithm used on the three-dimensional SVM and the proper design of the PI controller for balancing the voltage on each capacitor.

Fig. 6.17 presents the transient response for the load impact of a $1.27kW$ three-phase full wave diode bridge rectifier of Table II. Even considering that this is a critical load impact, the controller can reject disturbances after approximately $16ms$ (6-7 cycles). As the capacitor placed at the *dc* side of the rectifier is not charged before the load impact, it behaves as a short circuit and the voltage is not controllable for around 1 cycle. Additionally, the limitation given by the standard in [10] for transient operation has been also depicted in Fig. 6.17a. It can be noticed that the transient response accomplish with required standard , which still allows an overvoltage of $118Vrms$ after $87.5ms$.

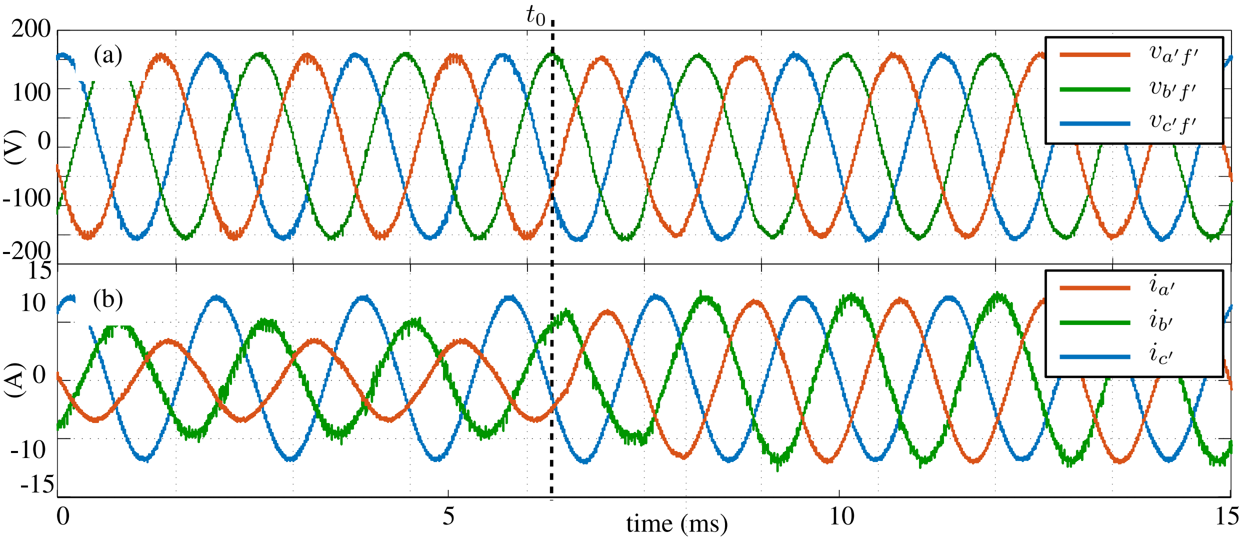

Figure 6.15: (a) output phase-to-neutral voltages $v_{a'f'}$, $v_{b'f'}$, $v_{c'f'}$ and (b) line currents i'_a, i'_b and i'_c for load impact from unbalanced load Z_1, Z_2, Z_3 to a balanced load of $2.8kW$.

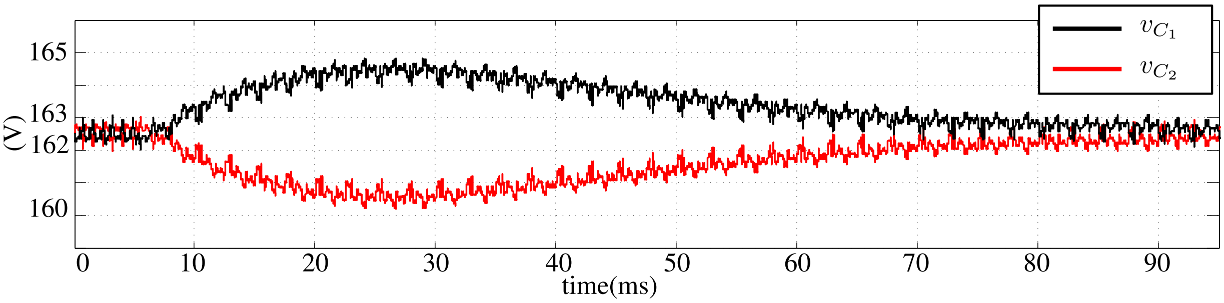

Figure 6.16: Voltage on the dc-link capacitors C_1 and C_2 from open circuit to a balanced load of $2.8kW$.

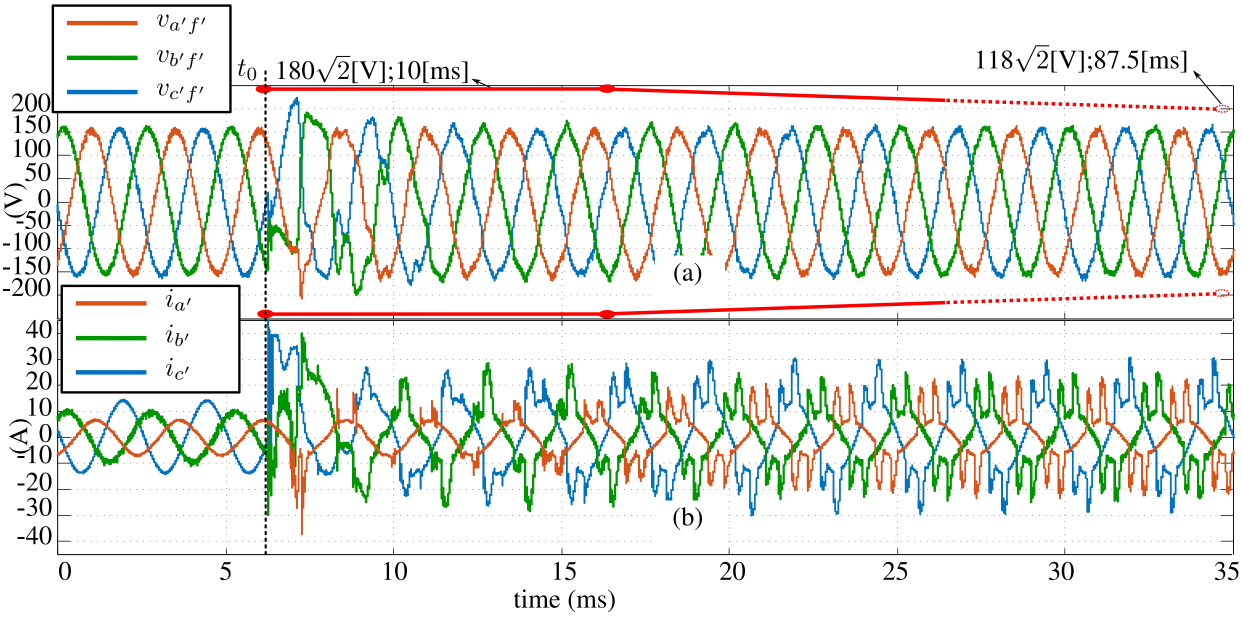

Figure 6.17: (a) Output voltages $v_{a'f'}$, $v_{b'f'}$ and $v_{c'f'}$ and (b) output currents $i_{a'}$, $i_{a'}$, $i_{c'}$ for the transient response fo the connection of the three-phase rectifier of Table II. Previous the impact the unbalanced linear load (Z_1,Z_2,Z_3) of Table II is connected.

6.3 Final Remarks

In this Chapter it has been shown that the four-leg NPC converter can be successfully implemented as a GPU for aerospace applications. The higher equivalent frequency of the modulated output voltages, compared to a two-level topology, allows to compensate higher harmonic components, reduce the output filter and reduce the switching frequency, i.e. power losses, in each switching device of the converter. A controller designed for compensation until 11^{th} order harmonic was implemented reducing the *THD* of the output voltages to a maximum of 3.3% even under very unbalanced and non-linear load conditions. Additionally, the transients response provided by the converter accomplishes easily with the requirements of the standards.

The implementation of this application serves also to demonstrate the excellent performance of the proposed three-dimensional SVM algorithm, the implementation of the switching pattern and the algorithm to actively balance the voltages of the dc-link capacitors in a real application and under demanding conditions.

It is important to remark the importance of the discretization process of the controller and the compensation of the phase-shift produced by the LC filter and the computational delay before implementation. The incorporation of these factors are crucial to avoid malfunction of the converter under different loads, specially non desirable resonances of the high order controlled harmonics.

CHAPTER 7

Conclusions

Throughout this dissertation, the reader has been provided with an extensive analysis and discussion of modulation techniques implemented in power electronics converters for four-wire applications. It has been demonstrated that four-leg converters provides a superior performance, better utilization of the dc-link voltage and less harmonic distortion, compared to the three-leg four-wire converters, becoming the most promising topology to be the standard solution for four-wire applications.

Three-dimensional SVM algorithm has demonstrated to be the most flexible and suitable solution to synthesize output voltages in four-leg converters. Moreover, its implementation in $\alpha\beta\gamma$ coordinate frame provides several advantages, such as:

- Very simple calculation of dwell-times.
- Direct control of zero-sequence component.
- Flexibility to design different switching patterns and control the devices switching frequency.
- Optimal utilization of redundant vectors to balance the voltages of the dc-link capacitors in multilevel converters.
- Possibility to shape the harmonic spectrum, i.g. even order harmonics elimination.
- Simple extension to further four-leg topologies.

A novel three-dimensional overmodulation algorithm proposed in this work has demonstrated to be an effective method to maintain the reference vector inside the allowable modulation space, without incorporate additional undesirable harmonic components into the modulated waveforms. This is of special interest in four-leg converters, which are usually implemented for compensation of harmonic distortion, where the addition of unexpected harmonics can originate harmful resonances or malfunction of the external controllers.

Regarding the balance of the voltages on the dc-link capacitors of a four-leg NPC converter, it was demonstrated that the balance is always possible as long as the output line currents of the converter do not contain a *dc* component. The incorporation of a *dc* component limits the voltage balance capability even using an active control for maintaining the voltages balanced. The limitation is restricted to the magnitude of the *dc* component and the path described by the reference voltage vector. Thereby, the balance is possible only when the dwell times of the redundant vectors used in the modulation over one fundamental period are large enough to compensate the *dc* component introduced by the current.

The four-leg NPC converter has proven to be a suitable solution to implement it as a GPU. Its multilevel nature allows compensation of high order harmonics, while maintaining a low switching frequency in each device of the converter. Thereby, harmonic components of $4.4kHz$ were compensated with a switching frequency of only approximately $8.4kHz$ in each device of the converter. The discretization method used to implement the resonant controller in a digital platform is of fundamental importance for achieving an stable operation. Thereby, TPW and FOH methods are the most suitable approximations, as they maintain the infinitive gain and the resonance frequency unalterable after the discretization process. Likewise, the compensation of the time delay produced by the computational calculation is also crucial to ensure stability when high order harmonics are being compensated. This is mainly because this time represents an important portion of the period of high order harmonics. A lack of compensation of this delay can directly originate an unstable close-loop system, which was analyzed in an Nyquist analysis.

Finally, it is important to mention that for a successful experimental implementation, the following technical issues were of crucial importance:

- The utilization of fiber optic for sending the gate signals from the real time system to the converter is very important to avoid false trigger of the switching devices. This is specially important when voltages over $350V$ are used in the dc-link.

- The type of cable and method for transmitting the measured variables from the measurement boards to the real time controller is crucial to achieve a noiseless measurement. In this work, the measurements were sent as differential signal using a $5m$ pair-crossed and shielded cable.

- As the four-leg NPC converter is not a commercial topology, the design of the electronic board is very important to reduce the drop voltage and losses of the power stage and reduce the noise in the drive circuit of each switching device. For this proposed, a six layer PCB was designed in cooperation with Nottingham University.

7.1 Outlook

In its current state, the two-level four-leg converter is the only topology that can be considered as a mature technology, which has been in commercial applications, such as: active filters and programmable power supplies, mainly for research purpose.

The use of multilevel four-leg converters is still mainly limited to experimental prototypes and represents still an open and interesting field for future research. The following points gives a guide, to the opinion of he author, for continue the research in this field:

- Different strategies for balancing the voltage on the dc-link capacitors in a four-leg NPC converter can be implemented to overcome the limitation occurred when the line currents posses *dc* component.
- The proposed algorithm can be implemented in different promising topologies, such as: Matrix Converters or flying capacitors converters.
- In order to improve the harmonic distortion, reduce the switching frequency per device and reduce the size of output filter in a GPU application, the implementation of the proposed modulation technique can be applied in a higher order multilevel converter. This can proof the simple extension of the algorithm.
- The implementation of four-leg converters as part of a μGrid is still a topic which can be further explored. Several challenges are still open in this field, such as: analysis of low-voltage ride-through capabilities considering zero-sequence component, analysis of droop control or faster methods for controlling power flow in four-wire networks or capability of a coordinated transition of a set of converters from island mode to grid connected operation.
- The use of back-to-back converters using a standard rectifier and a four-leg converter for direct connection of generation units to four-wire systems also represent an interesting future application. This avoids the use of transformes, which have to be connected in Delta-Wye to provide a neutral connection and have to be oversized to be able to handle unbalances and distorted currents typically found in distribution systems.
- Another interesting application is to use a combined control scheme based on a non-linear controller, such as FS-MPC, with a modulated scheme, such as SVM. This can be applicable when compensation of several harmonics is required, as the implementation of the controller become very demanding in computational effort.

APPENDIX A

Tables Background Theory

Table A.1: *Redundant Symmetric n-type* sequence. P=1; N=-1

Sector I	$v^0_{\alpha\beta\gamma}$ [NNN]	$v^1_{\alpha\beta\gamma}$ [PNN]	$v^2_{\alpha\beta\gamma}$ [PPN]	$v^7_{\alpha\beta\gamma}$ [PPP]	$v^2_{\alpha\beta\gamma}$ [PPN]	$v^1_{\alpha\beta\gamma}$ [PNN]	$v^0_{\alpha\beta\gamma}$ [NNN]
Sector II	$v^0_{\alpha\beta\gamma}$ [NNN]	$v^3_{\alpha\beta\gamma}$ [NPN]	$v^2_{\alpha\beta\gamma}$ [PPN]	$v^7_{\alpha\beta\gamma}$ [PPP]	$v^2_{\alpha\beta\gamma}$ [PPN]	$v^3_{\alpha\beta\gamma}$ [NPN]	$v^0_{\alpha\beta\gamma}$ [NNN]
Sector III	$v^0_{\alpha\beta\gamma}$ [NNN]	$v^3_{\alpha\beta\gamma}$ [NPN]	$v^4_{\alpha\beta\gamma}$ [NPP]	$v^7_{\alpha\beta\gamma}$ [PPP]	$v^4_{\alpha\beta\gamma}$ [NPP]	$v^3_{\alpha\beta\gamma}$ [NPN]	$v^0_{\alpha\beta\gamma}$ [NNN]
Sector IV	$v^0_{\alpha\beta\gamma}$ [NNN]	$v^5_{\alpha\beta\gamma}$ [NNP]	$v^4_{\alpha\beta\gamma}$ [NPP]	$v^7_{\alpha\beta\gamma}$ [PPP]	$v^4_{\alpha\beta\gamma}$ [NPP]	$v^5_{\alpha\beta\gamma}$ [NNP]	$v^0_{\alpha\beta\gamma}$ [NNN]
Sector V	$v^0_{\alpha\beta\gamma}$ [NNN]	$v^5_{\alpha\beta\gamma}$ [NNP]	$v^6_{\alpha\beta\gamma}$ [PNP]	$v^7_{\alpha\beta\gamma}$ [PPP]	$v^6_{\alpha\beta\gamma}$ [PNP]	$v^5_{\alpha\beta\gamma}$ [NNP]	$v^0_{\alpha\beta\gamma}$ [NNN]
Sector VI	$v^0_{\alpha\beta\gamma}$ [NNN]	$v^1_{\alpha\beta\gamma}$ [PNN]	$v^6_{\alpha\beta\gamma}$ [PNP]	$v^7_{\alpha\beta\gamma}$ [PPP]	$v^6_{\alpha\beta\gamma}$ [PNP]	$v^1_{\alpha\beta\gamma}$ [PNN]	$v^0_{\alpha\beta\gamma}$ [NNN]

Table A.2: *Redundant Symmetric p-type* sequence. P=1; N=-1

Sector I	$v^7_{\alpha\beta\gamma}$ [PPP]	$v^2_{\alpha\beta\gamma}$ [PPN]	$v^1_{\alpha\beta\gamma}$ [PNN]	$v^0_{\alpha\beta\gamma}$ [NNN]	$v^1_{\alpha\beta\gamma}$ [PNN]	$v^2_{\alpha\beta\gamma}$ [PPN]	$v^7_{\alpha\beta\gamma}$ [PPP]
Sector II	$v^7_{\alpha\beta\gamma}$ [PPP]	$v^2_{\alpha\beta\gamma}$ [PPN]	$v^3_{\alpha\beta\gamma}$ [NPN]	$v^0_{\alpha\beta\gamma}$ [NNN]	$v^3_{\alpha\beta\gamma}$ [NPN]	$v^2_{\alpha\beta\gamma}$ [PPN]	$v^7_{\alpha\beta\gamma}$ [PPP]
Sector III	$v^7_{\alpha\beta\gamma}$ [PPP]	$v^4_{\alpha\beta\gamma}$ [NPP]	$v^3_{\alpha\beta\gamma}$ [NPN]	$v^0_{\alpha\beta\gamma}$ [NNN]	$v^3_{\alpha\beta\gamma}$ [NPN]	$v^4_{\alpha\beta\gamma}$ [NPP]	$v^7_{\alpha\beta\gamma}$ [PPP]
Sector IV	$v^7_{\alpha\beta\gamma}$ [PPP]	$v^4_{\alpha\beta\gamma}$ [NPP]	$v^5_{\alpha\beta\gamma}$ [NNP]	$v^0_{\alpha\beta\gamma}$ [NNN]	$v^5_{\alpha\beta\gamma}$ [NNP]	$v^4_{\alpha\beta\gamma}$ [NPP]	$v^7_{\alpha\beta\gamma}$ [PPP]
Sector V	$v^7_{\alpha\beta\gamma}$ [PPP]	$v^6_{\alpha\beta\gamma}$ [PNP]	$v^5_{\alpha\beta\gamma}$ [NNP]	$v^0_{\alpha\beta\gamma}$ [NNN]	$v^5_{\alpha\beta\gamma}$ [NNP]	$v^6_{\alpha\beta\gamma}$ [PNP]	$v^7_{\alpha\beta\gamma}$ [PPP]
Sector VI	$v^7_{\alpha\beta\gamma}$ [PPP]	$v^6_{\alpha\beta\gamma}$ [PNP]	$v^1_{\alpha\beta\gamma}$ [PNN]	$v^0_{\alpha\beta\gamma}$ [NNN]	$v^1_{\alpha\beta\gamma}$ [PNN]	$v^6_{\alpha\beta\gamma}$ [PNP]	$v^7_{\alpha\beta\gamma}$ [PPP]

Table A.3: *Redundant Asymmetric n-type* sequence. P=1; N=-1

Sector I	$v^0_{\alpha\beta\gamma}$ [NNN]	$v^1_{\alpha\beta\gamma}$ [PNN]	$v^2_{\alpha\beta\gamma}$ [PPN]	$v^7_{\alpha\beta\gamma}$ [PPP]
Sector II	$v^0_{\alpha\beta\gamma}$ [NNN]	$v^3_{\alpha\beta\gamma}$ [NPN]	$v^2_{\alpha\beta\gamma}$ [PPN]	$v^7_{\alpha\beta\gamma}$ [PPP]
Sector III	$v^0_{\alpha\beta\gamma}$ [NNN]	$v^3_{\alpha\beta\gamma}$ [NPN]	$v^4_{\alpha\beta\gamma}$ [NPP]	$v^7_{\alpha\beta\gamma}$ [PPP]
Sector IV	$v^0_{\alpha\beta\gamma}$ [NNN]	$v^5_{\alpha\beta\gamma}$ [NNP]	$v^4_{\alpha\beta\gamma}$ [NPP]	$v^7_{\alpha\beta\gamma}$ [PPP]
Sector V	$v^0_{\alpha\beta\gamma}$ [NNN]	$v^5_{\alpha\beta\gamma}$ [NNP]	$v^6_{\alpha\beta\gamma}$ [PNP]	$v^7_{\alpha\beta\gamma}$ [PPP]
Sector VI	$v^0_{\alpha\beta\gamma}$ [NNN]	$v^1_{\alpha\beta\gamma}$ [PNN]	$v^6_{\alpha\beta\gamma}$ [PNP]	$v^7_{\alpha\beta\gamma}$ [PPP]

Table A.4: *Redundant Asymmetric p-type* sequence. P=1; N=-1

Sector I	$v^7_{\alpha\beta\gamma}$ [PPP]	$v^2_{\alpha\beta\gamma}$ [PPN]	$v^1_{\alpha\beta\gamma}$ [PNN]	$v^0_{\alpha\beta\gamma}$ [NNN]
Sector II	$v^7_{\alpha\beta\gamma}$ [PPP]	$v^2_{\alpha\beta\gamma}$ [PPN]	$v^3_{\alpha\beta\gamma}$ [NPN]	$v^0_{\alpha\beta\gamma}$ [NNN]
Sector III	$v^7_{\alpha\beta\gamma}$ [PPP]	$v^4_{\alpha\beta\gamma}$ [NPP]	$v^3_{\alpha\beta\gamma}$ [NPN]	$v^0_{\alpha\beta\gamma}$ [NNN]
Sector IV	$v^7_{\alpha\beta\gamma}$ [PPP]	$v^4_{\alpha\beta\gamma}$ [NPP]	$v^5_{\alpha\beta\gamma}$ [NNP]	$v^0_{\alpha\beta\gamma}$ [NNN]
Sector V	$v^7_{\alpha\beta\gamma}$ [PPP]	$v^6_{\alpha\beta\gamma}$ [PNP]	$v^5_{\alpha\beta\gamma}$ [NNP]	$v^0_{\alpha\beta\gamma}$ [NNN]
Sector VI	$v^7_{\alpha\beta\gamma}$ [PPP]	$v^6_{\alpha\beta\gamma}$ [PNP]	$v^1_{\alpha\beta\gamma}$ [PNN]	$v^0_{\alpha\beta\gamma}$ [NNN]

Table A.5: *Redundant Symmetric n-p alternating type* sequence for even-order harmonics elimination. P=1; N=-1

Sector In	$v^{0}_{\alpha\beta\gamma}$ [NNN]	$v^{1}_{\alpha\beta\gamma}$ [PNN]	$v^{2}_{\alpha\beta\gamma}$ [PPN]	$v^{7}_{\alpha\beta\gamma}$ [PPP]	$v^{2}_{\alpha\beta\gamma}$ [PPN]	$v^{1}_{\alpha\beta\gamma}$ [PNN]	$v^{0}_{\alpha\beta\gamma}$ [NNN]
Sector Ip	$v^{0}_{\alpha\beta\gamma}$ [PPP]	$v^{2}_{\alpha\beta\gamma}$ [PPN]	$v^{1}_{\alpha\beta\gamma}$ [PNN]	$v^{7}_{\alpha\beta\gamma}$ [NNN]	$v^{1}_{\alpha\beta\gamma}$ [PNN]	$v^{2}_{\alpha\beta\gamma}$ [PPN]	$v^{0}_{\alpha\beta\gamma}$ [PPP]
Sector IIp	$v^{0}_{\alpha\beta\gamma}$ [PPP]	$v^{2}_{\alpha\beta\gamma}$ [PPN]	$v^{3}_{\alpha\beta\gamma}$ [NPN]	$v^{7}_{\alpha\beta\gamma}$ [NNN]	$v^{3}_{\alpha\beta\gamma}$ [NPN]	$v^{2}_{\alpha\beta\gamma}$ [PPN]	$v^{0}_{\alpha\beta\gamma}$ [PPP]
Sector IIn	$v^{0}_{\alpha\beta\gamma}$ [NNN]	$v^{3}_{\alpha\beta\gamma}$ [NPN]	$v^{2}_{\alpha\beta\gamma}$ [PPN]	$v^{7}_{\alpha\beta\gamma}$ [PPP]	$v^{2}_{\alpha\beta\gamma}$ [PPN]	$v^{3}_{\alpha\beta\gamma}$ [NPN]	$v^{0}_{\alpha\beta\gamma}$ [NNN]
Sector IIIn	$v^{0}_{\alpha\beta\gamma}$ [NNN]	$v^{3}_{\alpha\beta\gamma}$ [NPN]	$v^{4}_{\alpha\beta\gamma}$ [NPP]	$v^{7}_{\alpha\beta\gamma}$ [PPP]	$v^{4}_{\alpha\beta\gamma}$ [NPP]	$v^{3}_{\alpha\beta\gamma}$ [NPN]	$v^{0}_{\alpha\beta\gamma}$ [NNN]
Sector IIIp	$v^{0}_{\alpha\beta\gamma}$ [PPP]	$v^{4}_{\alpha\beta\gamma}$ [NPP]	$v^{3}_{\alpha\beta\gamma}$ [NPN]	$v^{7}_{\alpha\beta\gamma}$ [NNN]	$v^{3}_{\alpha\beta\gamma}$ [NPN]	$v^{4}_{\alpha\beta\gamma}$ [NPP]	$v^{0}_{\alpha\beta\gamma}$ [PPP]
Sector IVp	$v^{0}_{\alpha\beta\gamma}$ [PPP]	$v^{4}_{\alpha\beta\gamma}$ [NPP]	$v^{5}_{\alpha\beta\gamma}$ [NNP]	$v^{7}_{\alpha\beta\gamma}$ [NNN]	$v^{5}_{\alpha\beta\gamma}$ [NNP]	$v^{4}_{\alpha\beta\gamma}$ [NPP]	$v^{0}_{\alpha\beta\gamma}$ [PPP]
Sector IVn	$v^{0}_{\alpha\beta\gamma}$ [NNN]	$v^{5}_{\alpha\beta\gamma}$ [NNP]	$v^{4}_{\alpha\beta\gamma}$ [NPP]	$v^{7}_{\alpha\beta\gamma}$ [PPP]	$v^{4}_{\alpha\beta\gamma}$ [NPP]	$v^{5}_{\alpha\beta\gamma}$ [NNP]	$v^{0}_{\alpha\beta\gamma}$ [NNN]
Sector Vn	$v^{0}_{\alpha\beta\gamma}$ [NNN]	$v^{5}_{\alpha\beta\gamma}$ [NNP]	$v^{6}_{\alpha\beta\gamma}$ [PNP]	$v^{7}_{\alpha\beta\gamma}$ [PPP]	$v^{6}_{\alpha\beta\gamma}$ [PNP]	$v^{5}_{\alpha\beta\gamma}$ [NNP]	$v^{0}_{\alpha\beta\gamma}$ [NNN]
Sector V	$v^{0}_{\alpha\beta\gamma}$ [PPP]	$v^{6}_{\alpha\beta\gamma}$ [PNP]	$v^{5}_{\alpha\beta\gamma}$ [NNP]	$v^{7}_{\alpha\beta\gamma}$ [NNN]	$v^{5}_{\alpha\beta\gamma}$ [NNP]	$v^{6}_{\alpha\beta\gamma}$ [PNP]	$v^{0}_{\alpha\beta\gamma}$ [PPP]
Sector VIn	$v^{0}_{\alpha\beta\gamma}$ [NNN]	$v^{1}_{\alpha\beta\gamma}$ [PNN]	$v^{6}_{\alpha\beta\gamma}$ [PNP]	$v^{7}_{\alpha\beta\gamma}$ [PPP]	$v^{6}_{\alpha\beta\gamma}$ [PNP]	$v^{1}_{\alpha\beta\gamma}$ [PNN]	$v^{0}_{\alpha\beta\gamma}$ [NNN]
Sector VIp	$v^{0}_{\alpha\beta\gamma}$ [PPP]	$v^{6}_{\alpha\beta\gamma}$ [PNP]	$v^{1}_{\alpha\beta\gamma}$ [PNN]	$v^{7}_{\alpha\beta\gamma}$ [NNN]	$v^{1}_{\alpha\beta\gamma}$ [PNN]	$v^{6}_{\alpha\beta\gamma}$ [PNP]	$v^{0}_{\alpha\beta\gamma}$ [PPP]

Table A.6: *Non-Redundant Symmetric n-type* sequence. P=1; N=-1

						Clamped Phase
Sector I	$v^0_{\alpha\beta\gamma}$ [NNN]	$v^1_{\alpha\beta\gamma}$ [PNN]	$v^2_{\alpha\beta\gamma}$ [PPN]	$v^1_{\alpha\beta\gamma}$ [PNN]	$v^0_{\alpha\beta\gamma}$ [NNN]	v_{cz}=-1
Sector II	$v^0_{\alpha\beta\gamma}$ [NNN]	$v^3_{\alpha\beta\gamma}$ [NPN]	$v^2_{\alpha\beta\gamma}$ [PPN]	$v^3_{\alpha\beta\gamma}$ [NPN]	$v^0_{\alpha\beta\gamma}$ [NNN]	v_{cz}=-1
Sector III	$v^0_{\alpha\beta\gamma}$ [NNN]	$v^3_{\alpha\beta\gamma}$ [NPN]	$v^4_{\alpha\beta\gamma}$ [NPP]	$v^3_{\alpha\beta\gamma}$ [NPN]	$v^0_{\alpha\beta\gamma}$ [NNN]	v_{az}=-1
Sector IV	$v^0_{\alpha\beta\gamma}$ [NNN]	$v^5_{\alpha\beta\gamma}$ [NNP]	$v^4_{\alpha\beta\gamma}$ [NPP]	$v^5_{\alpha\beta\gamma}$ [NNP]	$v^0_{\alpha\beta\gamma}$ [NNN]	v_{az}=-1
Sector V	$v^0_{\alpha\beta\gamma}$ [NNN]	$v^5_{\alpha\beta\gamma}$ [NNP]	$v^6_{\alpha\beta\gamma}$ [PNP]	$v^5_{\alpha\beta\gamma}$ [NNP]	$v^0_{\alpha\beta\gamma}$ [NNN]	v_{bz}=-1
Sector VI	$v^0_{\alpha\beta\gamma}$ [NNN]	$v^1_{\alpha\beta\gamma}$ [PNN]	$v^6_{\alpha\beta\gamma}$ [PNP]	$v^1_{\alpha\beta\gamma}$ [PNN]	$v^0_{\alpha\beta\gamma}$ [NNN]	v_{bz}=-1

Table A.7: *Non-Redundant Symmetric p-type* sequence. P=1; N=-1

						Clamped Phase
Sector I	$v^{7}_{\alpha\beta\gamma}$ [PPP]	$v^{2}_{\alpha\beta\gamma}$ [PPN]	$v^{1}_{\alpha\beta\gamma}$ [PNN]	$v^{2}_{\alpha\beta\gamma}$ [PPN]	$v^{7}_{\alpha\beta\gamma}$ [PPP]	v_{az}=1
Sector II	$v^{7}_{\alpha\beta\gamma}$ [PPP]	$v^{2}_{\alpha\beta\gamma}$ [PPN]	$v^{3}_{\alpha\beta\gamma}$ [NPN]	$v^{2}_{\alpha\beta\gamma}$ [PPN]	$v^{7}_{\alpha\beta\gamma}$ [PPP]	v_{bz}=1
Sector III	$v^{7}_{\alpha\beta\gamma}$ [PPP]	$v^{4}_{\alpha\beta\gamma}$ [NPP]	$v^{3}_{\alpha\beta\gamma}$ [NPN]	$v^{4}_{\alpha\beta\gamma}$ [NPP]	$v^{7}_{\alpha\beta\gamma}$ [PPP]	v_{bz}=1
Sector IV	$v^{7}_{\alpha\beta\gamma}$ [PPP]	$v^{4}_{\alpha\beta\gamma}$ [NPP]	$v^{5}_{\alpha\beta\gamma}$ [NNP]	$v^{4}_{\alpha\beta\gamma}$ [NPP]	$v^{7}_{\alpha\beta\gamma}$ [PPP]	v_{cz}=1
Sector V	$v^{7}_{\alpha\beta\gamma}$ [PPP]	$v^{6}_{\alpha\beta\gamma}$ [PNP]	$v^{5}_{\alpha\beta\gamma}$ [NNP]	$v^{6}_{\alpha\beta\gamma}$ [PNP]	$v^{7}_{\alpha\beta\gamma}$ [PPP]	v_{cz}=1
Sector VI	$v^{7}_{\alpha\beta\gamma}$ [PPP]	$v^{6}_{\alpha\beta\gamma}$ [PNP]	$v^{1}_{\alpha\beta\gamma}$ [PNN]	$v^{6}_{\alpha\beta\gamma}$ [PNP]	$v^{7}_{\alpha\beta\gamma}$ [PPP]	v_{az}=1

Table A.8: *Non-Redundant Symmetric p-n alternating type* sequence. P=1; N=-1

						Clamped Phase
Sector I	$v^7_{\alpha\beta\gamma}$ [PPP]	$v^2_{\alpha\beta\gamma}$ [PPN]	$v^1_{\alpha\beta\gamma}$ [PNN]	$v^2_{\alpha\beta\gamma}$ [PPN]	$v^7_{\alpha\beta\gamma}$ [PPP]	v_{az}=1
Sector II	$v^0_{\alpha\beta\gamma}$ [NNN]	$v^3_{\alpha\beta\gamma}$ [NPN]	$v^2_{\alpha\beta\gamma}$ [PPN]	$v^3_{\alpha\beta\gamma}$ [NPN]	$v^0_{\alpha\beta\gamma}$ [NNN]	v_{cz}=-1
Sector III	$v^7_{\alpha\beta\gamma}$ [PPP]	$v^4_{\alpha\beta\gamma}$ [NPP]	$v^3_{\alpha\beta\gamma}$ [NPN]	$v^4_{\alpha\beta\gamma}$ [NPP]	$v^7_{\alpha\beta\gamma}$ [PPP]	v_{bz}=1
Sector IV	$v^0_{\alpha\beta\gamma}$ [NNN]	$v^5_{\alpha\beta\gamma}$ [NNP]	$v^4_{\alpha\beta\gamma}$ [NPP]	$v^5_{\alpha\beta\gamma}$ [NNP]	$v^0_{\alpha\beta\gamma}$ [NNN]	v_{az}=-1
Sector V	$v^7_{\alpha\beta\gamma}$ [PPP]	$v^6_{\alpha\beta\gamma}$ [PNP]	$v^5_{\alpha\beta\gamma}$ [NNP]	$v^6_{\alpha\beta\gamma}$ [PNP]	$v^7_{\alpha\beta\gamma}$ [PPP]	v_{cz}=1
Sector VI	$v^0_{\alpha\beta\gamma}$ [NNN]	$v^1_{\alpha\beta\gamma}$ [PNN]	$v^6_{\alpha\beta\gamma}$ [PNP]	$v^1_{\alpha\beta\gamma}$ [PNN]	$v^0_{\alpha\beta\gamma}$ [NNN]	v_{bz}=-1

Table A.9: Switching combination for a three-level NPC Converter. For convenience P=1, O=0 and N=-1. It is considered that $i_a + i_b + i_c$=0.

$\boldsymbol{v}^{i}_{abc}$=V_{dc}^{-1} [v_{az}, v_{bz}, v_{cz}]	$\boldsymbol{v}^{i}_{\alpha\beta\gamma}$= [$v_\alpha$, v_β, v_γ]	i_z
$\boldsymbol{v}^{0}_{abc}$= [P, P, P]	$\boldsymbol{v}^{0_p}_{\alpha\beta\gamma}$= [0, 0, 1]	0
$\boldsymbol{v}^{1}_{abc}$= [O, O, O]	$\boldsymbol{v}^{0_z}_{\alpha\beta\gamma}$= [0, 0, 0]	0
$\boldsymbol{v}^{2}_{abc}$= [N, N, N]	$\boldsymbol{v}^{0_n}_{\alpha\beta\gamma}$= [0, 0, -1]	0
$\boldsymbol{v}^{3}_{abc}$= [P, O, O]	$\boldsymbol{v}^{1_p}_{\alpha\beta\gamma}$= [$\frac{2}{3}$, 0, 1]	-i_a
$\boldsymbol{v}^{4}_{abc}$= [O, N, N]	$\boldsymbol{v}^{1_n}_{\alpha\beta\gamma}$= [$\frac{2}{3}$, 0, 0]	i_a
$\boldsymbol{v}^{5}_{abc}$= [P, P, O]	$\boldsymbol{v}^{2_p}_{\alpha\beta\gamma}$= [$\frac{1}{3}$, $\frac{\sqrt{3}}{3}$, 1]	i_c
$\boldsymbol{v}^{6}_{abc}$= [O, O, N]	$\boldsymbol{v}^{2_n}_{\alpha\beta\gamma}$= [$\frac{1}{3}$, $\frac{\sqrt{3}}{3}$, 0]	-i_c
$\boldsymbol{v}^{7}_{abc}$= [O, P, O]	$\boldsymbol{v}^{3_p}_{\alpha\beta\gamma}$= [-$\frac{1}{3}$, $\frac{\sqrt{3}}{3}$, 0]	-i_b
$\boldsymbol{v}^{8}_{abc}$= [N, O, N]	$\boldsymbol{v}^{3_n}_{\alpha\beta\gamma}$= [-$\frac{1}{3}$, $\frac{\sqrt{3}}{3}$, -1]	i_b
$\boldsymbol{v}^{9}_{abc}$= [O, P, P]	$\boldsymbol{v}^{4_p}_{\alpha\beta\gamma}$= [-$\frac{2}{3}$, 0, 0]	i_a
$\boldsymbol{v}^{10}_{abc}$= [N, O, O]	$\boldsymbol{v}^{4_n}_{\alpha\beta\gamma}$= [-$\frac{2}{3}$, 0, -1]	-i_a
$\boldsymbol{v}^{11}_{abc}$= [O, O, P]	$\boldsymbol{v}^{5_p}_{\alpha\beta\gamma}$= [-$\frac{1}{3}$, -$\frac{\sqrt{3}}{3}$, 0]	-i_c
$\boldsymbol{v}^{12}_{abc}$= [N, N, O]	$\boldsymbol{v}^{5_n}_{\alpha\beta\gamma}$= [-$\frac{1}{3}$, -$\frac{\sqrt{3}}{3}$, -1]	i_c
$\boldsymbol{v}^{13}_{abc}$= [P, O, P]	$\boldsymbol{v}^{6_p}_{\alpha\beta\gamma}$= [$\frac{1}{3}$, -$\frac{\sqrt{3}}{3}$, 1]	i_b
$\boldsymbol{v}^{14}_{abc}$= [O, N, O]	$\boldsymbol{v}^{6_n}_{\alpha\beta\gamma}$= [$\frac{1}{3}$, -$\frac{\sqrt{3}}{3}$, 0]	-i_b
$\boldsymbol{v}^{15}_{abc}$= [P, O, N]	$\boldsymbol{v}^{7}_{\alpha\beta\gamma}$= [1, $\frac{\sqrt{3}}{3}$, 1]	i_b
$\boldsymbol{v}^{16}_{abc}$= [O, P, N]	$\boldsymbol{v}^{8}_{\alpha\beta\gamma}$= [0, $\frac{2\sqrt{3}}{3}$, 0]	i_a
$\boldsymbol{v}^{17}_{abc}$= [N, P, O]	$\boldsymbol{v}^{9}_{\alpha\beta\gamma}$= [-1, $\frac{\sqrt{3}}{3}$, -1]	i_c
$\boldsymbol{v}^{18}_{abc}$= [N, O, P]	$\boldsymbol{v}^{10}_{\alpha\beta\gamma}$= [-1, -$\frac{\sqrt{3}}{3}$, -1]	i_b
$\boldsymbol{v}^{19}_{abc}$= [O, N, P]	$\boldsymbol{v}^{11}_{\alpha\beta\gamma}$= [0, -$\frac{2\sqrt{3}}{3}$, 0]	i_a
$\boldsymbol{v}^{20}_{abc}$= [P, N, O]	$\boldsymbol{v}^{12}_{\alpha\beta\gamma}$= [1, -$\frac{\sqrt{3}}{3}$, 1]	i_c
$\boldsymbol{v}^{21}_{abc}$= [P, N, N]	$\boldsymbol{v}^{13}_{\alpha\beta\gamma}$= [$\frac{4}{3}$, 0, 1]	0
$\boldsymbol{v}^{22}_{abc}$= [P, P, N]	$\boldsymbol{v}^{14}_{\alpha\beta\gamma}$= [$\frac{2}{3}$, $\frac{2\sqrt{3}}{3}$, 1]	0
$\boldsymbol{v}^{23}_{abc}$= [N, P, N]	$\boldsymbol{v}^{15}_{\alpha\beta\gamma}$= [-$\frac{2}{3}$, $\frac{2\sqrt{3}}{3}$, -1]	0
$\boldsymbol{v}^{24}_{abc}$= [N, P, P]	$\boldsymbol{v}^{16}_{\alpha\beta\gamma}$= [-$\frac{4}{3}$, 0, -1]	0
$\boldsymbol{v}^{25}_{abc}$= [N, N, P]	$\boldsymbol{v}^{17}_{\alpha\beta\gamma}$= [-$\frac{2}{3}$, -$\frac{2\sqrt{3}}{3}$, -1]	0
$\boldsymbol{v}^{26}_{abc}$= [P, N, P]	$\boldsymbol{v}^{18}_{\alpha\beta\gamma}$= [$\frac{2}{3}$, -$\frac{2\sqrt{3}}{3}$, 1]	0

Table A.10: *dwell time* calculation for *sector* k, with $\hat{\theta} = \theta - (k-1)\frac{\pi}{3}$ for $k \in \{1, 2, 3, 4, 5, 6\}$.

ρ	d_1/T_s	d_2/T_s	d_3/T_s
1	$\sqrt{3}m_a \sin\left(\frac{\pi}{3} - \hat{\theta}\right)$	$\left(1 - \sqrt{3}m_a \sin\left(\frac{\pi}{3} + \hat{\theta}\right)\right)$	$\sqrt{3}m_a \sin\left(\hat{\theta}\right)$
2	$\left(1 - \sqrt{3}m_a \sin\left(\hat{\theta}\right)\right)$	$\left(\sqrt{3}m_a \sin\left(\frac{\pi}{3} + \hat{\theta}\right) - 1\right)$	$\left(1 - \sqrt{3}m_a \sin\left(\frac{\pi}{3} - \hat{\theta}\right)\right)$
3	$\left(1 - \sqrt{3}m_a \sin\left(\frac{\pi}{3} + \hat{\theta}\right)\right)$	$\left(\sqrt{3}m_a \sin\left(\hat{\theta}\right)\right)$	$\left(\sqrt{3}m_a \sin\left(\frac{\pi}{3} - \hat{\theta}\right) - 1\right)$
4	$\left(\sqrt{3}m_a \sin\left(\hat{\theta}\right) - 1\right)$	$\left(\sqrt{3}m_a \sin\left(\frac{\pi}{3} - \hat{\theta}\right)\right)$	$\left(1 - \sqrt{3}m_a \sin\left(\frac{\pi}{3} + \hat{\theta}\right)\right)$

Table A.11: *Redundant Symmetric n-type* sequence for the *sector I* of the modulation region for a NPC converter.

Sector I, ρ=$1A$	$v_{\alpha\beta}^{1_n}$ [ONN]	$v_{\alpha\beta}^{2_n}$ [OON]	$v_{\alpha\beta}^{0_z}$ [OOO]	$v_{\alpha\beta}^{1_p}$ [POO]	$v_{\alpha\beta}^{0_z}$ [OOO]	$v_{\alpha\beta}^{2_n}$ [OON]	$v_{\alpha\beta}^{1_n}$ [ONN]
Sector I, ρ=$1B$	$v_{\alpha\beta}^{2_n}$ [OON]	$v_{\alpha\beta}^{0_z}$ [OOO]	$v_{\alpha\beta}^{1_p}$ [POO]	$v_{\alpha\beta}^{2_p}$ [PPO]	$v_{\alpha\beta}^{1_p}$ [POO]	$v_{\alpha\beta}^{0_z}$ [OOO]	$v_{\alpha\beta}^{2_n}$ [OON]
Sector I, ρ=$2A$	$v_{\alpha\beta}^{1_n}$ [ONN]	$v_{\alpha\beta}^{2_n}$ [OON]	$v_{\alpha\beta}^{7}$ [PON]	$v_{\alpha\beta}^{1_p}$ [POO]	$v_{\alpha\beta}^{7}$ [PON]	$v_{\alpha\beta}^{2_n}$ [OON]	$v_{\alpha\beta}^{1_n}$ [ONN]
Sector I, ρ=$2B$	$v_{\alpha\beta}^{2_n}$ [OON]	$v_{\alpha\beta}^{7}$ [PON]	$v_{\alpha\beta}^{1_p}$ [POO]	$v_{\alpha\beta}^{2_p}$ [PPO]	$v_{\alpha\beta}^{1_p}$ [POO]	$v_{\alpha\beta}^{7}$ [PON]	$v_{\alpha\beta}^{2_n}$ [OON]
Sector I, ρ=3	$v_{\alpha\beta}^{1_n}$ [ONN]	$v_{\alpha\beta}^{13}$ [PNN]	$v_{\alpha\beta}^{7}$ [PON]	$v_{\alpha\beta}^{1_p}$ [POO]	$v_{\alpha\beta}^{7}$ [PON]	$v_{\alpha\beta}^{13}$ [PNN]	$v_{\alpha\beta}^{1_n}$ [ONN]
Sector I, ρ=4	$v_{\alpha\beta}^{2_n}$ [OON]	$v_{\alpha\beta}^{7}$ [PON]	$v_{\alpha\beta}^{14}$ [PPN]	$v_{\alpha\beta}^{2_p}$ [PPO]	$v_{\alpha\beta}^{14}$ [PPN]	$v_{\alpha\beta}^{7}$ [PON]	$v_{\alpha\beta}^{2_n}$ [OON]

Table A.12: *Redundant Symmetric n-p-type* sequence for the *sector I* of the modulation region for a NPC converter for achieving even-order harmonics elimination.

Sector I, ρ=$1A$	$v_{\alpha\beta}^{1_p}$ [POO]	$v_{\alpha\beta}^{0_z}$ [OOO]	$v_{\alpha\beta}^{2_n}$ [OON]	$v_{\alpha\beta}^{1_n}$ [ONN]	$v_{\alpha\beta}^{2_n}$ [OON]	$v_{\alpha\beta}^{0_z}$ [OOO]	$v_{\alpha\beta}^{1_p}$ [POO]
Sector I, ρ=$1B$	$v_{\alpha\beta}^{2_n}$ [OON]	$v_{\alpha\beta}^{0_z}$ [OOO]	$v_{\alpha\beta}^{1_p}$ [POO]	$v_{\alpha\beta}^{2_p}$ [PPO]	$v_{\alpha\beta}^{1_p}$ [POO]	$v_{\alpha\beta}^{0_z}$ [OOO]	$v_{\alpha\beta}^{2_n}$ [OON]
Sector I, ρ=$2A$	$v_{\alpha\beta}^{1_p}$ [POO]	$v_{\alpha\beta}^{7}$ [PON]	$v_{\alpha\beta}^{2_n}$ [OON]	$v_{\alpha\beta}^{1_n}$ [ONN]	$v_{\alpha\beta}^{2_n}$ [OON]	$v_{\alpha\beta}^{7}$ [PON]	$v_{\alpha\beta}^{1_p}$ [POO]
Sector I, ρ=$2B$	$v_{\alpha\beta}^{2_n}$ [OON]	$v_{\alpha\beta}^{7}$ [PON]	$v_{\alpha\beta}^{1_p}$ [POO]	$v_{\alpha\beta}^{2_p}$ [PPO]	$v_{\alpha\beta}^{1_p}$ [POO]	$v_{\alpha\beta}^{7}$ [PON]	$v_{\alpha\beta}^{2_n}$ [OON]
Sector I, ρ=3	$v_{\alpha\beta}^{1_p}$ [POO]	$v_{\alpha\beta}^{7}$ [PON]	$v_{\alpha\beta}^{13}$ [PNN]	$v_{\alpha\beta}^{1_n}$ [ONN]	$v_{\alpha\beta}^{13}$ [PNN]	$v_{\alpha\beta}^{7}$ [PON]	$v_{\alpha\beta}^{1_p}$ [POO]
Sector I, ρ=4	$v_{\alpha\beta}^{2_n}$ [OON]	$v_{\alpha\beta}^{7}$ [PON]	$v_{\alpha\beta}^{14}$ [PPN]	$v_{\alpha\beta}^{2_p}$ [PPO]	$v_{\alpha\beta}^{14}$ [PPN]	$v_{\alpha\beta}^{7}$ [PON]	$v_{\alpha\beta}^{2_n}$ [OON]

APPENDIX B

Tables Two Level four-wire Converters

Table B.1: Switching combination for a two-level four-leg VSI. For convenience P=1, O=0 and N=-1.

$\boldsymbol{v}^{i}_{abcf}= [v_{az}, v_{bz}, v_{cz}, v_{fz}]$	$\boldsymbol{v}^{i}_{abc_f}= [v_{af}, v_{bf}, v_{cf}]$	$\boldsymbol{v}^{i}_{\alpha\beta\gamma}= [v_{\alpha}, v_{\beta}, v_{\gamma}]$
$\boldsymbol{v}^{0_p}_{abcf}=$ [P,P,P,P]	$\boldsymbol{v}^{0_n}_{abcf}=$ [O,O,O]	$\boldsymbol{v}^{0_p}_{\alpha\beta\gamma}= [0, 0, 0]$
$\boldsymbol{v}^{0_n}_{abcf}=$ [N,N,N,N]	$\boldsymbol{v}^{0_p}_{abcf}=$ [O,O,O]	$\boldsymbol{v}^{0_n}_{\alpha\beta\gamma}= [0, 0, 0]$
$\boldsymbol{v}^{1}_{abcf}=$ [P,P,P,N]	$\boldsymbol{v}^{1}_{abcf}=$ [2P, 2P, 2P]	$\boldsymbol{v}^{1}_{\alpha\beta\gamma}= [0, 0, 2]$
$\boldsymbol{v}^{2}_{abcf}=$ [N,N,N,P]	$\boldsymbol{v}^{2}_{abcf}=$ [-2P,-2P,-2P]	$\boldsymbol{v}^{2}_{\alpha\beta\gamma}= [0, 0, -2]$
$\boldsymbol{v}^{3}_{abcf}=$ [P,N,N,P]	$\boldsymbol{v}^{3}_{abcf}=$ [O,-2P,-2P]	$\boldsymbol{v}^{3}_{\alpha\beta\gamma}= [\frac{4}{3}, 0, -\frac{4}{3}]$
$\boldsymbol{v}^{4}_{abcf}=$ [P,P,N,P]	$\boldsymbol{v}^{4}_{abcf}=$ [O,O,-2P]	$\boldsymbol{v}^{4}_{\alpha\beta\gamma}= [\frac{2}{3}, \frac{2}{\sqrt{3}},-\frac{1}{3}]$
$\boldsymbol{v}^{5}_{abcf}=$ [N,P,N,P]	$\boldsymbol{v}^{5}_{abcf}=$ [-2P,O,-2P]	$\boldsymbol{v}^{5}_{\alpha\beta\gamma}= [-\frac{2}{3}, \frac{2}{\sqrt{3}}, -\frac{4}{3}]$
$\boldsymbol{v}^{6}_{abcf}=$ [N,P,P,P]	$\boldsymbol{v}^{6}_{abcf}=$ [-2P,O,O]	$\boldsymbol{v}^{6}_{\alpha\beta\gamma}= [-\frac{4}{3}, 0, -\frac{2}{3}]$
$\boldsymbol{v}^{7}_{abcf}=$ [N,N,P,P]	$\boldsymbol{v}^{7}_{abcf}=$ [-2P,-2P,O]	$\boldsymbol{v}^{7}_{\alpha\beta\gamma}= [-\frac{2}{3}, -\frac{2}{\sqrt{3}}, -\frac{4}{3}]$
$\boldsymbol{v}^{8}_{abcf}=$ [P,N,P,P]	$\boldsymbol{v}^{8}_{abcf}=$ [O,-2P,O]	$\boldsymbol{v}^{8}_{\alpha\beta\gamma}= [\frac{2}{3}, -\frac{2}{\sqrt{3}}, -\frac{2}{3}]$
$\boldsymbol{v}^{9}_{abcf}=$ [P,N,N,N]	$\boldsymbol{v}^{9}_{abcf}=$ [2P,O,O]	$\boldsymbol{v}^{9}_{\alpha\beta\gamma}= [\frac{4}{3}, 0, \frac{2}{3}]$
$\boldsymbol{v}^{10}_{abcf}=$ [P,P,N,N]	$\boldsymbol{v}^{10}_{abcf}=$ [2P,2P,O]	$\boldsymbol{v}^{10}_{\alpha\beta\gamma}= [\frac{2}{3}, \frac{2}{\sqrt{3}}, \frac{4}{3}]$
$\boldsymbol{v}^{11}_{abcf}=$ [N,P,N,N]	$\boldsymbol{v}^{11}_{abcf}=$ [O,2P,O]	$\boldsymbol{v}^{11}_{\alpha\beta\gamma}= [-\frac{2}{3}, \frac{2}{\sqrt{3}}, \frac{2}{3}]$
$\boldsymbol{v}^{12}_{abcf}=$ [N,P,P,N]	$\boldsymbol{v}^{12}_{abcf}=$ [O,2P,2P]	$\boldsymbol{v}^{12}_{\alpha\beta\gamma}= [-\frac{4}{3}, 0, \frac{4}{3}]$
$\boldsymbol{v}^{13}_{abcf}=$ [N,N,P,N]	$\boldsymbol{v}^{13}_{abcf}=$ [O,O,2P]	$\boldsymbol{v}^{13}_{\alpha\beta\gamma}= [-\frac{2}{3}, -\frac{2}{\sqrt{3}}, \frac{2}{3}]$
$\boldsymbol{v}^{14}_{abcf}=$ [P,N,P,N]	$\boldsymbol{v}^{14}_{abcf}=$ [2P,O,2P]	$\boldsymbol{v}^{14}_{\alpha\beta\gamma}= [\frac{2}{3}, -\frac{2}{\sqrt{3}}, \frac{4}{3}]$

Table B.2: *Single-Redundancy Symmetric n-type* sequence for a two-level four-leg VSI. P=1; N=-1

Sector I T_1	$v^{0_n}_{\alpha\beta\gamma}$ [NNNN]	$v^{9}_{\alpha\beta\gamma}$ [PNNN]	$v^{10}_{\alpha\beta\gamma}$ [PPNN]	$v^{1}_{\alpha\beta\gamma}$ [PPPN]	$v^{0_p}_{\alpha\beta\gamma}$ [PPPP]	$v^{1}_{\alpha\beta\gamma}$ [PPPN]	$v^{10}_{\alpha\beta\gamma}$ [PPNN]	$v^{9}_{\alpha\beta\gamma}$ [PNNN]	$v^{0_n}_{\alpha\beta\gamma}$ [NNNN]
Sector I T_2	$v^{0_n}_{\alpha\beta\gamma}$ [NNNN]	$v^{9}_{\alpha\beta\gamma}$ [PNNN]	$v^{10}_{\alpha\beta\gamma}$ [PPNN]	$v^{4}_{\alpha\beta\gamma}$ [PPNP]	$v^{0_p}_{\alpha\beta\gamma}$ [PPPP]	$v^{4}_{\alpha\beta\gamma}$ [PPNP]	$v^{10}_{\alpha\beta\gamma}$ [PPNN]	$v^{9}_{\alpha\beta\gamma}$ [PNNN]	$v^{0_n}_{\alpha\beta\gamma}$ [NNNN]
Sector I T_3	$v^{0_n}_{\alpha\beta\gamma}$ [NNNN]	$v^{9}_{\alpha\beta\gamma}$ [PNNN]	$v^{3}_{\alpha\beta\gamma}$ [PNNP]	$v^{4}_{\alpha\beta\gamma}$ [PPNP]	$v^{0_p}_{\alpha\beta\gamma}$ [PPPP]	$v^{4}_{\alpha\beta\gamma}$ [PPNP]	$v^{3}_{\alpha\beta\gamma}$ [PNNP]	$v^{9}_{\alpha\beta\gamma}$ [PNNN]	$v^{0_n}_{\alpha\beta\gamma}$ [NNNN]
Sector I T_4	$v^{0_n}_{\alpha\beta\gamma}$ [NNNN]	$v^{2}_{\alpha\beta\gamma}$ [NNNP]	$v^{3}_{\alpha\beta\gamma}$ [PNNP]	$v^{4}_{\alpha\beta\gamma}$ [PPNP]	$v^{0_p}_{\alpha\beta\gamma}$ [PPPP]	$v^{4}_{\alpha\beta\gamma}$ [PPNP]	$v^{3}_{\alpha\beta\gamma}$ [PNNP]	$v^{2}_{\alpha\beta\gamma}$ [NNNP]	$v^{0_n}_{\alpha\beta\gamma}$ [NNNN]
Sector II T_1	$v^{0_n}_{\alpha\beta\gamma}$ [NNNN]	$v^{11}_{\alpha\beta\gamma}$ [NPNN]	$v^{10}_{\alpha\beta\gamma}$ [PPNN]	$v^{1}_{\alpha\beta\gamma}$ [PPPN]	$v^{0_p}_{\alpha\beta\gamma}$ [PPPP]	$v^{1}_{\alpha\beta\gamma}$ [PPPN]	$v^{10}_{\alpha\beta\gamma}$ [PPNN]	$v^{11}_{\alpha\beta\gamma}$ [NPNN]	$v^{0_n}_{\alpha\beta\gamma}$ [NNNN]
Sector II T_2	$v^{0_n}_{\alpha\beta\gamma}$ [NNNN]	$v^{11}_{\alpha\beta\gamma}$ [NPNN]	$v^{10}_{\alpha\beta\gamma}$ [PPNN]	$v^{4}_{\alpha\beta\gamma}$ [PPNP]	$v^{0_p}_{\alpha\beta\gamma}$ [PPPP]	$v^{4}_{\alpha\beta\gamma}$ [PPNP]	$v^{10}_{\alpha\beta\gamma}$ [PPNN]	$v^{11}_{\alpha\beta\gamma}$ [NPNN]	$v^{0_n}_{\alpha\beta\gamma}$ [NNNN]
Sector II T_3	$v^{0_n}_{\alpha\beta\gamma}$ [NNNN]	$v^{11}_{\alpha\beta\gamma}$ [NPNN]	$v^{5}_{\alpha\beta\gamma}$ [NPNP]	$v^{4}_{\alpha\beta\gamma}$ [PPNP]	$v^{0_p}_{\alpha\beta\gamma}$ [PPPP]	$v^{4}_{\alpha\beta\gamma}$ [PPNP]	$v^{5}_{\alpha\beta\gamma}$ [NPNP]	$v^{11}_{\alpha\beta\gamma}$ [NPNN]	$v^{0_n}_{\alpha\beta\gamma}$ [NNNN]
Sector II T_4	$v^{0_n}_{\alpha\beta\gamma}$ [NNNN]	$v^{2}_{\alpha\beta\gamma}$ [NNNP]	$v^{5}_{\alpha\beta\gamma}$ [NPNP]	$v^{4}_{\alpha\beta\gamma}$ [PPNP]	$v^{0_p}_{\alpha\beta\gamma}$ [PPPP]	$v^{4}_{\alpha\beta\gamma}$ [PPNP]	$v^{5}_{\alpha\beta\gamma}$ [NPNP]	$v^{2}_{\alpha\beta\gamma}$ [NNNP]	$v^{0_n}_{\alpha\beta\gamma}$ [NNNN]
Sector III T_1	$v^{0_n}_{\alpha\beta\gamma}$ [NNNN]	$v^{11}_{\alpha\beta\gamma}$ [NPNN]	$v^{12}_{\alpha\beta\gamma}$ [NPPN]	$v^{1}_{\alpha\beta\gamma}$ [PPPN]	$v^{0_p}_{\alpha\beta\gamma}$ [PPPP]	$v^{1}_{\alpha\beta\gamma}$ [PPPN]	$v^{12}_{\alpha\beta\gamma}$ [NPPN]	$v^{11}_{\alpha\beta\gamma}$ [NPNN]	$v^{0_n}_{\alpha\beta\gamma}$ [NNNN]
Sector III T_2	$v^{0_n}_{\alpha\beta\gamma}$ [NNNN]	$v^{11}_{\alpha\beta\gamma}$ [NPNN]	$v^{12}_{\alpha\beta\gamma}$ [NPPN]	$v^{6}_{\alpha\beta\gamma}$ [NPPP]	$v^{0_p}_{\alpha\beta\gamma}$ [PPPP]	$v^{6}_{\alpha\beta\gamma}$ [NPPP]	$v^{12}_{\alpha\beta\gamma}$ [NPPN]	$v^{11}_{\alpha\beta\gamma}$ [NPNN]	$v^{0_n}_{\alpha\beta\gamma}$ [NNNN]
Sector III T_3	$v^{0_n}_{\alpha\beta\gamma}$ [NNNN]	$v^{11}_{\alpha\beta\gamma}$ [NPNN]	$v^{5}_{\alpha\beta\gamma}$ [NPNP]	$v^{6}_{\alpha\beta\gamma}$ [NPPP]	$v^{0_p}_{\alpha\beta\gamma}$ [PPPP]	$v^{6}_{\alpha\beta\gamma}$ [NPPP]	$v^{5}_{\alpha\beta\gamma}$ [NPNP]	$v^{11}_{\alpha\beta\gamma}$ [NPNN]	$v^{0_n}_{\alpha\beta\gamma}$ [NNNN]
Sector III T_4	$v^{0_n}_{\alpha\beta\gamma}$ [NNNN]	$v^{2}_{\alpha\beta\gamma}$ [NNNP]	$v^{5}_{\alpha\beta\gamma}$ [NPNP]	$v^{6}_{\alpha\beta\gamma}$ [NPPP]	$v^{0_p}_{\alpha\beta\gamma}$ [PPPP]	$v^{6}_{\alpha\beta\gamma}$ [NPPP]	$v^{5}_{\alpha\beta\gamma}$ [NPNP]	$v^{2}_{\alpha\beta\gamma}$ [NNNP]	$v^{0_n}_{\alpha\beta\gamma}$ [NNNN]

Table B.3: *Single-Redundancy Symmetric n-type* sequence for a two-level four-leg VSI. P=1; N=-1

Sector IV T_1	$v^{0_n}_{\alpha\beta\gamma}$ [NNNN]	$v^{13}_{\alpha\beta\gamma}$ [NNPN]	$v^{12}_{\alpha\beta\gamma}$ [NPPN]	$v^{1}_{\alpha\beta\gamma}$ [PPPN]	$v^{0_p}_{\alpha\beta\gamma}$ [PPPP]	$v^{1}_{\alpha\beta\gamma}$ [PPPN]	$v^{12}_{\alpha\beta\gamma}$ [NPPN]	$v^{13}_{\alpha\beta\gamma}$ [NNPN]	$v^{0_n}_{\alpha\beta\gamma}$ [NNNN]
Sector IV T_2	$v^{0_n}_{\alpha\beta\gamma}$ [NNNN]	$v^{13}_{\alpha\beta\gamma}$ [NNPN]	$v^{12}_{\alpha\beta\gamma}$ [NPPN]	$v^{6}_{\alpha\beta\gamma}$ [NPPP]	$v^{0_p}_{\alpha\beta\gamma}$ [PPPP]	$v^{6}_{\alpha\beta\gamma}$ [NPPP]	$v^{12}_{\alpha\beta\gamma}$ [NPPN]	$v^{13}_{\alpha\beta\gamma}$ [NNPN]	$v^{0_n}_{\alpha\beta\gamma}$ [NNNN]
Sector IV T_3	$v^{0_n}_{\alpha\beta\gamma}$ [NNNN]	$v^{13}_{\alpha\beta\gamma}$ [NNPN]	$v^{7}_{\alpha\beta\gamma}$ [NNPP]	$v^{6}_{\alpha\beta\gamma}$ [NPPP]	$v^{0_p}_{\alpha\beta\gamma}$ [PPPP]	$v^{6}_{\alpha\beta\gamma}$ [NPPP]	$v^{7}_{\alpha\beta\gamma}$ [NNPP]	$v^{13}_{\alpha\beta\gamma}$ [NNPN]	$v^{0_n}_{\alpha\beta\gamma}$ [NNNN]
Sector IV T_4	$v^{0_n}_{\alpha\beta\gamma}$ [NNNN]	$v^{2}_{\alpha\beta\gamma}$ [NNNP]	$v^{7}_{\alpha\beta\gamma}$ [NNPP]	$v^{6}_{\alpha\beta\gamma}$ [NPPP]	$v^{0_p}_{\alpha\beta\gamma}$ [PPPP]	$v^{6}_{\alpha\beta\gamma}$ [NPPP]	$v^{7}_{\alpha\beta\gamma}$ [NNPP]	$v^{2}_{\alpha\beta\gamma}$ [NNNP]	$v^{0_n}_{\alpha\beta\gamma}$ [NNNN]
Sector V T_1	$v^{0_n}_{\alpha\beta\gamma}$ [NNNN]	$v^{13}_{\alpha\beta\gamma}$ [NNPN]	$v^{14}_{\alpha\beta\gamma}$ [PNPN]	$v^{1}_{\alpha\beta\gamma}$ [PPPN]	$v^{0_p}_{\alpha\beta\gamma}$ [PPPP]	$v^{1}_{\alpha\beta\gamma}$ [PPPN]	$v^{14}_{\alpha\beta\gamma}$ [PNPN]	$v^{13}_{\alpha\beta\gamma}$ [NNPN]	$v^{0_n}_{\alpha\beta\gamma}$ [NNNN]
Sector V T_2	$v^{0_n}_{\alpha\beta\gamma}$ [NNNN]	$v^{13}_{\alpha\beta\gamma}$ [NNPN]	$v^{14}_{\alpha\beta\gamma}$ [PNPN]	$v^{8}_{\alpha\beta\gamma}$ [PNPP]	$v^{0_p}_{\alpha\beta\gamma}$ [PPPP]	$v^{8}_{\alpha\beta\gamma}$ [PNPP]	$v^{14}_{\alpha\beta\gamma}$ [PNPN]	$v^{13}_{\alpha\beta\gamma}$ [NNPN]	$v^{0_n}_{\alpha\beta\gamma}$ [NNNN]
Sector V T_3	$v^{0_n}_{\alpha\beta\gamma}$ [NNNN]	$v^{13}_{\alpha\beta\gamma}$ [NNPN]	$v^{7}_{\alpha\beta\gamma}$ [NNPP]	$v^{8}_{\alpha\beta\gamma}$ [PNPP]	$v^{0_p}_{\alpha\beta\gamma}$ [PPPP]	$v^{8}_{\alpha\beta\gamma}$ [PNPP]	$v^{7}_{\alpha\beta\gamma}$ [NNPP]	$v^{13}_{\alpha\beta\gamma}$ [NNPN]	$v^{0_n}_{\alpha\beta\gamma}$ [NNNN]
Sector V T_4	$v^{0_n}_{\alpha\beta\gamma}$ [NNNN]	$v^{2}_{\alpha\beta\gamma}$ [NNNP]	$v^{7}_{\alpha\beta\gamma}$ [NNPP]	$v^{8}_{\alpha\beta\gamma}$ [PNPP]	$v^{0_p}_{\alpha\beta\gamma}$ [PPPP]	$v^{8}_{\alpha\beta\gamma}$ [PNPP]	$v^{7}_{\alpha\beta\gamma}$ [NNPP]	$v^{2}_{\alpha\beta\gamma}$ [NNNP]	$v^{0_n}_{\alpha\beta\gamma}$ [NNNN]
Sector VI T_1	$v^{0_n}_{\alpha\beta\gamma}$ [NNNN]	$v^{9}_{\alpha\beta\gamma}$ [PNNN]	$v^{14}_{\alpha\beta\gamma}$ [PNPN]	$v^{1}_{\alpha\beta\gamma}$ [PPPN]	$v^{0_p}_{\alpha\beta\gamma}$ [PPPP]	$v^{1}_{\alpha\beta\gamma}$ [PPPN]	$v^{14}_{\alpha\beta\gamma}$ [PNPN]	$v^{9}_{\alpha\beta\gamma}$ [PNNN]	$v^{0_n}_{\alpha\beta\gamma}$ [NNNN]
Sector VI T_2	$v^{0_n}_{\alpha\beta\gamma}$ [NNNN]	$v^{9}_{\alpha\beta\gamma}$ [PNNN]	$v^{14}_{\alpha\beta\gamma}$ [PNPN]	$v^{8}_{\alpha\beta\gamma}$ [PNPP]	$v^{0_p}_{\alpha\beta\gamma}$ [PPPP]	$v^{8}_{\alpha\beta\gamma}$ [PNPP]	$v^{14}_{\alpha\beta\gamma}$ [PNPN]	$v^{9}_{\alpha\beta\gamma}$ [PNNN]	$v^{0_n}_{\alpha\beta\gamma}$ [NNNN]
Sector VI T_3	$v^{0_n}_{\alpha\beta\gamma}$ [NNNN]	$v^{9}_{\alpha\beta\gamma}$ [PNNN]	$v^{3}_{\alpha\beta\gamma}$ [PNNP]	$v^{8}_{\alpha\beta\gamma}$ [PNPP]	$v^{0_p}_{\alpha\beta\gamma}$ [PPPP]	$v^{8}_{\alpha\beta\gamma}$ [PNPP]	$v^{3}_{\alpha\beta\gamma}$ [PNNP]	$v^{9}_{\alpha\beta\gamma}$ [PNNN]	$v^{0_n}_{\alpha\beta\gamma}$ [NNNN]
Sector VI T_4	$v^{0_n}_{\alpha\beta\gamma}$ [NNNN]	$v^{2}_{\alpha\beta\gamma}$ [NNNP]	$v^{3}_{\alpha\beta\gamma}$ [PNNP]	$v^{8}_{\alpha\beta\gamma}$ [PNPP]	$v^{0_p}_{\alpha\beta\gamma}$ [PPPP]	$v^{8}_{\alpha\beta\gamma}$ [PNPP]	$v^{3}_{\alpha\beta\gamma}$ [PNNP]	$v^{2}_{\alpha\beta\gamma}$ [NNNP]	$v^{0_n}_{\alpha\beta\gamma}$ [NNNN]

APPENDIX C

Tables three-level four-leg NPC Converter

Table C.1: The 81 different switching combinations for a four-leg NPC converter in the $\alpha\beta\gamma$ space.(P=1, O=0 and N=-1)

$\boldsymbol{v}^i_{abcf}$ $[v_{az}, v_{bz}, v_{cz}, v_{fz}]$	abc Vector $\boldsymbol{v}^i_{abc}$ $[v^i_{af}, v^i_{bf}, v^i_{cf}]$	$\alpha\beta\gamma$ Vector $\boldsymbol{v}^i_{\alpha\beta\gamma}$ $[v^i_{\alpha}, v^i_{\beta}, v^i_{\gamma}]$	Current NP $i_z(\boldsymbol{v}^i_{\alpha\beta\gamma})$	Vector Magnitude $\lvert\boldsymbol{v}^i_{\alpha\beta\gamma}\rvert$	Vector Classification
[OOOO]	$\boldsymbol{v}^{0z}_{abc}$=[0,0,0]	$\boldsymbol{v}^{0z}_{\alpha\beta\gamma}$=[0, 0, 0]	0	0	Zero Vectors
[PPPP]	$\boldsymbol{v}^{0p}_{abc}$=[0,0,0]	$\boldsymbol{v}^{0p}_{\alpha\beta\gamma}$=[0, 0, 0]	0		
[NNNN]	$\boldsymbol{v}^{0n}_{abc}$=[0,0,0]	$\boldsymbol{v}^{0n}_{\alpha\beta\gamma}$=[0, 0, 0]	0		
[ONNN]	$\boldsymbol{v}^{1n}_{abc}$=[1,0,0]	$\boldsymbol{v}^{1n}_{\alpha\beta\gamma}$=[$\frac{2}{3}$, 0, $\frac{1}{3}$]	i_a	$\frac{\sqrt{5}}{3}$	Redundant Vectors
[POOO]	$\boldsymbol{v}^{1p}_{abc}$=[1,0,0]	$\boldsymbol{v}^{1p}_{\alpha\beta\gamma}$=[$\frac{2}{3}$, 0, $\frac{1}{3}$]	-i_a		
[NONN]	$\boldsymbol{v}^{2n}_{abc}$=[0,1,0]	$\boldsymbol{v}^{2n}_{\alpha\beta\gamma}$=[-$\frac{1}{3}$, $\frac{\sqrt{3}}{3}$, $\frac{1}{3}$]	i_b		
[OPOO]	$\boldsymbol{v}^{2p}_{abc}$=[0,1,0]	$\boldsymbol{v}^{2p}_{\alpha\beta\gamma}$=[-$\frac{1}{3}$, $\frac{\sqrt{3}}{3}$, $\frac{1}{3}$]	-i_b		
[NNON]	$\boldsymbol{v}^{3n}_{abc}$=[0,0,1]	$\boldsymbol{v}^{3n}_{\alpha\beta\gamma}$=[-$\frac{1}{3}$, -$\frac{\sqrt{3}}{3}$, $\frac{1}{3}$]	i_c		
[OOPO]	$\boldsymbol{v}^{3p}_{abc}$=[0,0,1]	$\boldsymbol{v}^{3p}_{\alpha\beta\gamma}$=[-$\frac{1}{3}$, -$\frac{\sqrt{3}}{3}$, $\frac{1}{3}$]	-i_c		
[OONO]	$\boldsymbol{v}^{4n}_{abc}$=[0,0,-1]	$\boldsymbol{v}^{4n}_{\alpha\beta\gamma}$=[$\frac{1}{3}$, $\frac{\sqrt{3}}{3}$, -$\frac{1}{3}$]	-i_c		
[PPOP]	$\boldsymbol{v}^{4p}_{abc}$=[0,0,-1]	$\boldsymbol{v}^{4p}_{\alpha\beta\gamma}$=[$\frac{1}{3}$, $\frac{\sqrt{3}}{3}$, -$\frac{1}{3}$]	i_c		
[ONOO]	$\boldsymbol{v}^{5n}_{abc}$=[0,-1,0]	$\boldsymbol{v}^{5n}_{\alpha\beta\gamma}$=[$\frac{1}{3}$, -$\frac{\sqrt{3}}{3}$, -$\frac{1}{3}$]	-i_b		
[POPP]	$\boldsymbol{v}^{5p}_{abc}$=[0,-1,0]	$\boldsymbol{v}^{5p}_{\alpha\beta\gamma}$=[$\frac{1}{3}$, -$\frac{\sqrt{3}}{3}$, -$\frac{1}{3}$]	i_b		
[NOOO]	$\boldsymbol{v}^{6n}_{abc}$=[-1,0,0]	$\boldsymbol{v}^{6n}_{\alpha\beta\gamma}$=[-$\frac{2}{3}$, 0, -$\frac{1}{3}$]	-i_a		
[OPPP]	$\boldsymbol{v}^{6p}_{abc}$=[-1,0,0]	$\boldsymbol{v}^{6p}_{\alpha\beta\gamma}$=[-$\frac{2}{3}$, 0, -$\frac{1}{3}$]	i_a		
[OONN]	$\boldsymbol{v}^{7n}_{abc}$=[1,1,0]	$\boldsymbol{v}^{7n}_{\alpha\beta\gamma}$=[$\frac{1}{3}$, $\frac{\sqrt{3}}{3}$, $\frac{2}{3}$]	i_a + i_b	$\frac{2\sqrt{2}}{3}$	
[PPOO]	$\boldsymbol{v}^{7p}_{abc}$=[1,1,0]	$\boldsymbol{v}^{7p}_{\alpha\beta\gamma}$=[$\frac{1}{3}$, $\frac{\sqrt{3}}{3}$, $\frac{2}{3}$]	-i_a - i_b		
[ONON]	$\boldsymbol{v}^{8n}_{abc}$=[1,0,1]	$\boldsymbol{v}^{8n}_{\alpha\beta\gamma}$=[$\frac{1}{3}$, -$\frac{\sqrt{3}}{3}$, $\frac{2}{3}$]	i_a + i_c		
[POPO]	$\boldsymbol{v}^{8p}_{abc}$=[1,0,1]	$\boldsymbol{v}^{8p}_{\alpha\beta\gamma}$=[$\frac{1}{3}$, -$\frac{\sqrt{3}}{3}$, $\frac{2}{3}$]	-i_a - i_c		
[NOON]	$\boldsymbol{v}^{9n}_{abc}$=[0,1,1]	$\boldsymbol{v}^{9n}_{\alpha\beta\gamma}$=[-$\frac{2}{3}$, 0, $\frac{2}{3}$]	i_b + i_c		
[OPPO]	$\boldsymbol{v}^{9p}_{abc}$=[0,1,1]	$\boldsymbol{v}^{9p}_{\alpha\beta\gamma}$=[-$\frac{2}{3}$, 0, $\frac{2}{3}$]	-i_b - i_c		
[ONNO]	$\boldsymbol{v}^{10n}_{abc}$=[0,-1,-1]	$\boldsymbol{v}^{10n}_{\alpha\beta\gamma}$=[$\frac{2}{3}$, 0, -$\frac{2}{3}$]	-i_b - i_c		
[POOP]	$\boldsymbol{v}^{10p}_{abc}$=[0,-1,-1]	$\boldsymbol{v}^{10p}_{\alpha\beta\gamma}$=[$\frac{2}{3}$, 0, -$\frac{2}{3}$]	i_b + i_c		
[NONO]	$\boldsymbol{v}^{11n}_{abc}$=[-1,0,-1]	$\boldsymbol{v}^{11n}_{\alpha\beta\gamma}$=[-$\frac{1}{3}$, $\frac{\sqrt{3}}{3}$, -$\frac{2}{3}$]	-i_a - i_c		
[OPOP]	$\boldsymbol{v}^{11p}_{abc}$=[-1,0,-1]	$\boldsymbol{v}^{11p}_{\alpha\beta\gamma}$=[-$\frac{1}{3}$, $\frac{\sqrt{3}}{3}$, -$\frac{2}{3}$]	i_a + i_c		
[NNOO]	$\boldsymbol{v}^{12n}_{abc}$=[-1,-1,0]	$\boldsymbol{v}^{12n}_{\alpha\beta\gamma}$=[-$\frac{1}{3}$, -$\frac{\sqrt{3}}{3}$, -$\frac{2}{3}$]	-i_a - i_b		
[OOPP]	$\boldsymbol{v}^{12p}_{abc}$=[-1,-1,0]	$\boldsymbol{v}^{12p}_{\alpha\beta\gamma}$=[-$\frac{1}{3}$, -$\frac{\sqrt{3}}{3}$, -$\frac{2}{3}$]	i_a + i_b		
[OOON]	$\boldsymbol{v}^{13n}_{abc}$=[1,1,1]	$\boldsymbol{v}^{13n}_{\alpha\beta\gamma}$=[0, 0, 1]	i_a + i_b + i_c	1	
[PPPO]	$\boldsymbol{v}^{13p}_{abc}$=[1,1,1]	$\boldsymbol{v}^{13p}_{\alpha\beta\gamma}$=[0, 0, 1]	-i_a - i_b - i_c		
[NNNO]	$\boldsymbol{v}^{14n}_{abc}$=[-1,-1,-1]	$\boldsymbol{v}^{14n}_{\alpha\beta\gamma}$=[0, 0, -1]	-i_a - i_b - i_c		
[OOOP]	$\boldsymbol{v}^{14p}_{abc}$=[-1,-1,-1]	$\boldsymbol{v}^{14p}_{\alpha\beta\gamma}$=[0, 0, -1]	i_a + i_b + i_c		

Table C.2: Continuation of Table C.2.

$\boldsymbol{v}^i_{abcf}$ $[v_{az}, v_{bz}, v_{cz}, v_{fz}]$	abc Vector $\boldsymbol{v}^i_{abc}$ $[v^i_{af}, v^i_{bf}, v^i_{cf}]$	$\alpha\beta\gamma$ Vector $\boldsymbol{v}^i_{\alpha\beta\gamma}$ $[v^i_{\alpha}, v^i_{\beta}, v^i_{\gamma}]$	Current NP $i_z(\boldsymbol{v}^i_{\alpha\beta\gamma})$	Vector Magnitude $\lvert\boldsymbol{v}^i_{\alpha\beta\gamma}\rvert$	Vector Classification
[PONO]	$\boldsymbol{v}^{15}_{abc}$=[1,0,-1]	$\boldsymbol{v}^{15}_{\alpha\beta\gamma}$=[1, $\frac{\sqrt{3}}{3}$, 0]	-i_a - i_c	$2\frac{\sqrt{3}}{3}$	Non-Red Vectors
[OPNO]	$\boldsymbol{v}^{16}_{abc}$=[0,1,-1]	$\boldsymbol{v}^{16}_{\alpha\beta\gamma}$=[0, $\frac{2\sqrt{3}}{3}$, 0]	-i_b - i_c		
[PNOO]	$\boldsymbol{v}^{17}_{abc}$=[1,-1,0]	$\boldsymbol{v}^{17}_{\alpha\beta\gamma}$=[1, -$\frac{\sqrt{3}}{3}$, 0]	-i_a - i_b		
[ONPO]	$\boldsymbol{v}^{18}_{abc}$=[0,-1,1]	$\boldsymbol{v}^{18}_{\alpha\beta\gamma}$=[0, -$\frac{2\sqrt{3}}{3}$, 0]	-i_b - i_c		
[NPOO]	$\boldsymbol{v}^{19}_{abc}$=[-1,1,0]	$\boldsymbol{v}^{19}_{\alpha\beta\gamma}$=[-1, $\frac{\sqrt{3}}{3}$, 0]	-i_a - i_b		
[NOPO]	$\boldsymbol{v}^{20}_{abc}$=[-1,0,1]	$\boldsymbol{v}^{20}_{\alpha\beta\gamma}$=[-1, -$\frac{\sqrt{3}}{3}$, 0]	-i_a - i_c		
[PPNO]	$\boldsymbol{v}^{21}_{abc}$=[1,1,-1]	$\boldsymbol{v}^{21}_{\alpha\beta\gamma}$=[$\frac{2}{3}$, $\frac{2\sqrt{3}}{3}$, $\frac{1}{3}$]	-i_a - i_b - i_c	$\frac{\sqrt{17}}{3}$	
[PNPO]	$\boldsymbol{v}^{22}_{abc}$=[1,-1,1]	$\boldsymbol{v}^{22}_{\alpha\beta\gamma}$=[$\frac{2}{3}$, -$\frac{2\sqrt{3}}{3}$, $\frac{1}{3}$]	-i_a - i_b - i_c		
[NPPO]	$\boldsymbol{v}^{23}_{abc}$=[-1,1,1]	$\boldsymbol{v}^{23}_{\alpha\beta\gamma}$=[-$\frac{4}{3}$, 0, $\frac{1}{3}$]	-i_a - i_b - i_c		
[PNNO]	$\boldsymbol{v}^{24}_{abc}$=[1,-1,-1]	$\boldsymbol{v}^{24}_{\alpha\beta\gamma}$=[$\frac{4}{3}$, 0, -$\frac{1}{3}$]	-i_a - i_b - i_c		
[NPNO]	$\boldsymbol{v}^{25}_{abc}$=[-1,1,-1]	$\boldsymbol{v}^{25}_{\alpha\beta\gamma}$=[-$\frac{2}{3}$, $\frac{2\sqrt{3}}{3}$, -$\frac{1}{3}$]	-i_a - i_b - i_c		
[NNPO]	$\boldsymbol{v}^{26}_{abc}$=[-1,-1,1]	$\boldsymbol{v}^{26}_{\alpha\beta\gamma}$=[-$\frac{2}{3}$, -$\frac{2\sqrt{3}}{3}$, -$\frac{1}{3}$]	-i_a - i_b - i_c		
[POON]	$\boldsymbol{v}^{27}_{abc}$=[2,1,1]	$\boldsymbol{v}^{27}_{\alpha\beta\gamma}$=[$\frac{2}{3}$, 0, $\frac{4}{3}$]	i_b + i_c	$\frac{2\sqrt{5}}{3}$	
[OPON]	$\boldsymbol{v}^{28}_{abc}$=[1,2,1]	$\boldsymbol{v}^{28}_{\alpha\beta\gamma}$=[-$\frac{1}{3}$, $\frac{\sqrt{3}}{3}$, $\frac{4}{3}$]	i_a + i_c		
[OOPN]	$\boldsymbol{v}^{29}_{abc}$=[1,1,2]	$\boldsymbol{v}^{29}_{\alpha\beta\gamma}$=[-$\frac{1}{3}$, -$\frac{\sqrt{3}}{3}$, $\frac{4}{3}$]	i_a + i_b		
[PNNN]	$\boldsymbol{v}^{30}_{abc}$=[2,0,0]	$\boldsymbol{v}^{30}_{\alpha\beta\gamma}$=[$\frac{4}{3}$, 0, $\frac{2}{3}$]	0		
[NPNN]	$\boldsymbol{v}^{31}_{abc}$=[0,2,0]	$\boldsymbol{v}^{31}_{\alpha\beta\gamma}$=[-$\frac{2}{3}$, $\frac{2\sqrt{3}}{3}$, $\frac{2}{3}$]	0		
[NNPN]	$\boldsymbol{v}^{32}_{abc}$=[0,0,2]	$\boldsymbol{v}^{32}_{\alpha\beta\gamma}$=[-$\frac{2}{3}$, -$\frac{2\sqrt{3}}{3}$, $\frac{2}{3}$]	0		
[PPNP]	$\boldsymbol{v}^{33}_{abc}$=[0,0,-2]	$\boldsymbol{v}^{33}_{\alpha\beta\gamma}$=[$\frac{2}{3}$, $\frac{2\sqrt{3}}{3}$, -$\frac{2}{3}$]	0		
[PNPP]	$\boldsymbol{v}^{34}_{abc}$=[0,-2,0]	$\boldsymbol{v}^{34}_{\alpha\beta\gamma}$=[$\frac{2}{3}$, -$\frac{2\sqrt{3}}{3}$, -$\frac{2}{3}$]	0		
[NPPP]	$\boldsymbol{v}^{35}_{abc}$=[-2,0,0]	$\boldsymbol{v}^{35}_{\alpha\beta\gamma}$=[-$\frac{4}{3}$, 0, -$\frac{2}{3}$]	0		
[OONP]	$\boldsymbol{v}^{36}_{abc}$=[-1,-1,-2]	$\boldsymbol{v}^{36}_{\alpha\beta\gamma}$=[$\frac{1}{3}$, $\frac{\sqrt{3}}{3}$, -$\frac{4}{3}$]	i_a + i_b		
[ONOP]	$\boldsymbol{v}^{37}_{abc}$=[-1,-2,-1]	$\boldsymbol{v}^{37}_{\alpha\beta\gamma}$=[$\frac{1}{3}$, -$\frac{\sqrt{3}}{3}$, -$\frac{4}{3}$]	i_a + i_c		
[NOOP]	$\boldsymbol{v}^{38}_{abc}$=[-2,-1,-1]	$\boldsymbol{v}^{38}_{\alpha\beta\gamma}$=[-$\frac{2}{3}$, 0, -$\frac{4}{3}$]	i_b + i_c		
[PONN]	$\boldsymbol{v}^{39}_{abc}$=[2,1,0]	$\boldsymbol{v}^{39}_{\alpha\beta\gamma}$=[1, $\frac{\sqrt{3}}{3}$, 1]	i_b	$\frac{\sqrt{21}}{3}$	
[OPNN]	$\boldsymbol{v}^{40}_{abc}$=[1,2,0]	$\boldsymbol{v}^{40}_{\alpha\beta\gamma}$=[0, $\frac{2\sqrt{3}}{3}$, 1]	i_a		
[PNON]	$\boldsymbol{v}^{41}_{abc}$=[2,0,1]	$\boldsymbol{v}^{41}_{\alpha\beta\gamma}$=[1, -$\frac{\sqrt{3}}{3}$, 1]	i_c		
[ONPN]	$\boldsymbol{v}^{42}_{abc}$=[1,0,2]	$\boldsymbol{v}^{42}_{\alpha\beta\gamma}$=[0, -$\frac{2\sqrt{3}}{3}$, 1]	i_a		
[NPON]	$\boldsymbol{v}^{43}_{abc}$=[0,2,1]	$\boldsymbol{v}^{43}_{\alpha\beta\gamma}$=[-1, $\frac{\sqrt{3}}{3}$, 1]	i_c		
[NOPN]	$\boldsymbol{v}^{44}_{abc}$=[0,1,2]	$\boldsymbol{v}^{44}_{\alpha\beta\gamma}$=[-1, -$\frac{\sqrt{3}}{3}$, 1]	i_b		
[PONP]	$\boldsymbol{v}^{45}_{abc}$=[0,-1,-2]	$\boldsymbol{v}^{45}_{\alpha\beta\gamma}$=[1, $\frac{\sqrt{3}}{3}$, -1]	i_b		
[OPNP]	$\boldsymbol{v}^{46}_{abc}$=[-1,0,-2]	$\boldsymbol{v}^{46}_{\alpha\beta\gamma}$=[0, $\frac{2\sqrt{3}}{3}$, -1]	i_a		
[PNOP]	$\boldsymbol{v}^{47}_{abc}$=[0,-2,-1]	$\boldsymbol{v}^{47}_{\alpha\beta\gamma}$=[1, -$\frac{\sqrt{3}}{3}$, -1]	i_c		
[ONPP]	$\boldsymbol{v}^{48}_{abc}$=[-1,-2,0]	$\boldsymbol{v}^{48}_{\alpha\beta\gamma}$=[0, -$\frac{2\sqrt{3}}{3}$, -1]	i_a		
[NPOP]	$\boldsymbol{v}^{49}_{abc}$=[-2,0,-1]	$\boldsymbol{v}^{49}_{\alpha\beta\gamma}$=[-1, $\frac{\sqrt{3}}{3}$, -1]	i_c		
[NOPP]	$\boldsymbol{v}^{50}_{abc}$=[-2,-1,0]	$\boldsymbol{v}^{50}_{\alpha\beta\gamma}$=[-1, -$\frac{\sqrt{3}}{3}$, -1]	i_b		

APPENDIX D

List of symbols and abbreviations

D.1 List of symbols

General remark:
The following convention was used for variables:

Scalars are italic letters: x
Vectors are bold lower case letters: $\boldsymbol{x}$
Matrices are bold upper case letters: $\boldsymbol{X}$
References are marked with a star superscript: x^*

D.2 List of abbreviations

APU	Auxiliar Power Unit
APF	Active Power Filter
ACER	Agency for Cooperation of Energy Regulators
ac	Alternating Current
CPU	Central Processing Unit
dc	Direct Current
DSO	Distribution System Operator
DVR	Dynamic Voltage Restorer
DTC	Direct Torque Control
DPGS	Distribute Power Generation System
EDSO	European Distribution System Operators
EMI	Electromagnetic Interference
EWEA	The European Wind Energy Association
FPGA	Field Programmable Gate Array
FOH	First-Order Hold (approximation)
FFT	Fast Fourier Transformation
FS-MPC	Finite-Set Model Predictive Control
GTO	Gate Turn-off (Thyristor)
GPU	Ground Power Unit
HVDC	High Voltage Direct Current (System)
IGBT	Insulated Gate Bipolar Transistor
IGCT	Integrated Gate-Commutated Thyristor
ISA	Industry Standard Architecture (bus)
LC	Inductive and Capacitive (filter)
MV	Medium Voltage
NP	Neutral Point
NBPT	Non-Break Power Transfer
MOSFET	Metal Oxide Semiconductor Field Effect Transistor
NPC	Neutral Point Clamped
OPP	Optimal Pulse Pattern
PI	Proportional Integral (controller)
PC	Programmable Computer
PWM	Pulse Width Modulation
PLL	Phase Lock Loop
PR	Proportional Resonant (controller)
RTAI	Real-Time Application Interface
RES	Renewable Energy System
RL	Resistive and Inductive (load)
SVM	Space Vector Modulation
SPWM	Sinusoidal PWM
SVPWM	Space Vector PWM
TSO	Transmission System Operator
THIPWM	Third Harmonic Injection PWM
THD	Total Harmonic Distortion
TPW	Tustin with Prewarping
TT_i	Tetrahedron Type i
UPS	Uninterruptible Power Supply
VSVPWM	Virtual Space Vector PWM
VSI	Voltage Source Inverter
ZOH	Zero-Order Hold (approximation)

List of Figures

List of Tables

Bibliography

[1] W. S. J. John Grainger, *Power System Analysis*. Mc-Graw Hill, 1994.

[2] U. S. D. of Energy, "Final Report on the August 14, 2003 Blackout in the United States and Canada," Tech. Rep.

[3] R. S. Baker, "Peter Cooper Hewitt – Inventor; Three Great Achievements In Electrical Science," *McClure's Magazine XXI: 172–178. Retrieved 2009-08-07.*, 1903.

[4] L. J. Buttolph, "The Cooper Hewitt Lamp: Part II. Development And Application," *General Electric Review. XXIII (11): 909–916. Retrieved 2009-08-07.*, 1920.

[5] M. H. Rashid et. al., *Power Electronics Handbook*. Academic Press, 2001.

[6] F. Blaabjerg, R. Teodorescu, M. Liserre, and A. Timbus, "Overview of Control and Grid Synchronization for Distributed Power Generation Systems," *IEEE Transactions on Industrial Electronics*, vol. 53, no. 5, pp. 1398–1409, oct 2006.

[7] M. Liserre, R. Cardenas, M. Molinas, and J. Rodriguez, "Overview of Multi-MW Wind Turbines and Wind Parks," *IEEE Transactions on Industrial Electronics*, vol. 58, no. 4, pp. 1081–1095, apr 2011.

[8] The European Wind Energy Association, "Wind in power 2014 European statistics," Tech. Rep., 2015.

[9] E. D. S. Operators and f. S. G. (EDSO), "Coordination of transmission and distribution system operators: a key step for the Energy Union," Tech. Rep.

[10] MILITARY STANDARD, "MIL-STD-704F Aircraft Electric Power Characteristics."

[11] M. Aredes and E. Watanabe, "New control algorithms for series and shunt three-phase four-wire active power filters," *IEEE Transactions on Power Delivery*, vol. 10, no. 3, pp. 1649–1656, jul 1995.

[12] Y.-K. Lo, "Three-phase four wire voltage controlled AC line conditioner with unity input power factor and minimised output voltage harmonics," *IEE Proceedings - Electric Power Applications*, vol. 142, no. 1, p. 43, 1995.

[13] M. Aredes, J. Hafner, and K. Heumann, "Three-phase four-wire shunt active filter control strategies," *IEEE Transactions on Power Electronics*, vol. 12, no. 2, pp. 311–318, mar 1997.

[14] P. Verdelho and G. Marques, "An active power filter and unbalanced current compensator," *IEEE Transactions on Industrial Electronics*, vol. 44, no. 3, pp. 321–328, jun 1997.

[15] J.-H. Kim and S.-K. Sul, "A Carrier-Based PWM Method for Three-Phase Four-Leg Voltage Source Converters," *IEEE Transactions on Power Electronics*, vol. 19, no. 1, pp. 66–75, jan 2004.

[16] Z. Liu, J. Liu, and J. Li, "Modeling, Analysis, and Mitigation of Load Neutral Point Voltage for Three-Phase Four-Leg Inverter," *IEEE Transactions on Industrial Electronics*, vol. 60, no. 5, pp. 2010–2021, may 2013.

[17] O. Ojo and P. Kshirsagar, “Concise Modulation Strategies for Four-Leg Voltage Source Inverters,” *IEEE Transactions on Power Electronics*, vol. 19, no. 1, pp. 46–53, jan 2004.

[18] M. Perales, M. Prats, R. Portillo, J. Mora, J. Leon, and L. Franquelo, “Three-dimensional space vector modulation in abc coordinates for four-leg voltage source converters,” *IEEE Power Electronics Letters*, vol. 99, no. 4, pp. 104–109, dec 2003.

[19] M. Rivera, V. Yaramasu, A. Llor, J. Rodriguez, B. Wu, and M. Fadel, “Digital Predictive Current Control of a Three-Phase Four-Leg Inverter,” *IEEE Transactions on Industrial Electronics*, vol. 60, no. 11, pp. 4903–4912, nov 2013.

[20] R. Zhang, “High Performance Power Converter System for Nonlinear and Unbalanced Load/Source,” Ph.D. dissertation, Virginia Polytechnic Institute and State University, 1998.

[21] R. Cardenas, C. Juri, R. Pena, P. Wheeler, and J. Clare, “The Application of Resonant Controllers to Four-Leg Matrix Converters Feeding Unbalanced or Nonlinear Loads,” *IEEE Transactions on Power Electronics*, vol. 27, no. 3, pp. 1120–1129, mar 2012.

[22] F. Yue, P. W. Wheeler, N. Mason, L. Empringham, and J. C. Clare, “Indirect Space Vector Modulation for a 4-Leg Matrix Converter,” in *Power Electronics Specialists Conference, 2007. PESC 2007. IEEE*, 2007, pp. 639–645.

[23] P. Wheeler, A. Trentin, S. Bozhko, and J. Clare, “Regeneration of energy onto an aircraft electrical power system from an electro-mechanical actuator,” in *2012 Electrical Systems for Aircraft, Railway and Ship Propulsion*. IEEE, oct 2012, pp. 1–6.

[24] A. Nabae, I. Takahashi, and H. Akagi, “A New Neutral-Point-Clamped PWM Inverter,” *IEEE Transactions on Industry Applications*, vol. IA-17, no. 5, pp. 518–523, sep 1981.

[25] S.-J. Chee, S. Ko, H.-S. Kim, and S.-K. Sul, “Common-mode Voltage Reduction of Three Level Four Leg PWM Converter,” *IEEE Transactions on Industry Applications*, vol. PP, no. 99, pp. 1–1, 2015.

[26] Jang-Hwan Kim and Seung-Ki Sul, “Overmodulation strategy for a three-phase four-leg voltage source converter,” in *38th IAS Annual Meeting on Conference Record of the Industry Applications Conference, 2003.*, vol. 1. IEEE, 2003, pp. 656–663.

[27] H. Ghoreishy, Z. Zhang, O. C. Thomsen, and M. a. E. Andersen, “A fast-processing modulation strategy for three-phase four-leg neutral-point-clamped inverter based on the circuit-level decoupling concept,” *Proceedings of The 7th International Power Electronics and Motion Control Conference*, pp. 274–280, jun 2012.

[28] Ning-Yi Dai, Man-Chung Wong, Fan Ng, and Ying-Duo Han, “A FPGA-Based Generalized Pulse Width Modulator for Three-Leg Center-Split and Four-Leg Voltage Source Inverters,” *IEEE Transactions on Power Electronics*, vol. 23, no. 3, pp. 1472–1484, may 2008.

[29] V. Yaramasu, M. Rivera, B. Wu, and J. Rodriguez, “Model Predictive Current Control of Two-Level Four-Leg Inverters—Part I: Concept, Algorithm, and Simulation Analysis,” *IEEE Transactions on Power Electronics*, vol. 28, no. 7, pp. 3459–3468, jul 2013.

[30] M. Rivera, V. Yaramasu, J. Rodriguez, and B. Wu, “Model Predictive Current Control of Two-Level Four-Leg Inverters—Part II: Experimental Implementation and Validation,” *IEEE Transactions on Power Electronics*, vol. 28, no. 7, pp. 3469–3478, jul 2013.

[31] L. Franquelo, M. Prats, R. Portillo, J. Galvan, M. Perales, J. Carrasco, E. Diez, and J. Jimenez, “Three-dimensional space-vector modulation algorithm for four-leg multilevel converters using abc coordinates,” *IEEE Transactions on Industrial Electronics*, vol. 53, no. 2, pp. 458–466, apr 2006.

[32] R. Zhang, V. Prasad, D. Boroyevich, and F. Lee, “Three-dimensional space vector modulation for four-leg voltage-source converters,” *IEEE Transactions on Power Electronics*, vol. 17, no. 3, pp. 314–326, may 2002.

[33] J. Lai, F. Lee, D. Boroyevich, and R. Zhang, "Four-legged converter 3-D SVM scheme over-modulation study," in *APEC 2000. Fifteenth Annual IEEE Applied Power Electronics Conference and Exposition (Cat. No.00CH37058)*, vol. 1. IEEE, 2000, pp. 562–568.

[34] V. Prasad, D. Borojevic, and R. Zhang, "Analysis and comparison of space vector modulation schemes for a four-leg voltage source inverter," in *Proceedings of APEC 97 - Applied Power Electronics Conference*, vol. 2. IEEE, 1997, pp. 864–871.

[35] J. Yao and T. Green, "Three-dimensional space vector modulation for a four-leg three-level inverter," in *2005 European Conference on Power Electronics and Applications*. IEEE, 2005, pp. 9 pp.–P.9.

[36] Ning-Yi Dai, Man-Chung Wong, and Ying-Duo Han, "Application of a three-level NPC inverter as a three-phase four-wire power quality compensator by generalized 3DSVM," *IEEE Transactions on Power Electronics*, vol. 21, no. 2, pp. 440–449, mar 2006.

[37] A. Mohd, E. Ortjohann, N. Hamsic, W. Sinsukthavorn, M. Lingemann, A. Schmelter, and D. Morton, "Control strategy and space vector modulation for three-leg four-wire voltage source inverters under unbalanced load conditions," *IET Power Electronics*, vol. 3, no. 3, p. 323, 2010.

[38] J. Rodriguez, S. Bernet, B. Wu, J. O. Pontt, and S. Kouro, "Multilevel Voltage-Source-Converter Topologies for Industrial Medium-Voltage Drives," *IEEE Transactions on Industrial Electronics*, vol. 54, no. 6, pp. 2930–2945, dec 2007.

[39] R. Petrella, N. Buonocunto, A. Revelant, and P. Stocco, "Equalization of dc bus voltage in three-level NPC half-brige inverters for PV applications by even harmonics injection or fundamental phase modulation," in *2011 IEEE Energy Conversion Congress and Exposition*. IEEE, sep 2011, pp. 3427–3434.

[40] O. Husev, S. Stepenko, C. Roncero-Clemente, E. Romero-Cadaval, and R. Strzelecki, "Experimental Investigation of high frequency 3L-NPC qZS inverter for photovoltaic application," in *IECON 2013 - 39th Annual Conference of the IEEE Industrial Electronics Society*. IEEE, nov 2013, pp. 5969–5974.

[41] T. L. D. Grahame Holmes, *Pulse Width Modulation for Power Converters: Principles and Practice*. IEEE Press Series on POwer Engineering, 2003.

[42] J. Holtz, "Pulsewidth modulation-a survey," in *PESC '92 Record. 23rd Annual IEEE Power Electronics Specialists Conference*. IEEE, 1992, pp. 11–18.

[43] S. Kouro, P. Cortes, R. Vargas, U. Ammann, and J. Rodriguez, "Model Predictive Control—A Simple and Powerful Method to Control Power Converters," *IEEE Transactions on Industrial Electronics*, vol. 56, no. 6, pp. 1826–1838, jun 2009.

[44] J. Rodriguez, M. P. Kazmierkowski, J. R. Espinoza, P. Zanchetta, H. Abu-Rub, H. A. Young, and C. A. Rojas, "State of the Art of Finite Control Set Model Predictive Control in Power Electronics," *IEEE Transactions on Industrial Informatics*, vol. 9, no. 2, pp. 1003–1016, may 2013.

[45] N. Oikonomou, "Control of Medium Voltage Drives at very Low Switching Frequency," Ph.D. dissertation, Bergischen Universitaet Wuppertal, 2008.

[46] M. Kazmierkowski and M. Dzieniakowski, "Review of current regulation techniques for three-phase PWM inverters," in *Proceedings of IECON'94 - 20th Annual Conference of IEEE Industrial Electronics*, vol. 1. IEEE, 1994, pp. 567–575.

[47] J. Holtz, "Pulsewidth modulation for electronic power conversion," *Proceedings of the IEEE*, vol. 82, no. 8, pp. 1194–1214, 1994.

[48] A. S. Stemmler and H., "Static frequency changers with subharmonic control in conjunction with reversible variable a.c. drives," *Brown-Boveri Rev*, vol. 51, no. 3, pp. 133–148, 1985.

[49] A. Hava, R. Kerkman, and T. Lipo, "Carrier-based PWM-VSI overmodulation strategies: analysis, comparison, and design," *IEEE Transactions on Power Electronics*, vol. 13, no. 4, pp. 674–689, jul 1998.

[50] J. Kolar, H. Ertl, and F. Zach, "Influence of the modulation method on the conduction and switching losses of a PWM converter system," *IEEE Transactions on Industry Applications*, vol. 27, no. 6, pp. 1063–1075, 1991.

[51] Dae-Woong Chung, Joohn-Sheok Kim, and Seung-Ki Sul, “Unified voltage modulation technique for real-time three-phase power conversion,” *IEEE Transactions on Industry Applications*, vol. 34, no. 2, pp. 374–380, 1998.

[52] M. Depenbrock, “Pulse Width Control of a 3-Phase Inverter with Non-Sinusoidal Phase Voltages.” *IEEE IAS International Semiconductor Power Converter Conference , Orlando (Florida)*, pp. 399–403, 1977.

[53] S. Ogasawara, H. Akagi and A. Nabae, “A novel PWM scheme of voltage source inverter based on space vector theory,” *European Power Electron Conference, Aachen, Germany*, pp. 1197–1202, 1989.

[54] B. Wu, *High Power Converters and AC Drives*. IEEE Press Editorial Board, 2006.

[55] M. W. S. W. C. Duesterhoeft and E. Clarke, “Determination of Instantaneous Current and Voltage by Means of Alpha, Beta, and Zero Components,” *Transaction of the American Institute of Electrical Engineers*, pp. 1248–1255, 1951.

[56] A. Trzynadlowski and S. Legowski, “Minimum-loss vector PWM strategy for three-phase inverters,” *IEEE Transactions on Power Electronics*, vol. 9, no. 1, pp. 26–34, 1994.

[57] “519-1992 - IEEE Recommended Practices and Requirements for Harmonic Control in Electrical Power Systems.”

[58] V. Stefanovic and S. Vukosavic, “Space-vector PWM voltage control with optimized switching strategy,” in *Conference Record of the 1992 IEEE Industry Applications Society Annual Meeting*. IEEE, 1992, pp. 1025–1033.

[59] J. Holtz, W. Lotzkat, and A. Khambadkone, “On continuous control of PWM inverters in the overmodulation range including the six-step mode,” in *Proceedings of the 1992 International Conference on Industrial Electronics, Control, Instrumentation, and Automation*. IEEE, 1992, pp. 307–312.

[60] A. G. Yepes, F. D. Freijedo, O. Lopez, and J. Doval-Gandoy, “Analysis and Design of Resonant Current Controllers for Voltage-Source Converters by Means of Nyquist Diagrams and Sensitivity Function,” *IEEE Transactions on Industrial Electronics*, vol. 58, no. 11, pp. 5231–5250, nov 2011.

[61] SEMIKRON, “Application Note: 3L NPC & TNPC Topology,” 2012.

[62] Dong-Myung Lee, Jin-Woo Jung and S.-S. Kwak, “Simple Space vector PWM Scheme for 3-level NPC Inverters Including the Overmodulation Region,” *Journal of Power Electronics*, vol. 11, no. 5, 2011.

[63] D. Feng and D. Xu, “Space vector modulation for neutral point clamped multilevel inverter with even order harmonic elimination,” in *Canadian Conference on Electrical and Computer Engineering 2004 (IEEE Cat. No.04CH37513)*, vol. 3. IEEE, 2004, pp. 1471–1475.

[64] L. Helle, S. Munk-Nielsen, and P. Enjeti, “Generalized discontinuous DC-link balancing modulation strategy for three-level inverters,” in *Proceedings of the Power Conversion Conference-Osaka 2002 (Cat. No.02TH8579)*, vol. 2. IEEE, 2002, pp. 359–366.

[65] Hee-Jung Kim, Dae-Woong Jung, and Seung-Ki Sul, “A new discontinuous PWM strategy of neutral-point clamped inverter,” in *Conference Record of the 2000 IEEE Industry Applications Conference. Thirty-Fifth IAS Annual Meeting and World Conference on Industrial Applications of Electrical Energy (Cat. No.00CH37129)*, vol. 3. IEEE, 2000, pp. 2017–2023.

[66] N. Celanovic and D. Boroyevich, “A comprehensive study of neutral-point voltage balancing problem in three-level neutral-point-clamped voltage source PWM inverters,” *IEEE Transactions on Power Electronics*, vol. 15, no. 2, pp. 242–249, mar 2000.

[67] Yao Wenxi, L. Zhengyu, Zhao Rongxiang, Fei Wanmin, and Qiao Zhaoming, “Hysteresis-band control based PWM strategy of three-level neutral-point balance,” in *Twentieth Annual IEEE Applied Power Electronics Conference and Exposition, 2005. APEC 2005.*, vol. 1. IEEE, 2005, pp. 415–418.

[68] Kai Yan, Wei Wang, Zhongni Zhu, and Q. lu, “Study on neutral-point balancing for three-level space voltage vector pulse-width modulation inverter,” pp. 1571–1576, 2008.

[69] S. Busquets-Monge, J. Bordonau, D. Boroyevich, and S. Somavilla, “The nearest three virtual space vector PWM - a modulation for the comprehensive neutral-point balancing in the three-level NPC inverter,” *IEEE Power Electronics Letters*, vol. 2, no. 1, pp. 11–15, mar 2004.

[70] A. K. Gupta and A. M. Khambadkone, “A Simple Space Vector PWM Scheme to Operate a Three-Level NPC Inverter at High Modulation Index Including Overmodulation Region, With Neutral Point Balancing,” *IEEE Transactions on Industry Applications*, vol. 43, no. 3, pp. 751–760, 2007.

[71] G. D. Gretsch and R., “Kompensator fuer oberschwingungen und blindleistung,” *ETZ Archiv*, vol. 9, no. 1, pp. 9–14, 1987.

[72] Ning-Yi Dai, Man-Chung Wong, and Ying-Duo Han, “Three leg center-split inverter controlled by 3D SVM under DC variation,” pp. 1362–1367 Vol.3, 2004.

[73] A. Dastfan, V. Gosbell, and D. Platt, “Control of a new active power filter using 3-D vector control,” *IEEE Transactions on Power Electronics*, vol. 15, no. 1, pp. 5–12, 2000.

[74] V. George and M. Mishra, “User-defined constant switching frequency current control strategy for a four-leg inverter,” *IET Power Electronics*, vol. 2, no. 4, pp. 335–345, jul 2009.

[75] S. R. Naidu and D. A. Fernandes, “Dynamic voltage restorer based on a four-leg voltage source converter,” *Generation, Transmission Distribution, IET*, vol. 3, no. 5, pp. 437–447, 2009.

[76] R. Shan, Z. Yin, X. Xiao, and C. Dai, “A Novel Hybrid Dynamic Reactive Power Compensator,” in *2009 Asia-Pacific Power and Energy Engineering Conference*. IEEE, mar 2009, pp. 1–5.

[77] S. A. Oliveira da Silva, R. A. Modesto, A. Goedtel, and C. F. Nascimento, “Compensation Algorithms Applied to Power Quality conditioners in three-phase four-wire systems,” in *2010 IEEE International Symposium on Industrial Electronics*. IEEE, jul 2010, pp. 730–735.

[78] D. Shen and P. Lehn, “Fixed-frequency space-vector-modulation control for three-phase four-leg active power filters,” *IEE Proceedings - Electric Power Applications*, vol. 149, no. 4, p. 268, 2002.

[79] F. Rojas-Lobos, R. Kennel, and R. Cardenas-Dobson, “3D-SVM algorithm and capacitor voltage balancing in a 4-leg NPC converter operating under unbalanced and non-linear loads,” in *2013 15th European Conference on Power Electronics and Applications (EPE)*. IEEE, sep 2013, pp. 1–10.

[80] Y. Li, D. Vilathgamuwa, and P. Loh, “Microgrid Power Quality Enhancement Using a Three-Phase Four-Wire Grid-Interfacing Compensator,” *IEEE Transactions on Industry Applications*, vol. 41, no. 6, pp. 1707–1719, nov 2005.

[81] M. Dai, M. N. Marwali, J.-W. Jung, and A. Keyhani, “A Three-Phase Four-Wire Inverter Control Technique for a Single Distributed Generation Unit in Island Mode,” *IEEE Transactions on Power Electronics*, vol. 23, no. 1, pp. 322–331, jan 2008.

[82] I. Vechiu, O. Curea, and H. Camblong, “Transient Operation of a Four-Leg Inverter for Autonomous Applications With Unbalanced Load,” *IEEE Transactions on Power Electronics*, vol. 25, no. 2, pp. 399–407, feb 2010.

[83] E. C. dos Santos, C. B. Jacobina, N. Rocha, J. A. A. Dias, and M. B. R. Correa, “Single-phase to three-phase four-leg converter applied to distributed generation system,” *Power Electronics, IET*, vol. 3, no. 6, pp. 892–903, 2010.

[84] N. Mendalek, “Modeling and control of three-phase four-leg split-capacitor shunt active power filter,” in *2009 International Conference on Advances in Computational Tools for Engineering Applications*. IEEE, jul 2009, pp. 121–126.

[85] S. Ceballos, J. Pou, J. Zaragoza, J. Martin, E. Robles, I. Gabiola, and P. Ibanez, “Efficient Modulation Technique for a Four-Leg Fault-Tolerant Neutral-Point-Clamped Inverter,” *IEEE Transactions on Industrial Electronics*, vol. 55, no. 3, pp. 1067–1074, mar 2008.

[86] F. Meinguet and J. Gyselinck, “Control strategies and reconfiguration of four-leg inverter PMSM drives in case of single-phase open-circuit faults,” in *2009 IEEE International Electric Machines and Drives Conference*. IEEE, may 2009, pp. 299–304.

[87] E. Demirkutlu, S. Cetinkaya, and A. M. Hava, “Output Voltage Control of A Four-Leg Inverter Based Three-Phase UPS by Means of Stationary Frame Resonant Filter Banks,” in *2007 IEEE International Electric Machines & Drives Conference*, vol. 1. IEEE, may 2007, pp. 880–885.

[88] Jin Huang, Rui Xiong, Zhi Wang, Wenping Zuo, Yunping Zhou, and Haixia Shi, “A Novel SPWM control strategy to reduce common-mode voltage in three-phase four-leg inverters,” pp. 1526–1530, 2008.

[89] A. Julian, G. Oriti, and T. Lipo, “Elimination of common-mode voltage in three-phase sinusoidal power converters,” *IEEE Transactions on Power Electronics*, vol. 14, no. 5, pp. 982–989, 1999.

[90] P. W. Wheeler, P. Zanchetta, J. C. Clare, L. Empringham, M. Bland, and D. Katsis, “A Utility Power Supply Based on a Four-Output Leg Matrix Converter,” *IEEE Transactions on Industry Applications*, vol. 44, no. 1, pp. 174–186, 2008.

[91] S. Khwan-on, L. de Lillo, P. Wheeler, and L. Empringham, “Fault tolerant four-leg matrix converter drive topologies for aerospace applications,” in *2010 IEEE International Symposium on Industrial Electronics*. IEEE, jul 2010, pp. 2166–2171.

[92] M. Sedlak, S. Stynski, M. P. Kazmierkowski, and M. Malinowski, “Operation of four-leg three-level flying capacitor grid-connected converter for RES,” in *IECON 2013 - 39th Annual Conference of the IEEE Industrial Electronics Society*. IEEE, nov 2013, pp. 1100–1105.

[93] ——, “Control of three-level four-leg flying capacitor converter with active filtering function for RES,” in *2013 Eighth International Conference and Exhibition on Ecological Vehicles and Renewable Energies (EVER)*. IEEE, mar 2013, pp. 1–7.

[94] F. Rojas-Lobos, R. Kennel, and R. Cardenas-Dobson, “Current control and capacitor balancing for 4-leg NPC converters using finite set model predictive control,” in *IECON 2013 - 39th Annual Conference of the IEEE Industrial Electronics Society*. IEEE, nov 2013, pp. 590–595.

[95] P. Verdelho and G. Marques, “Four-wire current-regulated PWM voltage converter,” *IEEE Transactions on Industrial Electronics*, vol. 45, no. 5, pp. 761–770, 1998.

[96] Man-Chung Wong, Zheng-Yi Zhao, Ying-Duo Han, and Liang-Bing Zhao, “Three-dimensional pulse-width modulation technique in three-level power inverters for three-phase four-wired system,” *IEEE Transactions on Power Electronics*, vol. 16, no. 3, pp. 418–427, may 2001.

[97] Man-Chung Wong, Ning-Yi Dai, Jing Tang, and Ying-Duo Han, “Theoretical study of 3 dimensional hysteresis PWM techniques,” pp. 1635–1640 Vol.3, 2004.

[98] R. Zhang, D. Boroyevich, V. Prasad, H.-C. Mao, F. Lee, and S. Dubovsky, “A three-phase inverter with a neutral leg with space vector modulation,” in *Proceedings of APEC 97 - Applied Power Electronics Conference*, vol. 2. IEEE, 1997, pp. 857–863.

[99] W. Wu, Y. He, T. Tang, and F. Blaabjerg, “A New Design Method for the Passive Damped LCL and LLCL Filter-Based Single-Phase Grid-Tied Inverter,” *IEEE Transactions on Industrial Electronics*, vol. 60, no. 10, pp. 4339–4350, oct 2013.

[100] H. Akagi, Y. Kanazawa, and A. Nabae, “Instantaneous Reactive Power Compensators Comprising Switching Devices without Energy Storage Components,” *IEEE Transactions on Industry Applications*, vol. IA-20, no. 3, pp. 625–630, may 1984.

[101] H. Akagi, A. Nabae, and S. Atoh, “Control Strategy of Active Power Filters Using Multiple Voltage-Source PWM Converters,” *IEEE Transactions on Industry Applications*, vol. IA-22, no. 3, pp. 460–465, may 1986.

[102] E. Watanabe, R. Stephan, and M. Aredes, “New concepts of instantaneous active and reactive powers in electrical systems with generic loads,” *IEEE Transactions on Power Delivery*, vol. 8, no. 2, pp. 697–703, apr 1993.

[103] M. M. Kouzou A and B. M.S, *The Space Vector Modulation PWM Control Methods Applied on Four Leg Inverters, Electric Machines and Drives, Dr. Miroslav Chomat*.

[104] S. Ali and M. Kazmierkowski, "PWM voltage and current control of four-leg VSI," in *IEEE International Symposium on Industrial Electronics. Proceedings. ISIE'98 (Cat. No.98TH8357)*, vol. 1. IEEE, 1998, pp. 196–201.

[105] P. Verdelho, "Space vector based current controller in $\alpha\beta0$ coordinate system for the PWM voltage converter connected to the AC mains," in *PESC97. Record 28th Annual IEEE Power Electronics Specialists Conference. Formerly Power Conditioning Specialists Conference 1970-71. Power Processing and Electronic Specialists Conference 1972*, vol. 2. IEEE, 1997, pp. 1115–1120.

[106] Man-Chung Wong, Jing Tang, and Ying-Duo Han, "Cylindrical coordinate control of three-dimensional PWM technique in three-phase four-wired trilevel inverter," *IEEE Transactions on Power Electronics*, vol. 18, no. 1, pp. 208–220, jan 2003.

[107] R. Ghosh and G. Narayanan, "Control of Three-Phase, Four-Wire PWM Rectifier," *IEEE Transactions on Power Electronics*, vol. 23, no. 1, pp. 96–106, jan 2008.

[108] N. Dai, M. Wong, and Y. Han, "Three-dimensional space vector modulation with DC voltage variation control in a three-leg centre-split power quality compensator," *IEE Proceedings - Electric Power Applications*, vol. 151, no. 2, p. 198, 2004.

[109] J.-H. Kim, S.-K. Sul, and P. N. Enjeti, "A Carrier-Based PWM Method With Optimal Switching Sequence for a Multilevel Four-Leg Voltage-Source Inverter," *IEEE Transactions on Industry Applications*, vol. 44, no. 4, pp. 1239–1248, 2008.

[110] P. S. Arne Linder, Rahul Kanchan, Ralph Kennel, *Model-Based Predictive Control of Electric Drives*. Cuvillier Verlag Goettingen, 2010.

[111] K. Astrom, *Introduction to Stochastic Control Theory*. New York: Academic Press, 1970.

[112] C. E. García, D. M. Prett, and M. Morari, "Model predictive control: Theory and practice—A survey," *Automatica*, vol. 25, no. 3, pp. 335–348, may 1989.

[113] P. J. Stolze, "Advanced Finite-Set Model Predictive Control for Power Electronics and Electrical Drives," Ph.D. dissertation, Technischen Universitaet Muenchen, 2013.

[114] V. Yaramasu, B. Wu, M. Rivera, J. Rodriguez, and A. Wilson, "Cost-function based predictive voltage control of two-level four-leg inverters using two step prediction horizon for standalone power systems," in *2012 Twenty-Seventh Annual IEEE Applied Power Electronics Conference and Exposition (APEC)*. IEEE, feb 2012, pp. 128–135.

[115] V. Yaramasu, M. Rivera, M. Narimani, B. Wu, and J. Rodriguez, "Model Predictive Approach for a Simple and Effective Load Voltage Control of Four-Leg Inverter With an Output LC Filter," *Industrial Electronics, IEEE Transactions on*, vol. 61, no. 10, pp. 5259–5270, 2014.

[116] P. Cortes, S. Kouro, B. La Rocca, R. Vargas, J. Rodriguez, J. I. Leon, S. Vazquez, and L. G. Franquelo, "Guidelines for weighting factors design in Model Predictive Control of power converters and drives," in *2009 IEEE International Conference on Industrial Technology*. IEEE, feb 2009, pp. 1–7.

[117] P. C. Jose Rodriguez, *Predictive Control of Power Converters and Electrical Drives*. Wiley-IEEE Press, 2012.

[118] E. Fuentes, D. Kalise, J. Rodriguez, and R. M. Kennel, "Cascade-Free Predictive Speed Control for Electrical Drives," *IEEE Transactions on Industrial Electronics*, vol. 61, no. 5, pp. 2176–2184, may 2014.

[119] P. Delarue, A. Bouscayrol, and E. Semail, "Generic control method of multileg voltage-source-converters for fast practical implementation," *IEEE Transactions on Power Electronics*, vol. 18, no. 2, pp. 517–526, mar 2003.

[120] A. Lega, M. Mengoni, G. Serra, A. Tani, and L. Zarri, "Space Vector Modulation for Multiphase Inverters Based on a Space Partitioning Algorithm," *IEEE Transactions on Industrial Electronics*, vol. 56, no. 10, pp. 4119–4131, oct 2009.

[121] O. Lopez, J. Alvarez, J. Doval-Gandoy, and F. D. Freijedo, “Multilevel Multiphase Space Vector PWM Algorithm,” *IEEE Transactions on Industrial Electronics*, vol. 55, no. 5, pp. 1933–1942, may 2008.

[122] J. I. Leon, O. Lopez, L. G. Franquelo, J. Doval-Gandoy, S. Vazquez, J. Alvarez, and F. D. Freijedo, “Multilevel Multiphase Feedforward Space-Vector Modulation Technique,” *IEEE Transactions on Industrial Electronics*, vol. 57, no. 6, pp. 2066–2075, jun 2010.

[123] ABB, “DTC Eine Motorregelungstechnik für alle Bedingungen,” *White Paper*.

[124] D. Zmood and D. Holmes, “Stationary frame current regulation of PWM inverters with zero steady-state error,” *IEEE Transactions on Power Electronics*, vol. 18, no. 3, pp. 814–822, may 2003.

[125] R. Bojoi, G. Griva, V. Bostan, M. Guerriero, F. Farina, and F. Profumo, “Current Control Strategy for Power Conditioners Using Sinusoidal Signal Integrators in Synchronous Reference Frame,” *IEEE Transactions on Power Electronics*, vol. 20, no. 6, pp. 1402–1412, nov 2005.

[126] L. Limongi, R. Bojoi, G. Griva, and A. Tenconi, “Digital current-control schemes,” *IEEE Industrial Electronics Magazine*, vol. 3, no. 1, pp. 20–31, mar 2009.

[127] R. Bojoi, L. Limongi, D. Roiu, and A. Tenconi, “Frequency-domain analysis of resonant current controllers for active power conditioners,” in *2008 34th Annual Conference of IEEE Industrial Electronics*. IEEE, nov 2008, pp. 3141–3148.

[128] S. Fukuda and T. Yoda, “A novel current-tracking method for active filters based on a sinusoidal internal model [for PWM invertors],” *IEEE Transactions on Industry Applications*, vol. 37, no. 3, pp. 888–895, 2001.

[129] W. Merk, H. Stemmler, and J. Allmeling, “Stationary-frame generalized integrators for current control of active power filters with zero steady-state error for current harmonics of concern under unbalanced and distorted operating conditions,” *IEEE Transactions on Industry Applications*, vol. 38, no. 2, pp. 523–532, 2002.

[130] C. Lascu, L. Asiminoaei, I. Boldea, and F. Blaabjerg, “High Performance Current Controller for Selective Harmonic Compensation in Active Power Filters,” *IEEE Transactions on Power Electronics*, vol. 22, no. 5, pp. 1826–1835, sep 2007.

[131] ——, “Frequency Response Analysis of Current Controllers for Selective Harmonic Compensation in Active Power Filters,” *IEEE Transactions on Industrial Electronics*, vol. 56, no. 2, pp. 337–347, feb 2009.

[132] J. Miret, M. Castilla, J. Matas, J. Guerrero, and J. Vasquez, “Selective Harmonic-Compensation Control for Single-Phase Active Power Filter With High Harmonic Rejection,” *IEEE Transactions on Industrial Electronics*, vol. 56, no. 8, pp. 3117–3127, aug 2009.

[133] D. Basic, V. Ramsden, and P. Muttik, “Harmonic filtering of high-power 12-pulse rectifier loads with a selective hybrid filter system,” *IEEE Transactions on Industrial Electronics*, vol. 48, no. 6, pp. 1118–1127, 2001.

[134] T. Glasberger and Z. Peroutka, “Control of power supply unit for military vehicles based on four-leg three-phase VSI with proportional-resonant controllers,” in *2008 13th International Power Electronics and Motion Control Conference*. IEEE, sep 2008, pp. 1268–1273.

[135] G. Escobar, A. A. Valdez, J. Leyva-Ramos, and P. Mattavelli, “Repetitive-Based Controller for a UPS Inverter to Compensate Unbalance and Harmonic Distortion,” *IEEE Transactions on Industrial Electronics*, vol. 54, no. 1, pp. 504–510, feb 2007.

[136] R. Cardenas, C. Juri, R. Pena, P. Wheeler, and J. Clare, “Resonant controllers for the control of 4-leg Matrix Converters,” pp. 1–10, 2011.

[137] J. D. Barros and J. F. Silva, “Multilevel Optimal Predictive Dynamic Voltage Restorer,” *IEEE Transactions on Industrial Electronics*, vol. 57, no. 8, pp. 2747–2760, aug 2010.

[138] P. Lezana, C. A. Silva, J. Rodrguez, and M. A. Prez, “Zero-Steady-State-Error Input-Current Controller for Regenerative Multilevel Converters Based on Single-Phase Cells,” *IEEE Transactions on Industrial Electronics*, vol. 54, no. 2, pp. 733–740, apr 2007.

[139] M. Bierhoff and F. Fuchs, “Active Damping for Three-Phase PWM Rectifiers With High-Order Line-Side Filters,” *IEEE Transactions on Industrial Electronics*, vol. 56, no. 2, pp. 371–379, feb 2009.

[140] W. M. Rohouma, L. Empringham, P. Zanchetta, and P. W. Wheeler, “A four legs matrix converter based ground power unit with selective harmonic control,” in *2011 IEEE Energy Conversion Congress and Exposition*. IEEE, sep 2011, pp. 799–805.

[141] Zixin Li, Ping Wang, Haibin Zhu, Yaohua Li, Longcheng Tan, Yonggang Chen, and Fanqiang Gao, “A new digital control method for high performance 400 Hz ground power unit,” in *2008 13th International Power Electronics and Motion Control Conference*. IEEE, sep 2008, pp. 515–520.

[142] M. Castilla, “Linear Current Control Scheme With Series Resonant Harmonic Compensator for Single-Phase Grid-Connected Photovoltaic Inverters,” *IEEE Transactions on Industrial Electronics*, vol. 55, no. 7, pp. 2724–2733, jul 2008.

[143] M. Castilla, J. Miret, J. Matas, L. Garcia de Vicuna, and J. Guerrero, “Control Design Guidelines for Single-Phase Grid-Connected Photovoltaic Inverters With Damped Resonant Harmonic Compensators,” *IEEE Transactions on Industrial Electronics*, vol. 56, no. 11, pp. 4492–4501, nov 2009.

[144] C. Liu, F. Blaabjerg, W. Chen, and D. Xu, “Stator Current Harmonic Control With Resonant Controller for Doubly Fed Induction Generator,” *IEEE Transactions on Power Electronics*, vol. 27, no. 7, pp. 3207–3220, jul 2012.

[145] C. Liu, W. Chen, F. Blaabjerg, and D. Xu, “Optimized design of resonant controller for stator current harmonic compensation in DFIG wind turbine systems,” in *2012 Twenty-Seventh Annual IEEE Applied Power Electronics Conference and Exposition (APEC)*. IEEE, feb 2012, pp. 2038–2044.

[146] H. Hu, W. Wei, Y. Peng, and J. Lei, “Optimized design of damped proportional-resonant controllers for grid-connected inverters through genetic algorithm,” in *2014 International Power Electronics and Application Conference and Exposition*. IEEE, nov 2014, pp. 1265–1270.

[147] Hongsheng Wang, Wei Zhang, Jiabing Hu, and Yikang He, “Design and optimization of proportional resonant controller for rotor current of a wind turbine driven DFIG,” pp. 2502–2506, 2008.

[148] P. Mattavelli, “A closed-loop selective harmonic compensation for active filters,” *IEEE Transactions on Industry Applications*, vol. 37, no. 1, pp. 81–89, 2001.

[149] A. G. Yepes, F. D. Freijedo, J. Doval-Gandoy, O. Lopez, J. Malvar, and P. Fernandez-Comesana, “Effects of Discretization Methods on the Performance of Resonant Controllers,” *IEEE Transactions on Power Electronics*, vol. 25, no. 7, pp. 1692–1712, jul 2010.

[150] R. Dorf, Richard; Bishop, *Modern Control Systems*, 10th ed., P. P. Hall, Ed., 2005.

[151] M. S. Graham C. Goodwin, Stefan Greabe, *Control System Design*. Addison Wesley Pub Co Inc, 2000.

[152] L. Jin, Y. Kim, and B. Leon De La Barra, “Issues in Linear Feedback Control Design with Notch Filters,” in *2006 Chinese Control Conference*. IEEE, aug 2006, pp. 102–107.

[153] J. K. Roberge, *Operationa Amplifiers: Theory and Practice*. Wiley, 1975.

[154] Zixin Li, Yaohua Li, Ping Wang, Haibin Zhu, Congwei Liu, and Fanqiang Gao, “Single-Loop Digital Control of High-Power 400-Hz Ground Power Unit for Airplanes,” *IEEE Transactions on Industrial Electronics*, vol. 57, no. 2, pp. 532–543, feb 2010.

[155] W. Rohouma, L. de Lillo, S. Lopez, P. Zanchetta, and P. Wheeler, “A single loop repetitive voltage controller for a four legs matrix converter ground power unit,” pp. 1–9.

[156] M. Liserre, A. Dell’Aquila, and F. Blaabjerg, “Genetic Algorithm-Based Design of the Active Damping for an LCL-Filter Three-Phase Active Rectifier,” *IEEE Transactions on Power Electronics*, vol. 19, no. 1, pp. 76–86, jan 2004.

[157] Y. Tang, P. C. Loh, P. Wang, F. H. Choo, F. Gao, and F. Blaabjerg, “Generalized Design of High Performance Shunt Active Power Filter With Output LCL Filter,” *IEEE Transactions on Industrial Electronics*, vol. 59, no. 3, pp. 1443–1452, mar 2012.

[158] K. Ogata, *Discrete-Time Contro Systems*, 2nd ed. Pearson.

[159] M. Sedighy, S. Dewan, and F. Dawson, “A robust digital current control method for active power filters,” *IEEE Transactions on Industry Applications*, vol. 36, no. 4, pp. 1158–1164, 2000.

[160] A. G. Yepes, “Digital Resonant Current Controllers for Voltage Source Converters,” Ph.D. dissertation, Universidad de Vigo, 2011.

[161] A. G. Yepes, F. D. Freijedo, J. Doval-Gandoy, Ó. Lopez, J. Malvar, and P. Fernandez-Comesaña, “Correction to "Effects of Discretization Methods on the Performance of Resonant Controllers" [Jul 10 1692-1712],” *IEEE Transactions on Power Electronics*, vol. 27, no. 12, pp. 4976–4976, dec 2012.

[162] P. Mattavelli, F. Polo, F. Dal Lago, and S. Saggini, “Analysis of Control-Delay Reduction for the Improvement of UPS Voltage-Loop Bandwidth,” *IEEE Transactions on Industrial Electronics*, vol. 55, no. 8, pp. 2903–2911, aug 2008.

[163] A. M. Trzynadlowski and S. Legowski, “Minimum-loss vector PWM strategy for three-phase inverters,” *Power Electronics, IEEE Transactions on*, vol. 9, no. 1, pp. 26–34, jan 1994.

[164] C. Newton and M. Sumner, “Neutral point control for multi-level inverters: theory, design and operational limitations,” in *Industry Applications Conference, 1997. Thirty-Second IAS Annual Meeting, IAS ’97., Conference Record of the 1997 IEEE*, vol. 2, 1997, pp. 1336–1343 vol.2.

[165] K. Cheng, “Comparative study of AC/DC converters for More Electric Aircraft,” in *Seventh International Conference on Power Electronics and Variable Speed Drives*, vol. 1998. IEE, 1998, pp. 299–304.

[166] T. Wijekoon, L. Empringham, P. W. Wheeler, J. C. Clare, C. Whitley, and G. Towers, “Aircraft Electrical Landing Gear Actuation Using Dual-output Power Converter with Mutual Power Circuit Components,” in *2009 Twenty-Fourth Annual IEEE Applied Power Electronics Conference and Exposition*. IEEE, feb 2009, pp. 1263–1268.

[167] SAE, “AIR6139 Ways of Dealing with Power Regeneration onto an Aircraft Electrical Power System Bus.”

[168] T. B. Owen, J. A. Murray, and A. Rosenstein, “Ground Power Supply for Modern Aircraft,” *Transactions of the American Institute of Electrical Engineers*, vol. 66, no. 1, pp. 1296–1303, jan 1947.

[169] U. Jensen, F. Blaabjerg, and J. Pedersen, “A new control method for 400-Hz ground power units for airplanes,” *IEEE Transactions on Industry Applications*, vol. 36, no. 1, pp. 180–187, 2000.

[170] Muthu, “US5387859 A Stepped waveform VSCF system with engine start capability,” 1993.

[171] S. Lopez Arevalo, P. Zanchetta, P. W. Wheeler, A. Trentin, and L. Empringham, “Control and Implementation of a Matrix-Converter-Based AC Ground Power-Supply Unit for Aircraft Servicing,” *IEEE Transactions on Industrial Electronics*, vol. 57, no. 6, pp. 2076–2084, jun 2010.

[172] D. Floricau, G. Gateau, A. Leredde, and R. Teodorescu, “The efficiency of three-level Active NPC converter for different PWM strategies,” pp. 1–9, 2009.

[173] A. von Jouanne, P. Enjeti, and D. Lucas, “DSP control of high-power UPS systems feeding nonlinear loads,” *IEEE Transactions on Industrial Electronics*, vol. 43, no. 1, pp. 121–125, 1996.

[174] P. Cortes, G. Ortiz, J. Yuz, J. Rodriguez, S. Vazquez, and L. Franquelo, “Model Predictive Control of an Inverter With Output LC Filter for UPS Applications,” *IEEE Transactions on Industrial Electronics*, vol. 56, no. 6, pp. 1875–1883, jun 2009.